Study of Particle Suspensions in Microfluidics for the Development of Optical Devices

Aminuddin Bin Ahmad Kayani

(*Doctor of Philosophy*)

2012

RMIT University

Study of Particle Suspensions in Microfluidics for the Development of Optical Devices

A thesis submitted in fulfillment of the requirements for the degree of Doctor of Philosophy

Aminuddin Bin Ahmad Kayani

BSEE, MBA, MEngSc.

School of Electrical and Computer Engineering
RMIT University
April, 2012

Declaration

I certify that except where due acknowledgement has been made, the work is that of the author alone; the work has not been submitted previously, in whole or in part, to qualify for any other academic award; the content of the thesis is the result of work which has been carried out since the official commencement date of the approved research program; any editorial work, paid or unpaid, carried out by a third party is acknowledged; and, ethics procedures and guidelines have been followed.

.....

Aminuddin Bin Ahmad Kayani

Date: 16th April, 2012.

Acknowledgements

I would like to thank my senior supervisor Associate Professor Kourosh Kalantar-zadeh for providing me the opportunity to conduct my PhD research program under his supervision. In particular, I express my appreciation for his close supervision, creative ideas and technical support during the course of my PhD research project at RMIT University. He has demonstrated great insight in strategizing and planning research activities and he is passionate and genuinely enthusiastic about the research carried out by his students.

I would like to thank my second supervisor, Professor Arnan Mitchell for his valuable supervision and suggestions. In addition, I also wish to thank several current and former researchers and students within the Microplatforms Research Group at the School of Electrical and Computer Engineering (SECE), RMIT University: Dr. Khashayar Khoshmanesh, Dr. Thach Nguyen, Dr. Chen Zhang, Dr. Gorgi Kostovski, Mr. Eike Zeller, Dr. Vijay Sivan, Mr. Adam Chrimes, Mr. Tristan Casto, Mr. Mahyar Nasabi, Ms. Pyshar Yi for their assistance and for providing a conducive atmosphere for conducting the research. I thank Mr. Philip Francis of the Department of Applied Physics, RMIT University, for his guidance in using the scanning electron microscopes and to Mr. Paul Jones, Mr. Yuxun Cao and Ms. Chiping Wu of the Microelectronics, Materials and Technology Centre, RMIT University, for their technical support particularly in using various clean room and micro-machining laboratory equipments.

I would like to thank the Australian Department of Industry, Innovation, Science, Research and Tertiary Education for providing me with the Australian Postgraduate Awards (APA) scholarship. I also thank the SECE for providing me a scholarship top-up. I thank the School of Graduate Research and the Pro Vice Chancellor Research and Innovation's office for providing the International Conference Travel Grant twice, which gave me the opportunity to present at major international conferences. I also thank the Commonwealth Scientific and Industrial Research Organisation (CSIRO) for providing a travel grant, which enabled me to present and attend a conference organized at their research campus in New South Wales, Australia.

Dedication

To my beloved wife, Fararishah and lovely children,

Nazim, Aishah, Husayn and Sara

Abstract

The vision of this PhD research project is to create a microfluidic system for controlling the locations of suspended particles in order to form three dimensional (3D) objects on demand. The author developed a set of objectives to realize this vision which include: (1) Forming a system that can apply suitable and desired forces on particles on demand in microfluidic units (2) Placing particles of various refractive indices close to each other in order to form a media having reconfigurable and tuneable properties (3) Coupling light into such well-controlled particles and testing the concept of forming dynamically tuned objects suspended in liquid by forming optical objects such as optical waveguides.

The author reviewed and considered several active particle manipulation mechanisms for controlling the motion of suspended particles. The dielectrophoretic (DEP) force was selected as it is capable of focusing and scattering suspended particles from pre-determined locations in the microfluidics by the virtue of the polarizability of the particles relative to the suspending medium and vice versa. Additionally, when combined with hydrodynamic forces, the DEP force was able to form densely packed areas of such particles with non-turbulent boundaries. Consequently, using the DEP force, the author showed that the regions of the packed particles in microfluidic channels could demonstrate dynamically reconfigurable optical properties.

The author implemented the research in a staged approach in order to achieve the set objectives. In particular, the research was divided into three stages. In the first stage, the author developed a platform consisting of a microfluidic system integrated with DEP microelectrodes, microfluidics and optical peripherals used for the coupling of light. The author demonstrated the direct coupling of light into the densely packed silicon dioxide (SiO_2) particles with diameters of 230 and 450 nm, respectively. Light was transmitted *via* the closely packed 230 nm particles and in contrast was significantly scattered by the 450 nm particles. The outcomes, which were resulted from this initial stage platform, were the first ever demonstration of a dynamically tuneable optical waveguide based on the DEP focused particles in microfluidics.

In the second stage of this research, the author developed a multi mode polymeric waveguide and integrated it into the microfluidic system combined with the DEP microelectrodes. The goal was to couple light into the densely packed regions *via* the polymeric waveguide to avoid the inlet and outlet scattering. The author used two different types of particles, tungsten trioxide (WO_3) and SiO_2 with diameters of 80 and 450 nm and refractive indices of 2.3 and 1.47, respectively. These refractive indices were either much higher or lower than the refractive index of that of the polymeric waveguide, which was 1.592, formed by a photoresist polymer known as SU-8. It was observed that the densely packed WO_3 particles were able to couple light from the polymeric waveguide, while the SiO_2 particles did not affect the transmission of the optical signals significantly. This was attributed to the fact that the media formed by the DEP focused WO_3 particles had attained a refractive index larger than that of the polymeric waveguide causing the optical waves in the waveguide to couple into the particles. Conversely, the refractive index of the media formed by the densely packed SiO_2 particles could not exceed that of the polymeric waveguide. The investigations of the second stage platform resulted in the first demonstration of optical waveguide tuning based on DEP focused particles.

In the third stage of this research, the author implemented a quasi single mode polymeric waveguide integrated with the microfluidics and the DEP microelectrodes to enhance the platform's performance and to observe the behavior of optical guided modes. The author used WO_3, zinc oxide (ZnO) and SiO_2 particles with diameters of 80, 50 and 72 nm and refractive indices of 2.3, 2.0 and 1.47, respectively. Under the DEP force influence, the packed areas of these particles were able to interact with the optical guided waves of the quasi single mode waveguide and alter their behavior. Interestingly, the author discovered that when WO_3 particles were packed, they became capable of forming resonant and anti-resonant layers when focused under the DEP force. In particular, the fundamental mode of the polymeric waveguide could be strongly coupled to the regions of densely packed WO_3 particles. However, under certain DEP focusing conditions, which resulted in specific particle concentrations and media refractive index profiles, the first order mode of the optical waves remained largely isolated and was anti-resonant to the layer of closely packed WO_3 particles. Such interesting behavior of the third stage platform resulted in the first demonstration of the dynamic manipulation and coupling of optical

guided modes using DEP focused particles. Additionally, it was also the first demonstration of establishing dynamic layers consisting of packed particles using the DEP force, which exhibited resonant and anti-resonant behaviors towards the optical guided optical modes in a polymeric waveguide.

List of Symbols

n	refractive index
ε	permittivity
μ	permeability
d_s	inter particle spacing
d_p	particle diameter
Re_d	Reynolds number
ρ_m	fluid medium density
v_f	average velocity of the medium inside the microchannel
L	length of the equivalent diameter of the microchannel
μ_m	fluid viscosity
F_{drag}	drag force
r	particle radius
$\bar{U}$	average velocity of the medium inside the microchannel
F_r	acoustic force
P_0	pressure amplitude of the acoustic wave
V_p	particle volume
β	particle/liquid compressibility
ρ	particle/liquid density
λ	wavelength of the acoustic wave
x	distance to the nearest pressure node
F_{el}	electrophoretic force
F_{fr}	friction force
F_{ret}	electrophoretic retardation force
μ_{el}	electrophoretic mobility

κ^{-1}	Debye length
ε_r	relative permittivity
ζ	Zeta potential
η	viscosity of liquid
ε_o	permittivity of vacuum (8.854×10^{-12} F m^{-1})
$f_{CM}(\omega)$	Clausius-Mossotti factor
Re[$f_{CM}(\omega)$]	real part of the Clausius-Mossotti factor
Im[$f_{CM}(\omega)$]	imaginary part of the Clausius-Mossoti factor
ε_p^*	complex permittivity of the particle
ε_m^*	complex permittivity of the suspending medium
σ_m	medium conductivity
σ_p	particle conductivity
ω	angular frequency of the applied electric field
J	mass flux of particle flow
c	particle concentration
D	Brownian diffusion coefficient
D_T	thermal diffusion coefficient
∇T	temperature gradient
F_{grad}	optical gradient force
∇I_o	gradient of light intensity
c_o	speed of light (3×10^8 m s^{-1})
k	absorption coefficient
F_{scat}	scattering force
F_{abs}	absorption force
F_{mag}	magnetic force
χ_p	magnetic susceptibility of the particle
χ_m	magnetic susceptibility of the suspending medium

μ_o	permeability of free space ($4\pi \times 10^{-7}$ H m^{-1})
E	non uniform electric field
P	dipole moment of a polarizable particle
φ	phase component of the applied electric field
t	time
∇E	gradient of the electric field
E_{rms}	root mean square of the electric field
V_p	peak voltage
$n_{DI\text{-}water}$	refractive index of deionized water
n_{SiO2}	refractive index of silicon dioxide
n_{WO3}	refractive index of tungsten trioxide
n_{ZnO}	refractive index of zinc oxide
f	frequency
x,y,z	three dimensional reference lines used for simulating electric fields
n_{liq}	refractive index of liquid
$n_{SU\text{-}8}$	refractive index of SU-8
n_{KMPR}	refractive index of KMPR
Δn	refractive index contrast
M	number of modes
NA	numerical aperture
APF	atomic packing factor
n_{max}	maximum refractive index
$pf_{particle}$	packing fraction of particle
$pf_{suspending\text{-}media}$	packing fraction of the suspending media
$n_{particle}$	refractive index of the particle material
$n_{suspending\text{-}media}$	refractive index of the suspending media

$n_{waveguide}$	refractive index of the waveguide
n_{min}	minimum refractive index
n_{media}	media refractive index

List of Abbreviations

AC	alternating current
ARROW	Anti Resonant Reflecting Optical Waveguide
ADS	Advanced Design System
CCD	charged couple device
cm	centimeter
DEP	Dielectrophoretic
DI	deionized
FDTD	Finite Difference Time Domain
IR	Infrared
kHz	kilo Hertz
min	minute
mJ	milli Joule
mm	millimeter
mS	milli Siemen
MHz	mega Hertz
nm	nanometer
sec	seconds
SiO_2	silicon dioxide
SEM	scanning electron microscope
TE	transverse electric
v/v	volume-in-volume
WO_3	tungsten trioxide
w/w	weight-in-weight
ZnO	zinc oxide

List of Figures

Table of Contents

Chapter 1

Introduction

1.1 Motivations

The field of optofluidics refers to the integration of microfluidics and optics into the same platform, where fluids and light are driven to interact [1]. This integration has led to the realization of a wide range of applications which have impacted upon different areas of engineering, chemistry and life sciences. Such applications include platforms for forming liquid optical components [2], microscopy and imaging systems [3, 4], flow cytometers [5] and optofluidic platforms incorporating Raman specstroscopy analysis [6]. Optofluidic systems have also been used for biological and chemical sensing with extremely small detection volumes (femtolitres to nanolitres) [7-9]. This is possible because many optical properties, such as refractive index, fluorescence, Raman scattering, absorption and polarization, can be exploited in microfluidics to generate and enhance the desired sensing signal [10].

One of the most researched types of optofluidic systems are those which are categorized as "multi-phase". "Multi-phase" optofluidics refers to a system that consist of homogenous

liquids of varying physical, chemical or optical properties [11]. The advantages of multi-phase systems include liquid mobility, large ranges of index modulation and abrupt interfaces that can be easily reshaped [12, 13]. The development of such systems has resulted in numerous liquid optical components such as liquid waveguides [14-18], attenuators [19], lasers [20, 21], filters [22, 23], switches [24, 25] and lenses [26, 27].

However, the implementation of multi-phase systems is not perceived as representing the most flexible or elegant approach, as liquids either do not easily mix or when they are miscible, they are not easily separated or reconfigured. Moreover, these systems generally rely on homogeneous liquids with fixed properties. One means of addressing this shortcoming is to use liquid with suspended micro/nano particles, which is the aim of this PhD research project.

The properties of a particle suspension can be tuned from those of liquid to that of the suspended particles by adjusting the particle concentration (Figure 1.1). When suspended particles are dispersed at low concentrations (Figure 1.1A), the physical properties of the media such as the refractive index (n), permittivity (ε) and permeability (μ) values are closer to that of the suspending media. Alternatively, when they are closely packed, then these properties are close to that of the particles themselves (Figure 1.1B) [15].

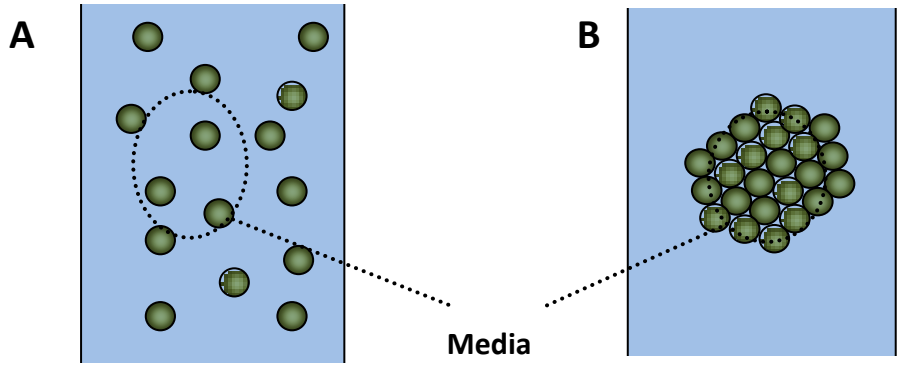

Figure 1.1: Tuning the media properties using suspended particles: (A) Properties of a media with particles dispersed at low concentrations are close to those of the suspending media. (B) Properties of closely packed particles in a suspending media are close to those of the particles.

Particle dimensions play an important role in their interactions with light [28]. Relative to the optical wavelength, and depending on the particles' dimensions and inter particle spacing, light incident on an assembly of particles can either be deflected (reflected, refracted and/or diffracted) and/or absorbed (Figure 1.2) [29-31]. For instance, if particles are randomly dispersed in a suspension and the particle size and inter particle spacings are comparable or larger than that of the wavelength of the coupled light, the incident light will experience significant deflection (Figure 1.2A). Conversely, if the particles are much smaller than the wavelength of the coupled light, then light will not be deflected by the individual particles. In fact, when they are closely packed (such that the inter particle spacings become much smaller than the wavelength), they can be perceived as a single phase homogenous medium [32] that promotes the transmission of light (Figure 1.2B) [33]. However, the challenge associated with the implementation of particles is the ability to control their location: *placing them, precisely where they are needed, when desired*. Therefore, there is a need to have particle manipulation mechanisms that are able to dictate the particles' motion accurately in liquid.

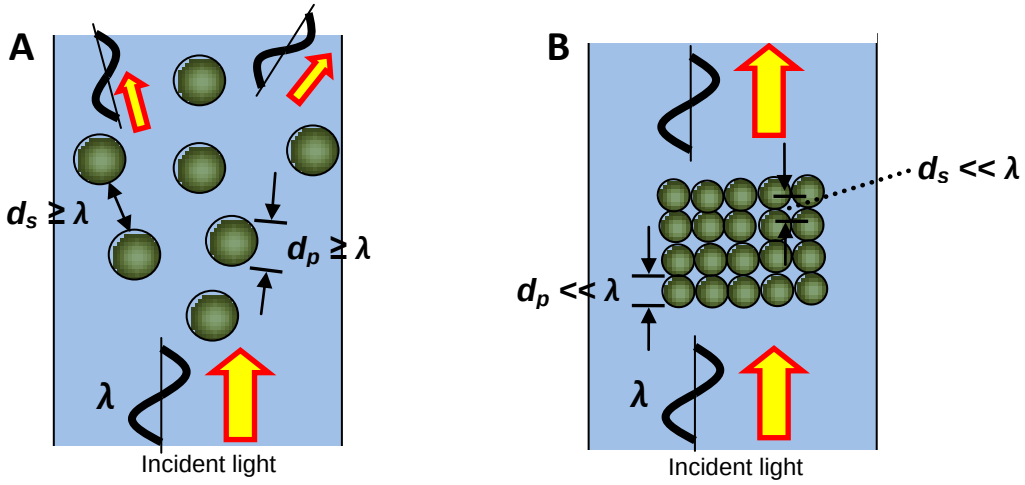

Figure 1.2: Scattering and transmission of light via a suspension of particles: (A) Light incident on suspended particles with random inter particle spacings, d_s and diameters, d_p, much larger than the optical wavelength. Incident light is mostly scattered (B) Light incident on closely packed particles with inter particle spacings and diameters, much smaller compared to the optical wavelength. Incident light is mostly transmitted.

Particles can be manipulated either “passively” or “actively”. Passive manipulation forces include Van der Waals attraction [34], self assembly [35], stearic interaction [36], Brownian motion [37] and charged dipole interaction [38]. Unfortunately, such passive manipulation techniques [39-42] are not capable of high levels of control, consistency and repeatability [43]. In contrast, active forces are externally applied and are able to provide particle displacements and motional trajectories which are consistent and precise to a high degree of accuracy. The opportunities for realizing optofluidic systems incorporating such precise particle motions are therefore much more promising. For example, in biological/chemical sensing, active manipulation forces can place suspended particles at desired locations in the fluidics and sort or separate them according to their properties as a preparative procedure before the particles undergo some form of analysis or interrogation. Such active forces are classified into mechanical [44-48], electrical [49-53], optical [54, 55], thermal [56-58] and magnetic [59-61] force categories.

Among the manipulation mechanisms that can be integrated into microfluidic systems, electrical forces have widely been implemented [62-66]. The two electrical forces used to manipulate suspended particles are electrophoresis and dielectrophoresis. Electrophoresis refers to the process of manipulating charged particles using applied electric fields [67]. Dielectrophoresis refers to the manipulation of neutral particles using non-uniform electric fields [50, 68].

Dielectrophoresis was first discovered by Herbert Pohl [69] in the 1950’s. Since then, dielectrophoretic (DEP) systems have been used for a wide range of applications that among others include particle separation [70], trapping [71], sorting [72, 73], detection [74], characterization [74, 75], filtration [76] and patterning [77]. DEP forces can be either positive or negative, depending on the polarizability of the particles and the suspending medium. Positive DEP forces attract particles to the regions of high electric field gradients; negative DEP forces repel them from such regions [78]. The DEP force can be used to concentrate or disperse the particles at predetermined locations depending on their polarization and the magnitude and frequency of the applied electric field.

In this thesis, the author has used the DEP force to manipulate the motion of the particles. The DEP force was chosen as the author found that it could provide the best form of applied force for manipulating neutral and semi-conducting particles efficiently. For instance, by

applying DEP forces of varying frequencies, the author was able to focus and repel particles from regions of high electric field gradients based on their permittivity and conductivity properties relative to the suspending media or vice versa. The strength of the applied forces can be simply adjusted by tuning the DEP signal amplitudes. In addition, in the early stages of the PhD research project, the author was introduced to the curved microelectrode design [79], which was capable of concentrating particles in between the tips of the microelectrode pairs where the electric field gradients are highest. The author used the concept and developed an improvised microelectrode design which was capable of producing dense particle streams, imitating optical waveguides within microfluidics, when combined with hydrodynamic forces from the microfluidic flow.

Through his investigations the author found that under positive DEP forces, the distribution of particles across the microfluidic channel formed a refractive index profile resembling that of a waveguide, with smooth and well defined boundaries. In particular, the author hypothesized that the dense particle stream could represent the "core of the waveguide" having a higher average refractive index compared to the "cladding of the waveguide" composed of media surrounding the particle stream (which may have consisted of dispersed particles in low concentrations).

The author intended to investigate whether the dense particles acted as waveguiding or scattering channels in the liquid. He integrated a microfluidic platform ("Platform 1") which consisted of DEP microelectrodes and a microfluidic chip with an optical apparatus used for coupling visible light into the focused particles. Visible light ($\lambda \sim 635$ nm) was chosen as it was easily observed under the microscope and could be captured by charged couple device cameras. The author conducted the investigations using silicon dioxide (SiO_2) particles of 230 and 450 nm diameters. He chose such particles due their inert nature and that they could be easily suspended. The sizes were chosen as the dimensions of the SiO_2 particles were either smaller or almost comparable to the wavelength of the incident light to see the waveguiding and scattering behaviors. When light was coupled into the DEP focused particles, as anticipated, the smaller particles promoted the transmission of light while the larger particles deflected the light.

Despite the great results achieved using Platform 1, the author felt that the demonstrations were rather crude as light was coupled directly into the microfluidics via media interfaces

and particles flowing into and out of the fluidic reservoirs causing significant deflections of light. As a result, he devised an approach to improve the platform so that light could be coupled into the densely packed particles more efficiently and with minimal interferences.

Hence, a multimode polymeric waveguide was designed by the author. He used a polymeric waveguide as it could be integrated into the microfluidic platform relatively easily using advanced microfabrication methods and such waveguides could be enclosed directly by liquid media to enable the highest interaction between the optical waves and the suspended particles. “Platform 2” was developed by the author such that the waveguide was positioned in the center of the curved microelectrodes where the particles were found to be densely concentrated under the positive DEP force.

Implementing Platform 2, the visible light was coupled into the multi mode waveguide and particles were dispersed in the microfluidics and subjected to the DEP forces. The author realized that in order for light to couple out of the waveguide, the refractive index of the media formed by the particles had to be higher than that of the waveguide. He chose tungsten trioxide (WO_3) as a suitable particle candidate as it had a higher refractive index compared to the polymeric waveguide and also was readily suspendable. The author also found that, just as in the case of the SiO_2 particles, the WO_3 particles could also be forced into forming dense particle streams and then be repelled using the DEP forces. For comparison in the second set of experiments, he used WO_3 particles while SiO_2 particles were used for benchmarking, since SiO_2 has a lower refractive index compared to the polymeric waveguide. The outcome was that the author was able to couple light from the multi mode waveguide into the DEP focused WO_3 particles, while light was not coupled in the case of the SiO_2 particles. This was a great demonstration for the versatility of the system.

At this stage of the research, the author had established that light can be coupled into the DEP focused particles and in fact, a crude version of a tuneable waveguide based on DEP controlled particles was realized. The author decided to further enhance this platform as a template for accurate optofluidic waveguiding and sensing incorporating well controlled suspended particles. Considering the limitation of Platform 2, allowing the propagation of multi mode, it was difficult to trace the behavior of individual modes, extract information or obtain definitive evidence regarding the interaction of the optical waves with the suspended

particles and media surrounding them. In addition, modal dispersions and propagation losses were high in multi mode platforms, hence inhibiting the potential development of this Platform as a sensor with low detection limits. To make the system more robust, the author decided to introduce a quasi single mode waveguide into the subsequent platform ("Platform 3").

In this platform, the author again took advantage of the WO_3 particles as they were proven capable of coupling light from the multi mode waveguides, due to their high refractive index, and the control of their motions were well established in the preceding experiments. The developed platform was a quasi single mode system. Using such a platform, the author was able to observe distinct modal behaviours, which was previously unnoticeable using the multi mode platform. For instance, under certain applied DEP conditions, the fundamental mode transitioned into the first order mode and gradually faded away. The author then correlated the experimental results with simulations of the particle packing concentrations and the waveguide modes in the fluidics to understand the phenomena. The author established that under certain particle packing concentrations, the fundamental mode was completely coupled into the DEP focused particles, while the first order mode remained isolated in the waveguide. The analyses also reaffirmed that DEP focused particles could act as waveguiding media and that light could be coupled into the dense concentration of particles. The author managed to show that by manipulating the concentration of particles using the DEP forces, specific waveguide modes could be coupled into or isolated from the packed particles.

All in all, the objectives of the PhD research project were accomplished adding significant and novel discoveries to the body of knowledge in this field. The results obtained in each stage of research led to the significant achievements for the author which is described in the following section.

1.2 Achievements

This PhD research project has successfully produced a significant contribution to the field of optofluidics and dynamically controlled particles. The major outcomes from this PhD research program may be summarized as follows:

- To the best of the author's knowledge, the manipulation of SiO_2 particles and the use of optical lasers to investigate the transmission of light via closely packed particles was demonstrated for the first time using dielectrophoresis. The work demonstrated the ability of DEP focused SiO_2 particles to act as dynamically controlled tuneable particle waveguides in liquid. This work was published in two journals, "*Electrophoresis*" [80] and "*Applied Physics Letters*" [81].

- The author designed and fabricated a multi mode waveguide integrated with DEP microelectrodes and microfluidics. The work demonstrated that multi mode light can be coupled quite efficiently to the DEP focused WO_3 particles under specific particle assembly conditions. The demonstration of such a tuneable waveguide based on dielectrophoretically controlled particles has not been demonstrated before in literature. This work was published in the journal, "*Microfluidics and Nanofluidics*" [82].

- The author proceeded to fabricate a quasi single mode platform in the final stage of his research. WO_3 particles were used to couple light from the single mode waveguide. It was discovered that resonant and anti-resonant layers of packed particles were formed using DEP force. Further, it was established that selected modes were strongly coupled and isolated from dense particle concentrations. Both, the formation of resonant and anti-resonant layers of particles using DEP forces and the coupling and isolation of modes of quasi single mode light into DEP focused particles were demonstrated for the first time. This work was published in the journal, "*Electrophoresis*" [83].

- The author published a critical review paper entitled "Optofluidics Incorporating Actively Controlled Micro- and Nano-particles". In this review, the author presented active particle manipulation forces in microfluidics and the application of controllable particles in optofluidic systems. Particle manipulation forces include electrical, mechanical, optical,

thermal and magnetic forces. The applications of such controllable particles include optical components, particle detection and analysis platforms, particle transport, plasmonics and Raman systems, thermal and energy related platforms and bio-related systems. This review article was published in the Journal of Biomicrofluidics [84].

To summarize, out of these achievements, several key outcomes have been published in referred journals and presented at international conferences. These include:

A) Three first authored and five co-authored publications in refereed journals, which include: (1) *Electrophoresis* (3 papers), *Microfluidics and Nanofluidics* (2 papers), *Applied Physics Letters* (1 paper), *Lab on a Chip* (1 paper) and Analytical Chemistry (1 paper).

B) One first authored critical review paper: (1) *Biomicrofluidics* (1 paper)

C) Six first authored publications in the proceedings of international conferences. The author's work has been presented both personally and on his behalf at several international conferences as follows:

- 2nd Nano Today Conference, Waikoloa, Hawaii, USA, 11-15 December, 2011.
- 1st European Optical Society (EOS) Conference on Optofluidics 2011, Munich, Germany, 23-25 May, 2011.
- Conference on Lasers and Electro Optics (CLEO) 2011, Baltimore, Maryland, USA, 1-5 May, 2011.
- SPIE International Symposium on Defense, Security and Sensing, Orlando, Florida, USA, 25-29 April, 2011.
- 2nd European Conference on Microfluidics 2010, Toulouse, France, December 8-10, 2010.
- American Institute of Chemical Engineers Annual Meeting 2010, Salt Lake City, UT, USA, November 7-12, 2010.

1.3 Thesis Organization

This thesis is primarily dedicated to investigating the manipulation of suspended particles using the DEP force and the coupling of light into the DEP controlled particles. The major sections of this thesis are listed as below:

Chapter 2 provides the literature review of this thesis. This chapter begins with a description of active particle manipulation forces in microfluidics. Subsequently, the author provides examples of optofluidic systems which incorporate suspended particles and an extended review of the DEP force.

Chapter 3 describes the design and fabrication of the experimental platforms used in this PhD thesis. There were three platforms developed and each of these platforms were used for each stage of the PhD research project.

Chapter 4 presents the direct coupling of light into the DEP focused particles using Platform 1. SiO_2 particles of two distinct diameters, 230 and 450 nm were focused using the DEP force. Subsequently, light was directly coupled into the densely packed particle concentration and the optical responses were recorded and investigated.

Chapter 5 presents the coupling of light into the DEP focused particles via a multi mode polymeric waveguide using Platform 2. SiO_2 and WO_3 particles of 450 and 80 nm diameters, respectively were focused in close vicinity of the polymeric waveguide. Light was then coupled into the DEP focused particles and the optical responses for both particle types were analyzed.

Chapter 6 presents the implementation of a quasi single polymeric waveguide used for the coupling of light into the DEP focused particles using Platform 3. WO_3, ZnO and SiO_2 particles with diameters 80, 50 and 72 nm, respectively were used to analyze the interaction of optical guided modes with the DEP focused particles. The coupling and isolation of the optical guided modes were investigated.

Finally, chapter 7 presents the concluding remarks and suggests possible future works.

References

[1] Monat, C., P. Domachuk, C. Grillet, M. Collins, B. Eggleton, M. Cronin-Golomb, S. Mutzenich, T. Mahmud, G. Rosengarten, and A. Mitchell, Optofluidics: a novel generation of reconfigurable and adaptive compact architectures. *Microfluidics and Nanofluidics*, vol. 4, pp. 81-95, 2008.

[2] Erickson, D., T. Rockwood, T. Emery, A. Scherer, and D. Psaltis, Nanofluidic tuning of photonic crystal circuits. *Optics Letters*, vol. 31, pp. 59-61, 2006.

[3] Cui, X., L.M. Lee, X. Heng, W. Zhong, P.W. Sternberg, D. Psaltis, and C. Yang, Lensless high-resolution on-chip optofluidic microscopes for Caenorhabditis elegans and cell imaging. *Proceedings of the National Academy of Sciences of the United States of America*, vol. 105, pp. 10670-10675, 2008.

[4] Vig, A.L., R. Marie, E. Jensen, and A. Kristensen, Optofluidic microscope with 3D spatial resolution. *Optics Express*, vol. 18, pp. 4158-4169, 2010.

[5] Cho, S.H., J.M. Godin, C.-H. Chen, W. Qiao, H. Lee, and Y.-H. Lo, Review Article: Recent advancements in optofluidic flow cytometer. *Biomicrofluidics*, vol. 4, 2010.

[6] Lim, C., J. Hong, B.G. Chung, A.J. deMello, and J. Choo, Optofluidic platforms based on surface-enhanced Raman scattering. *Analyst*, vol. 135, pp. 837-844, 2010.

[7] Mandal, S., J.M. Goddard, and D. Erickson, A multiplexed optofluidic biomolecular sensor for low mass detection. *Lab on a Chip*, vol. 9, pp. 2924-2932, 2009.

[8] Measor, P., L. Seballos, D. Yin, J.Z. Zhang, E.J. Lunt, A.R. Hawkins, and H. Schmidt, On-chip surface enhanced Raman scattering detection using integrated liquid core waveguides. *Applied Physics Letters*, vol. 90, pp. 211107-1 to 211107-3, 2007.

[9] Hunt, H.C. and J.S. Wilkinson, Optofluidic integration for microanalysis. *Microfluidics and Nanofluidics*, vol. 4, pp. 53-79, 2008.

[10] Fan, X. and I.M. White, Optofluidic microsystems for chemical and biological analysis. *Nature Photonics*, vol. 5, pp. 591-597, 2011.

[11] Fainman, Y., *Optofluidics: Fundamentals, Devices, and Applications*. 2010, New York: McGraw-Hill.

[12] Monat, C., P. Domachuk, and B.J. Eggleton, Integrated optofluidics: A new river of light. *Nature Photonics*, vol. 1, pp. 106-114, 2007.

[13] Psaltis, D., S.R. Quake, and C. Yang, Developing optofluidic technology through the fusion of microfluidics and optics. *Nature*, vol. 442, pp. 381-386, 2006.

[14] Schmidt, H. and A.R. Hawkins, Optofluidic waveguides: I. Concepts and implementations. *Microfluidics and Nanofluidics*, vol. 4, pp. 3-16, 2008.

[15] Hawkins, A.R. and H. Schmidt, Optofluidic waveguides: II. Fabrication and structures. *Microfluidics and Nanofluidics*, vol. 4, pp. 17-32, 2008.

[16] Li, X.C., J. Wu, A.Q. Liu, Z.G. Li, Y.C. Soew, H.J. Huang, K. Xu, and J.T. Lin, A liquid waveguide based evanescent wave sensor integrated onto a microfluidic chip. *Applied Physics Letters*, vol. 93, pp. 193901, 2008.

[17] Lim, J.-M., J.P. Urbanski, J.-H. Choi, T. Thorsen, and S.-M. Yang, Liquid Waveguide-Based Evanescent Wave Sensor That Uses Two Light Sources with Different Wavelengths. *Analytical Chemistry*, vol. 83, pp. 585-590, 2011.

[18] Mayers, B.T., D.V. Vezenov, V.I. Vullev, and G.M. Whitesides, Arrays and Cascades of Fluorescent Liquid−Liquid Waveguides: Broadband Light Sources for Spectroscopy in Microchannels. *Analytical Chemistry*, vol. 77, pp. 1310-1316, 2005.

[19] Zhu, L., Y.Y. Huang, and A. Yariv, Integrated microfluidic variable optical attenuator. *Optics Express*, vol. 13, pp. 9916-9921, 2005.

[20] Galas, J.C., J. Torres, M. Belotti, Q. Kou, and Y. Chen, Microfluidic tunable dye laser with integrated mixer and ring resonator. *Applied Physics Letters*, vol. 86, 2005.

[21] Li, Z.Y., Z.Y. Zhang, T. Emery, A. Scherer, and D. Psaltis, Single mode optofluidic distributed feedback dye laser. *Optics Express*, vol. 14, pp. 696-701, 2006.

[22] Mach, P., M. Dolinski, K.W. Baldwin, J.A. Rogers, C. Kerbage, R.S. Windeler, and B.J. Eggleton, Tunable microfluidic optical fiber. *Applied Physics Letters*, vol. 80, pp. 4294-4296, 2002.

[23] Levy, U., K. Campbell, A. Groisman, S. Mookherjea, and Y. Fainman, On-chip microfluidic tuning of an optical microring resonator. *Applied Physics Letters*, vol. 88, 2006.

[24] Groisman, A., S. Zamek, K. Campbell, L. Pang, U. Levy, and Y. Fainman, Optofluidic 1x4 switch. *Optics Express*, vol. 16, pp. 13499-13508, 2008.

[25] Seow, Y.C., S.P. Lim, and H.P. Lee, Tunable optofluidic switch via hydrodynamic control of laminar flow rate. *Applied Physics Letters*, vol. 95, pp. 114105, 2009.

[26] Li, H., T.N. Wong, and N.-T. Nguyen, A tunable optofluidic lens based on combined effect of hydrodynamics and electroosmosis. *Microfluidics and Nanofluidics*, vol. 10, pp. 1033-1043, 2011.

[27] Nguyen, N.T., Micro-optofluidic Lenses: A review. *Biomicrofluidics*, vol. 4, pp. 031501-031516, 2010.

[28] de Abajo, F.J.G., Colloquium: Light scattering by particle and hole arrays. *Reviews of Modern Physics*, vol. 79, pp. 1267-1290, 2007.

[29] Tribelsky, M.I., Anomalous light absorption by small particles. *Europhysics Letters*, vol. 94, pp. 14004, 2011.

[30] Wriedt, T., A review of elastic light scattering theories. *Particle & Particle Systems Characterization*, vol. 15, pp. 67-74, 1998.

[31] Chylek, P., G.W. Grams, and R.G. Pinnick, Light-scattering by irregular randomly oriented particles. *Science*, vol. 193, pp. 480-482, 1976.

[32] Johnson, P., Light scattering in the study of colloidal and macromolecular systems. *International Reviews in Physical Chemistry*, vol. 12, pp. 61-87, 1993.

[33] Blaustein, G.S., M.I. Gozman, O. Samoylova, I.Y. Polishchuk, and A.L. Burin, Guiding optical modes in chains of dielectric particles. *Optics Express*, vol. 15, pp. 17380-17391, 2007.

[34] Hamaker, H.C., The London - Van Der Waals attraction between spherical particles. *Physica*, vol. 4, pp. 1058-1072, 1937.

[35] Glotzer, S.C., M.J. Solomon, and N.A. Kotov, Self-assembly: From nanoscale to microscale colloids. *Aiche Journal*, vol. 50, pp. 2978-2985, 2004.

[36] Larson-Smith, K. and D.C. Pozzo, Scalable synthesis of self-assembling nanoparticle clusters based on controlled steric interactions. *Soft Matter*, vol. 7, pp. 5339-5347, 2011.

[37] Russel, W.B., Brownian-motion of small particles suspended in liquids. *Annual Review of Fluid Mechanics*, vol. 13, pp. 425-455, 1981.

[38] Walker, D.A., C.E. Wilmer, B. Kowalczyk, K.J.M. Bishop, and B.A. Grzybowski, Precision Assembly of Oppositely and Like-Charged Nanoobjects Mediated by Charge-Induced Dipole Interactions. *Nano Letters*, vol. 10, pp. 2275-2280, 2010.

[39] Boeker, A., J. He, T. Emrick, and T.P. Russell, Self-assembly of nanoparticles at interfaces. *Soft Matter*, vol. 3, pp. 1231-1248, 2007.

[40] Bishop, K.J.M., C.E. Wilmer, S. Soh, and B.A. Grzybowski, Nanoscale Forces and Their Uses in Self-Assembly. *Small*, vol. 5, pp. 1600-1630, 2009.

[41] Liang, Y., N. Hilal, P. Langston, and V. Starov, Interaction forces between colloidal particles in liquid: Theory and experiment. *Advances in Colloid and Interface Science*, vol. 134-35, pp. 151-166, 2007.

[42] Di Carlo, D., Inertial microfluidics. *Lab on a Chip*, vol. 9, pp. 3038-3046, 2009.

[43] Tsutsui, H. and C.-M. Ho, Cell separation by non-inertial force fields in microfluidic systems. *Mechanics Research Communications*, vol. 36, pp. 92-103, 2009.

[44] Rhodes, M.J., *Introduction to particle technology*. 2nd ed. 2008, Hoboken: Wiley. 450.

[45] Guha, A., *Transport and deposition of particles in turbulent and laminar flow*, in *Annual Review of Fluid Mechanics*. 2008. p. 311-341.

[46] Whitesides, G.M., The origins and the future of microfluidics. *Nature*, vol. 442, pp. 368-373, 2006.

[47] Batchelor, G.K., *An Introduction to Fluid Dynamics*. 1999, Cambridge: Cambridge University Press.

[48] Friend, J. and L.Y. Yeo, Microscale acoustofluidics: Microfluidics driven via acoustics and ultrasonics. *Reviews of Modern Physics*, vol. 83, pp. 647-704, 2011.

[49] Zhang, C., K. Khoshmanesh, A. Mitchell, and K. Kalantar-zadeh, Dielectrophoresis for manipulation of micro/nano particles in microfluidic systems. *Analytical and Bioanalytical Chemistry*, vol. 396, pp. 401-420, 2010.

[50] Pethig, R., Review Article-Dielectrophoresis: Status of the theory, technology, and applications. *Biomicrofluidics*, vol. 4, 2010.

[51] Khoshmanesh, K., S. Nahavandi, S. Baratchi, A. Mitchell, and K. Kalantar-zadeh, Dielectrophoretic platforms for bio-microfluidic systems. *Biosensors & Bioelectronics*, vol. 26, pp. 1800-1814, 2011.

[52] Kleparnik, K. and P. Bocek, Electrophoresis today and tomorrow: helping biologists' dreams come true. *Bioessays*, vol. 32, pp. 218-226, 2010.

[53] Gas, B., Theory of electrophoresis: Fate of one equation. *Electrophoresis*, vol. 30, pp. S7-S15, 2009.

[54] Erickson, D., X. Serey, Y.F. Chen, and S. Mandal, Nanomanipulation using near field photonics. *Lab on a Chip*, vol. 11, pp. 995-1009, 2011.

[55] Jonas, A. and P. Zemanek, Light at work: The use of optical forces for particle manipulation, sorting, and analysis. *Electrophoresis*, vol. 29, pp. 4813-4851, 2008.

[56] Parola, A. and R. Piazza, Particle thermophoresis in liquids. *European Physical Journal E*, vol. 15, pp. 255-263, 2004.

[57] Piazza, R. and A. Parola, Thermophoresis in colloidal suspensions. *Journal of Physics-Condensed Matter*, vol. 20, 2008.

[58] Vigolo, D., R. Rusconi, H.A. Stone, and R. Piazza, Thermophoresis: microfluidics characterization and separation. *Soft Matter*, vol. 6, pp. 3489-3493, 2010.

[59] Suwa, M. and H. Watarai, Magnetoanalysis of micro/nanoparticles: A review. *Analytica Chimica Acta*, vol. 690, pp. 137-147, 2011.

[60] Peyman, S.A., E.Y. Iwan, O. Margarson, A. Iles, and N. Pamme, Diamagnetic repulsion-A versatile tool for label-free particle handling in microfluidic devices. *Journal of Chromatography A*, vol. 1216, pp. 9055-9062, 2009.

[61] Gosse, C. and V. Croquette, Magnetic tweezers: Micromanipulation and force measurement at the molecular level. *Biophysical Journal*, vol. 82, pp. 3314-3329, 2002.

[62] Cetin, B. and D. Li, Dielectrophoresis in microfluidics technology. *Electrophoresis*, vol. 32, pp. 2410-2427, 2011.

[63] Voldman, J., *Electrical forces for microscale cell manipulation*, in *Annual Review of Biomedical Engineering*. 2006. p. 425-454.

[64] Dolnik, V., S.R. Liu, and S. Jovanovich, Capillary electrophoresis on microchip. *Electrophoresis*, vol. 21, pp. 41-54, 2000.

[65] Belder, D. and M. Ludwig, Surface modification in microchip electrophoresis. *Electrophoresis*, vol. 24, pp. 3595-3606, 2003.

[66] Velev, O.D. and K.H. Bhatt, On-chip micromanipulation and assembly of colloidal particles by electric fields. *Soft Matter*, vol. 2, pp. 738-750, 2006.

[67] Melvin, M., *Electrophoresis*, ed. D. Kealey. 1987, Chichester: John Wiley & Sons.

[68] Kuzyk, A., Dielectrophoresis at the nanoscale. *Electrophoresis*, vol. 32, pp. 2307-2313, 2011.

[69] Pohl, H.A., The motion and precipitation of suspensoids in divergent electric fields. *Journal of Applied Physics*, vol. 22 pp. 869-871, 1951.

[70] Zhang, C., K. Khoshmanesh, A. Mitchell, and K. Kalantar-zadeh, Dielectrophoresis for manipulation of micro/nano particles in microfluidic systems. *Analytical and Bioanalytical Chemistry*, vol. 396, pp. 1-20, 2009, 2010.

[71] Zhang, C., K. Khoshmanesh, A.A. Kayani, F.J. Tovar-Lopez, W. Wlodarski, A. Mitchell, and K. Kalantar-Zadeh. *Dielectrophoretic manipulation of polystyrene micro particles in microfluidic systems*. 2010. Shanghai.

[72] Vahey, M.D. and J. Voldman, An equilibrium method for continuous-flow cell sorting using dielectrophoresis. *Analytical Chemistry*, vol. 80, pp. 3135-3143, 2008.

[73] Wang, Z., O. Hansen, P.K. Petersen, A. Rogeberg, J.P. Kutter, D.D. Bang, and A. Wolff, Dielectrophoresis microsystem with integrated flow cytometers for on-line monitoring of sorting efficiency. *Electrophoresis*, vol. 27, pp. 5081-5092, 2006.

[74] Ramon-Azcon, J., R. Kunikata, F.J. Sanchez, M.P. Marco, H. Shiku, T. Yasukawa, and T. Matsue, Detection of pesticide residues using an immunodevice based on negative dielectrophoresis. *Biosensors & Bioelectronics*, vol. 24, pp. 1592-1597, 2009.

[75] Kumatani, A. and P.A. Warburton, Characterization of the disaggregation state of single-walled carbon nanotube bundles by dielectrophoresis and Raman spectroscopy. *Applied Physics Letters*, vol. 92, pp. 1-3, 2008.

[76] Pethig, R., Dielectrophoresis: Status of the theory, technology, and applications. *Biomicrofluidics*, vol. 4, pp. 022811, 2010.

[77] Gagnon, Z.R., Cellular dielectrophoresis: Applications to the characterization, manipulation, separation and patterning of cells. *Electrophoresis*, vol. 32, pp. 2466-2487, 2011.

[78] Pethig, R., Dielectrophoresis: Using inhomogeneous AC electrical fields to separate and manipulate cells. *Critical Reviews in Biotechnology*, vol. 16, pp. 331-348, 1996.

[79] Khoshmanesh, K., C. Zhang, F.J. Tovar-Lopez, S. Nahavandi, S. Baratchi, K. Kalantar-zadeh, and A. Mitchell, Dielectrophoretic manipulation and separation of microparticles using curved microelectrodes. *Electrophoresis*, vol. 30, pp. 3707-3717, 2009.

[80] Kayani, A., C. Zhang, K. Khoshmanesh, J.L. Campbell, A. Mitchell, and K. Kalantar-zadeh, Novel tuneable optical elements based on nanoparticle suspensions in microfluidics. *Electrophoresis*, vol. 31, pp. 1071-1079, 2010.

[81] Kalantar-zadeh, K., K. Khoshmanesh, A.A. Kayani, S. Nahavandi, and A. Mitchell, Dielectrophoretically tuneable optical waveguides using nanoparticles in microfluidics. *Applied Physics Letters*, vol. 96, pp. 101108, 2010.

[82] Kayani, A.A., A.F. Chrimes, K. Khoshmanesh, V. Sivan, E. Zeller, K. Kalantar-zadeh, and A. Mitchell, Interaction of guided light in rib polymer waveguides with dielectrophoretically controlled nanoparticles. *Microfluid Nanofluid*, vol. 11, pp. 93-104, 2011.

[83] Kayani, A.A., K. Khoshmanesh, T.G. Nguyen, G. Kostovski, A.F. Chrimes, M. Nasabi, D.A. Heller, A. Mitchell, and K. Kalantar-zadeh, Dynamic Manipulation of Modes in an Optical Waveguide Using Dielectrophoresis, *Electrophoresis*, vol. 33, pp. 2075-2085, 2012.

[84] Kayani, A.A., K. Khoshmanesh, S. Ward, A. Mitchell, and K. Kalantar-zadeh, Optofluidics Incorporating Actively Controlled Micro- and Nano-particles, *Biomicrofluidics*, vol. 6, 2012.

Chapter 2

Literature review

2.1 Introduction

In this chapter, the author reviews the active particle manipulation forces, which can be applied for controlling the motion of suspended particles. This review is of utmost importance as it identifies the most suitable force that can be used in this PhD research. The author divides these forces into mechanical (hydrodynamic and acoustic), electrical (electrophoretic and dielectrophoretic (DEP)), optical, thermal and magnetic categories.

Subsequently, the author reviews the application of optofluidic systems which incorporate suspended particles, as this background knowledge is necessary for understanding the type of optical wave interactions with particles within each applications. These applications include optofluidic devices used for realizing optical components such as waveguides and lenses, particle detection and analysis platforms, Raman systems, platforms which

incorporate plasmonics, thermal and energy related applications and platforms which incorporate bio-particles.

In this PhD research project, the candidate justifies the selection of the DEP force for manipulating the motion of particles into forming three dimensional (3D) suspended tuneable objects in liquid. Hence, at the end of this chapter, the author provides an extended review of dielectrophoresis. This extended review briefly describes the derivations of the DEP force theory, the "DEP spectrum" concept, commonly used microelectrode configurations and the justification and strategies for implementing DEP particle manipulation in this PhD research project.

2.2 Manipulation of suspended micro/nano particles

Particles can be manipulated either "actively" or "passively". As described in chapter 1, passive manipulation forces (e.g. Van der Waals attraction, stearic interaction, Brownian motion, charged dipole interaction) [1-4] are unpredictable, inconsistent and not appropriate for accurately controlling particle motions [5]. Active manipulation forces however, are capable of moving particles with motional trajectories which are precise, accurate and repeatable. In this section, the author elaborates the fundamentals of these active forces.

2.2.1 Mechanical

Particles can be manipulated in microfluidic systems using mechanically induced forces. These forces are categorized into two types which include "hydrodynamic forces" induced motion, and those forces induced by varying pressure profiles, commonly known as "acoustic forces".

2.2.1.1 Hydrodynamic

Hydrodynamic manipulation in microfluidic systems refers to the control of particle displacement as a result of liquid motion. These forces, which are used to manipulate the movements of particles, are known as hydrodynamic forces. They are imposed on particles using liquid motion against them or around them, such that liquid motion is able to control particle displacements and their trajectories [6].

Two types of liquid flows which are important in the definition of liquid motion include: "Laminar flow", which corresponds to the flow of more than one liquid media exhibiting minimal turbulent mixing at the liquid interface; and "non-laminar flow" (also called "turbulent flow") which refers to the flow of multi-phase liquid media when it is turbulent to the extent that there is a mixing of two or more liquids at the liquid interface [7]. Laminar and non-laminar flow behaviors are important characteristics of multi-phase liquid media as they govern the motion of suspended particles in microfluidics.

The Reynolds number, Re_d, describes the presence of Laminar or non-laminar flows. This number represents the ratio of the inertial force to the viscous force and is expressed as [8, 9]:

$$\mathrm{Re}_d = \frac{\rho_m \bar{U} L}{\mu_m} \tag{2.1}$$

where ρ_m is the fluid medium density, v_f is average velocity of the medium inside the microchannel, L is the length of the equivalent diameter of the microchannel and μ_m is the viscosity of the fluid. Generally, an Re_d of less than 2000, corresponds to the Laminar regime, while an Re_d of more than 2000 corresponds to the turbulent regime [6].

The drag force, F_{drag}, refers to the force propelling a particle as it moves through a body of fluid (Figure 2.1). It is proportional to the particle size, dynamic viscosity of the fluid and the difference in fluid and particle velocities. The drag force, F_{drag} is approximated using the Stokes law as [10]:

$$F_{drag} = 6\pi\mu_m r\bar{U} \tag{2.2}$$

where r is the particle radius and $\bar{U}$ is the average velocity of the medium inside the microchannel, respectively.

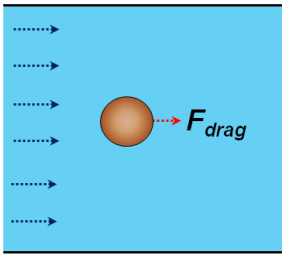

Figure 2.1: Drag force acting on a particle under microfluidic flow

One of the most common applications of hydrodynamic manipulation is the flow focusing of particles. In this process, particles are focused using a pair of liquid flows that sandwich a stream of liquid containing the particles. The liquid that focuses the particle stream is known as the sheath flow (Figure 2.2) while the process is known as sheath flow focusing [11]. This method is used in the sorting, counting, separation and detection of particles as it provides reasonably accurate and reproducible particle trajectories in liquid.

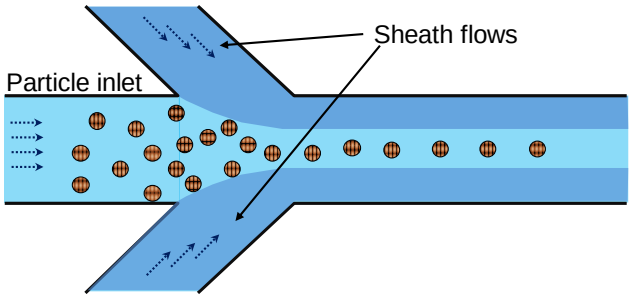

Figure 2.2: Sheath flow focusing

Sheathless particle focusing is another method of manipulating particles [11]. This process does not rely on a pair of sheath liquid flows to focus the particles. Instead, it employs hydrodynamic lift and drag forces that induce the particles to flow to their equilibrium positions according to the velocity profile of the liquid stream (Figure 2.3) [12].

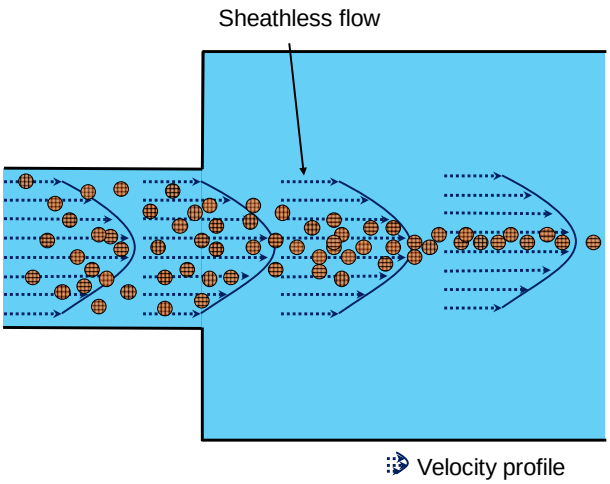

Figure 2.3: Sheathless flow focusing

Hydrodynamic forces are used for particle sorting and separation applications as well [13, 14]. Figure 2.4 presents a T-shaped inlet and outlet microfluidic system that separates a solution containing a mixture of particles [15, 16]. The particle mixture is a dilute solution of different-sized particles, each of which experiences a different magnitude of hydrodynamic drag and lateral lift forces. The channel length, dual fluid outlets and flow rates are appropriately designed to allow smaller particles to diffuse and fill the channel before they exit. The larger particles experience a higher hydrodynamic drag force causing them to remain mostly confined to the upper half of the channel. A reverse T-channel then separates the particles into two streams, one of which contains mostly small particles, and the other both, small and large particles.

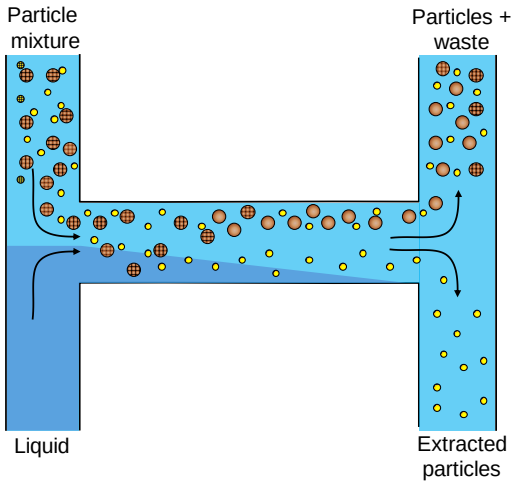

Figure 2.4: T-shaped inlet and outlet microfluidic separation system

Hydrodynamic traps in the form of microfluidic stagnation points, micro vortices or micro eddies can also manipulate the motion of particles in liquid [17, 18]. These traps are realized using cross-flow forces of two or more opposing laminar streams of liquid which meet at an intersection. As the opposing liquid streams meet, a flow field with a stagnation point, where the particles are trapped, is generated. This entrapment provides high resolution manipulation of a small quantity of particles. The inclusion of such methods in present day optofluidic devices is still quite rare and we will certainly see more of them used in future systems.

The motion of particles using hydrodynamic forces is affected by channel topology and uses carefully selected flow rates at which the suspended particles are able to form the desired flow trajectory or particle assembly [13]. This requires meticulous design and simulation of microfluidic flow rates, understanding of the forces affecting particles and channel geometries. However, understanding of liquid flow trajectories under various conditions provides reasonable particle control abilities.

2.2.1.2 Acoustic

Acoustic waves of varying pressure profiles induce an acoustic force on the particles which causes them to move [19, 20]. The process of manipulating particles using such acoustic forces is called acoustophoresis. The acoustic waves are typically generated by inter-digitated, ultrasonic or piezoelectric acoustic transducers [21, 22].

The acoustic force, F_r experienced by a spherical particle suspended in liquid is given by [19]:

$$F_r = -\left(\frac{\pi P_o^2 V_p \beta_m}{2\lambda}\right).\phi(\beta,\rho).\sin(\frac{2\pi x}{\lambda}) \tag{2.3}$$

$$\varphi(\beta,\rho) = \frac{5\rho_p - 2\rho_m}{2\rho_p + \rho_m} - \frac{\beta_p}{\beta_m}, \tag{2.4}$$

where P_0 is the pressure amplitude of the acoustic wave, V_p is the particle volume, β and ρ are the particle or liquid compressibilities and densities, respectively, λ is the wavelength of the acoustic wave and x is the distance to the nearest pressure node. Subscripts p and m denote particle and suspending medium, respectively. The acoustic force experienced by a particle is influenced by the magnitude and frequency of the acoustic waves, the size and elasticity of the particle and the liquid that surrounds it.

Particles exposed to the acoustic wave are either pushed to the pressure nodes or the pressure anti-nodes. The pressure node is the location where the acoustic waves form a pressure maximum, while the pressure anti-node is the location where the acoustic waves form a pressure minimum in the liquid [23]. The direction of particle motion depends on the density and compressibility properties of the particles relative to the surrounding liquid (Figure 2.5A). For example, particles with a higher density and lower compressibility compared to the suspending liquid moves toward the pressure node while particles with a lower density and higher compressibility moves toward the pressure anti-nodes (Figure 2.5B).

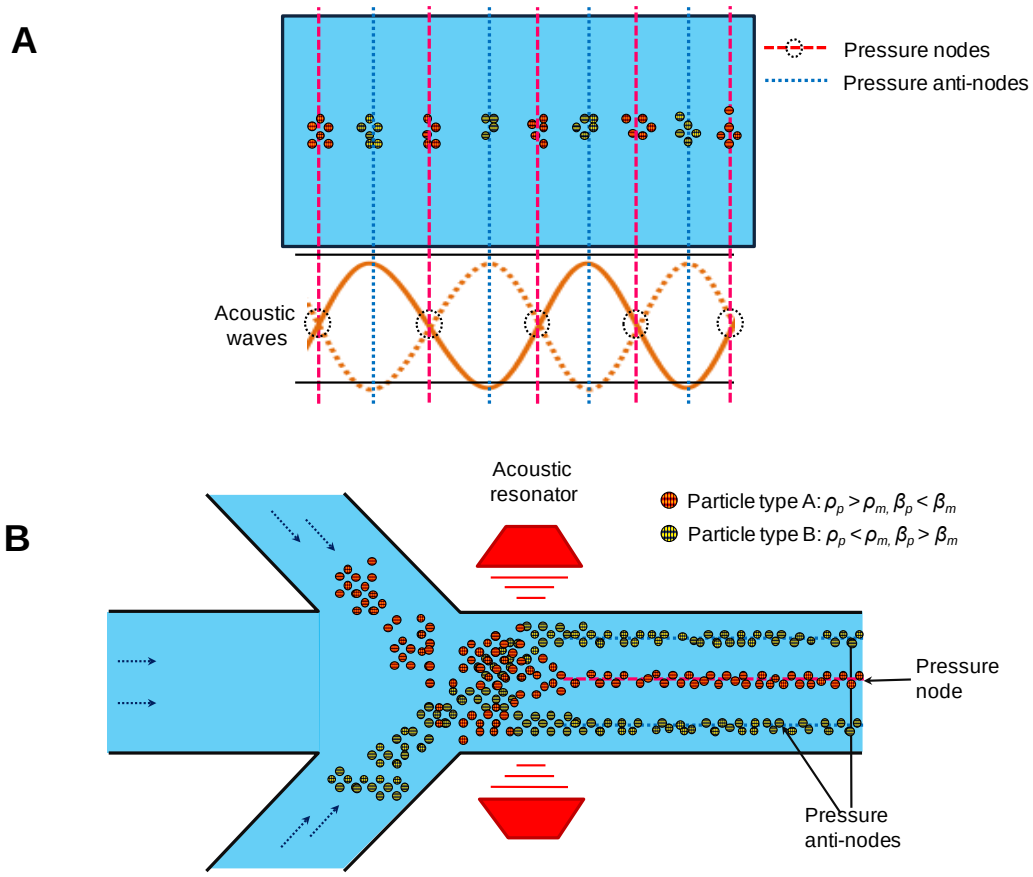

Figure 2.5: Acoustophoretic manipulation of suspended particles: (A) Acoustophoretic manipulation of particles when subject to acoustic waves (B) Schematic of acoustophoretic sorting of a mixture of particles with different density and compressibility properties.

Acoustic manipulation of particles provides the ability to separate particles of similar sizes and densities. If one particle is more compressible than the liquid, while another is less compressible, the acoustic force displacing the two particles will be in the opposite direction, causing them to separate. As such, a mixture of particles can be trapped and sorted by the acoustic field and collected at different outlets of a microfluidic channel [24].

Acoustic manipulation has been applied for the concentration [25] and separation [20] of particles. The drawbacks of acoustophoresis arise from the difficulty of integrating acoustic transducers into microfluidic devices, the difficulty of controlling small nano-scale particles and the fact that particle separations can only be conducted by virtue of their size, density and compressibility differences [20, 26].

2.2.2 Electrical

Particles can be manipulated in microfluidic systems using electrically induced forces. These forces are generally grouped into the electrophoretic and dielectrophoretic (DEP) forces. They are applied using electrically generated uniform and non-uniform electric fields, for charged and neutral particles suspended in liquid, respectively.

2.2.2.1 Electrophoresis

"Electrophoresis" refers to the motion of charged particles, relative to a fluid, under the influence of an electric field [27]. The induced motion depends on the polarity and magnitude of the net electrical charge of the particle. Generally, electrophoretic force is generated by a pair of electrodes connected to a direct current (DC) power source. The electrodes are placed in an ionic solution which contains the particles. When the electric field is applied, particles experience an electrophoretic force, F_{el}, which induces motion toward the electrode bearing the opposite charge polarity to that of the particle (Figure 2.6) [28].

There are also two forces that oppose the particles' movement: the "friction" and "electrophoretic retardation" forces. The friction force, F_{fr}, is the viscous force opposing the electrophoretically induced motion of the particle as it moves through the body of a liquid [29]. The friction force is dependant upon the viscosity of the liquid medium, as well as the size and shape of the particle. For example, larger particles moving in a more viscous liquid medium experience a higher friction force compared with smaller particles moving in a less viscous liquid medium.

The electrophoretic retardation force, F_{ret}, refers to the force exerted on the diffuse cloud of ions surrounding the particle known as the "Debye layer". The ions in the Debye layer have the opposite charge polarity to the particle and therefore the electrophoretic retardation force results in a fluid flow around the particle [30]. The direction of fluid flow is in the opposing direction to the electrophoretic force. This fluid flow causes a frictional drag that is partially transferred to the particle, causing a "retardation" of the electrophoretically induced motion.

The electrophoretic force increases proportionally with a higher magnitude of net electrical charge of the particle [27]. For instance, in the case of two particles of similar size, the particle having a larger net electrical charge would move faster in the electric field. Particle size also affects particle mobility under an electric field as larger particles which generally have a higher mass, experience a higher frictional drag while moving through liquid. Accordingly, electrophoretic mobility is influenced by the mass to charge ratio of the particle [29]. Particles with a high mass to charge ratio have a lower mobility compared to particles with a low mass to charge ratio. Similarly, two different sized particles, with the same mass to charge ratio would actually move with the same mobility in a uniform electric field.

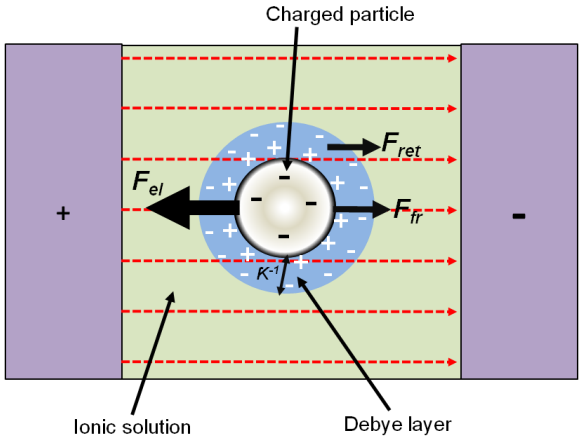

Figure 2.6: Schematic of a particle experiencing the electrophoretic force

Electrophoretic mobility, μ_{el}, is a measure of charged particle mobility when subjected to an electric field. Electrophoretic mobility of a charged particle in the case of a thin Debye layer such that $\kappa r >> 1$(where κ^{-1} is the Debye length) is defined as [29]:

$$\mu_{el} = \frac{\varepsilon_r \varepsilon_o \zeta}{\eta} \tag{2.5}$$

where ε_r is the relative permittivity of the particle, ζ is the zeta potential and η is the viscosity of the surrounding liquid. ζ is defined as [29]:

$$\varsigma = \frac{\sigma r}{\varepsilon(1+\kappa r)} \tag{2.6}$$

In the case where $\kappa r << 1$, the electrophoretic mobility is expressed as [29]:

$$\mu_{el} = \frac{2\varepsilon_r \varepsilon_o \varsigma}{3\eta} \tag{2.7}$$

Electrophoretic manipulation of particles has been used in the analyses and preparative separations of biological samples, such as proteins, peptides, DNA and RNA molecules [31]. It is also widely used in liquid purification processes and for the characterization of particles and their surface properties [29].

2.2.2.2 Dielectrophoresis

Dielectrophoresis is the motion of neutral or semi-conducting particles induced by a spatially non-uniform electric field [32]. When a polarizable particle is subjected to a spatially uniform electric field, electrical charges are induced on the particle/medium interface. These induced charges form dipoles aligned parallel to the applied electric field. In a uniform electric field, each half of the dipole experiences equal Columbic forces which results in no net motional force imposed on the particle [33]. However, when a polarizable particle is exposed to a non-uniform electric field, each half of the dipole experiences unequal Columbic forces which result in a net motional force imposed on the particle (Figure 2.7). This force is known as the dielectrophoretic (DEP) force and the motion of particles depends on whether the particle is more or less polarizable than the suspending medium [33, 34].

For a spherical particle, the DEP force is given by [32]:

$$\vec{F}_{DEP} = 2\pi r^3 \varepsilon_o \varepsilon_r \,\mathrm{Re}[f_{CM}(\omega)]\nabla E^2_{rms} \tag{2.8}$$

where r is the particle radius, ε_r is the permittivity of the suspending medium, $f_{CM}(\omega)$ is the Clausius-Mossotti (CM) factor and E_{rms} is the root mean square (*rms*) of the applied electric field. The CM factor is expressed as [34]:

$$f_{CM}(\omega) = \frac{\varepsilon_p^* - \varepsilon_m^*}{\varepsilon_p^* + 2\varepsilon_m^*} \tag{2.9}$$

The complex permittivity of the particle and the suspending medium, ε_p^* and ε_m^*, are given by [32]:

$$\varepsilon_p^* = \varepsilon_o \varepsilon_p - i\frac{\sigma_p}{\omega} \tag{2.10}$$

$$\varepsilon_m^* = \varepsilon_o \varepsilon_m - i\frac{\sigma_m}{\omega} \tag{2.11}$$

where $i=\sqrt{-1}$, σ_m and σ_p are the conductivities of the medium or the particle, respectively and ω is the angular frequency of the applied electric field.

Particles experiencing the DEP force are either attracted to or repelled from regions of high electric field gradients [32]. The sign of the Re[$f_{CM}(\omega)$], gives an indication of the behavior of the particles in response to an applied electric field. For instance, if Re[$f_{CM}(\omega)$] > 0, the particles will a experience positive DEP force such that they are pulled toward regions of high electric field gradients (Figure 2.7A). Conversely, if Re[$f_{CM}(\omega)$] < 0, the particles will experience a negative DEP force force such that they are repelled from regions of high electric field gradients (Figure 2.7B) [34].

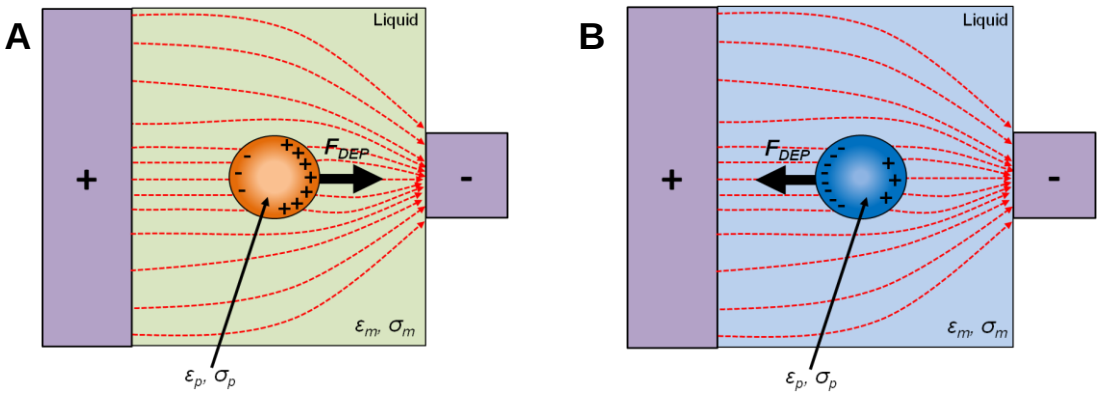

Figure 2.7: Schematic of DEP manipulation of particles. (A) When Re[$f_{CM}(\omega)$] > 0, the particle experiences a positive DEP pulling it towards the region of high electric field gradients (B) When Re[$f_{CM}(\omega)$] < 0, the particle experiences a negative DEP repelling it from the region of high electric field gradients.

The DEP force is typically generated by a pair of closely spaced microelectrodes. They can be used as individual pairs but more often they are designed in an array and integrated in a microfluidic system. The electrodes generate the electric field gradients necessary to induce the DEP force which transports, focuses or repels particles from regions of interest in the microfluidics. The intensity of the applied electric field gradient is generally highest in the region between the closely spaced electrodes. The electrodes are connected to an alternating current (AC) power source, while the amplitude and frequency of the applied AC signal is tuned to achieve the desired particle motion or positioning in liquid.

Dielectrophoresis has been widely used in applications involving particle separation [35], transport [36] and sorting [37]. One of the issues of DEP manipulation is the difficulty of controlling smaller nano-scale particles, which results from the DEP force being proportional to r^3 (see equation (2.8)) and the accuracy of particle motion relies on the design of the DEP electrodes and the microfluidics. Khoshmanesh et *al*.[33], Cetin et *al.*[38] and Kuzyk [39] have recently presented comprehensive reviews on DEP particle manipulation. In this thesis, the author selected the DEP force for controlling the motion of suspended particles. Hence, he has included an extended review (see section 2.4) covering key concepts such as the DEP force derivation, "DEP spectrum" concept, DEP microelectrode configurations and the motivations and strategies for implementing DEP manipulation in this PhD research project.

2.2.3 Thermal

Thermophoresis refers to the motion of particles suspended in liquid which is induced by a thermal gradient [40]. Although this phenomenon has been known for over 150 years, the theory is not well established [41]. It has been suggested that particle motion results from the inhomogeneity brought in by the thermal gradients in the thin layer that constitutes the interface between the particle and the suspension [40].

In addition to the usual Brownian motion, particles also show a systematic drift when they are placed in a thermal gradient [42]. In the presence of such a thermal gradient, the mass flux of particle flow, J in liquid is expressed as[43]:

$$J = -D\nabla c - cD_T\nabla T \tag{2.12}$$

where c the particle concentration, D is the Brownian diffusion coefficient, D_T is the thermal diffusion coefficient and ∇T is the temperature gradient. The thermal diffusion coefficient, D_T gives an indication of the particle motion behavior in a mixture in the presence of a thermal gradient. If $D_T > 0$, particles drift toward the cooler region and exhibit 'thermophobic' behavior. If $D_T < 0$, particles drift towards the warmer region, exhibiting 'thermophilic' behavior (Figure 2.8) [43].

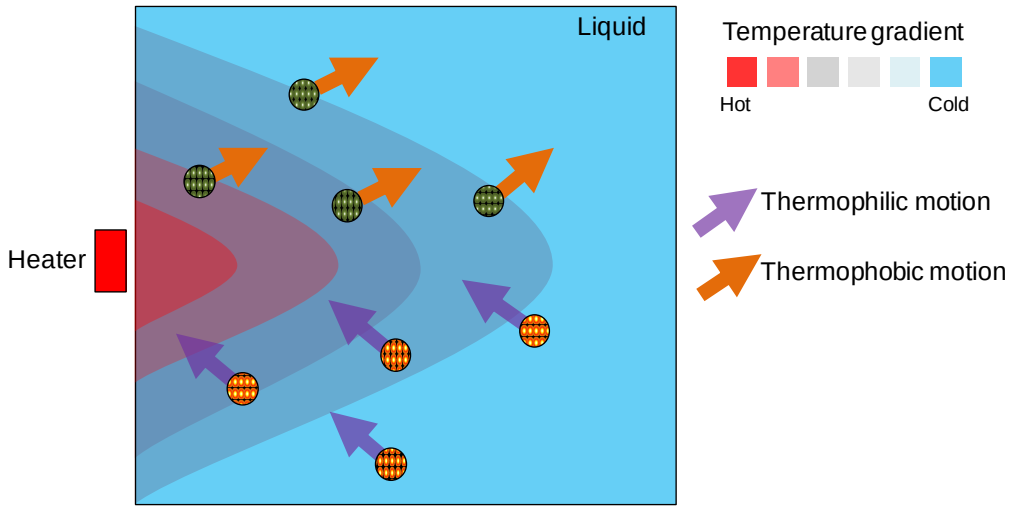

Figure 2.8: Schematic of thermophoretic manipulation of particles. Thermophilic particles drift toward hotter regions, while thermophobic particles drift toward the cooler regions.

Thermophoretic manipulation has been used for particle separation [44] and trapping [45]. Drawbacks of thermophoresis include the difficulty of transporting particles in low concentrations as they usually drift in clusters [46] and particle drift time is generally long [47].

2.2.4 Optical

Optical manipulation of particles is the control of particle motion using optically induced electromagnetic fields [48]. Electromagnetic fields are generated by the radiation of light from optical sources operating in the infrared, visible, and UV range of frequencies [49]. Particles that can be manipulated using optically induced forces scale from hundreds of

micrometers to a few nanometers in size [50] and are usually composed of neutral dielectrics [51]. However, the growth of near-field and plasmonic based optical manipulations (which will be described later) has expanded the type of particles that can be manipulated to include certain metallic [52, 53] and semi-conducting particles [54, 55].

Particles interact with optical waves depending primarily on their size. Particles smaller than the wavelength of light are pulled toward regions of high electromagnetic fields as they develop an electric dipole moment in response to the light's electric field. Particles comparable or larger than the wavelength of light, refract the rays of light and move as a result of a momentum transfer of the incident photons [56]. Optical manipulation of particles falls into two categories: (1) far field and near-field manipulation and (2) plasmonic manipulation.

2.2.4.1 Far and near-field manipulation

Far field optical manipulation, commonly known as optical tweezing, refers to the control of particle motion induced by a direct irradiation of optical electromagnetic fields [48]. When a particle is subjected to this field, the optical gradient force pulls the particle toward the region of highest field intensity where the optical beam is focused [49]. Scattering and absorption forces then cause the particle to move in the direction of beam propagation (Figure 2.9) [57].

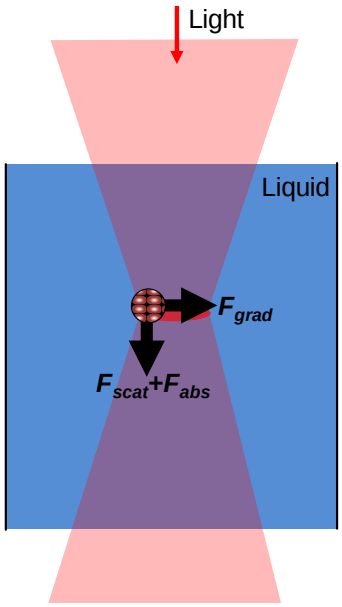

Figure 2.9: Optical manipulation of suspended particles using direct optical tweezing.

The optical gradient force, F_{grad} experienced by a spherical particle is expressed as [57]:

$$F_{grad} = \frac{2\pi \nabla I_o \alpha}{c_o} \tag{2.13}$$

where ∇I_o is the gradient of light intensity,

$$\alpha = 3V_p(\varepsilon_p - \varepsilon_m)/(\varepsilon_p + 2\varepsilon_m) \tag{2.14}$$

and c_o is the speed of light while V_p is the particle volume, and ε_p and ε_m are the permittivities of the particle and suspending medium, respectively. The dielectric constant is a function of wavelength and is comprised of a real and an imaginary component, such that $\varepsilon = \varepsilon_1 + i\varepsilon_2$, where $\varepsilon_1 = n^2 - k^2$ and $\varepsilon_2 = 2nk$. n and k are the refractive index and absorption coefficient, respectively [57]. In the case of a simple, non-absorbing dielectric, α is positive when the refractive index of the particle exceeds that of the surrounding medium. In this case, particles are attracted to the region of highest intensity, and if the particles' refractive index is lower, it will be forced away from the region of highest intensity [57].

The scattering, F_{scat} and absorption, F_{abs} forces are expressed as [57]:

$$F_{scat} = \frac{8\pi I_o \alpha^2 \varepsilon_m}{3c_o \lambda^4} \tag{2.15}$$

$$F_{abs} = \frac{2\pi \varepsilon_m I_o}{c_o \lambda} \mathrm{Im}(\alpha) \tag{2.16}$$

where λ is the optical wavelength.

Near-field manipulation refers to the optical manipulation of particles using evanescent fields [57]. When light travels through a waveguide, evanescent fields radiate from the waveguides' surface and decays exponentially with distance from the boundary of the waveguide where the optical wave originated [58]. The evanescent field generates a gradient force that attracts particles to the region of highest field intensity, before moving them, using scattering and absorption forces, in the direction of wave propagation [57] (Figure 2.10).

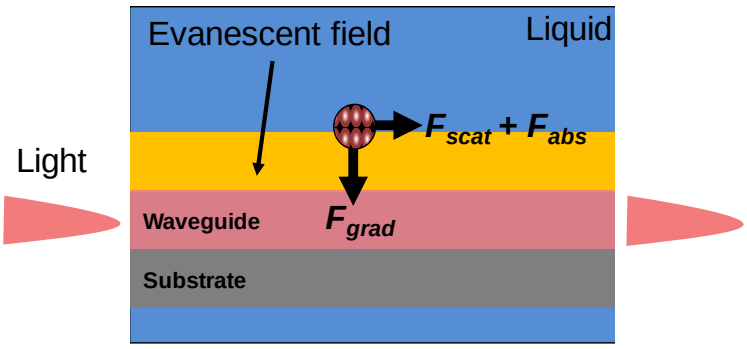

Figure 2.10: Near field optical manipulation of suspended particles

2.2.4.2 Plasmonic manipulation

Plasmonic manipulation refers to the control of particle motion induced by surface plasmons [59]. Surface plasmons are electromagnetic waves produced by coherent electron oscillations at the interface of any two materials where the real part of the dielectric function changes sign across their interface [60]. The most suitable media are generally the boundaries of a metal and a dielectric material [61]. Surface plasmons are confined to the metal surface with exponentially decaying fields. In many applications, surface plasmons are generated by impinging light in the visible range, although UV and infrared frequencies are also possible [62]. Surface plasmon resonances (SPR) refer to extremely large local enhancements of the electromagnetic field [57]. Plasmonic manipulation of particles can be achieved using either, plasmonic particles or metallic nanostructures that support SPRs.

2.2.4.2.1 Plasmonic particles and their interactions

Plasmonic optical forces have been used to control particles composed of neutral dielectrics [63], semi-conductors [64] or metallic [65] structures. For SPR modes generated using plasmonic particles, naturally, particles need to be metallic or at least have a metallic shell. Plasmonic particles are particles that support localized surface plasmon resonances (LSPR). LSPRs have the ability to strongly scatter and absorb light and to squeeze light into nanometer dimensions, producing large local enhancements of electromagnetic fields [66,

67]. LSPRs can be supported by a wide variety of metallic particles including interacting particle pairs, an array of particles with nanoscale gaps between them or individual particles interacting with another metal surface. LSPRs can also be supported by nano-scopic holes or voids rather than particles, or by particles that have holes in them, such as toroidal structures [62]. Core-shell particles utilizing dielectric cores and metallic shells have also supported LSPR activity originating from the interaction of optical electromagnetic waves and the oscillating surface charges generated on the inner and outer surfaces of the metal shells [68, 69].

When light is incident on a metallic particle and the SPR conditions are met, the oscillating electric field of the light produces a force on the mobile conduction electrons in the metal, the result of which induces the LSPR modes [62]. The LSPR modes then generate a gradient force capable of particle trapping and manipulation. For example, the LSPR between a pair of closely spaced gold nano-dots were used to create an optical trap with improved particle positioning by almost an order of magnitude compared to conventional optical tweezers [70].

2.2.4.2.2 Plasmonic nanostructures and traps

Plasmonic nanostructures refer to metallic structures capable of producing SPR fields. An appropriately designed and patterned metal surface is required to provide plasmonic field confinement. Generally, the metallic structures are designed with nanoscale gaps between them where the SPR fields are produced [62]. Figure 2.11 presents a plasmonic optical trap where a particle is held in place through the F_{grad} force, which acts to attract the particle to a surface bound metallic nanostructure [57]. Instead of using a highly focused laser beam (which is normally used in optical tweezing), surface plasmon-based optical traps as a result of plasmonic nanostructures can enable stable particle trapping at a patterned metal surface even when using unfocused and low intensity laser beams [59].

In summary, the optical manipulation of particles in microfluidic systems has been employed in order to achieve particle transport [71], cell separation [72], particle detection and particle characterization [73]. The merits of this manipulation method include the ability of localizing light to the single particle level (particularly using plasmonic fields), its being

non-invasive and not requiring on-chip infrastructure, given that light can be sourced externally to the chip [74]. However, there is a risk of particle damage, especially with regard to organic entities, given that highly focused beams of light (in the case of optical trapping) can sometimes generate excessive heat [75]. Other disadvantages also include the requirement of bulk optics (in the case of far and near field manipulations), such as high numerical aperture objective lenses (hence large optical components), which impede the miniaturization requirements of certain devices [59].

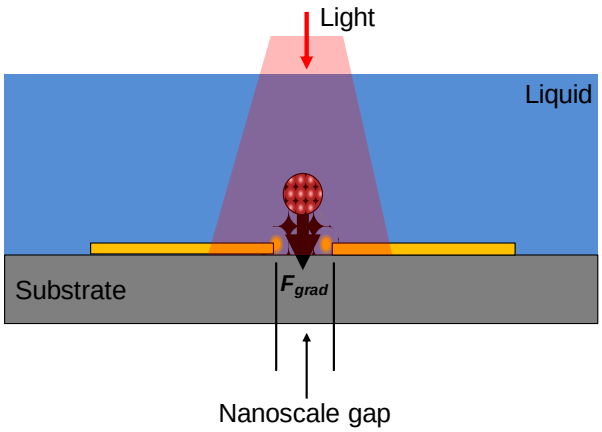

Figure 2.11: Manipulation of particles using plasmonic nanostructures.

2.2.5 Magnetic

Magnetophoresis is the motion of suspended magnetized particles relative to a fluid under the influence of a magnetic field with a gradient [76]. Generally, the magnetic properties of materials can be classified into three categories: ferromagnetic, diamagnetic or paramagnetic [76]. Diamagnetic materials are those whose electrons are all paired. The diamagnetic effect stems from changes in electron orbital motion induced by a magnetic field and leads to dipoles aligned against the magnetic field [76, 77]. Paramagnetic effects occur in materials whose electrons are unpaired and the spins of the unpaired electrons that align with the external magnetic field to produce a magnetic moment. Paramagnetism is exhibited when thermal fluctuations prevent the magnetic dipoles from locking in orientation aligned with the field. Ferromagnetism occurs in materials with unpaired electrons, when thermal fluctuations are small compared with the forces that lead magnetic dipoles to lock in orientation aligned with the field [76].

When a particle is subject to a magnetic field, the force experienced by the particle, F_{mag}, is given by [77, 78]:

$$F_{mag} = \frac{(\chi_p - \chi_m)V_p}{\mu_o}(B \cdot \nabla)B \tag{2.17}$$

where χ_p and χ_m are the magnetic susceptibilities of the particle and the suspending medium, respectively, V_p is the volume of the particle and μ_o is the permeability of free space ($4\pi \times 10^{-7}$ H m^{-1}). The magnetic susceptibility refers to the degree of magnetization of a material as a result of an applied magnetic field [79]. If the particle is magnetic ($\chi_p > 0$) and the medium diamagnetic ($\chi_m < 0$), the difference of $\chi_p - \chi_m$ is positive, resulting in a positive value of F_{mag} and indicating the particle experiences an attractive force towards an area of high magnetic flux density gradient (Figure 2.12A). Conversely, when the particle is diamagnetic ($\chi_p < 0$) and the medium is paramagnetic ($\chi_m > 0$), the difference of $\chi_p - \chi_m$ becomes negative, giving a negative F_{mag} value signifying that the particle is repelled from regions of high flux density gradient (Figure 2.12B) [77].

Magnetophoretic manipulation has been used for particle separation [80], sorting [81-83], transport [84, 85] and detection [86, 87]. Magnetophoresis has the advantage of angular particle positioning and rotation ability. It is minimally invasive and reduces the risk of particle damage in the process of particle control [84]. One of the problems associated with magnetophoresis involves the magnetic hysteresis of microparticles, when the magnetic field is turned off which can cause them to agglomerate into clusters. Smaller nano-scale particles however, display less hysteresis in the magnetic field, hence when the field is turned off, they redisperse in the suspension [88].

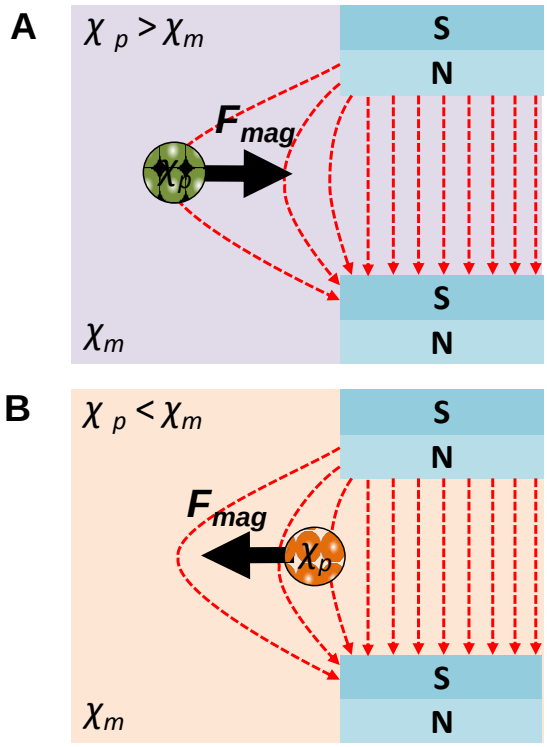

Figure 2.12: Magnetophoretic manipulation of suspended particles: (A) Particle is pulled toward the region of high magnetic field gradients when $\chi_p > \chi_m$ (B) Particle is repelled from the region of high magnetic field gradients when $\chi_p < \chi_m$.

Table 2.1: Summary of particle manipulation methods, features, limitations and references

Manipulation technique	Features	Limitations	Key references
Hydrodynamic	• Influenced by hydrodynamic drag force and governed by laminar flow regime • Sheath and sheathless focusing of particles extensively used • Depends on particle size, viscosity and flow rates of the fluids	• Extensive fluidics simulation and design of microchannel required • Small changes in microchannel dimensions alters particle motion trajectory • Sensitive to flow rate changes	Xuan et *al.* [38] Squires et *al.*[41] Tanyeri et *al.*[44]
Acoustic	• Acoustic waves exert acoustic forces on particles in liquid • Capable of particle separations based on size, charge and density • Depends on magnitude and frequency of the acoustic wave, size and elasticity of the particle and surrounding liquid	• Difficulty integrating micro-scale acoustic resonators into microfluidic structures • Ineffective manipulation accuracies for nano-scale particles • Differentiation of particles by size, density and compressibility differences only	Friend et *al.*[23] Shi et *al.*[50] Petersson *et al.* [46]
Electrophoresis	• Control of charged particles using uniform electric fields • Electrophoretic force induces motion of the charged particle towards the opposite charge electrode • Depends on permittivity and size of the particle and viscosity of the suspending medium	• Generally limited to purification and separation applications • Slow particle migration times • Limited to charged particles	Gas [28] Kleparnik [27] Melvin[54]
Dielectrophoresis	• Control of neutral / semiconducting particles in non-uniform electric fields • Motion depends on relative polarizabilities of the particle with respect to surrounding medium • Depends on particle size, permittivity and conductivity of the particle and suspending medium	• Motional accuracies limited by the performance of the DEP electrodes • Reduced particle sizes severely reduced magnitude of DEP force • Risk of bio-particle damage when subjected to high electric field gradients	Zhang et *al.* [24] Kuzyk [61] Khoshmanesh et *al.*[26]
Thermal	• Observed when a temperature gradient is applied to particles suspended in liquid • Used for particle separation and migration and motion based on particle thermophobicity or thermophilicity properties • Depends on particle concentration, thermal diffusion coefficient and temperature gradients	• Difficult to transport particles individually as particles move in clusters • Generally motion is from hot to cold regions (Particles thermophobic) • Typically slow particle drift times	Piazza et *al.*[62] Plyukhin et *al.*[64] Parola et *al.*[31]
Optical	• Classified as either direct tweezing, near-field or far field manipulation • Extensively used in particle transport, sorting and characterization • Depends on particle size, volume, permittivities of particle and suspension, optical wavelength and intensity gradients	• Extensive optical peripherals required for implementations • Generates excessive thermal heating due to high intensity optical beams • Generally not suitable for bio-particles due to risk of damage arising from heat absorption from optical waves	Jonas et *al.*[30] Erickson et *al.*[29] Halas et *al.*[79]
Magnetic	• Motion of particles subject to magnetic field gradients • Ability to induce angular rotation of particles, it is minimally invasive and generally safe for bio-particles • Depends on magnetic susceptibilities of the particle and suspending medium, particle volume and the applied magnetic field gradients	• Agglomeration of magnetic particles and hysteresis in on/off magnetization sequence • Limited to particles that are magnetic or have some magnetic content • Non-magnetic particles have to be chemically bound to magnetic particles which can be complex	Suwa et *al*.[34] Ivon Rodriguez-Villarreal et *al.*[95] Peyman et *al.*[35]

2.3 Applications of optofluidics with suspended particles

In this section, the author will describe novel optofluidic applications that have employed controllable particles suspended in liquid. First, applications of optical components which use particles as waveguiding media and lenses are covered. Subsequently, the author describes optofluidic applications that have been used for transporting, detecting and analyzing particles. Finally, the author covers applications related to Raman spectroscopy, plasmonics, heat and energy and eventually those that specifically involve biological particles.

2.3.1 Optical components

Multi-phase optofluidics have been used to create optical components that are compatible with liquids such as waveguides [91], lenses [92], and sensors [93]. However, a major setback of multi-phase systems is that liquids are not easily reconfigured and manipulated. One method of addressing this limitation is to use liquid with suspended particles. The properties of the suspension can be tuned from those of liquid to that of the particles by manipulating the particles concentrations at different locations within microfluidics. The concentrations of particles can be tuned using the externally applied forces described in section 2.2. In addition, the integration of suspended particles offers a wealth of added possibilities regarding the particles' interaction with light, which can be very useful for the development of particle detection and analysis platforms [94].

2.3.1.1 Particles as waveguiding media

One of the major works that directly related with the author's field of research is the works by Conroy et *al.* [95]. The author demonstrated a particle core/liquid cladding waveguide, which uses two types of suspended particles, polysterene and SiO_2 with diameters ranging from 30 to 900 nm (Ø30 to Ø900 nm). Both particle types were focused using hydrodynamic forces (Figure 2.13A). Visible light (λ = 635 nm) from an external laser source was coupled into the concentration of particles using a fiber embedded in the microfluidic channel. The output profiles, showing the intensity of light guided through the particle focused core was observed (Figure 2.13B). The analysis of core to cladding intensity ratios for the various particle sizes revealed that the smaller sized particle suspensions of higher concentrations guided light more effectively compared to the larger particles with lower concentrations. The authors attributed this to the smaller scattering cross sections exhibited by the smaller particles, when they were hydrodynamically focused. Additionally they suggested that suspensions with higher concentrations of particles had smaller inter particle spacings and therefore the light experienced reduced scattering.

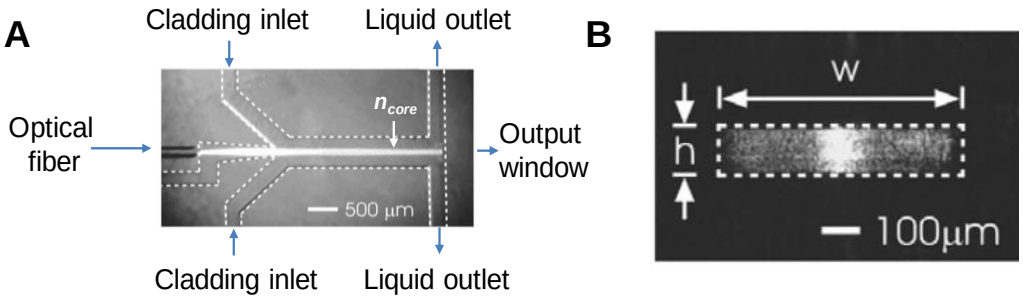

Figure 2.13: Hydrodynamically focused nanoparticles used as optical waveguiding media: (A) Schematic of nanoparticle optofluidic waveguide using polysterene nanobeads and DI water, as the core and cladding, respectively (B) Intensity distribution at the waveguide output showing a high core to cladding intensity ratio. [95]

2.3.1.2 Particles as lenses

Particles with suitable optical properties have been employed to focus light, similar to liquid lenses [96], based on two different approaches: (i) particles can be individually used as lenses [97, 98] and (ii) the accumulation of particles can be used to form particle arrays and media of different average refractive indices that could act as optical lenses [99, 100].

Individual particle lenses were demonstrated by several groups [101, 102]. Such lenses have been used as manipulators of light exhibiting the ability to control the amplitude, phase and polarization properties of light and its directions of propagation [103-107]. Beam control was demonstrated by displacing optically trapped particles such as an SiO_2 (Ø13 μm) microsphere though a light beam [108].

Figure 2.14 shows the schematic of the experimental geometry and simulation results of the particle light manipulation system using trapped silica particles. The microsphere caused the beam to be refracted by various degrees as a function of the sphere position, providing tuneable attenuation and beam-steering in the device. The device itself consisted of the manipulated light beam extending between two buried single mode fiber (SMF) waveguides which were on either side of a microfluidic channel (Figure 2.14A). This channel contained the microsphere, which was suspended in water. In the "on axis" transmission case, the microsphere was centered in the probe beam and acted as a spherical lens, providing enhanced coupling (Figure 2.14B). In the "off axis" case, the microsphere steered the beam away from the core of the output SMF (Figure 2.14C). In the "leaving beam" case, the microsphere was only slightly perturbing the probe beam, allowing most of the light to be collected (Figure 2.14D). When the particle was located out of the center position, the signal intensity decreased to –11 dB compared to a continuous SMF case. Figure 2.14E shows the experimental and numerical simulations of the insertion loss of the buried fiber device for various positions of the trapped microsphere, probed at a wavelength of 1.5 μm.

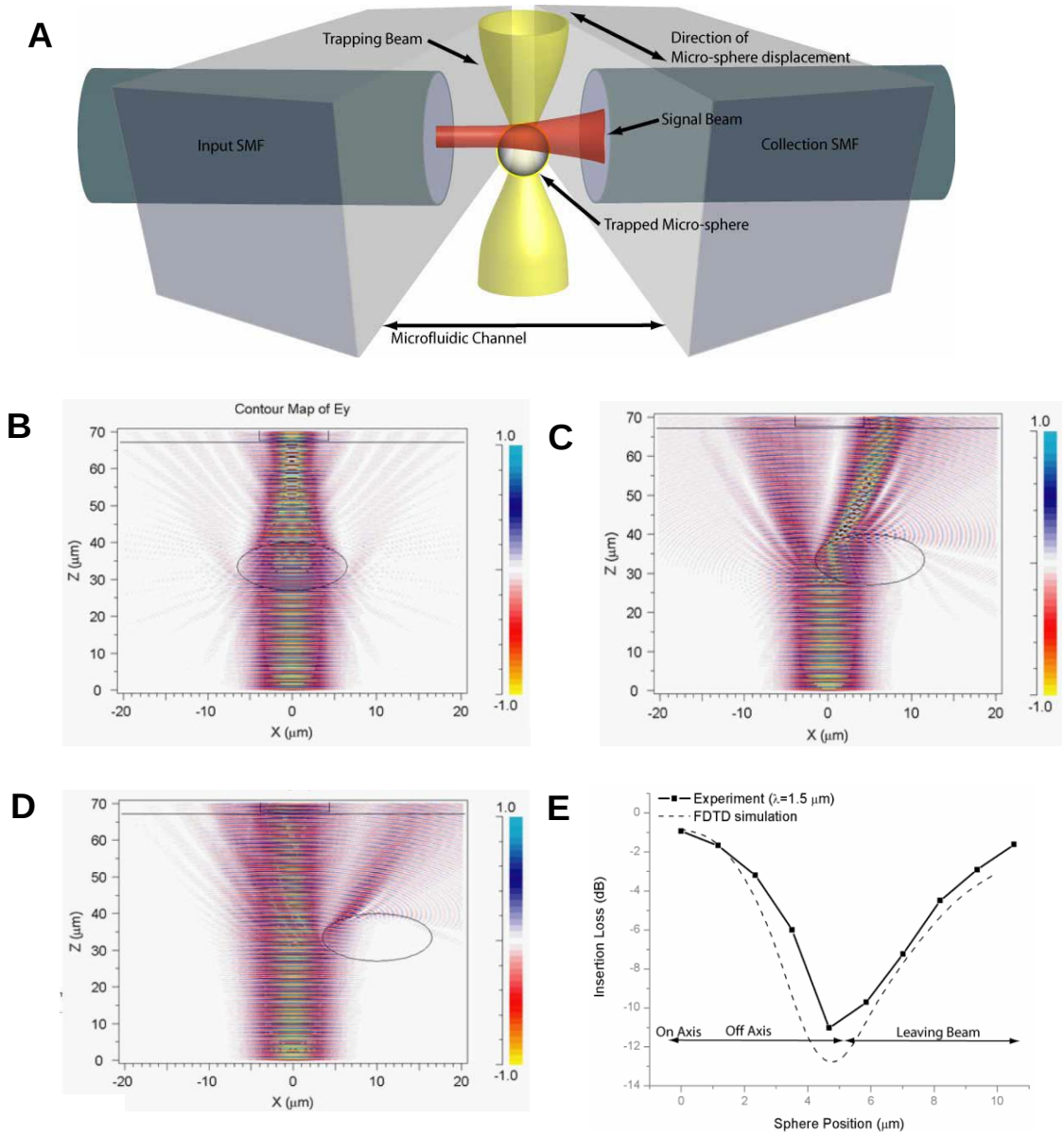

Figure 2.14: Optofluidic lens using suspended particles controlled by optical forces: (A) Schematic of the experimental geometry for beam manipulation. FDTD field output depending on the microsphere position: (B) on axis, (C) off axis, (D) leaving beam. (E) Insertion loss experimental and numerical simulation data with transmission regimes are identified. [108]

Accumulation of packed particles in microfluidics can also be used as optical lenses. For example, an optofluidic lens was realized by filling a hollow fiber with suspended superparamagnetic iron oxide (Fe_3O_4) particles for the manipulation of light. The lens was

constructed of a hollow fiber filled with superparamagnetic Fe_3O_4 nanoparticles (Ø10 nm) suspended in DI water at a 0.12 % volume-in-volume (*v/v*) concentration. When the magnetic field was activated, the particles became aligned to the core surface such that it stretched the beam into a 'ribbon shape' yielding a larger visible area and when the field was rotated, a larger beam spot size was formed. The ribbon shaped beam was formed by the diffraction of light incident on the particles in the fiber core [109]. In a separate work, the brightness and intensity of light was controlled with the aid of paramagnetic particles that were manipulated using magnetic fields on a magnetic film in a device known as an "optomagnetic dimmer" [110].

The integration of controllable particles as optofluidic lenses has provided the ability to image large fields of view at high temperatures, free from the restraints of index-matching fluids and is expected to improve the sensitivity of microscopes and biological detectors and also have applications in other areas of biology and analytical chemistry in the future [102].

2.3.2 Optofluidic platforms for particle transport

In the context of optofluidics, most particle transport examples use optical forces as described in section 2.4. In this section, the author will detail several novel examples of particle transport in optofluidic devices.

2.3.2.1 Transport of particles in liquid core waveguides

Particles can be transported in the core of waveguiding media using optical forces. In optofluidics, light in the core of waveguiding media can be confined by liquid and exerts optical forces that trap and transport the particles. One example of such devices is a photonic crystal fiber which consists of a high index liquid core surrounded by a lower index periodic lattice of air capillaries. Mandal et *al*. [111] demonstrated the transport of polystyrene particles (Ø3 µm) using a liquid core photonic crystal fiber. In a separate work, polystyrene particles (Ø1 µm and 3 µm) were shown to be drifted in a microfluidic channel using direct radiation of optical beams perpendicular to the fluid flow direction [112]. Light was focused into the microfluidic channel using on-chip lenses and their displacement in liquid was studied using various light focusing parameters.

2.3.2.2 Transport of particles using optofluidic waveguide near fields

As described in section 2.2.4.1, the optical near fields can be used for transporting particles in microfluidics. An application example involves the field of a Y-shaped optical waveguide which transported polystyrene particles (Ø6 µm) [113]. By shifting the position of the input fiber facet, power was directed to either side of the Y-branched output which caused the particles to follow and be sorted on demand.

Another platform is the slot waveguides. A slot waveguide is an optical waveguide that strongly confines light in a sub-wavelength scale region which is usually a low refractive index "slot" separated by slabs of high refractive index media [114, 115]. The cavities in such slot waveguides can be filled with a liquid media and particles can be transported using such platforms as strong intensities and gradients of light occur in these slot cavities. Yang et *al.*[116] investigated the trapping and transport of suspended polystyrene (Ø10-65 nm) and gold (Ø10-65 nm) particles using silicon slot waveguides. The authors studied the effects of particle size, refractive index and slot waveguide geometry on particle transport behavior. They also demonstrated the transport and trapping of λ-DNA molecules using such liquid core slot waveguides where the effects of varying slot widths were shown [71].

Optofluidic ring resonators are another device that uses optical evanescent fields for particle transport [117]. In ring resonators, particles are attracted and propelled by optical forces along the evanescent field of a waveguide that branches into a ring structure. Due to the re-circulation of optical power in the ring, the optical power is significantly enhanced under certain resonant conditions [118, 119]. The optofluidic ring resonators are highly suited for particle transport, separation and sensing applications [117, 120, 121].

Yang et *al.* [122] presented the transport of polystyrene particles (Ø3 µm) using an optofluidic ring resonator (Figure 2.15A). The resonator structure was made of a polymeric waveguide. A portion of the optical power extends into the ring waveguide structure in the region where the distance between waveguide and ring is smallest. When the light that has travelled around the ring is in phase with incoming optical radiation, the optical waves constructively interfere resulting in a stronger optical field. The optofluidic ring resonator

operates by alternating between an “on-resonance” and “off-resonance” state which depends on the wavelength of coupled light. When the ring is “on-resonance”, particles trapped on the bus waveguide will be routed to the ring due to optical gradient forces arising from stronger local field intensities in the ring (Figure 2.15B). In the “off-resonance” state, the waveguide has a relatively stronger intensity (compared to the ring) and so the particles remain on the waveguide (Figure 2.15C). Moving from the on-resonance to the off resonance states and vice-versa is achieved by tuning the wavelength of the coupled light. Similar systems were shown by Cai et *al.*[123, 124].

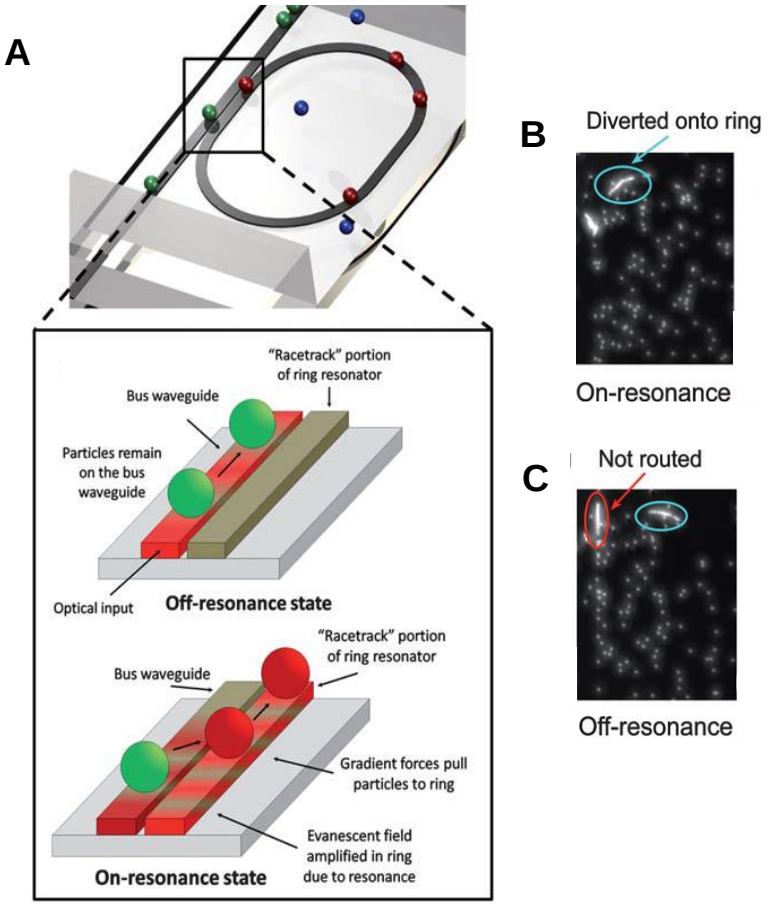

Figure 2.15: Optofluidic ring resonator: (A) Schematic of optofluidic ring resonator switch with boxed figure showing the switching mechanism due to optical forces when the ring is strongly coupled at the resonant wavelength (B) Trapped particles are diverted and continue to move forward on the ring under the on-resonance state (C) In the off-resonant state, particles pass through the switching junction and are not routed into the ring structure. [122]

2.3.2.3 Transport of particles using optically induced virtual electrodes

Particles can be transported using a projection of virtual microelectrodes in a technique known as optically induced DEP manipulation. Chiou et *al.* [75] presented the manipulation and transport of suspended polystyrene particles (Ø4.5 µm) and cells using this method. The liquid containing the cells or particles of interest is sandwiched between an upper transparent, conductive glass, and a lower photoconductive surface. These two surfaces are biased with an AC signal. When the projected light illuminates the photoconductive layer, it turns the virtual electrodes on, creating non-uniform electric fields and enabling particle transport and manipulation. Such optically induced DEP platforms are advantageous as they produce high optical powers and the small pixel sizes of the virtual electrodes result in highly dynamic and accurate particle displacements [125, 126].

2.3.3 Optofluidic devices for particle detection and analysis

In this section, the author describes optofluidic devices that have been used for detecting and analyzing particles. In such devices, generally, particles are transported using the manipulation forces (described in section 2.2) and then they are passed through an optical interrogation or excitation region, where they are detected and analyzed.

2.3.3.1 Detection based on fluorescence and light scattering

Fluorescence detection has been used in many areas, particularly bio-applications, by incorporating particles that show fluorescence emissions [127]. They are used as the labels for revealing the presence and tracing the movement of such particles. Light scattering is another method of detecting and analyzing particles. The analysis of scattered light allows the determination of particle characteristics such as size, refractive index and absorption coefficient [128]. Therefore, relevant information about a particle can be inferred from the analysis of the scattered light.

There are many examples of optofluidic applications that incorporate fluorescent particles. Perroud et *al.* [129] demonstrated the identification and sorting of macrophage cells based on fluorescent signals. Shi et *al.* [23] presented the fluorescent detection and tracking of polystyrene (Ø0.87 µm and 4.16 µm) beads in a microfluidic channel. Parallel inter-digitated acoustic resonators were used to position and separate the particles so that they could be sorted into three fluidic outlets. Fluorescence spectroscopy was then used to track the separation of the particle types.

There are also many examples of the analysis of particles based on scattering methods. Mitra et *al.* [130] demonstrated the detection, sorting and size characterization of viruses and particles using an optofluidic interferometer. The detection scheme used was able to detect and sort single viruses and also distinguish different kinds of virus types in a mixture of viruses.

2.3.3.2 Optofluidic ARROW platforms

The hollow core anti-resonant reflecting optical waveguide (ARROW) is often used for guiding light in liquid, particularly in microfluidic systems [131]. ARROWs can be formed by a low index core layer which is embedded between higher index layers. This addresses the difficulty of finding suitable optical cladding materials, with a lower refractive index than liquid making them well suited for optofluidic applications. ARROW platforms have the advantage of low loss of signal, almost single-mode behavior and they have high polarization selectivities [132].

The fabrication and operation of ARROW waveguides have been well documented [93]. An example by Measor et *al.* [133] is demonstrated in Figure 2.16. It is an optofluidic ARROW platform that provides a perpendicular excitation and detection geometry and that caters for sensitive particle and bio-molecular detection applications. The device was made of a high refractive index layer surrounding a hollow core filled with the suspended particles that needed to be analyzed (Figure 2.16A). Light that is coupled into the solid-core ARROW waveguide (Figure 2.16B) provides an optical excitation to the fluorescent labeled particles that flow through the hollow core waveguide (Figure 2.16C). The hollow core waveguide is filled with liquid and the particles that flow through the hollow core are transported using

dual beam optical trap. The ARROW platform has been used for detecting liposomes, DNA fluorophores and viruses [93, 134-137].

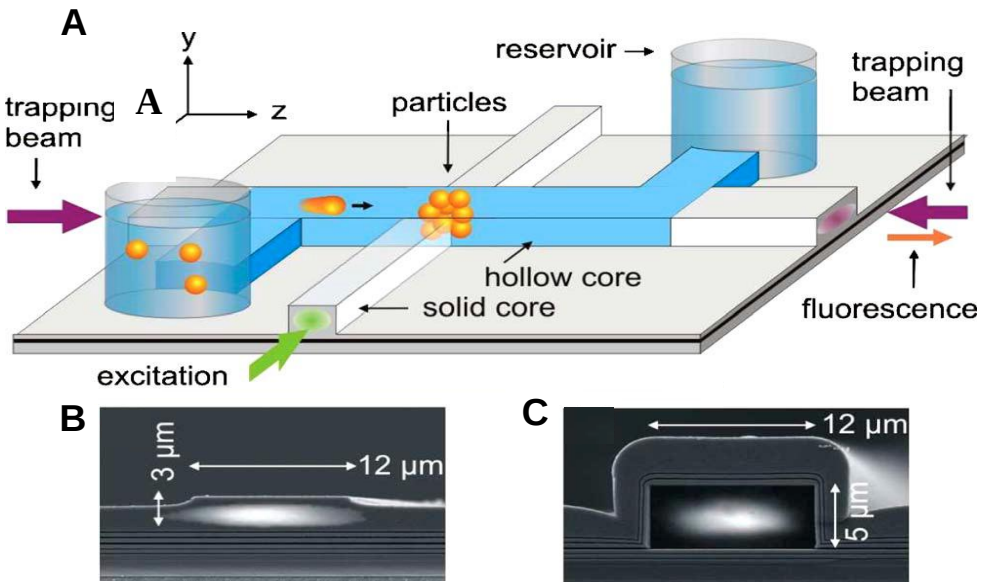

Figure 2.16: Optofluidic ARROW platform optimized for particle detection: (A) Schematic of the integrated optofluidic system with perpendicular excitation/collection geometry for detecting bio-molecules. (B) SEM images of solid core and (C) liquid core ARROW waveguide cross-sections (D) Actual image showing ARROW device. [133]

2.3.3.3 Optofluidic flow cytometers

The flow cytometer is perhaps one of the most important optofluidic detection platforms, as it provides *in situ* cell counting, fluorescence detection and cell sorting, all in an integrated device. This device provides fast quantification of different organic and inorganic particles and cells. Generally, the sample containing the particles is hydrodynamically sheath focused by a surrounding buffer liquid to obtain a stable particle line-up. The particles then pass through an optical interrogation region, where they are detected and characterized based on their fluorescence emissions and scattering of light [138].

Shvalov et *al.* [128] presented one of the earlier versions of the flow cytometer that was able to distinguish lymphocytes, erythrocytes and polystyrene particles of various sizes and refractive indices. The analysis of particles was conducted by examination of the unique

profiles of scattered light that had varying scattering angles from the particles. Steen [139] also presented the earlier version of the cytometers capable of detecting viruses of various sizes ranging from 70 - 300 nm.

Today, flow cytometry has evolved tremendously. Although fluorescent detection and hydrodynamic forces are conventionally used, new methods such as impedance detection is being integrated into microflow cytometers for microparticle-based assays and magnetophoresis of biomolecules is being used for particle sorting [140]. Modern cytometers also feature optofluidic liquid lenses that focus light into the particle interrogation region for more effective particle analysis [141]. Zhu et *al.* [142] presented a compact and cost-effective cytometer for resource limited regions integrated with cellular phone imaging. In this device, fluorescently labelled particles were continuously delivered to an imaging volume via a disposable microfluidic channel. The videos were captured by the cellular phone camera and analyzed for particle/cell counting. Such platforms could be useful for rapid and sensitive imaging of bodily fluids and for conducting various cell counts and analysis as well as for screening of water quality in remote and resource-poor settings.

Flow cytometers have also been integrated with DEP microelectrodes for the sorting and characterization of cells such as yeast [143]. In this work, positive DEP forces were used to sort between viable and non-viable yeast cells. This was possible as viable and non-viable yeast cells were found to have different DEP spectral behaviors so they could be sorted by these properties before being counted. After passing through the "DEP filter" region, light scattered from the specimens was collected by an integrated waveguide and analyzed.

2.3.4 Raman spectroscopy of particles

Raman spectroscopy (RS) provides analytical information about a samples' molecular structure and composition [144] and it has attracted considerable research due to its high sensitivity and low detection limits in sample detection. RS is a spectroscopy technique that relies on the inelastic scattering of monochromatic light from a sample [145]. A small portion of light scattered from the sample is scattered at a series of different wavelengths that are indicative of the vibrational transitions of the molecules [146]. Because different molecules have different vibrational modes, the spectrum of the inelastically scattered light

uniquely identifies the sample. Surface enhanced Raman spectroscopy (SERS) is a surface-sensitive technique that enhances the Raman scattering signal by molecules adsorbed on rough metal surfaces [145]. In SERS, the target molecule is brought into close proximity to a metallic (typically Ag, Au or Cu) surface with nanoscopically defined features or in solution of such metallic nanoparticles with feature sizes smaller than the wavelength of the excitation light. When light is incident on the surface or particle, a surface plasmon mode is excited which locally enhances the electromagnetic energy in the vicinity of the target molecule, significantly enhancing the intensity of the inelastically scattered light. The total enhancement to the Raman signal observed in response to this effect can be several orders of magnitude larger than that of the unenhanced Raman signal [146].

In microfluidic systems, the particle characterization process using RS analysis can be complex. The sensitivity of the Raman signal needs to be high but yet the challenge lies in developing a stable and reproducible Raman-active substrate under constant liquid flow. Also, it is complicated due to the non-uniform distribution of the SERS-active substrates when they are dispersed in liquids. One of the solutions to these underlying issues is to employ controllable particles. Particle manipulation forces that have been employed for controlling particles as SERS-active targets in the microfluidic-RS devices include hydrodynamic, dielectrophoretic and optical forces.

Wang et *al.* [147] demonstrated an optofluidic SERS device that uses a pinched and step microchannel junction that traps and assembles nanoparticles/target molecules into optically enhanced SERS active clusters by using hydrodynamic capillary forces. Chrimes et *al.* [148] demonstrated optofluidic SERS measurements (Figure 2.17A) with the aid of DEP microelectrodes for the mapping, recognition and concentration measurement of WO_3 nanoparticles (Ø80 nm, n = 2.3). A curved DEP microelectrode array concentrated the moving particles at the SERS detection region. When the particles were concentrated to the region between the electrodes, the Raman spectral peaks were higher indicating a higher concentration of particles. It was revealed that reducing the DEP applied frequency with a constant magnitude signal would increase the concentrations of particles in between the curved electrodes. Figure 2.17B presents the Raman spectral peaks as a function of DEP applied frequencies. It shows that as the DEP applied frequency is reduced, particle concentration increases and thus the Raman spectral peaks are amplified. This platform

enables *in situ* analysis of particles flowing in liquid, without the need for dehydration or immobilization as in conventional SERS analysis devices. It is also possible to establish particle concentration levels in microfluidic systems using such platforms.

White et *al.* [149] used optical gradient forces from the evanescent fields of optofluidic ring resonator waveguides to enhance SERS-detection where light was confined within the high refractive index liquid core of the waveguide. Rhodamine 6G mixed with silver particles (Ø50 - 100 nm) formed nanoclusters and were used as the target sample in the experiments. The liquid core optical ring resonator serves both as the microfluidic sample delivery mechanism and as a ring resonator, exciting the metal nano-clusters and target analytes as they pass through the channel. Tong et *al.* [150] demonstrated the use of optical and hydrodynamic forces to aggregate Ag particles (Ø40 nm) in the Raman-detection region. Thiophenol (TP) and 2-naphthalenethiol (2-NT) were adsorbed to the Ag particles to form the target sample. In a separate work, cell transport and sorting was achieved using a combination of hydrodynamic and optical forces while a RS signal was used for both, identification and simultaneous sorting of label-free leukemia cells [151]. Such platforms are suitable for automated particle identification and sorting.

The ARROW platform, described in section 2.3.3.2 of this chapter, has also been used for SERS detection. The high optical intensities of light that propagate along the liquid core of the ARROW waveguide were used to trap the target Rhodamine 6G molecules that were adsorbed to the Ag particles. The enhanced RS signal was able to detect the molecules at a low dispersion concentration of 30 nM [152].

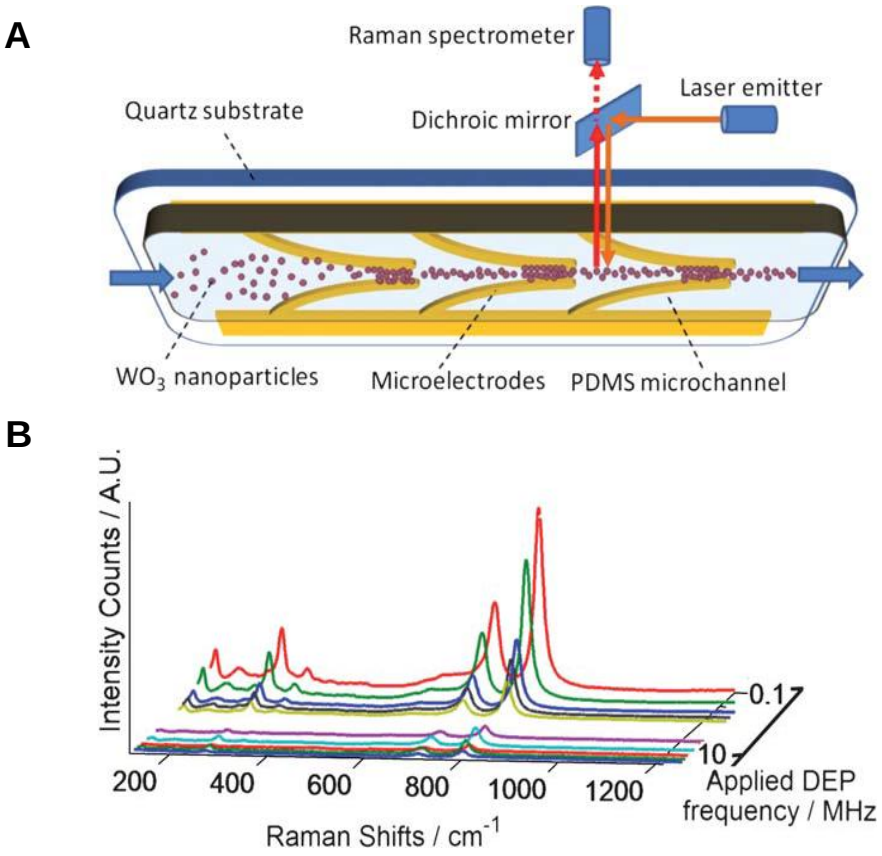

Figure 2.17: Raman spectroscopy analysis using a DEP microfluidic platform: (A) Schematic of DEP-Raman system layout (B) Plot of WO_3 nanoparticle Raman spectra at different DEP frequencies, decreasing in frequency along the *z*-axis. [148]

2.3.5 Plasmonic inspired optofluidics

In this section, we focus on describing optofluidic devices, which incorporate both plasmons and suspended particles. The applications of such optofluidic devices are mostly found in areas of particle manipulation [153-156] and sensing [65, 157]. Commonly in many plasmonic measurements and manipulations, metal (such as gold or silver) nanostructures or nanoparticles are used to provide the enhancement for surface plasmons. The systems are either based on prefabricated nanostructured surfaces (such as surfaces with arrays of nano posts and nano-roughened surfaces) or agglomerated nanoparticles. Nanostructured surfaces or agglomerated nanoparticles show significant hot-spot enhancement when grains or particles form optimum spacing in the order of several to tens of nanometers [158].

2.3.5.1 Plasmonic transport of particles

We described the features and advantages of plasmonic manipulation of particles in section 2.4. A good example is demonstrated by Wang et *al.* [159]. They used surface plasmons generated on a gold stripe in order to manipulate transport polystyrene (Ø1 - 2 µm) particles in a microfluidic channel (Figure 2.18A). The particle was moved using optical forces, which resulted from the SPR excitations of light in close vicinity of the gold stripe. Figure 2.18B shows the images of scattered light which gives an indication of the particles' locations for analyzing their motion and velocity.

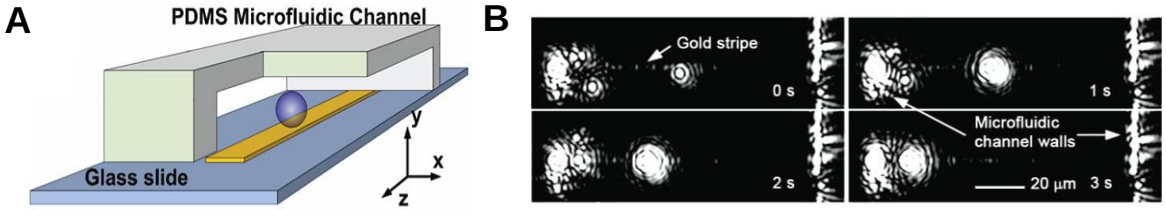

Figure 2.18: Optofluidic device used for plasmonic transport of particles: (A) Schematic of optofluidic-plasmonic trapping device, consisting of a gold stripe in a microfluidic channel formed on a microscope glass slide. (B) Time sequence of scattered light images of particles in the microfluidic channel. [159]

Plasmonic transport was also demonstrated using an array of gold micro-pads that acts as plasmonic traps using a visible laser to provide the SPR excitations [155]. In this work, polystyrene (Ø5 µm) particles and yeast cells were manipulated and trapped in close vicinity of the micro-pads, where the optical intensity gradients were high. In a separate work, the transport of polystyrene (Ø6 µm, 1 µm and 200 nm) particles was demonstrated near the surface of gold nano-structures (~130 nm diameter gold nano-dot pairs separated by a gap of 200 nm) [70]. When the laser excitation source was moved, the SPR fields close to the nano-dot array moved the particles as well.

2.3.5.2 Plasmonic sensing

SPR technology has been rapidly gaining acceptance as an advanced and reliable sensing technique [160-162]. This technique has the advantage of high sensitivity to refractive index changes, label free detection and it reduces the need for fluorescent binding of the target analytes [146]. A surface plasmon is excited by a light wave propagates along a metal film, and its evanescent field probes the target particle nearby. A perturbation in the refractive index of the target gives rise to a change in the surface plasmon characteristics. These characteristics include the coupling angle, coupling wavelength, intensity and phase of the light [160, 163].

A good example is the work of Hsu et *al.* [164]. They demonstrated a plasmonic sensor using a partially unclad optical fiber with gold (Ø16 nm) and silver (Ø32 nm) particles attached to the waveguide core surface. The unclad fiber was placed in the flow direction of a microfluidic channel to enable the delivery of target analytes by hydrodynamic forces. The detection and identification was based on the analyses of evanescent-wave absorption of the metallic particles located on the fiber surface. The plasmonic bio-sensor was able to detect streptavidin, dinitrophenol, ovalbumin antigens and matrix metalloproteinase-3 genes at low detection limits.

2.3.6 Thermal and energy related applications

2.3.6.1 Thermal

In this section, the author describes thermal and energy related applications of optofluidics which incorporate controllable particles. Thermally induced particle motion stands as the main kinetic process involved in "thermo-optofluidic" applications. In these applications, particles are either heated, causing them to migrate according to thermophoretic behavior that was described in section 2.2.3 [165, 166]. Sources of heat can be optical, mechanical or electrical. It has also been demonstrated that certain plasmonic nanostructures [167], and thermally responsive particle composites [168] absorb and induce localized heating upon exposure to light.

Duhr et *al.* [169] demonstrated the thermophoretic transport of deoxyribonucleic acid (DNA) molecules. In this work the tracing of the DNA molecule concentrations were recorded by fluorescence measurements. In a separate work, a focused beam of near-infrared light was used to induce heat and manipulate polystyrene (Ø49 and Ø100 nm) particles which were also fluorescently labeled for tracking purposes [170].

Baaske et *al.* [171] demonstrated the thermophoretic manipulation of aptamer bindings consisting of human blood serum (Figure 2.19). In the authors work, the blood serum inside a microfluidic capillary was locally heated using a focused infrared laser (Figure 2.19A). The aptamers motion in response to the locally generated heat was traced using fluorescence spectroscopy. When the laser was turned on, the aptamers moved away from the heated spot. When the laser was turned off, the aptamers diffused back (Figure 2.19B). The authors also used the device to quantify the biomolecular binding reactions of unlabelled aptamers to the target blood serums.

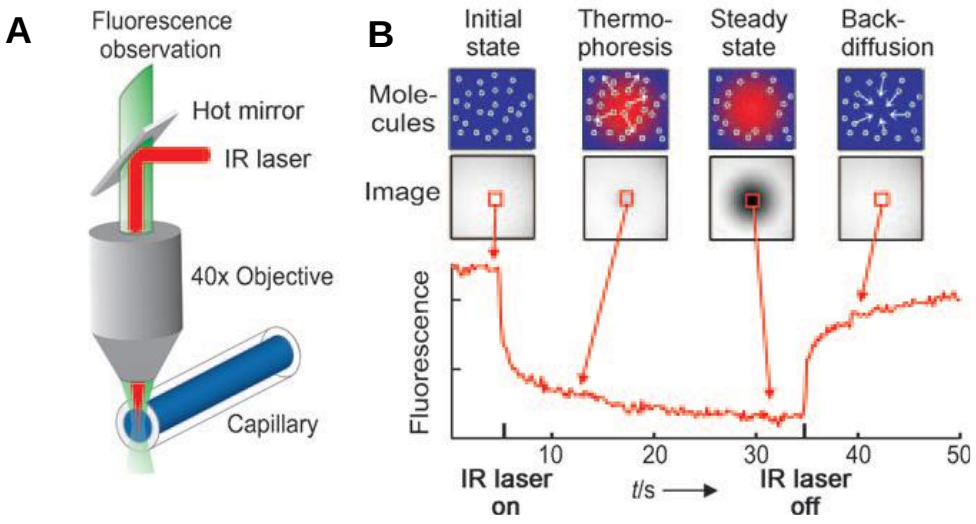

Figure 2.19: Thermophoretic transport of aptamer bindings: (A) Blood serum inside the capillary is locally heated with a focused IR laser, which is coupled into an epifluorescence microscope using a heat-reflecting “hot” mirror (B) The fluorescence inside the capillary is imaged with a CCD camera, and the normalized fluorescence in the heated spot is plotted against time. The IR laser is switched on at $t = 5$ sec, the fluorescence decreases as the temperature increases, and the labeled aptamers move away from the heated spot because of thermophoresis. When the IR laser is switched off, the molecules diffuse back. [171]

2.3.6.2 Energy generation

Recently, a review by Erickson et *al.* [172] described the potential opportunities in optofluidics research involving fuel production using photobioreactors and photocatalytic systems. Also, the author described optofluidic enabled solar energy collection and control.

Basically, the authors presented the opportunity of enhancing solar-energy based fuel production using photobioreactors containing photocatalytic particles such as TiO_2 in microfluidics. It was argued that these reactors could harvest optical energy generating entities such as oil, hydrogen and isobutanol from microorganisms. The second point presented was the conversion of water into its hydrogen and oxygen components, and the conversion of carbon dioxide and water into hydrocarbon fuels using photocatalytic reactions of micro/nano particles.

2.3.7 Optofluidics incorporating biological particles

Optofluidics research has had a remarkable impact on the life sciences field. Bio-particles such as proteins, DNAs, organelles, cells and other microorganisms have all been used and incorporated in optofluidic devices. In previous sections, the author mentioned some of the applications of bio-particles to highlight their relevant optofluidic properties, particularly in sections 2.3.3 and 2.3.4. However, the author exclusively devotes this section to bio-particles used in optofluidic systems which have not been discussed previously.

The use of bio-particles in optofluidics can be divided into two major categories: (1) Optofluidic devices used for the analyses and transport of bio-particles such as in filtering and sorting and (2) Optofluidic devices enabled with bio-particles, such as organic lasers. The author focuses on describing novel applications of such “bio-enabled” optofluidic devices with the emphasis on particles that are controlled by externally applied forces.

2.3.7.1 Optofluidics for the transport and analyses of biological components

There have been many applications of optofluidic devices being used for transporting and analyzing bio-particles. These particles were manipulated using a variety of forces such as magnetic, acoustic and optical forces.

Many optofluidic systems use the magnetic properties of particles for eventual bio-applications. An example of such manipulation is presented in the work of Lien et *al*. [173] They use antibody conjugated magnetic beads (Ø4.5 μm) to detect and isolate influenza A viruses. Target influenza A virus was immobilized onto the surface of the magnetic beads. This was followed by labeling the fluorescent signals onto the virus-bound magnetic complexes and analyzing them using an optical detection module. Another optofluidic bio-analysis platform involves a multi stage separation system that separated a cell mixture in blood based on their magnetic susceptibility properties [174]. The platform separated red and white blood human cells using the magnetophoretic force while fluorescent imaging was used to trace the particle separation efficiencies.

Lenshof et *al.* [175] reported an acoustophoretic manipulation platform that isolated plasma from whole blood. The acoustophoretic separator could remove enriched blood cells in multiple steps to yield high quality plasma of low cellular content. Based on fluorescence measurements, the plasma had erythrocyte concentrations of less than 6.0×10^9 units and a low concentration of prostate specific antigens.

Optical forces can exert force on bio-particles as described in section 2.2.4 *via* either far or near field. In one example, Hwang et *al.* [176] demonstrated the separation of *oocytes* (cell in the reproduction system produced by the human ovaries) in an optofluidic platform based on optically generated virtual electrodes for *in vitro* fertilization. The device was successful in separating the fertilizable and abnormal *oocytes* from the mixture based on their responses toward the generated optical fields and their motion velocity differences (Figure 2.20). Kim et *al.* [177] demonstrated an optofluidic device which consists of a microchannel and an optical waveguide structure inside fused silica for the interrogation and processing of single

cells. Single red blood cells (RBC) in diluted human blood inside of the microchannel were detected by the intensity change of the light delivered by the waveguide.

Plasmonic optical manipulations of bio-particles in microfluidics are great examples of near field forces on such particles. Biological particles were trapped using plasmonic induced forces. For example, Righini et *al.*[178] demonstrated the trapping of living Escherichia coli bacteria for several hours using moderate light intensities. The control of the bacteria was achieved using metallic nano-antennas patterned on a glass substrate to produce strong light intensity gradients when illuminated by a resonant optical source.

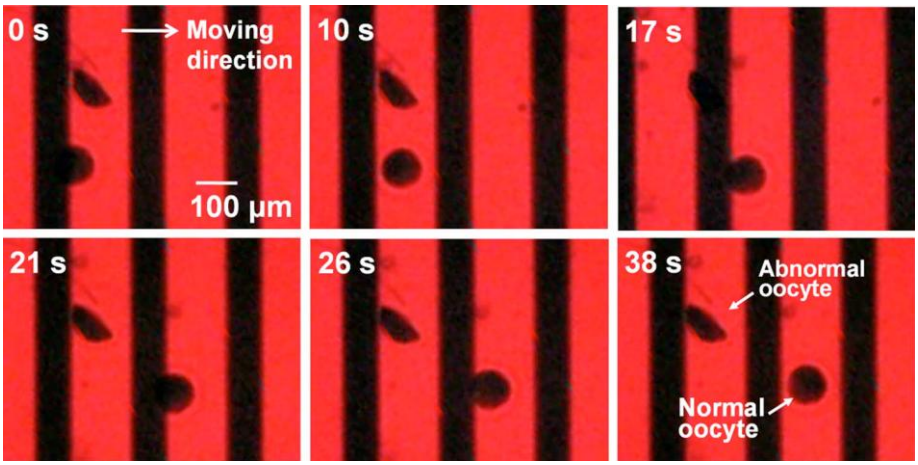

Figure 2.20: Captured images of the discrimination of normal and abnormal *oocytes* using an optically induced DEP electrode scanning from left to right. Samples were manipulated at the DEP voltage of 10 V_p at 1 MHz. When the DEP signal was applied and the projected DEP electrodes were moved, only the normal *oocyte* were displaced in the direction of image pattern, while the abnormal *oocytes* remained at the initial position. [176]

2.3.7.2 Optofluidics enabled with biological components

Optical components such as lasers have important applications ranging from optical communications and medicine to materials processing and analysis. In order to tailor the properties of light emitted by lasers, to the specific needs of each application, different optical gain materials are required. Until recently, however, little work has been done on using bio-particles in microfluidics as part of the "lasing medium" of lasers [179].

Lasers based in particles in microfluidics generally fall in the category of dye lasers. Dye lasers are generally wide bandwidth. The wide bandwidth range makes the dye lasers particularly suitable for tuneable and pulsed laser applications. Dye lasers are commonly used in medical spectroscopy, biochemical sensing or biophysics related applications.

Sun et *al.* [180] demonstrated a bio-inspired optofluidic dye laser excited by fluorescent resonance energy transfer (FRET) [181]. FRET describes the mechanism of energy transfer between donor and acceptor chromophores. In the authors work, DNA strands were used as nanoscale scaffolds to adjust the separation between donor and acceptor chromophores. The characteristics of the FRET lasers such as spectrum, threshold, and energy conversion efficiency were reported. They claimed that through the DNA scaffolds, nearly 100% energy transfer could be maintained regardless of the donor and acceptor concentration.

Gather et *al.* [179] demonstrated a dye laser which used colonies of *escherichia coli* bacteria as the lasing medium. The bacteria were genetically transformed to synthesize fluorescent protein. The optical gain effect in the laser was demonstrated by clear threshold behavior and discrete peaks in the laser emission spectrum. Demonstration of lasing from bacteria and other organic bio-species proves to be an important step towards realizing self-sustainable biological lasers.

2.4 Extended Review on Dielectrophoresis

In section 2.2.2.2, the author briefly described the fundamentals of DEP particle manipulations. In this section, he provides an extended review of this subject elaborating on the theoretical derivations of the DEP force, the “DEP spectrum” concept, commonly used DEP microelectrode configurations and the motivations and strategies for implementing DEP particle control in this PhD research project.

2.4.1 DEP Force

Dielectrophoresis is the motion of particles caused by the interaction of a non uniform electric field, E, with the induced dipole moment of a polarizable particle, P. The DEP force which creates such a motion, is defined as [182]:

$$F_{\text{DEP}} = (P.\nabla)E \tag{2.18}$$

The quasi-static electric field, E within a microfluidic system is expressed as [183]:

$$E(x,y,z,t) = E_x \cos(\omega t + \varphi_x)\vec{i} + E_y \cos(\omega t + \varphi_y)\vec{j} + +E_z \cos(\omega t + \varphi_z)\vec{k} \tag{2.19}$$

where φ is the phase component of the applied electric field, t is the time, and ω is the angular frequency of the electric field. The dipole moment, P, depends on the geometry of the particle and for a homogenous spherical particle, it is defined as [182]:

$$P = 4\pi r^3 \varepsilon_o \varepsilon_m f_{CM} E \tag{2.20}$$

where r is the radius of the particle, $\varepsilon_o = 8.854\times10^{-12}$ (F m^{-1}) is the permittivity of vacuum, ε_m is the dielectric constant of the medium and $f_{CM}(\omega)$ is the Clausius-Mossotti factor, which was defined in equation (2.9) of section 2.2.2.2. Combining equations (2.18-2.20), the time-averaged DEP force applied on a spherical particle is obtained as [182, 184]:

$$F_{DEP} = \underbrace{2\pi r^3 \varepsilon_o \varepsilon_m \,\text{Re}[f_{CM}]\nabla E^2_{rms}}_{\text{Classical DEP force}} + \underbrace{4\pi r^3 \varepsilon_o \varepsilon_m \,\text{Im}[f_{CM}] \sum_{x,y,z} \nabla E^2_{rms} \nabla\varphi}_{\text{Travelling wave DEP force}} \tag{2.21}$$

The above equation consists of two independent terms contributing to the DEP force. The first term is proportional to the real part of the $f_{CM}(\omega)$ and the spatial non-uniformity of the electric field, and it is referred to as the 'classical DEP force'. This force pushes the particles toward or away from the regions of high electric field gradients according to the polarity of Re[$f_{CM}(\omega)$].

Alternatively, the second term, describing the traveling wave DEP force is proportional to the imaginary part of the $f_{CM}(\omega)$, the gradient of the phase component and is referred to as the 'travelling wave (TW) DEP force'. This force pushes particles toward or away from the direction of wave propagation, according to the polarity of Im[$f_{CM}(\omega)$] [33]. When the TW DEP force is not employed, equation (2.21) simplifies to the classical DEP force equation expressed in section 2.2.2.2 as equation (2.8).

2.4.2 DEP Spectrum Concept

The "DEP spectrum" provides the variations of the Re[$f_{CM}(\omega)$] with respect to frequency and it indicates the predicted behavior of particles when they are subject to a DEP signal of varying frequencies. The Re[$f_{CM}(\omega)$] embodies five influential parameters of a DEP system including: (i) the dielectric properties of the particle reflected by its conductivity and permittivity, (ii) the shape of the particle, e.g. spherical, ellipsoidal or cylindrical geometries, (iii) the interior structure of the particle, e.g. homogenous and multi-layer structures, (iv) the dielectric properties of the suspending medium reflected by its conductivity and permittivity, and (v) magnitude and the frequency of the applied signal [33]. The first four parameters exhibit the characteristics of the particle and the suspending medium that depends on their intrinsic specifications while the last parameter can be selected and tuned according to the functionality required of the DEP system.

Figure 2.21 presents a schematic of a DEP system which shows the behavior of two distinct particles. When Re[$f_{CM}(\omega)$] > 0, particles experience a positive DEP force and are attracted to the regions of high electric field gradients. Conversely, when Re[$f_{CM}(\omega)$] < 0, particles experience a negative DEP force and are repelled from those regions (Figure 2.21). Therefore, prior knowledge of the Re[$f_{CM}(\omega)$] provides the user of DEP systems with a range of suitable DEP applied frequencies that can be used for manipulating the motion of particles as desired. In this PhD research project, the DEP spectrum for the particles used in each stage of the PhD research project are calculated and simulated in chapters 4, 5 and 6.

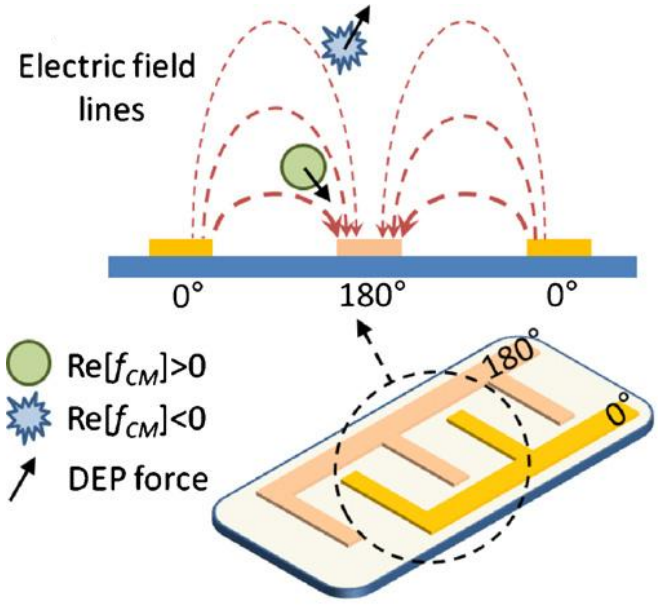

Figure 2.21: Schematic showing the behavior of particles exhibiting positive and negative DEP forces in response to high electric field gradients. [33]

2.4.3 Microelectrode Configurations

The electric field gradients, which are essential in inducing the DEP force, are generated by the DEP microelectrodes. These microelectrodes can be designed with a variety of configurations capable of producing distinct electric field gradients for achieving the desired placement and motion of particles. These microelectrode design configurations include: (1) Inter-digitated (2) Castellated (3) Quadruple and (4) Curved microelectrode configurations (Figure 2.22). The features of these microelectrode configurations are briefly described as follows.

- Inter-digitated

This microelectrode configuration is also known as the finger pair electrode (Figure 2.22A). The electrodes generate the greatest electric field gradients directly above their surface, and, hence, can effectively trap or repel the particles nearby. The design offers a large trapping area in microfluidic systems by adjusting the ratio of the length of the electrode "finger" to the micro-channel width [34]. This design is widely used in DEP platforms used for sensing and particle trapping [185-187].

- Castellated

  The electrodes generate the maximum electric field gradients between the tips, and hence generate a large trapping DEP force (Figure 2.22B). Electrodes can directly face each other (non-offset) or be offset by a certain distance producing distinct effective electric field gradients and particle trapping areas [34]. Multiple pairs of electrode tips are usually patterned to enhance the trapping efficiency and they are used for trapping small amounts of particles between the electrode pairs [188, 189].

- Quadruple

  Quadruple electrodes or also known as polynomial electrodes [34] operate in a different way to inter-digitated or castellated electrodes (Figure 2.22C). The quadruple electrodes produce the strongest electric field gradients along the pads, and the weakest at the center of the pattern [33]. Therefore, particles experiencing a negative DEP behavior would be repelled to the center of the pattern but particles experiencing positive DEP behavior would be focused along the pads. This configuration is commonly used for particle separation applications [190-192].

- Curved

  The curved microelectrode design generates the highest electric field gradients between the tips (Figure 2.22D). The microelectrode tips acts as discrete funnels and focuses the particles passing through the microfluidics along the centerline of the microchannel or repels them towards the sidewalls [10]. They are effectively used in combination with hydrodynamic forces and are suitable for trapping, separating and forming three dimensional dense particle streams in the microfluidics [148, 193, 194].

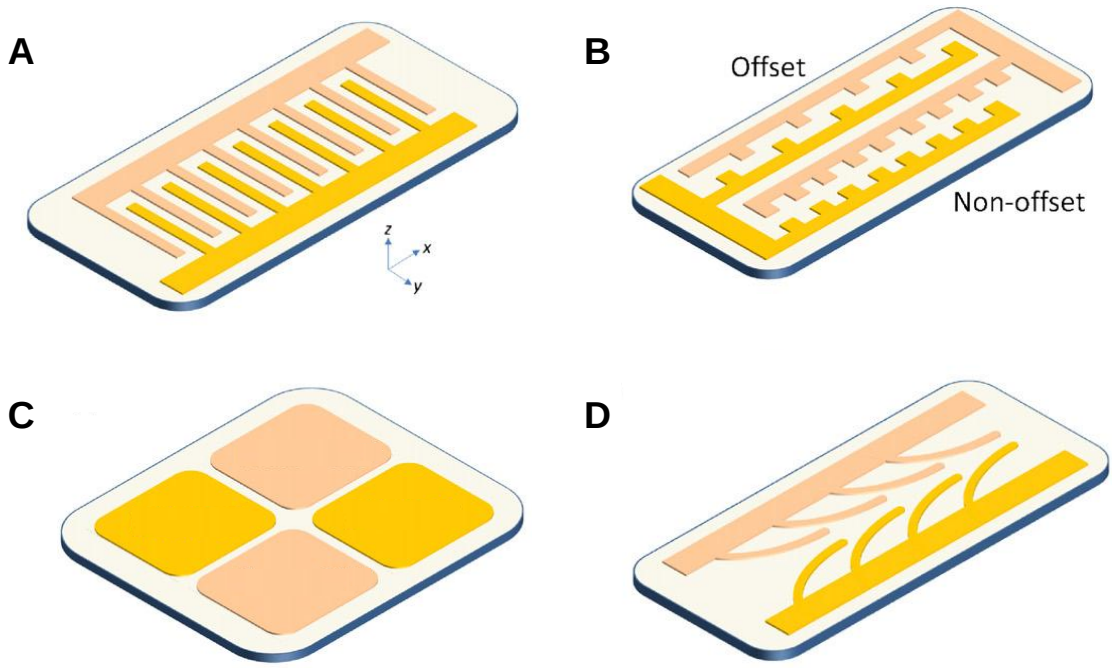

Figure 2.22: Commonly used DEP microelectrode configurations: (A) Inter-digitated (B) Castellated (C) Quadruple (D) Curved. [33]

2.4.4 Motivations and Strategies for Implementing DEP Manipulation

The objective of this PhD research project is to form 3D suspended objects in liquid using suspended particles. The DEP force was selected as it is able to control neutral and semi-conducting particles effectively, which are the types of particles used in this PhD research project. The author employed the curved microelectrode configuration as it provides the ability for bringing particles close to each other and then dispersing them on demand. Using this microelectrode design, the particles could be focused and repelled from regions of interest in the microfluidics by simply varying the applied frequency of the DEP AC signal. In particular, the DEP force was apt at establishing dense particle streams in the microfluidic channel (as will be seen in chapters 4, 5 and 6) which have smooth and non-turbulent boundaries when combined with hydrodynamic forces induced by the flow of liquids. The motional behaviors were precise and consistent as particles have distinct permittivity and conductivity properties relative to the suspending media.

The author utilized prior knowledge of the DEP spectrum for each of the particles used in the experiments to predict their behavior in response to an applied electric field. Additionally, the DEP spectra were implemented to provide the range of suitable frequencies which could be applied for accurately manipulating the particles in achieving the desired movements. For instance, by tuning the frequencies of the applied DEP signal, particles could be closely packed into forming 3D suspended objects having distinct refractive index profiles. The properties of these suspended objects were then adjusted by simply tuning the amplitude of the applied DEP signal. These parameters could be dynamically controlled and adjusted at the AC signal source. In essence, these were the motivations and strategies for implementing the DEP particle manipulations in this PhD research project.

2.5 Summary

In this chapter, the author presented active manipulation forces that control the motion of particles in microfluidics. In addition, he presented a considerable amount of examples of optofluidic systems which incorporate suspended particles. A major portion of this chapter was submitted for publication consideration in the Journal of Biomicrofluidics.

In this PhD research program, the DEP force was selected as it provides the most suitable form of the applied force for manipulating particles. The curved microelectrode configuration was chosen and its performance in controlling the motion of particles will be further elaborated in chapters 4, 5 and 6. In the next chapter, the author describes the design and fabrication of the experimental platforms used in his PhD research project.

References

[1] Boeker, A., J. He, T. Emrick, and T.P. Russell, Self-assembly of nanoparticles at interfaces. *Soft Matter*, vol. 3, pp. 1231-1248, 2007.

[2] Bishop, K.J.M., C.E. Wilmer, S. Soh, and B.A. Grzybowski, Nanoscale Forces and Their Uses in Self-Assembly. *Small*, vol. 5, pp. 1600-1630, 2009.

[3] Liang, Y., N. Hilal, P. Langston, and V. Starov, Interaction forces between colloidal particles in liquid: Theory and experiment. *Advances in Colloid and Interface Science*, vol. 134-35, pp. 151-166, 2007.

[4] Di Carlo, D., Inertial microfluidics. *Lab on a Chip*, vol. 9, pp. 3038-3046, 2009.

[5] Tsutsui, H. and C.-M. Ho, Cell separation by non-inertial force fields in microfluidic systems. *Mechanics Research Communications*, vol. 36, pp. 92-103, 2009.

[6] Rhodes, M.J., *Introduction to particle technology*. 2nd ed. 2008, Hoboken: Wiley. 450.

[7] Guha, A., *Transport and deposition of particles in turbulent and laminar flow*, in *Annual Review of Fluid Mechanics*. 2008. p. 311-341.

[8] Whitesides, G.M., The origins and the future of microfluidics. *Nature*, vol. 442, pp. 368-373, 2006.

[9] Batchelor, G.K., *An Introduction to fluid dynamics*. 1999, Cambridge: Cambridge University Press.

[10] Khoshmanesh, K., C. Zhang, F.J. Tovar-Lopez, S. Nahavandi, S. Baratchi, K. Kalantar-zadeh, and A. Mitchell, Dielectrophoretic manipulation and separation of microparticles using curved microelectrodes. *Electrophoresis*, vol. 30, pp. 3707-3717, 2009.

[11] Xuan, X., J. Zhu, and C. Church, Particle focusing in microfluidic devices. *Microfluidics and Nanofluidics*, vol. 9, pp. 1-16, 2010.

[12] Yang, S., J.Y. Kim, S.J. Lee, S.S. Lee, and J.M. Kim, Sheathless elasto-inertial particle focusing and continuous separation in a straight rectangular microchannel. *Lab on a Chip*, vol. 11, pp. 266-273, 2011.

[13] Hur, S.C., H.T.K. Tse, and D. Di Carlo, Sheathless inertial cell ordering for extreme throughput flow cytometry. *Lab on a Chip*, vol. 10, pp. 274-280, 2010.

[14] Squires, T.M. and S.R. Quake, Microfluidics: Fluid physics at the nanoliter scale. *Reviews of Modern Physics*, vol. 77, pp. 977-1026, 2005.

[15] Brody, J.P. and P. Yager, Diffusion-based extraction in a microfabricated device. *Sensors and Actuators A - Physical*, vol. 58, pp. 13-18, 1997.

[16] Brody, J.P., P. Yager, R.E. Goldstein, and R.H. Austin, Biotechnology at low Reynolds numbers. *Biophysical Journal*, vol. 71, pp. 3430-3441, 1996.

[17] Tanyeri, M., M. Ranka, N. Sittipolkul, and C.M. Schroeder, A microfluidic-based hydrodynamic trap: design and implementation. *Lab on a Chip*, vol. 11, pp. 1786-1794, 2011.

[18] Tanyeri, M., E.M. Johnson-Chavarria, and C.M. Schroeder, Hydrodynamic trap for single particles and cells. *Applied Physics Letters*, vol. 96, 2010.

[19] Petersson, F., L. Aberg, A.-M. Sward-Nilsson, and T. Laurell, Free flow acoustophoresis: Microfluidic-based mode of particle and cell separation. *Analytical Chemistry*, vol. 79, pp. 5117-5123, 2007.

[20] Evander, M., A. Lenshof, T. Laurell, and J. Nilsson, Acoustophoresis in wet-etched glass chips. *Analytical Chemistry*, vol. 80, pp. 5178-5185, 2008.

[21] Johnson, D.A. and D.L. Feke, Methodology for fractionating suspended particles using ultrasonic standing wave and divided flow fields. *Separations Technology*, vol. 5, pp. 251-258, 1995.

[22] Lilliehorn, T., U. Simu, M. Nilsson, M. Almqvist, T. Stepinski, T. Laurell, J. Nilsson, and S. Johansson, Trapping of microparticles in the near field of an ultrasonic transducer. *Ultrasonics*, vol. 43, pp. 293-303, 2005.

[23] Shi, J., H. Huang, Z. Stratton, Y. Huang, and T.J. Huang, Continuous particle separation in a microfluidic channel via standing surface acoustic waves (SSAW). *Lab on a Chip*, vol. 9, pp. 3354-3359, 2009.

[24] Koklu, M., A.C. Sabuncu, and A. Beskok, Acoustophoresis in shallow microchannels. *Journal of Colloid and Interface Science*, vol. 351, pp. 407-414, 2010.

[25] Li, H., J.R. Friend, and L.Y. Yeo, Surface acoustic wave concentration of particle and bioparticle suspensions. *Biomedical Microdevices*, vol. 9, pp. 647-656, 2007.

[26] Friend, J. and L.Y. Yeo, Microscale acoustofluidics: Microfluidics driven via acoustics and ultrasonics. *Reviews of Modern Physics*, vol. 83, pp. 647-704, 2011.

[27] Gas, B., Theory of electrophoresis: Fate of one equation. *Electrophoresis*, vol. 30, pp. S7-S15, 2009.

[28] Deyl, Z., *Electrophoresis, a survey of techniques and applications*. 1979, New York: Elsevier.

[29] Melvin, M., *Electrophoresis*, ed. D. Kealey. 1987, Chichester: John Wiley & Sons.

[30] Landers, J.P., *Handbook of capillary and microchip electrophoresis and associated microtechniques*. 2008, Boca Raton: CRC Press.

[31] Kleparnik, K. and P. Bocek, Electrophoresis today and tomorrow: helping biologists' dreams come true. *Bioessays*, vol. 32, pp. 218-226, 2010.

[32] Pohl, H., *Dielectrophoresis, The behavior of neutral matter in nonuniform electric fields*. 1st ed. 1978, New York: Cambridge University Press. 580.

[33] Khoshmanesh, K., S. Nahavandi, S. Baratchi, A. Mitchell, and K. Kalantar-zadeh, Dielectrophoretic platforms for bio-microfluidic systems. *Biosensors & Bioelectronics*, vol. 26, pp. 1800-1814, 2011.

[34] Zhang, C., K. Khoshmanesh, A. Mitchell, and K. Kalantar-zadeh, Dielectrophoresis for manipulation of micro/nano particles in microfluidic systems. *Analytical and Bioanalytical Chemistry*, vol. 396, pp. 401-420, 2010.

[35] Morganti, E., C. Collini, R. Cunaccia, A. Gianfelice, L. Odorizzi, A. Adami, L. Lorenzelli, E. Jacchetti, A. Podesta, C. Lenardi, and P. Milani, A dielectrophoresis-based microdevice coated with nanostructured TiO_2 for separation of particles and cells. *Microfluidics and Nanofluidics*, vol. 10, pp. 1211-1221, 2011.

[36] Choi, E., B. Kim, and J. Park, High-throughput microparticle separation using gradient traveling wave dielectrophoresis. *Journal of Micromechanics and Microengineering*, vol. 19, 2009.

[37] Vahey, M.D. and J. Voldman, An equilibrium method for continuous-flow cell sorting using dielectrophoresis. *Analytical Chemistry*, vol. 80, pp. 3135-3143, 2008.

[38] Cetin, B. and D. Li, Dielectrophoresis in microfluidics technology. *Electrophoresis*, vol. 32, pp. 2410-2427, 2011.

[39] Kuzyk, A., Dielectrophoresis at the nanoscale. *Electrophoresis*, vol. 32, pp. 2307-2313, 2011.

[40] Piazza, R., Thermophoresis: moving particles with thermal gradients. *Soft Matter*, vol. 4, pp. 1740-1744, 2008.

[41] Duhr, S. and D. Braun, Thermophoretic depletion follows Boltzmann distribution. *Physical Review Letters*, vol. 96, 2006.

[42] Plyukhin, A.V., Thermophoresis as persistent random walk. *Physics Letters A*, vol. 373, pp. 2122-2124, 2009.

[43] Piazza, R. and A. Parola, Thermophoresis in colloidal suspensions. *Journal of Physics-Condensed Matter*, vol. 20, 2008.

[44] Vigolo, D., R. Rusconi, H.A. Stone, and R. Piazza, Thermophoresis: microfluidics characterization and separation. *Soft Matter*, vol. 6, pp. 3489-3493, 2010.

[45] Duhr, S. and D. Braun, Two-dimensional colloidal crystals formed by thermophoresis and convection. *Applied Physics Letters*, vol. 86, 2005.

[46] Buongiorno, J., Convective transport in nanofluids. *Journal of Heat Transfer-Transactions of the Asme*, vol. 128, pp. 240-250, 2006.

[47] Jerabek-Willemsen, M., C.J. Wienken, D. Braun, P. Baaske, and S. Duhr, Molecular Interaction Studies Using Microscale Thermophoresis. *Assay and Drug Development Technologies*, vol. 9, pp. 342-353, 2011.

[48] Ashkin, A., Optical trapping and manipulation of neutral particles using lasers. *Proceedings of the National Academy of Sciences of the United States of America*, vol. 94, pp. 4853-4860, 1997.

[49] Jonas, A. and P. Zemanek, Light at work: The use of optical forces for particle manipulation, sorting, and analysis. *Electrophoresis*, vol. 29, pp. 4813-4851, 2008.

[50] Grier, D.G., A revolution in optical manipulation. *Nature*, vol. 424, pp. 810-816, 2003.

[51] Ashkin, A., History of optical trapping and manipulation of small-neutral particle, atoms, and molecules. *IEEE Journal of Selected Topics in Quantum Electronics*, vol. 6, pp. 841-856, 2000.

[52] Toussaint, K.C., Jr., M. Liu, M. Pelton, J. Pesic, M.J. Guffey, P. Guyot-Sionnest, and N.F. Scherer, Plasmon resonance-based optical trapping of single and multiple Au nanoparticles. *Optics Express*, vol. 15, pp. 12017-12029, 2007.

[53] Zelenina, A.S., R. Quidant, and M. Nieto-Vesperinas, Enhanced optical forces between coupled resonant metal nanoparticles. *Optics Letters*, vol. 32, pp. 1156-1158, 2007.

[54] Huisken, J. and E.H.K. Stelzer, Optical levitation of absorbing particles with a nominally Gaussian laser beam. *Optics Letters*, vol. 27, pp. 1223-1225, 2002.

[55] van der Horst, A., A.I. Campbell, L.K. van Vugt, D.A.M. Vanmaekelbergh, M. Dogterom, and A. van Blaaderen, Manipulating metal-oxide nanowires using counter-propagating optical line tweezers. *Optics Express*, vol. 15, pp. 11629-11639, 2007.

[56] Dholakia, K., P. Reece, and M. Gu, Optical micromanipulation. *Chemical Society Reviews*, vol. 37, pp. 42-55, 2008.

[57] Erickson, D., X. Serey, Y.F. Chen, and S. Mandal, Nanomanipulation using near field photonics. *Lab on a Chip*, vol. 11, pp. 995-1009, 2011.

[58] Bluestein, B.I., I.M. Walczak, and S.Y. Chen, Fiber optic evanescent wave immunosensors for medical diagnostics. *Trends in Biotechnology*, vol. 8, pp. 161-168, 1990.

[59] Quidant, R. and C. Girard, Surface-plasmon-based optical manipulation. *Laser & Photonics Reviews*, vol. 2, pp. 47-57, 2008.

[60] Maier, S., *Plasmonics: fundamentals and applications*. 2007, New York: Springer.

[61] Halas, N.J., S. Lal, W.-S. Chang, S. Link, and P. Nordlander, Plasmons in Strongly Coupled Metallic Nanostructures. *Chemical Reviews*, vol. 111, pp. 3913-3961, 2011.

[62] Murray, W.A. and W.L. Barnes, Plasmonic materials. *Advanced Materials*, vol. 19, pp. 3771-3782, 2007.

[63] Righini, M., A.S. Zelenina, C. Girard, and R. Quidant, Parallel and selective trapping in a patterned plasmonic landscape. *Nature Physics*, vol. 3, pp. 477-480, 2007.

[64] Huang, C., J. Jiang, C. Muangphat, X. Sun, and Y. Hao, Trapping Iron Oxide into Hollow Gold Nanoparticles. *Nanoscale Research Letters*, vol. 6, 2011.

[65] Zhang, W., L. Huang, C. Santschi, and O.J.F. Martin, Trapping and Sensing 10 nm Metal Nanoparticles Using Plasmonic Dipole Antennas. *Nano Letters*, vol. 10, pp. 1006-1011, 2010.

[66] Pelton, M., J. Aizpurua, and G. Bryant, Metal-nanoparticle plasmonics. *Laser & Photonics Reviews*, vol. 2, pp. 136-159, 2008.

[67] Bohren, C. and D. Huffman, *Absorption and scattering of light by small particles*. 1983, New York: Wiley.

[68] Sun, Y.G. and Y.N. Xia, Increased sensitivity of surface plasmon resonance of gold nanoshells compared to that of gold solid colloids in response to environmental changes. *Analytical Chemistry*, vol. 74, pp. 5297-5305, 2002.

[69] Van Dorpe, P. and J. Ye, Semishells: Versatile Plasmonic Nanoparticles. *ACS Nano*, vol. 5, pp. 6774-6778, 2011.

[70] Grigorenko, A.N., N.W. Roberts, M.R. Dickinson, and Y. Zhang, Nanometric optical tweezers based on nanostructured substrates. *Nature Photonics*, vol. 2, pp. 365-370, 2008.

[71] Yang, A.H.J., S.D. Moore, B.S. Schmidt, M. Klug, M. Lipson, and D. Erickson, Optical manipulation of nanoparticles and biomolecules in sub-wavelength slot waveguides. *Nature*, vol. 457, pp. 71-75, 2009.

[72] Ohta, A.T., P.-Y. Chiou, H.L. Phan, S.W. Sherwood, J.M. Yang, A.N.K. Lau, H.-Y. Hsu, A. Jamshidi, and M.C. Wu, Optically controlled cell discrimination and trapping using optoelectronic tweezers. *Ieee Journal of Selected Topics in Quantum Electronics*, vol. 13, pp. 235-243, 2007.

[73] Nitkowski, A., A. Gondarenko, and M. Lipson, On-chip supercontinuum optical trapping and resonance excitation of microspheres. *Optics Letters*, vol. 35, pp. 1626-1628, 2010.

[74] Zhao, Y., B.S. Fujimoto, G.D.M. Jeffries, P.G. Schiro, and D.T. Chiu, Optical gradient flow focusing. *Optics Express*, vol. 15, pp. 6167-6176, 2007.

[75] Chiou, P.Y., A.T. Ohta, and M.C. Wu, Massively parallel manipulation of single cells and microparticles using optical images. *Nature*, vol. 436, pp. 370-372, 2005.

[76] Kirby, B., *Micro- and Nanoscale Fluid Mechanics*. 2010, Cambridge: Cambridge University Press.

[77] Ivon Rodriguez-Villarreal, A., M.D. Tarn, L.A. Madden, J.B. Lutz, J. Greenman, J. Samitier, and N. Pamme, Flow focussing of particles and cells based on their intrinsic properties using a simple diamagnetic repulsion setup. *Lab on a Chip*, vol. 11, pp. 1240-1248, 2011.

[78] Peyman, S.A., E.Y. Iwan, O. Margarson, A. Iles, and N. Pamme, Diamagnetic repulsion-A versatile tool for label-free particle handling in microfluidic devices. *Journal of Chromatography A*, vol. 1216, pp. 9055-9062, 2009.

[79] Spaldin, N., *Magnetic materials: Fundamentals and Applications*. 2nd ed. 2011, Cambridge: Cambridge University Press.

[80] Wu, X., H. Wu, and Y. Hu, Enhancement of separation efficiency on continuous magnetophoresis by utilizing L/T-shaped microchannels. *Microfluidics and Nanofluidics*, vol. 11, pp. 11-24, 2011.

[81] Adams, J.D., U. Kim, and H.T. Soh, Multitarget magnetic activated cell sorter. *Proceedings of the National Academy of Sciences of the United States of America*, vol. 105, pp. 18165-18170, 2008.

[82] Pamme, N. and C. Wilhelm, Continuous sorting of magnetic cells via on-chip free-flow magnetophoresis. *Lab on a Chip*, vol. 6, pp. 974-980, 2006.

[83] Lim, J., C. Lanni, E.R. Evarts, F. Lanni, R.D. Tilton, and S.A. Majetich, Magnetophoresis of Nanoparticles. *ACS Nano*, vol. 5, pp. 217-226, 2011.

[84] Gosse, C. and V. Croquette, Magnetic tweezers: Micromanipulation and force measurement at the molecular level. *Biophysical Journal*, vol. 82, pp. 3314-3329, 2002.

[85] Kim, J., H.-H. Lee, U. Steinfeld, and H. Seidel, Fast Capturing on Micromagnetic Cell Sorter. *IEEE Sensors Journal*, vol. 9, pp. 908-913, 2009.

[86] Liu, C., T. Stakenborg, S. Peeters, and L. Lagae, Cell manipulation with magnetic particles toward microfluidic cytometry. *Journal of Applied Physics*, vol. 105, 2009.

[87] Kang, J.H. and J.-K. Park, Magnetophoretic continuous purification of single-walled carbon nanotubes from catalytic impurities in a microfluidic device. *Small*, vol. 3, pp. 1784-1791, 2007.

[88] Lenshof, A. and T. Laurell, Continuous separation of cells and particles in microfluidic systems. *Chemical Society Reviews*, vol. 39, pp. 1203-1217, 2010.

[89] Parola, A. and R. Piazza, Particle thermophoresis in liquids. *European Physical Journal E*, vol. 15, pp. 255-263, 2004.

[90] Suwa, M. and H. Watarai, Magnetoanalysis of micro/nanoparticles: A review. *Analytica Chimica Acta*, vol. 690, pp. 137-147, 2011.

[91] Chung, A.J. and D. Erickson, Optofluidic waveguides for reconfigurable photonic systems. *Optics Express*, vol. 19, pp. 8602-8609, 2011.

[92] Fei, P., Z. He, C. Zheng, T. Chen, Y. Men, and Y. Huang, Discretely tunable optofluidic compound microlenses. *Lab on a Chip*, vol. 11, pp. 2835-41, 2011.

[93] Hawkins, A.R. and H. Schmidt, Optofluidic waveguides: II. Fabrication and structures. *Microfluidics and Nanofluidics*, vol. 4, pp. 17-32, 2008.

[94] Su, X.-T., K. Singh, C. Capjack, J. Petracek, C. Backhouse, and W. Rozmus, Measurements of light scattering in an integrated microfluidic waveguide cytometer. *Journal of Biomedical Optics*, vol. 13, 2008.

[95] Conroy, R.S., B.T. Mayers, D.V. Vezenov, D.B. Wolfe, M.G. Prentiss, and G.M. Whitesides, Optical waveguiding in suspensions of dielectric particles. *Applied Optics*, vol. 44, pp. 7853-7857, 2005.

[96] Song, C., N.-T. Nguyen, Y.F. Yap, T.-D. Luong, and A.K. Asundi, Multi-functional, optofluidic, in-plane, bi-concave lens: tuning light beam from focused to divergent. *Microfluidics and Nanofluidics*, vol. 10, pp. 671-678, 2011.

[97] Brody, J.P. and S.R. Quake, A self-assembled microlensing rotational probe. *Applied Physics Letters*, vol. 74, pp. 144-146, 1999.

[98] Helseth, L.E. and T.M. Fischer, Cooperative microlenses. *Optics Express*, vol. 12, pp. 3428-3435, 2004.

[99] Kneipp, J., X. Li, M. Sherwood, U. Panne, H. Kneipp, M.I. Stockman, and K. Kneipp, Gold nanolenses generated by laser ablation-efficient enhancing structure for surface enhanced Raman scattering analytics and sensing. *Analytical Chemistry*, vol. 80, pp. 4247-4251, 2008.

[100] Wu, M.H. and G.M. Whitesides, Fabrication of arrays of two-dimensional micropatterns using microspheres as lenses for projection photolithography. *Applied Physics Letters*, vol. 78, pp. 2273-2275, 2001.

[101] Ebenstein, Y. and L.A. Bentolila, Single molecule detection: Focusing on the objective. *Nature Nanotechnology*, vol. 5, pp. 99-100, 2010.

[102] Schwartz, J.J., S. Stavrakis, and S.R. Quake, Colloidal lenses allow high-temperature single-molecule imaging and improve fluorophore photostability. *Nature Nanotechnology*, vol. 5, pp. 127-132, 2010.

[103] Bucaro, M.A., P.R. Kolodner, J.A. Taylor, A. Sidorenko, J. Aizenberg, and T.N. Krupenkin, Tunable Liquid Optics: Electrowetting-Controlled Liquid Mirrors Based on Self-Assembled Janus Tiles. *Langmuir*, vol. 25, pp. 3876-3879, 2009.

[104] Groisman, A., S. Zamek, K. Campbell, L. Pang, U. Levy, and Y. Fainman, Optofluidic 1x4 switch. *Optics Express*, vol. 16, pp. 13499-13508, 2008.

[105] Nguyen, N.T., T.F. Kong, J.H. Goh, and C.L.N. Low, A micro optofluidic splitter and switch based on hydrodynamic spreading. *Journal of Micromechanics and Microengineering*, vol. 17, pp. 2169-2174, 2007.

[106] Seow, Y.C., S.P. Lim, and H.P. Lee, Tunable optofluidic switch via hydrodynamic control of laminar flow rate. *Applied Physics Letters*, vol. 95, 2009.

[107] Zamek, S., B. Slutsky, L. Pang, U. Levy, and Y. Fainman, *Optofluidic Switches and Sensors*. Handbook of Optofluidics, ed. A.R. Hawkins and H. Schmidt. 2010, Boca Raton: Crc Press-Taylor & Francis Group.

[108] Domachuk, P., M. Cronin-Golomb, B.J. Eggleton, S. Mutzenich, G. Rosengarten, and A. Mitchell, Application of optical trapping to beam manipulation in optofluidics. *Optics Express*, vol. 13, pp. 7265-7275, 2005.

[109] Malynych, S.Z., A. Tokarev, S. Hudson, G. Chumanov, J. Ballato, and K.G. Kornev, Magneto-controlled illumination with opto-fluidics. *Journal of Magnetism and Magnetic Materials*, vol. 322, pp. 1894-1897.

[110] Helseth, L.E., H.Z. Wen, and T.M. Fischer, Colloidal optomagnetic dimmer. *Langmuir*, vol. 22, pp. 3941-3944, 2006.

[111] Mandal, S. and D. Erickson, Optofluidic transport in liquid core waveguiding structures. *Applied Physics Letters*, vol. 90, 2007.

[112] Guo, H., P. Zhao, G. Xiao, Z. Zhang, and J. Yao, Optical Manipulation of Microparticles in an SU-8/PDMS Hybrid Microfluidic Chip Incorporating a Monolithically Integrated On-Chip Lens Set. *Ieee Journal of Selected Topics in Quantum Electronics*, vol. 16, pp. 919-926, 2010.

[113] Grujic, K., O.G. Helleso, J.P. Hole, and J.S. Wilkinson, Sorting of polystyrene microspheres using a Y-branched optical waveguide. *Optics Express*, vol. 13, pp. 1-7, 2005.

[114] Almeida, V.R., Q.F. Xu, C.A. Barrios, and M. Lipson, Guiding and confining light in void nanostructure. *Optics Letters*, vol. 29, pp. 1209-1211, 2004.

[115] Saleh, B. and M.C. Teich, *Fundamentals of Photonics*. 2007, Hoboken, NJ: Wiley.

[116] Yang, A.H.J., T. Lerdsuchatawanich, and D. Erickson, Forces and Transport Velocities for a Particle in a Slot Waveguide. *Nano Letters*, vol. 9, pp. 1182-1188, 2009.

[117] Fan, X. and I.M. White, Optofluidic microsystems for chemical and biological analysis. *Nature Photonics*, vol. 5, pp. 591-597, 2011.

[118] Matsko, A.B. and V.S. Ilchenko, Optical resonators with whispering-gallery modes - Part I: Basics. *Ieee Journal of Selected Topics in Quantum Electronics*, vol. 12, pp. 3-14, 2006.

[119] Fainman, Y., L.P. Lee, D. Psaltis, and C. Yang, *Optofluidics, Fundamentals, Devices and Applications*. 2010, New York: McGraw-Hill.

[120] Sun, Y. and X. Fan, Optical ring resonators for biochemical and chemical sensing. *Analytical and Bioanalytical Chemistry*, vol. 399, pp. 205-211, 2011.

[121] Zhu, H., I.M. White, J.D. Suter, P.S. Dale, and X. Fan, Analysis of biomolecule detection with optofluidic ring resonator sensors. *Optics Express*, vol. 15, pp. 9139-9146, 2007.

[122] Yang, A.H.J. and D. Erickson, Optofluidic ring resonator switch for optical particle transport. *Lab on a Chip*, vol. 10, pp. 769-774, 2010.

[123] Cai, H. and A.W. Poon, Optical manipulation and transport of microparticles on silicon nitride microring-resonator-based add-drop devices. *Optics Letters*, vol. 35, pp. 2855-2857, 2010.

[124] Cai, H. and A.W. Poon, Optical manipulation of microparticles using whispering-gallery modes in a silicon nitride microdisk resonator. *Optics Letters*, vol. 36, pp. 4257-4259, 2011.

[125] Hwang, H., Y.-J. Choi, W. Choi, S.-H. Kim, J. Jang, and J.-K. Park, Interactive manipulation of blood cells using a lens-integrated liquid crystal display based optoelectronic tweezers system. *Electrophoresis*, vol. 29, pp. 1203-1212, 2008.

[126] Choi, W., S.-H. Kim, J. Jang, and J.-K. Park, Lab-on-a-display: a new microparticle manipulation platform using a liquid crystal display (LCD). *Microfluidics and Nanofluidics*, vol. 3, pp. 217-225, 2007.

[127] Lee, S.K., S.H. Kim, J.H. Kang, S.G. Park, W.J. Jung, S.H. Kim, G.R. Yi, and S.M. Yang, Optofluidics technology based on colloids and their assemblies. *Microfluidics and Nanofluidics*, vol. 4, pp. 129-144, 2008.

[128] Shvalov, A.N., I.V. Surovtsev, A.V. Chernyshev, J.T. Soini, and V.P. Maltsev, Particle classification from light scattering with the scanning flow cytometer. *Cytometry*, vol. 37, pp. 215-220, 1999.

[129] Perroud, T.D., J.N. Kaiser, J.C. Sy, T.W. Lane, C.S. Branda, A.K. Singh, and K.D. Patel, Microfluidic-based cell sorting of Francisella tularensis infected macrophages using optical forces. *Analytical Chemistry*, vol. 80, pp. 6365-6372, 2008.

[130] Mitra, A., B. Deutsch, F. Ignatovich, C. Dykes, and L. Novotny, Nano-optofluidic Detection of Single Viruses and Nanoparticles. *ACS Nano*, vol. 4, pp. 1305-1312, 2010.

[131] Schmidt, H. and A.R. Hawkins, Atomic spectroscopy and quantum optics in hollow-core waveguides. *Laser & Photonics Reviews*, vol. 4, pp. 720-737, 2010.

[132] Bernini, R., S. Campopiano, L. Zeni, and P.M. Sarro, ARROW optical waveguides based sensors. *Sensors and Actuators B-Chemical*, vol. 100, pp. 143-146, 2004.

[133] Measor, P., B.S. Phillips, A. Chen, A.R. Hawkins, and H. Schmidt, Tailorable integrated optofluidic filters for biomolecular detection. *Lab on a Chip*, vol. 11, pp. 899-904, 2011.

[134] Kuehn, S., E.J. Lunt, B.S. Phillips, A.R. Hawkins, and H. Schmidt, Optofluidic particle concentration by a long-range dual-beam trap. *Optics Letters*, vol. 34, pp. 2306-2308, 2009.

[135] Kuehn, S., B.S. Phillips, E.J. Lunt, A.R. Hawkins, and H. Schmidt, Ultralow power trapping and fluorescence detection of single particles on an optofluidic chip. *Lab on a Chip*, vol. 10, pp. 189-194, 2010.

[136] Kuhn, S., P. Measor, E.J. Lunt, B.S. Phillips, D.W. Deamer, A.R. Hawkins, and H. Schmidt, Loss-based optical trap for on-chip particle analysis. *Lab on a Chip*, vol. 9, pp. 2212-2216, 2009.

[137] Measor, P., S. Kuehn, E.J. Lunt, B.S. Phillips, A.R. Hawkins, and H. Schmidt, Multi-mode mitigation in an optofluidic chip for particle manipulation and sensing. *Optics Express*, vol. 17, pp. 24342-24348, 2009.

[138] Cho, S.H., J.M. Godin, C.-H. Chen, W. Qiao, H. Lee, and Y.-H. Lo, Review Article: Recent advancements in optofluidic flow cytometer. *Biomicrofluidics*, vol. 4, 2010.

[139] Steen, H.B., Light Scattering Measurement in an Arc Lamp Based Flow Cytometer. *Cytometry*, vol. 11, pp. 223-230, 1990.

[140] Kim, J.S. and F.S. Ligler, Utilization of microparticles in next-generation assays for microflow cytometers. *Analytical and Bioanalytical Chemistry*, vol. 398, pp. 2373-2382, 2010.

[141] Rosenauer, M. and M.J. Vellekoop, Characterization of a microflow cytometer with an integrated three-dimensional optofluidic lens system. *Biomicrofluidics*, vol. 4, 2010.

[142] Zhu, H., S. Mavandadi, A.F. Coskun, O. Yaglidere, and A. Ozcan, Optofluidic Fluorescent Imaging Cytometry on a Cell Phone. *Analytical Chemistry*, vol. 83, pp. 6641-6647, 2011.

[143] Wang, Z., O. Hansen, P.K. Petersen, A. Rogeberg, J.P. Kutter, D.D. Bang, and A. Wolff, Dielectrophoresis microsystem with integrated flow cytometers for on-line monitoring of sorting efficiency. *Electrophoresis*, vol. 27, pp. 5081-5092, 2006.

[144] Lim, C., J. Hong, B.G. Chung, A.J. deMello, and J. Choo, Optofluidic platforms based on surface-enhanced Raman scattering. *Analyst*, vol. 135, pp. 837-844, 2010.

[145] Gardiner, D.J., P.R. Graves, H.J. Bowley, D.L. Gerrard, J.D. Louden, and G. Turrell, *Practical Raman Spectroscopy*. 1989, New York: Springer-Verlag.

[146] Huh, Y.S., A.J. Chung, and D. Erickson, Surface enhanced Raman spectroscopy and its application to molecular and cellular analysis. *Microfluidics and Nanofluidics*, vol. 6, pp. 285-297, 2009.

[147] Wang, M., N. Jing, I.H. Chou, G.L. Cote, and J. Kameoka, An optofluidic device for surface enhanced Raman spectroscopy. *Lab on a Chip*, vol. 7, pp. 630-632, 2007.

[148] Chrimes, A.F., A.A. Kayani, K. Khoshmanesh, P.R. Stoddart, P. Mulvaney, A. Mitchell, and K. Kalantar-zadeh, Dielectrophoresis-Raman spectroscopy system for analysing suspended nanoparticles. *Lab on a Chip*, vol. 11, pp. 921-928, 2011.

[149] White, I.M., J. Gohring, and X. Fan, SERS-based detection in an optofluidic ring resonator platform. *Optics Express*, vol. 15, pp. 17433-17442, 2007.

[150] Tong, L., M. Righini, M. Ujue Gonzalez, R. Quidant, and M. Kall, Optical aggregation of metal nanoparticles in a microfluidic channel for surface-enhanced Raman scattering analysis. *Lab on a Chip*, vol. 9, pp. 193-195, 2009.

[151] Lau, A.Y., L.P. Lee, and J.W. Chan, An integrated optofluidic platform for Raman-activated cell sorting. *Lab on a Chip*, vol. 8, pp. 1116-1120, 2008.

[152] Measor, P., L. Seballos, D. Yin, J.Z. Zhang, E.J. Lunt, A.R. Hawkins, and H. Schmidt, On-chip surface enhanced Raman scattering detection using integrated liquid core waveguides. *Applied Physics Letters*, vol. 90, pp. 211107-1 to 211107-3, 2007.

[153] Huang, L., S.J. Maerkl, and O.J.F. Martin, Integration of plasmonic trapping in a microfluidic environment. *Optics Express*, vol. 17, pp. 6018-6024, 2009.

[154] Juan, M.L., M. Righini, and R. Quidant, Plasmon nano-optical tweezers. *Nature Photonics*, vol. 5, pp. 349-356, 2011.

[155] Wong, H.M.K., M. Righini, J.C. Gates, P.G.R. Smith, V. Pruneri, and R. Quidant, On-a-chip surface plasmon tweezers. *Applied Physics Letters*, vol. 99, 2011.

[156] Volpe, G., R. Quidant, G. Badenes, and D. Petrov, Surface plasmon radiation forces. *Physical Review Letters*, vol. 96, 2006.

[157] Cheng, Y., M. Wang, G. Borghs, and H. Chen, Gold Nanoparticle Dimers for Plasmon Sensing. *Langmuir*, vol. 27, pp. 7884-7891, 2011.

[158] Kneipp, K., M. Moskovits, and H. Kneipp, *Surface-Enhanced Raman Scattering: Physics and Applications*. 2006, Berlin.

[159] Wang, K., E. Schonbrun, P. Steinvurzel, and K.B. Crozier, Scannable Plasmonic Trapping Using a Gold Stripe. *Nano Letters*, vol. 10, pp. 3506-3511, 2010.

[160] Homola, J., S.S. Yee, and G. Gauglitz, Surface plasmon resonance sensors: review. *Sensors and Actuators B-Chemical*, vol. 54, pp. 3-15, 1999.

[161] Mullett, W.M., E.P.C. Lai, and J.M. Yeung, Surface plasmon resonance-based immunoassays. *Methods-a Companion to Methods in Enzymology*, vol. 22, pp. 77-91, 2000.

[162] Zhao, J., X.Y. Zhang, C.R. Yonzon, A.J. Haes, and R.P. Van Duyne, Localized surface plasmon resonance biosensors. *Nanomedicine*, vol. 1, pp. 219-228, 2006.

[163] Homola, J., Surface plasmon resonance sensors for detection of chemical and biological species. *Chemical Reviews*, vol. 108, pp. 462-493, 2008.

[164] Hsu, W.-T., W.-H. Hsieh, S.-F. Cheng, C.-P. Jen, C.-C. Wu, C.-H. Li, C.-Y. Lee, W.-Y. Li, L.-K. Chau, C.-Y. Chiang, and S.-R. Lyu, Integration of fiber optic-particle plasmon resonance biosensor with microfluidic chip. *Analytica Chimica Acta*, vol. 697, pp. 75-82, 2011.

[165] Weinert, F.M., C.B. Mast, and D. Braun, Optical fluid and biomolecule transport with thermal fields. *Physical Chemistry Chemical Physics*, vol. 13, pp. 9918-9928, 2011.

[166] Thamdrup, L.H., N.B. Larsen, and A. Kristensen, Light-Induced Local Heating for Thermophoretic Manipulation of DNA in Polymer Micro- and Nanochannels. *Nano Letters*, vol. 10, pp. 826-832, 2010.

[167] Donner, J.S., G. Baffou, D. McCloskey, and R. Quidant, Plasmon-Assisted Optofluidics. *Acs Nano*, vol. 5, pp. 5457-5462, 2011.

[168] Strong, L.E. and J.L. West, Thermally responsive polymer-nanoparticle composites for biomedical applications. *Wiley Interdisciplinary Reviews-Nanomedicine and Nanobiotechnology*, vol. 3, pp. 307-317, 2011.

[169] Duhr, S. and D. Braun, Optothermal molecule trapping by opposing fluid flow with thermophoretic drift. *Physical Review Letters*, vol. 97, 2006.

[170] Williams, S.J., A. Kumar, N.G. Green, and S.T. Wereley, A simple, optically induced electrokinetic method to concentrate and pattern nanoparticles. *Nanoscale*, vol. 1, pp. 133-137, 2009.

[171] Baaske, P., C.J. Wienken, P. Reineck, S. Duhr, and D. Braun, Optical Thermophoresis for Quantifying the Buffer Dependence of Aptamer Binding. *Angewandte Chemie-International Edition*, vol. 49, pp. 2238-2241, 2010.

[172] Erickson, D., D. Sinton, and D. Psaltis, Optofluidics for energy applications. *Nature Photonics*, vol. 5, pp. 583-590, 2011.

[173] Lien, K.Y., L.Y. Hung, T.B. Huang, Y.C. Tsai, H.Y. Lei, and G.B. Lee, Rapid detection of influenza A virus infection utilizing an immunomagnetic bead-based microfluidic system. *Biosensors & Bioelectronics*, vol. 26, pp. 3900-3907, 2011.

[174] Jung, Y., Y. Choi, K.-H. Han, and A.B. Frazier, Six-stage cascade paramagnetic mode magnetophoretic separation system for human blood samples. *Biomedical Microdevices*, vol. 12, pp. 637-645, 2010.

[175] Lenshof, A., A. Ahmad-Tajudin, K. Jaras, A.-M. Sward-Nilsson, L. Aberg, G. Marko-Varga, J. Malm, H. Lilja, and T. Laurell, Acoustic Whole Blood Plasmapheresis Chip for Prostate Specific Antigen Microarray Diagnostics. *Analytical Chemistry*, vol. 81, pp. 6030-6037, 2009.

[176] Hwang, H., D.-H. Lee, W. Choi, and J.-K. Park, Enhanced discrimination of normal oocytes using optically induced pulling-up dielectrophoretic force. *Biomicrofluidics*, vol. 3, 2009.

[177] Kim, M., D.J. Hwang, H. Jeon, K. Hiromatsu, and C.P. Grigoropoulos, Single cell detection using a glass-based optofluidic device fabricated by femtosecond laser pulses. *Lab on a Chip*, vol. 9, pp. 311-318, 2009.

[178] Righini, M., P. Ghenuche, S. Cherukulappurath, V. Myroshnychenko, F.J. Garcia de Abajo, and R. Quidant, Nano-optical Trapping of Rayleigh Particles and Escherichia coli Bacteria with Resonant Optical Antennas. *Nano Letters*, vol. 9, pp. 3387-3391, 2009.

[179] Gather, M.C. and S.H. Yun, Lasing from Escherichia coli bacteria genetically programmed to express green fluorescent protein. *Optics Letters*, vol. 36, pp. 3299-3301, 2011.

[180] Sun, Y., S.I. Shopova, C.-S. Wu, S. Arnold, and X. Fan, Bioinspired optofluidic FRET lasers via DNA scaffolds. *Proceedings of the National Academy of Sciences of the United States of America*, vol. 107, pp. 16039-16042, 2010.

[181] Alvarez-Curto, E., J.D. Pediani, and G. Milligan, Applications of fluorescence and bioluminescence resonance energy transfer to drug discovery at G protein coupled receptors. *Analytical and Bioanalytical Chemistry*, vol. 398, pp. 167-180, 2010.

[182] Morgan, M. and N. Green, *AC Electrokinetics: colloids and nanoparticles*. 2003, Baldock: Research Studies Press Ltd.

[183] Lei, U., C.W. Huang, J. Chen, C.Y. Yang, Y.J. Lo, A. Wo, C.F. Chen, and T.W. Fung, A travelling wave dielectrophoretic pump for blood delivery. *Lab on a Chip*, vol. 9, pp. 1349-1356, 2009.

[184] Pethig, R., Dielectrophoresis: Status of the theory, technology, and applications. *Biomicrofluidics*, vol. 4, pp. 022811, 2010.

[185] Crews, N., J. Darabi, P. Voglewede, F. Guo, and A. Bayoumi, An analysis of interdigitated electrode geometry for dielectrophoretic particle transport in micro-fluidics. *Sensors and Actuators B-Chemical*, vol. 125, pp. 672-679, 2007.

[186] Auerswald, J. and H.F. Knapp, Quantitative assessment of dielectrophoresis as a micro fluidic retention and separation technique for beads and human blood erythrocytes. *Microelectronic Engineering*, vol. 67-8, pp. 879-886, 2003.

[187] Gascoyne, P.R.C., X.B. Wang, Y. Huang, and F.F. Becker, Dielectrophoretic separation of cancer cells from blood. *IEEE Transactions on Industry Applications*, vol. 33, pp. 670-678, 1997.

[188] Zhang, C., K. Khoshmanesh, F.J. Tovar-Lopez, A. Mitchell, W. Wlodarski, and K. Klantar-zadeh, Dielectrophoretic separation of carbon nanotubes and polystyrene microparticles. *Microfluidics and Nanofluidics*, vol. 7, pp. 633-645, 2009.

[189] Ramon-Azcon, J., T. Yasukawa, and F. Mizutani, Immunodevice for simultaneous detection of two relevant tumor markers based on separation of different microparticles by dielectrophoresis. *Biosensors & Bioelectronics*, vol. 28, pp. 443-449, 2011.

[190] Asokan, S.B., L. Jawerth, R.L. Carroll, R.E. Cheney, S. Washburn, and R. Superfine, Two-dimensional manipulation and orientation of actin-myosin systems with dielectrophoresis. *Nano Letters*, vol. 3, pp. 431-437, 2003.

[191] Grom, F., J. Kentsch, T. Muller, T. Schnelle, and M. Stelzle, Accumulation and trapping of hepatitis A virus particles by electrohydrodynamic flow and dielectrophoresis. *Electrophoresis*, vol. 27, pp. 1386-1393, 2006.

[192] Morgan, H., M.P. Hughes, and N.G. Green, Separation of submicron bioparticles by dielectrophoresis. *Biophysical Journal*, vol. 77, pp. 516-525, 1999.

[193] Khoshmanesh, K., C. Zhang, F.J. Tovar-Lopez, S. Nahavandi, S. Baratchi, A. Mitchell, and K. Kalantar-Zadeh, Dielectrophoretic-activated cell sorter based on curved microelectrodes. *Microfluidics and Nanofluidics*, vol. 9, pp. 411-426, 2010.

[194] Zhang, C., K. Khoshmanesh, A.A. Kayani, F.J. Tovar-Lopez, W. Wlodarski, A. Mitchell, and K. Kalantar-Zadeh. *Dielectrophoretic manipulation of polystyrene micro particles in microfluidic systems*. 2010. Shanghai.

Chapter 3

Design and Fabrication

3.1 Introduction

The author designed three experimental platforms in this PhD research project for testing and characterizing the concept of implementing the coupling of light into well controlled suspended particles. These platforms represent the step by step progress and improvement of the platform in the course of this PhD research. The first platform ("Platform 1") involved a dielectrophoretic (DEP) microelectrode array patterned on a glass slide. A microfluidic channel was made and then attached to the glass slide. This platform was used for the coupling of light into the microfluidic channel via a multi mode fiber into the DEP focused particles without the incorporation of the polymeric waveguide. The second platform ("Platform 2") involved a DEP microelectrode array that was patterned and incorporated in a system with a polymer waveguide structure. This was used to improve the quality of light coupling into and out of the systems and reducing the scattering of light by particles at the

fluidic reservoirs. This platform had an integrated multi mode raised rib polymeric waveguide. The purpose of the waveguide was to couple light from a multi mode waveguide into the DEP focused particles in its vicinity within the microfluidics. The third platform ("Platform 3") consisted of a quasi single mode inverted rib polymeric waveguide. The quasi single mode system significantly improves the potential for analyzing input and output optical signals, by allowing the propagation of light with clear modal responses.

The main components used in all three experimental platforms were: (1) The curved DEP microelectrode array (2) The microfluidic channel. The curved DEP microelectrodes were used to generate a non-uniform electric field that focused and repelled particles from the region of high electric field gradients. The microfluidic channel enabled the flow of particles suspended in liquid adjacent to the DEP microelectrodes. The rib polymeric waveguide (multi mode and quasi-single mode) was used for Platforms 2 and 3 guide light and enable the interaction of light with the suspended particles in the microfluidic channel in a low scattering regime.

In order to detail the fabrication of the platforms, it will be necessary to introduce their basic structures. In this chapter, the author describes the design and fabrication processes of the experimental platforms. This will include design of the DEP microelectrodes, the microfluidics and the rib waveguide structures. Simulations that are relevant for these platform structures will be provided in the methods section in chapters 4, 5 and 6.

3.2 Design of DEP Microelectrodes

The author used curved microelectrodes to generate the DEP force for the experimental platforms as it was capable of concentrating and dispersing the particles effectively [1] and forming them into narrow bands in the center of the microfluidic channel. The oblique microelectrode design [2] was initially tested. In oblique electrodes, the intensity of electric field gradients at the tips is too strong to form a uniform stream of compact particles along the centerline of the microchannel. The oblique microelectrodes creates a strong electric field at the microelectrode tips, which sharply decreases along the structure and leaving the rest of the microelectrode with a moderate electric field. Alternatively, the curved microelectrode design creates a high intensity electric field at the tips which decreases much

more smoothly along the structure, thus increasing the effective portion of the microelectrodes for dielectrophoresis. As such, the author found that this design was not suitable for forming a waveguiding and uniform step index profile in the microfluidic channel (which will be discussed in chapters 4, 5 and 6).

First, the DEP microelectrode mask was designed using the Advanced Design System (ADS) 2009 software package. Five sets of curved and micro-tip shaped DEP microelectrode arrays were designed. Figure 3.1 presents the mask design produced by the author. The curved microelectrodes were designed with varying gaps between the tips. The gaps between the tips were 5 µm (Figure 3.1A-B), 10 µm (Figure 3.1C), 15 µm (Figure 3.1D) and 20 µm (Figure 3.1E).

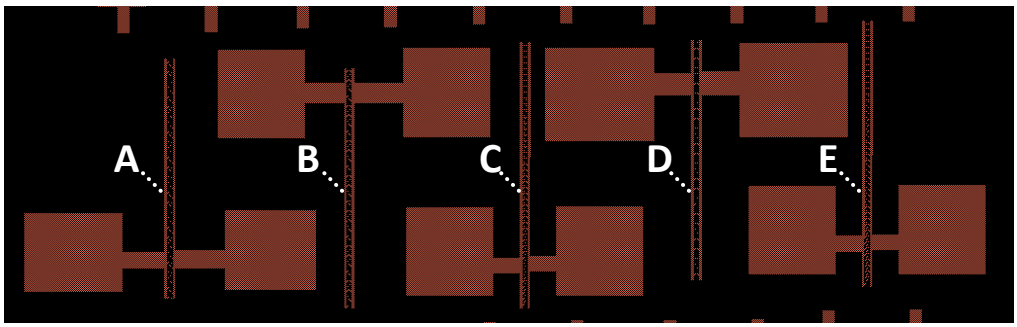

Figure 3.1: Schematic of curved DEP microelectrode designs on the mask design patterned on a 4 × 4 inch chrome mask substrate. The electrode designs were separated by a gap spacing of: (A-B) 5 µm (C) 10 µm (D) 15 µm (E) 20 µm.

The curved microelectrode configuration with the 20 µm gap spacing (Figure 3.1E) was used to generate the DEP force for the experiments in this PhD research project. The author chose the 20 µm gap spacing design as it was initially thought that the particles would be manipulated using this electrode spacing and if the particles could not be controlled effectively, the author would gradually decrease the electrode spacing to the smaller spacing designs. It turned out that for all the particles investigated in this PhD thesis (as will be seen in chapters 4, 5 and 6), the 20 µm gap spacing design was sufficient to induce a DEP field capable of manipulating the particles' motion and location effectively. The author will demonstrate in the next chapters that the formation of a narrow band in the center or wider

bands near the side walls, consisting of particles, is due to the combination effect of DEP and hydrodynamic forces in three dimensions.

Microelectrodes with different spacings were designed for the author's potential collaborators. For instance, the 5 µm spacing pattern was used by the author's collaborator, Mr. Adam Chrimes for conducting research into Raman spectroscopy analysis enhanced by DEP forces. He chose the electrode design with a smaller gap distance as it generated strong electric field gradients necessary to trap the silver particles (Ø60 nm) and generate the highest possible concentration, which would result in enhanced Raman response signals.

For this PhD research project, a detailed image of the curved microelectrode design is presented in Figure 3.2A-C. The distance between the microelectrodes at the tips and at the base is 20 µm and 50 µm, respectively. The electrode pairs were positioned ~ 300 µm from each other (Figure 3.2C). This design was found to generate strong electric field gradients between the microelectrode tips which when combined with hydrodynamic forces due to the flow of liquids in the microfluidic channel, causes the particles to be pushed either toward the sidewalls or focused into dense concentrations in the microchannel center.

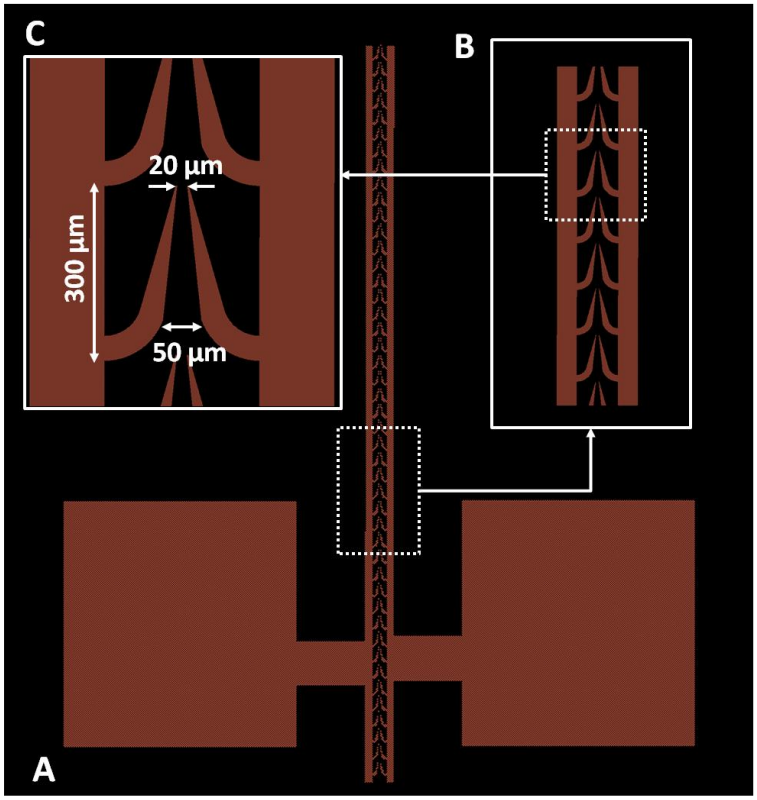

Figure 3.2: Curved microelectrode array design: (A) Curved microelectrodes with the conducting pads (B) Close-up image of electrode pattern (C) Dimensions of electrode design.

3.3 Design of Microfluidic Channels

The microfluidic channels were designed using Adobe Illustrator CS4 software package. Figure 3.3A presents the microfluidic channel designed for Platform 1 and Figure 3.3B presents the microfluidic channel designed for Platforms 2 and 3.

For Platform 1, the microfluidic channel consists of a straight line having a width of 1 mm and a length of ~ 18 mm. The length of the channel was intended to accommodate the length of the DEP microelectrode array which is ~ 17 mm long while the width of the microchannel was selected to be sufficiently wide such that it could enclose the array of microelectrode pairs and that it could be easily aligned and attached to the glass substrate which contains the microelectrode patterns. The design of the microchannel incorporates two bends in order to

couple light into the channel. The first bend has a 130 μm wide strip adjacent to it, which was made for inserting the core of a fiber to couple light into the microfluidic channel. The black circles represent 5 mm diameter microfluidic reservoirs which provide access for the liquids into and out of the microfluidic channel. The width was chosen as it matched the diameter of the microfluidic punching tools used to make the fluidic reservoirs.

Figure 3.3B presents the microfluidic channel design used for Platforms 2 and 3 which consists of a straight microchannel with two reservoirs. The size of the reservoirs was 3 mm in diameter, which is smaller than the diameter of the reservoirs in Platform 1. The width of the microchannels was 400 and 200 μm for Platforms 2 and 3, respectively. The width of the microchannels were reduced from the 1 mm channel width used in Platform 1 as the author realized the benefit of a narrower microchannel which enables the microelectrodes to better focus and repel particles as the confines of the microfluidic channel were smaller. Additionally, the size of the reservoirs was reduced from 5 mm in Platform 1 to 3 mm in Platforms 2 and 3 as the smaller fluidic reservoirs were thought to reduce the occurrence of chaotic motions due to the formation of micro-vortices and the issue of agglomeration of particles at the edges of the reservoirs could be addressed. Additionally, at the subsequent stage of research, the author was able to do the microfluidic channel alignment under the observation of an optical microscope for Platform 2 and to photolithographically align the channel to the substrate for Platform 3 (as will be described later in section 3.5).

The length of the microchannel for Platforms 2 and 3 are 15 mm. The 15 mm length was designed to be slightly shorter than the length of the microelectrode array as it was thought that the decreased length would reduce the occurrence of uneven refractive index profiles caused by non-focused particles.

The microfluidic channel was assembled with the DEP microelectrode patterns such that the center of the curved microelectrode patterns was aligned to the center of the microfluidic channel. Figures 3.3C and 3.3D present the schematic of the DEP microelectrodes integrated with the microfluidic channel for Platforms 1 and Platforms 2/3, respectively.

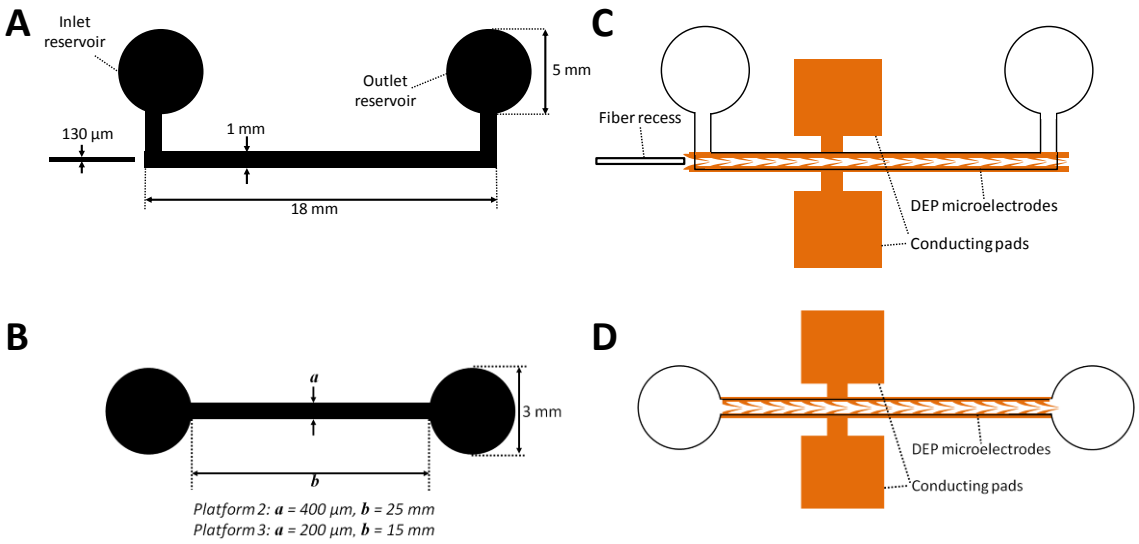

Figure 3.3: Microfluidic channel configuration for: (A) Platform 1 and (B) Platforms 2 and 3; Microfluidic channel assembled with DEP microelectrodes for (C) Platform 1 and (D) Platforms 2 and 3.

3.4 Design of the Polymeric Rib Waveguide

The waveguides used in this PhD research project were designed as straight lines on a chrome mask (Figure 3.4) by the authors' collaborator, Dr. Gorgi Kostovski from the School of Electrical and Computer Engineering, RMIT University. The waveguides on this mask were defined by chrome strips, surrounded by a clear-field. The widths of the waveguides on this mask range from 3 to 7 µm and the widths increment in 0.1 µm steps. The waveguides were separated by a spacing of approximately 40 µm.

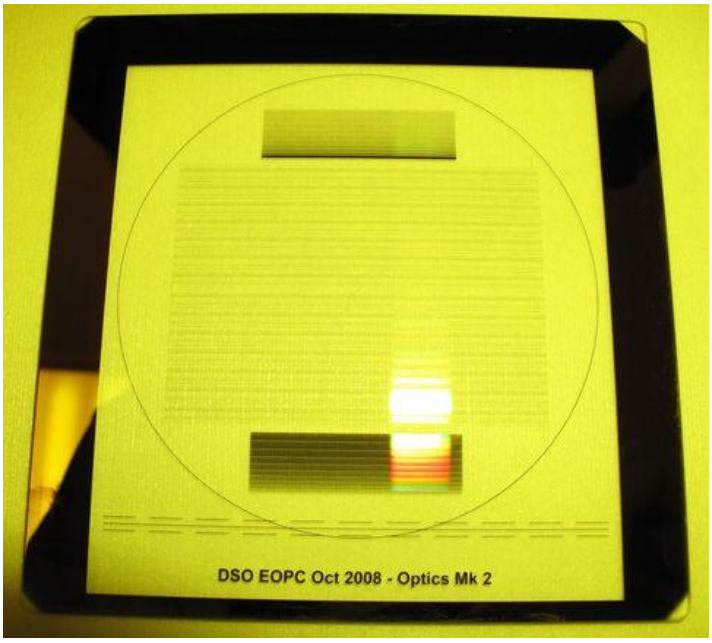

Figure 3.4: Photograph of waveguide mask used for fabrication.

In the experiments, two types of waveguides were used. Platform 2 uses a multi mode waveguide while Platform 3 uses a quasi single mode waveguide (further details on the waveguide fabrication procedures are provided in sections 3.5.2 and 3.5.3). Basically, the waveguides in Platform 2 and 3 differed in terms of their dimensions and geometry. In particular, the multi mode waveguide in Platform 2 has a raised rib configuration (Figure 3.5A) while the quasi single mode waveguide in Platform 3 has an inverted rib configuration (Figure 3.5B).

The lower cladding for both waveguides consisted of a polymer and air as the upper cladding. Additionally, the dimensions for the quasi single mode waveguide rib features are 4.5×0.3 μm ($w \times h$) while the dimensions for that of the multi mode waveguide are 7×0.35 μm ($w \times h$). These waveguide configuration and dimensions were selected to guarantee the propagation of quasi single mode in contrast to larger waveguides with different configurations that allow the propagation of many modes simultaneously [4].

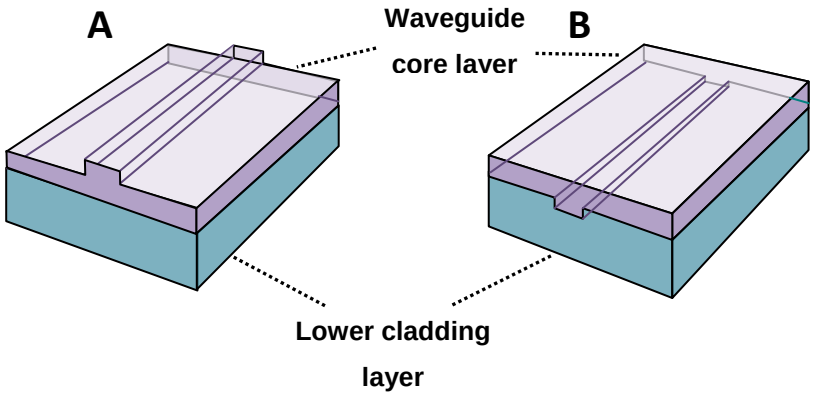

Figure 3.5: Three dimensional schematic of: (A) Raised rib multi mode waveguide used for Platform 2 (B) Inverted rib quasi single mode waveguide used for Platform 3.

3.5 Fabrication

In this section, the author describes the fabrication process for the experimental platforms. There are two methods which can be used to fabricate the DEP microelectrodes: (1) Etching and (2) Lift-off. In this thesis, the author implemented the etching method for patterning the DEP microelectrodes. The DEP microelectrodes were either fabricated on a glass substrate (Platform 1) or on a polymer substrate (Platforms 2 and 3). The etching method was used for the three platforms because it produces well defined structures without sacrificing the structural integrity of the glass or polymer substrates.

Soft lithography techniques [4] were employed for the fabrication of the polydimethylsiloxane (PDMS) blocks such that a photoresist mould was pre-fabricated on silicon (Si) wafer and the PDMS elastomer and curing agents were mixed at an appropriate mixing ratio and cured at the optimized temperature. Nano-imprint photolithography [5] techniques were employed for the fabrication of the polymeric waveguides such that a PDMS mould was pre-fabricated on a Si wafer and used to imprint the waveguide features.

The fabrication activities were conducted in the Microelectronics and Materials Technology Center (MMTC), clean-room and vacuum laboratory facilities of RMIT University.

3.5.1 Platform 1

The fabrication procedures for Platform 1 is divided into three stages. The first stage involves the fabrication of the DEP microeletrodes. The second stage involves the fabrication of the microfluidic channel in PDMS. The final stage involves assembling the device.

3.5.1.1 Fabrication of DEP microelectrodes

In this section, the author will describe the procedures for the fabrication of the DEP microelectrodes on the glass substrate used for Platform 1.

3.5.1.1.1 Substrate preparation

Cleaning the substrates and masks using a standardized procedure was necessary to ensure the quality of the fabricated devices. This was important as the existence of particles or impurities on the substrate or mask would result in irreversible faults.

The substrate was first cleaned in acetone and methanol to remove grease and particles from the substrate surface. This was followed by drenching with deionized (DI) water and blow drying using nitrogen (N_2). In order to ensure that the substrate was properly cleaned, a visual inspection was conducted using an optical microscope prior to subsequent fabrication steps.

3.5.1.1.2 Deposition of chromium and gold

Chromium (Cr) and gold (Au) were deposited onto the glass slide substrate using electron beam evaporation at thicknesses of 100 and 150 nm, respectively (Figure 3.6A). The Cr layer was deposited as an electrically conductive adhesion layer for the Au layer to the substrate surface.

3.5.1.1.3 Photolithography

The photolithographic patterning processes were conducted in a class-1000 clean room environment with an average temperature of 22 °C and a relative humidity of 40%. First, a layer of positive photoresist known as AZ1512 (Microchemicals) was spun on the glass slide substrate using a wafer spinner (Karl Suss RC8) at a revolutionary speed of 500 rpm and acceleration of 100 rpm sec^{-1} for 5 seconds, known as the "spread coat" cycle. This was followed by a spinning speed of 3000 rpm and acceleration of 300 rpm sec^{-1} for 30 seconds, which is known as the "spin coat" cycle (Figure 3.6B).

The sample was then oven baked for 20 minutes at 90°C to evaporate the solvents from the photoresist. This was followed by an ultraviolet (UV) exposure (using the DEP mask pattern depicted in Figure 3.2) with an exposure dose of 125 mJ cm^{-2} (Karl Suss, MJB3). The sample was then developed using the AZ400 photoresist developer (Microchemicals) which was diluted with DI water at a volumetric dilution ratio of 1:4 (AZ400 developer: DI water) for 17 seconds (Figure 3.6D). After development, the sample was rinsed with DI water and blow dried with N_2. The developed microelectrode patterns were examined under an optical microscope to ensure the patterns were not over or under developed.

3.5.1.1.4 Wet etching

The etching of the undesired Au patterns was conducted using "Aqua Regia", which is a mixture formed by concentrated nitric acid (HNO_3) and hydrochloric acid (HCl) according to a volumetric ratio of 1:3 respectively. The etching of Au was conducted for 15 seconds after which the sample was rinsed in DI water for 30 seconds. Next, Cr etching was conducted for 120 seconds using a solution of 4% nitric acid, 11% ceric ammonium nitrate ($Ce(NH_4)_2(NO_3)_6$) and 85% water (Figure 3.6E). The residual photoresist on the sample was then removed by rinsing the sample with acetone and DI water. The sample was then blow dried with N_2. Finally, the sample (Figure 3.6F) was inspected under an optical microscope to ensure no photoresist remained on the sample and that the microelectrode patterns were not over/under etched.

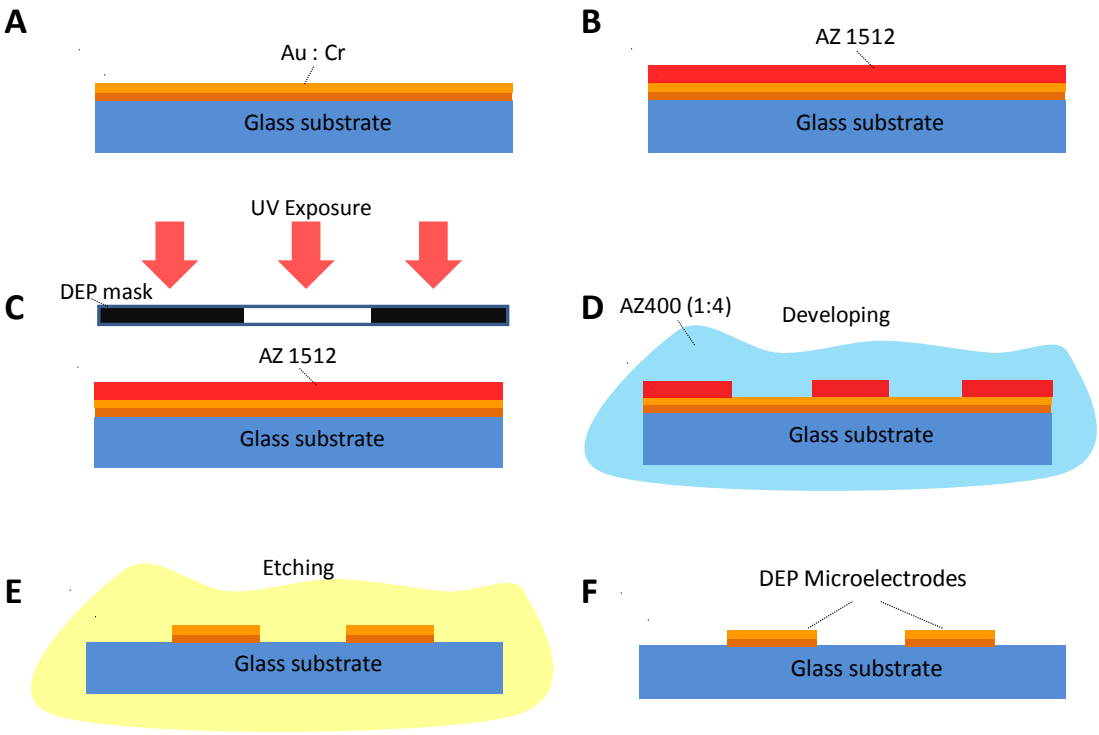

Figure 3.6: Fabrication of DEP microelectrodes.

3.5.1.2 Fabrication of PDMS microfluidics

The fabrication of the PDMS microfluidics was conducted in two stages. The first stage involved the fabrication of the microfluidic channel mould on a Si wafer. The second stage involved the fabrication of the PDMS block using a fabricated channel mould.

3.5.1.2.1 Fabrication of Microchannel Mould

SU-8 2050 (Microchem) was applied to build the microfluidic channel moulds. Since SU-8 2050 is a negative photoresist, a dark field mask was required. The dark field of the mask depicted in Figure 3.3A was used. The Si wafer was first cleaned using the standard cleaning procedure described in section 3.5.1.1.1. Then, SU-8 2050 photoresist was spun at a speed of 500 rpm and acceleration of 100 rpm sec^{-1} for 5 seconds followed by a spinning speed of 1250 rpm and acceleration of 300 rpm sec^{-1} for 30 seconds to achieve a feature height of 125 µm (Figure 3.7A). The mould was soft baked on a hotplate at 65 °C for 5 minutes followed by 95 °C for 25 minutes to evaporate the solvents from the photoresist.

The sample was taken off the hotplate and allowed to cool for 2 minutes at room temperature.

Next, the sample was UV exposed through the microfluidic channel mask with an exposure dose of 250 mJ cm^{-2}. The sample was post-exposure baked for 5 minutes at 65 °C and 12 minutes at 95 °C until an image of the mask was visible in the resist coating. The development process of the photoresist layer was conducted using the SU-8 developer (Microchem) for 6 minutes (Figure 3.7C). This was followed by rinsing with isopropanol for 10 seconds and blow drying with N_2.

3.5.1.2.2 Fabrication of PDMS microfluidic block

For the fabrication of the PDMS microfluidic block, polymer and curing agents were mixed at a weight ratio of 10:1 and stirred for 2 minutes. The mixture was then degassed in a vacuum chamber for 30 minutes to remove any bubbles from the mixture. A pre-milled frame made of perspex was then placed on the microchannel mould. A diced Si wafer was attached to the side of the perspex frame (close to the microfluidic channel bends at the outlet) so that the PDMS was cured against a smooth surface. The degassed liquid PDMS mixture was then poured into the perspex frame and cured at 75 °C for 2 hours in an oven (Figure 3.7D). The PDMS block was then removed from the frame and placed on a clean mat (Figure 3.7E). The holes for the microfluidic tubes were punched at the center of the inlet and outlet reservoirs.

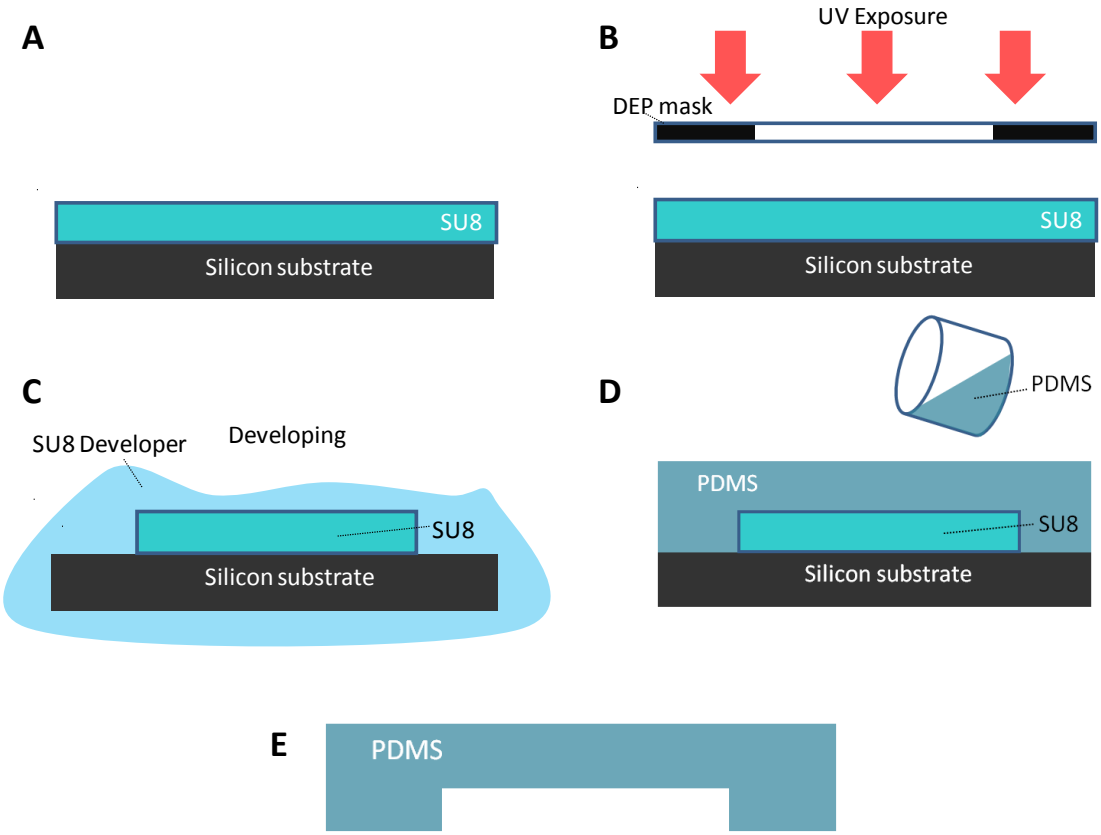

Figure 3.7: Fabrication of PDMS microfluidics.

3.5.1.3 Assembly of the device

The device assembly process involves attaching the PDMS block to the substrate, wire bonding, inserting the fiber into the PDMS block and testing the device with the flow of liquid.

3.5.1.3.1 PDMS attachment

Before assembling the device, the PDMS block was plasma treated with a hand-held Tesla coil plasma wand (Electro-Technic Products, BD-20V) for 2 minutes to activate the PDMS surface and enhance adhesion to the substrate. The plasma wand used the flow of O_2 from the atmosphere and outputs a voltage ranging from 10 to 50 kV in the discharge space for 2 minutes. The PDMS block was then attached to the glass slide while observing the device

under an optical microscope. The DEP microelectrodes were aligned so that they were at the center of the microfluidic channel as depicted in Figure 3.8.

3.5.1.3.2 Wire bonding

Next, wires were bonded to the conducting pads of the DEP microelectrodes. Two components of silver conductive epoxy (Epo-Tek H20E) consisting of a silver resin paste and silver resin hardener were mixed at a weight ratio of 1:1. A few drops of the mixture were poured to bond the wires to the conducting pads. The epoxy was cured at 60 °C for 12 hours.

3.5.1.3.3 Inserting the fiber

A multi mode fiber cable was used to direct light in the center of the DEP microelectrodes in the microfluidic channel. The fiber cable was cleaved to strip off the outer fiber jacket and cladding layers, leaving only the core. The fiber core was then inserted into the fiber recess which was formed against the microfluidic channel mould.

3.5.1.3.4 Microfluidic assembly and testing

Microfluidic tubes were inserted into the inlet and outlet reservoirs. The outlet reservoir was connected to a 5 ml syringe (Becton D. Plastic) mounted on a syringe pump (Harvard Apparatus PHD 2000). The inlet reservoir was connected to a beaker containing isopropanol. Using the syringe pump, isopropanol was flushed through the microfluidic channel by suction to ascertain that there was no fluidic leakage and to clean the microfluidic channel before conducting any experiments.

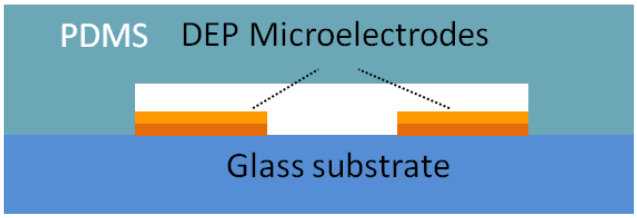

Figure 3.8: Assembly of Platform 1.

3.5.2 Platform 2

The fabrication procedures for Platform 2 are divided into six stages. These include the fabrication of the waveguides lower cladding, DEP microelectrodes, waveguide core, waveguide testing, fabrication of the PDMS microfluidic block and assembly of the device. SU-8 2002 (MicroChem) was used for the core and KMPR 1035 (MicroChem) for the lower cladding. SU-8 was chosen as the waveguide core material due to its relatively high refractive index and low loss over a wide visible wavelength range [6].

3.5.2.1 Lower cladding preparation

A 4 inch Si wafer was cleaned using procedures described in section 3.5.1.1.1. Next, a layer of KMPR 1035 was spun at a speed of 500 rpm and acceleration of 100 rpm sec^{-1} for 5 seconds followed by a speed of 3000 rpm and acceleration of 300 rpm sec^{-1} for 30 seconds to achieve a feature height of 35 μm (Figure 3.9A). The sample was soft baked at 100 °C for 14 minutes on a hotplate. Next, the sample was exposed with no mask (known as a "flood exposure") to UV light (Karl Suss MA6) with an exposure dose of 700 mJ cm^{-2} (Figure 3.9B) and then post exposure baked for 3 minutes at 100 °C on a hotplate. This completed the preparation of the lower cladding layer of the waveguide.

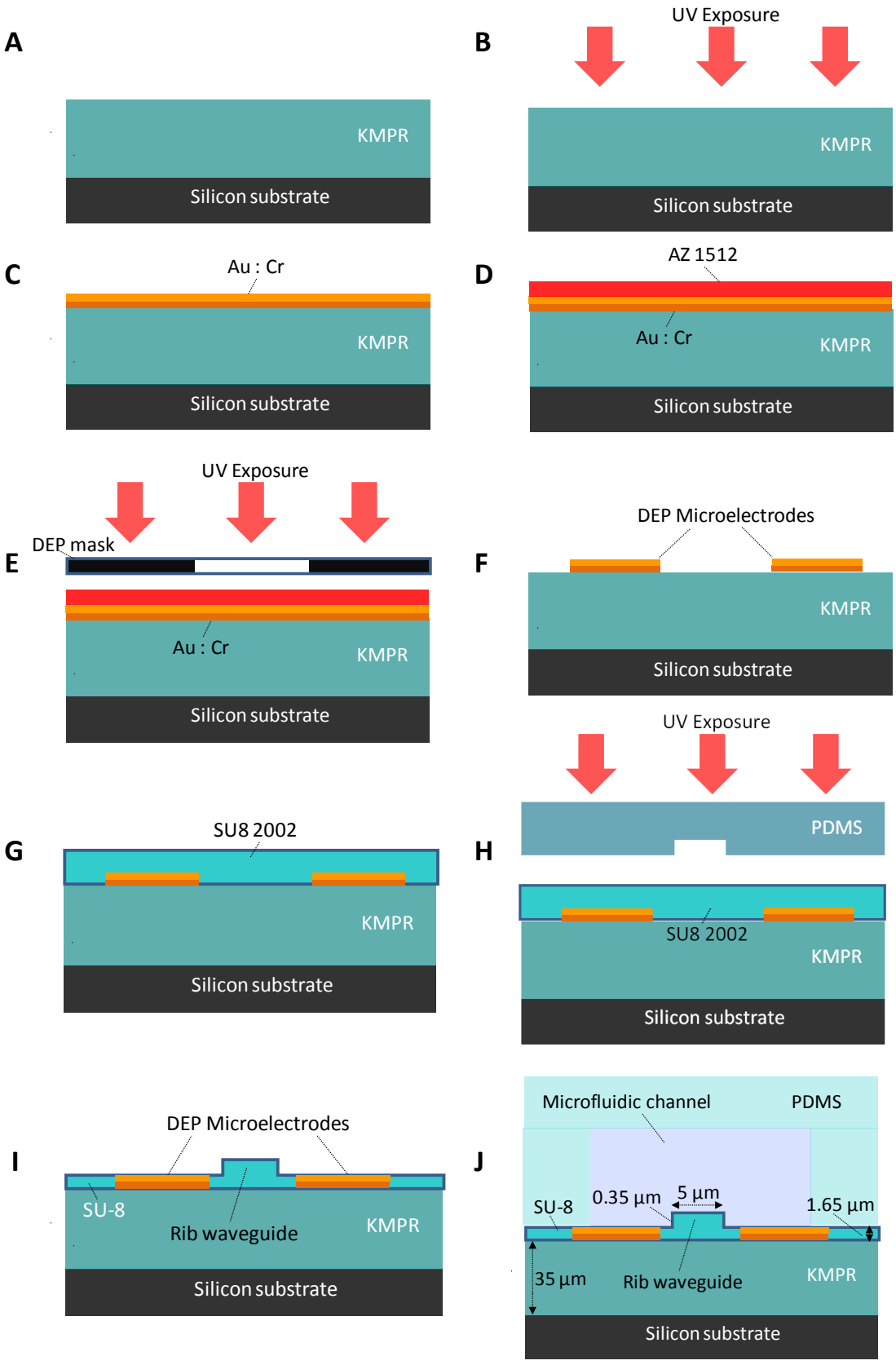

Figure 3.9: Platform 2 fabrication process.

3.5.2.2 Fabrication of DEP microelectrodes

The DEP microelectrodes were patterned on top of the cured KMPR layer which forms the lower cladding of the waveguide. Cr and Au were deposited onto the surface of the KMPR epoxy at thicknesses of 100 and 150 nm, respectively (Figure 3.9C). The DEP microelectrodes were then patterned using photolithography (Figure 3.9D-3.9E) and wet etching techniques (Figure 3.9F) as described in sections 3.5.1.1.3 and 3.5.1.1.4, respectively.

3.5.2.3 Waveguide core preparation

The waveguide core preparation process involves the fabrication of the waveguide cast master followed by the PDMS waveguide mould. Once the mould was ready, the waveguide core layer was imprinted.

3.5.2.3.1 Waveguide cast master

A waveguide cast master was fabricated using a diluted version of SU-8 2000.5 (Microchem) photoresist. The cast master was prepared as follows. First, a Si wafer was cleaned using the standard substrate preparation procedures outlined in section 3.5.1.1.1. Then the diluted photoresist was spun at a speed of 500 rpm and acceleration of 100 rpm sec^{-1} for 5 seconds followed by a speed of 3000 rpm and acceleration of 300 rpm sec^{-1} for 30 seconds to achieve a feature height of 350 nm. The sample was soft baked for 1 minute at 65 °C and 1 minute at 95 °C on a hotplate. The sample was then UV exposed with an exposure dose of 50 mJ cm^{-2} using the waveguide mask described in section 3.4. Next, the sample was post exposure baked for 1 minute at 65 °C and 1 minute at 95 °C on a hotplate. The sample was then developed using SU-8 developer (Microchem) for 1 minute. The sample was rinsed with DI water and blow dried with N_2. This completed the preparation of the waveguide cast master.

3.5.2.3.2 PDMS waveguide mould

A PDMS waveguide mould was used to imprint the waveguide onto the sample forming a raised rib replica of the waveguide cast master. For the fabrication of the PDMS waveguide mould, PDMS polymer and curing agents were mixed and degassed as described in section 3.5.1.2.2. A pre-milled circular frame made of perspex was then placed on the waveguide cast master sample. The degassed liquid PDMS mixture was then poured into the circular perspex frame and cured at 75 °C for 2 hours in an oven. The PDMS waveguide mould was then removed from the perspex frame completing the preparation of the PDMS waveguide mould.

3.5.2.3.3 Waveguide core imprinting

The waveguide core was imprinted using the PDMS waveguide mould as follows. The waveguide core layer was fabricated by spin coating SU-8 2002 (Microchem) photoresist at a speed of 500 rpm and acceleration of 100 rpm sec^{-1} for 5 seconds followed by a speed of 4000 rpm and acceleration of 300 rpm sec^{-1} for 30 seconds to achieve a feature height of 1.65 μm (Figure 3.9G). Using the PDMS waveguide mould, the waveguides were imprinted while the SU-8 2002 was wet. The author selected the waveguide which had a width of 7 μm as it was the widest waveguide in the mask (waveguide widths range from 3 – 7 μm on the mask) as it was easier to couple light through an objective lens to a larger waveguide and coupling losses experienced by the coupled light was expected to be lower.

The sample with the imprinted waveguide was then soft baked while in contact with the PDMS mould in an oven at 65 ℃ for 20 minutes. The sample was taken out of the oven and then flood exposed with UV light at an exposure dose of 350 mJ cm^{-2} (Figure 3.9H). The PDMS mould was then peeled off from the sample and the sample was post exposure baked at 65 ℃ for 1 minute followed by 90 ℃ for 10 minutes on a hotplate (Figure 3.9I). The sample was then diced using a dicing machine (DAD321) to obtain optically smooth end-faces. The dimensions of the diced sample were 25 mm × 25 mm ($w \times h$).

3.5.2.4 Waveguide testing

Before proceeding to the next step, the waveguide must be tested to ascertain that it can accurately propagate light. This test was conducted by coupling visible light (λ = 635 nm) from a laser source into one end-face and imaging the light that emerges from the opposite end-face of the waveguide. The image shows the optical power distribution within the waveguide, referred to as the mode intensity profile. The light that emerges from the output end-face was focused by an objective lens onto a charge coupled device (CCD) camera. Figure 3.10A shows light successfullycoupled into the waveguide and imaged at the output while Figure 3.10B shows light propagating though a possibly defective waveguide as it suffers severe lateral leakage of light. In the case of light propagating with such leakage or not propagating at all, the author would have to repeat the waveguide fabrication process. Subsequently, the author would dice the sample in order to conduct a cross sectional SEM to investigate why the waveguide did not propagate light accurately. After ascertaining that the waveguide successfully propagates light, the PDMS microfluidic block was fabricated.

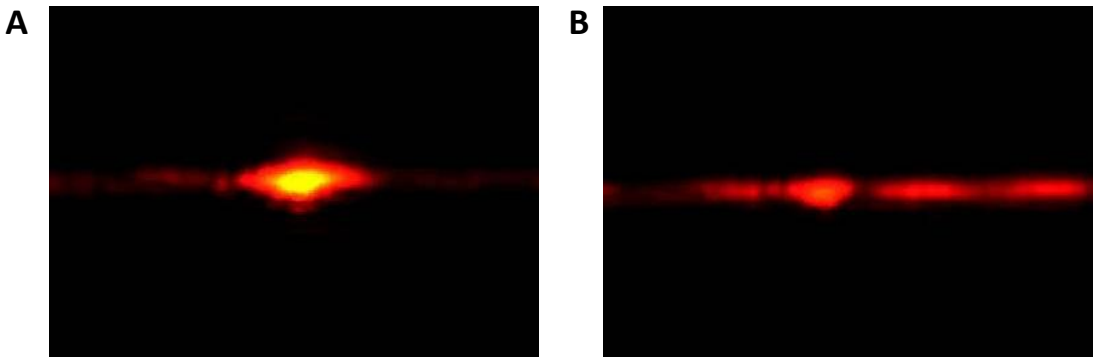

Figure 3.10: Waveguide testing using light from a visible laser source. (A) Light coupled into polymeric waveguide propagates with minimal lateral leakage (B) Light propagating through a defective waveguide experiences severe lateral leakage of light.

3.5.2.5 PDMS microfluidic block

The PDMS microfluidic block was fabricated using soft lithography techniques as described in sections 3.5.1.2.1 and 3.5.1.2.2. The dark field presented in Figure 3.3B was used. After the PDMS block was fabricated, it was then attached to the sample.

3.5.2.6 Assembly of the device

The PDMS block was attached to the sample using procedures described in section 3.5.1.3.1 (Figure 3.9J). After attachment, wires were bonded to the sample and the microfluidics were assembled and tested before conducting the experiments according to procedures described in section 3.5.1.3.2 and 3.5.1.3.4.

3.5.3 Platform 3

The fabrication procedures for Platform 3 are composed of five stages. They include the imprinting of the waveguide trenches, fabrication of the waveguide core, patterning the DEP microelectrodes, fabrication of the microfluidic sidewalls and sealing the microchannel with a PDMS block.

3.5.3.1 Imprinting of waveguide trenches

A waveguide cast master and a PDMS waveguide mould was fabricated using procedures outlined in sections 3.5.2.3.1 and 3.5.2.3.2, respectively. Next, a Si wafer was cleaned using the standard substrate preparation procedures outlined in section 3.5.1.1.1. A layer of KMPR 1035 was spun at a speed of 500 rpm and acceleration of 100 rpm/sec for 5 seconds followed by a speed of 3000 rpm and acceleration of 300 rpm sec^{-1} for 30 seconds to achieve a feature height of 40 μm (Figure 3.11A).

Immediately after the spinning cycle was completed, the PDMS waveguide mould was used to imprint the waveguide trenches while the KMPR was wet (Figure 3.11B). The imprinted KMPR was then baked in an oven at 85 ^{o}C for 20 minutes. The sample was then removed

from the oven and immediately flood-exposed with an exposure dose of 840 mJ cm^{-2} while the sample was still hot. This was done in order to prevent the sample from cooling, which causes shrinkage and thermal stress on the sample patterns. The sample was then post-exposure baked at 95 ^{o}C in the oven for 10 minutes. The sample was then taken out of the oven and the PDMS waveguide mould was peeled off the sample (Figure 3.11C).

3.5.3.2 Waveguide core fabrication

Next, the waveguide core was fabricated by plasma treating the KMPR surface for 2 minutes. This was followed by spin coating a layer of SU-8 2002 (Microchem) at a speed of 500 rpm and acceleration of 100 rpm sec^{-1} for 5 seconds followed by a speed of 2500 rpm and acceleration of 300 rpm sec^{-1} for 30 seconds to achieve a feature height of 2.5 µm (Figure 3.11D). The sample was then soft baked at 65 ^{o}C for 1 minute, 95 ^{o}C for 2 minutes and 65 ^{o}C for 1 minute on a hotplate. Next, the sample was flood exposed with an exposure dose of 210 mJ cm^{-2}. The sample was then post exposure baked at 65 ^{o}C for 1 minute, 95 ^{o}C for 3 minutes and 65 ^{o}C for 1 minute on a hotplate. The sample was then diced to the dimensions 25 mm × 25 mm (*w* x *h*). After dicing, the waveguide was tested as outlined in section 3.5.2.4.

3.5.3.3 DEP microelectrode patterning

The process was continued with the fabrication of the DEP microelectrodes. Cr and Au layers were deposited onto the surface of the SU-8 epoxy as described in section 3.5.1.1.2. Subsequently, the DEP microelectrodes were patterned using photolithography as described in section 3.5.1.1.3. The width of the quasi single mode waveguide was 4.5 µm. The author aligned the 4.5 µm waveguide to be at the center of the curved DEP microelectrodes using the mask aligner (Karl Suss, MA6). After photolithography was completed, the undesired Au and Cr patterns were etched using wet etching techniques as described in section 3.5.1.1.4 (Figure 3.11E).

3.5.3.4 Microfluidic sidewalls

The microfluidic sidewalls were fabricated with cured photoresist. The author spin coated a layer of KMPR 1035 at a speed of 500 rpm and acceleration of 100 rpm sec^{-1} for 5 seconds followed by a speed of 2500 rpm and acceleration of 300 rpm sec^{-1} for 30 seconds to achieve a feature height of 40 µm on top of the waveguide core layer. The sample was then soft baked at 100 ^{o}C for 15 minutes on a hotplate. Next, the sample was exposed using the dark field of the mask depicted in Figure 3.3B with an exposure dose of 800 mJ cm^{-2}. The sample was then post exposure baked at 100 ^{o}C for 3 minutes on a hotplate. Then, the photoresist was developed in SU-8 developer (Microchem) for 6 minutes. The development process was stopped by rinsing the sample with isopropanol and DI water followed by a blow dry with N_2 (Figure 3.11F).

3.5.3.5 PDMS block

After the microfluidic sidewalls were formed, the microfluidic channel was sealed with a PDMS block. The PDMS block was a flat block cured in a perspex frame. The purpose of the PDMS block was to prevent liquid from leaking out of the channel and to provide access for the microfluidic tubes to the channel.

The PDMS block was fabricated using procedures described in section 3.5.1.2.2. The only difference was the PDMS mixture was poured inside the perspex frame on a flat Si wafer (to produce a flat block). After curing, the PDMS block was removed from the frame and holes were punched to provide access to the inlet and outlet reservoirs. The PDMS block then was attached to seal the microchannel (Figure 3.10G).

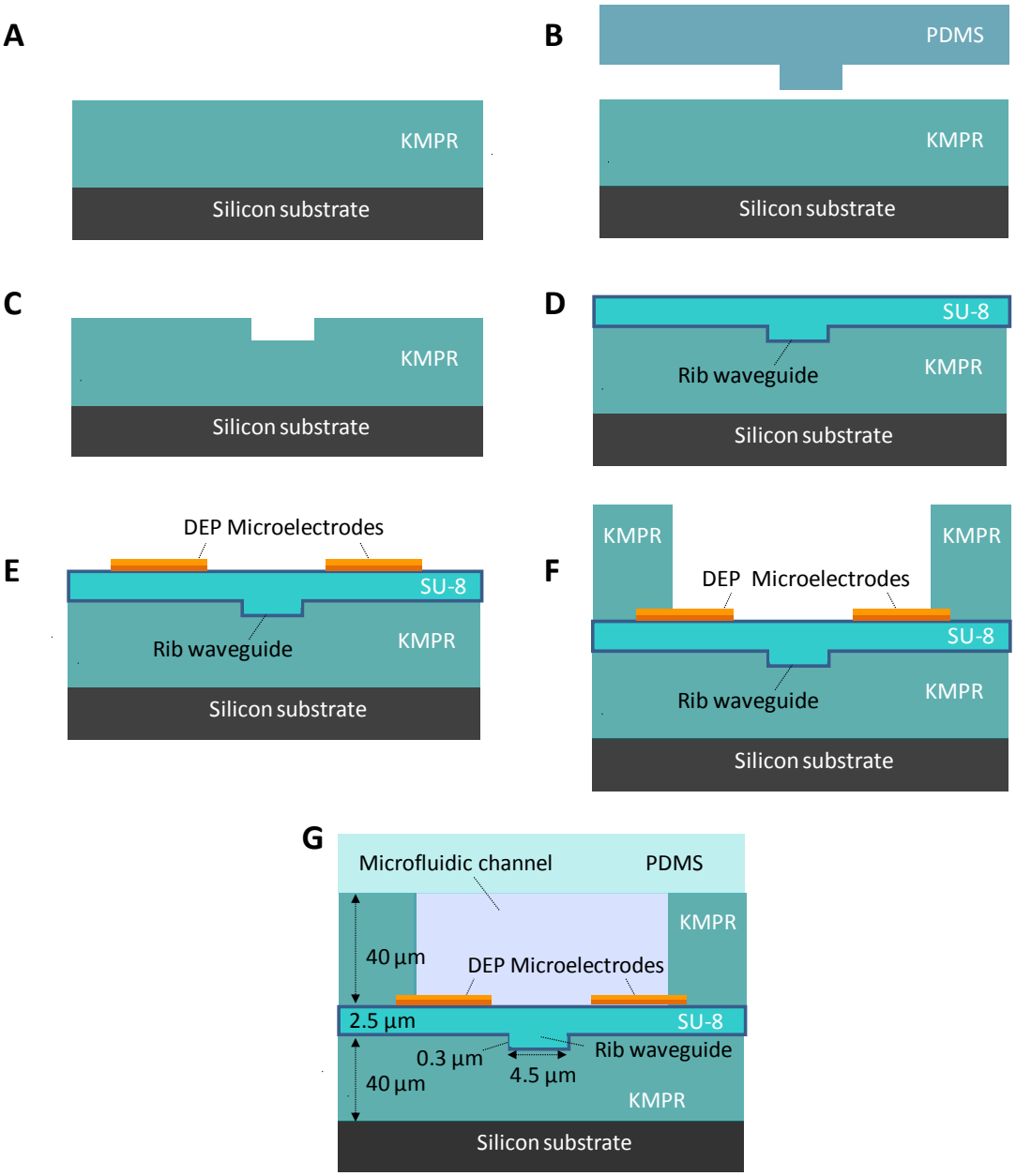

Figure 3.11: Platform 3 fabrication process.

3.6 Summary

The author presented the design and fabrication of the three experimental platforms used in his PhD research. Curved DEP microelectrodes were used to generate the DEP forces and manipulate the particle positions and concentrations in the microfluidic channel. The rib waveguides were designed to interact with the dielectrophoretically controlled particles in the microfluidic channel. The author described the fabrication processes for the platforms in sufficient detail so the procedures could be verified and replicated without difficulty.

In chapter 4, the author will demonstrate the use of Platform 1 for coupling light directly into the DEP concentrated particles suspended in liquid. Subsequently, in chapter 5, Platform 2 will be used to demonstrate the coupling of light into the DEP focused particles via the multi mode polymeric waveguide. Finally, in chapter 6, the author uses Platform 3 to demonstrate the coupling of guided modes from a quasi single mode waveguide into the DEP focused particles.

References

[1] Khoshmanesh, K., C. Zhang, F.J. Tovar-Lopez, S. Nahavandi, S. Baratchi, K. Kalantar-zadeh, and A. Mitchell, Dielectrophoretic manipulation and separation of microparticles using curved microelectrodes. *Electrophoresis*, vol. 30, pp. 3707-3717, 2009.

[2] Zhang, C., K. Khoshmanesh, A. Mitchell, and K. Kalantar-zadeh, Dielectrophoresis for manipulation of micro/nano particles in microfluidic systems. *Analytical and Bioanalytical Chemistry*, vol. , pp. 1-20, 2009.

[3] Khoshmanesh, K., C. Zhang, F.J. Tovar-Lopez, S. Nahavandi, K. Baratchi, and K. Kalantar-zadeh, Dielectrophoretic Manipulation and Separation of Microparticles Using Curved Microelectrodes. *Electrophoresis*, vol. 30, pp. 3707-3717, 2009.

[4] Friend, J. and L. Yeo, Fabrication of microfluidic devices using polydimethylsiloxane. *Biomicrofluidics*, vol. 4, 2010.

[5] Perentos, A., G. Kostovski, and A. Mitchell, Polymer long-period raised rib waveguide gratings using nano-imprint lithography. *IEEE Photonics Technology Letters*, vol. 17, pp. 2595-2597, 2005.

[6] Jiang, L., K.P. Gerhardt, B. Myer, Y. Zohar, and S. Pau, Evanescent-wave spectroscopy using an SU-8 waveguide for rapid quantitative detection of biomolecules. *Journal of Microelectromechanical Systems*, vol. 17, pp. 1495-1500, 2008.

Chapter 4

Direct Coupling of Light into Dielectrophoretically Focused Particles

4.1 Introduction

As described in chapter 1, the aim of this PhD project is to develop a microfluidic system for coupling light into regions of highly packed particles suspended in liquid. The author decided to follow a strategic step-by-step approach to achieve the aim of the PhD project. The first stage (which will be detailed in this chapter) involved direct coupling of light into the densely packed concentration of suspended particles. Platform 1 was used in this stage of the PhD research project. The fabrication and structure of Platform 1 was described in chapter 3.

The author developed a system with three main componenets: (a) Microfluidics that contains mesoparticles (b) Dielectrophoretic (DEP) microelectrodes for applying force on particles

and (c) Peripherals for coupling of 635 nm wavelength laser beam into and for detecting the output profile.

The author hypothesized that when DEP forces pack the particles into a narrowband at the center of the microfluidic channel, they can create a region of different refractive index, which can act as an optical waveguide. In order to gain understanding about the dimensions of the particles on the performance of the system, the author assumed that the particles size and inter particles spacing determine, whether the particle-packed area will exhibit scattering or propagating properties.

The author will show the manipulation of SiO_2 particles into forming a high refractive index media in liquid surrounded by a low refractive index media, which resembles the structure of an aqueous waveguide [1]. The core of this dynamically formed waveguide is composed of the densely packed particles, while the cladding of the waveguide is composed of the liquid in the microfluidics channel.

In this chapter, the author will demonstrate the "direct" coupling of light into the densely packed regions of silicon dioxide (SiO_2) particles suspended in liquid. Particle diameters of 230 and 450 nm were selected, as the author had the insight that the transmission of light via the suspension of 450 nm particles would be dominated by scattering loss, while the loss on transmission through 230 nm particle suspension would be greatly reduced. The SiO_2 particles were dynamically controlled using the DEP force.

In the subsequent sections of this chapter, the author will demonstrate the manipulation of SiO_2 particles by varying several externally applied parameters, such as the magnitude of the applied voltages, frequencies and the microfluidic flow rates. The externally applied parameters are varied in establishing and tuning the "particle waveguide" structure.

The author subsequently presents the direct coupling of laser beams (635 nm) into the densely packed SiO_2 particles using a visible light source while observing the optical intensity profile of the output. The author describes the optical responses, comparing the results for both particle sizes used.

4.2 Principles

An optical waveguide in liquid is formed when a fluid stream of one refractive index is in an intimate contact with a medium of different refractive index and forms smooth non-turbulent fluid boundaries [1, 2]. In a structure similar to commercial optical waveguides (with core and cladding), the main condition for waveguiding is that the core refractive index must be higher than the cladding so that light can be guided by total internal reflection [3].

At this stage of research, the author hypothesized that the DEP forces could be used to focus the suspended SiO_2 particles into forming the "core" of the waveguide composed of a stream of packed SiO_2 particles having a higher refractive index (n = 1.45) [4] than the cladding, composed primarily of DI water, having a lower refractive index (n = 1.33).

The principles of the DEP force have been presented in chapter 2. By varying the parameters of the applied DEP force such as the magnitude of the alternating current (AC) signal and the frequency, it is theoretically possible to manipulate the motion and concentrations of particles into forming such dense particle streams surrounded by lower refractive index media in a profile structure resembling that of a waveguide. Maintaining laminar flow [5] is also crucial to avoid mixing across parallel streams and so that the DEP force would not be dominated by turbulent mixing at the particle/liquid boundaries. The flow rates produced by the method of pumping or suction, as well as the microfluidic channel design, affects the particles' alignment, speed and flow stability [6]. Therefore, in establishing packed concentrations of particles with smooth boundaries, it is crucial to adhere to flow rates that promote laminar flows of liquid.

To illustrate the DEP behavior of the SiO_2 particles, the author plotted the real value of the Claussius-Mossoti factor $\mathrm{Re}[f_{CM}(\omega)]$ using equation (2.11) from chapter 2. The relative permittivity and conductivity of the suspending medium (DI water) was taken as $\varepsilon_m = 77.6$ and conductivity of medium, $\sigma_m = 0.2$ mS m^{-1} [7, 8]. It was assumed that the 230 and 450 nm particles have a relative permittivity of $\varepsilon_p = 4.5$ and conductivities of 0.3 and 0.5 nS m^{-1} respectively [9, 10]. According to Figure 4.1, $-0.47 < \mathrm{Re}[f_{CM}(\omega)] < 0.89$ and $-0.47 < \mathrm{Re}[f_{CM}(\omega)] < 0.85$ applies for 230 nm and 450 nm particles, respectively, for frequencies from 10 kHz to 10 MHz. The particles experience both negative and positive

DEP forces throughout the frequency range. The crossover frequency is 1 and 1.5 MHz for the 450 and 230 nm particles, respectively.

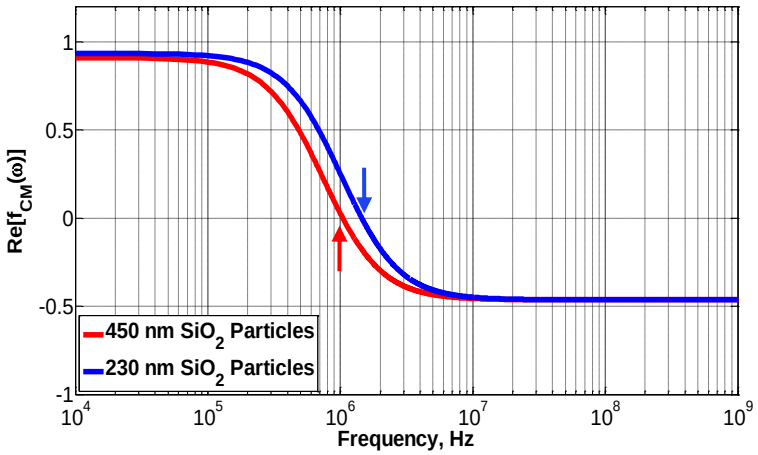

Figure 4.1: DEP spectrum for the 450 and 230 nm SiO_2 particles. The crossover frequencies are shown by the arrows.

4.3 Methods and Simulations

The particles used for the experiment were synthesized using the Stober method [11, 12], by a colleague of the author - Mr. Jos Campbell from the School of Applied Sciences, RMIT University, a process for the generation of mono-dispersed SiO_2 particles. The particles were analyzed using a scanning electron microscope (SEM) to assure their shape and size. The SEM images of the particles used in the experiments are presented in Figure 4.2.

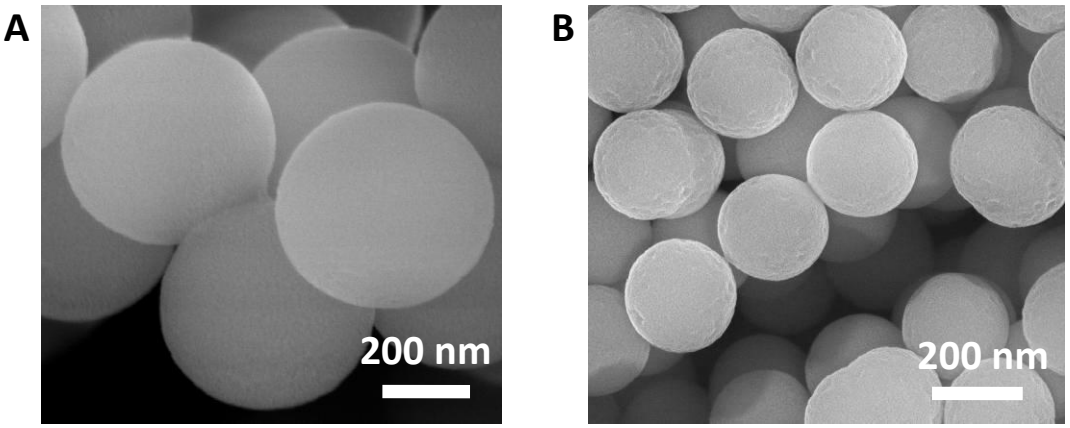

Figure 4.2: SEM images of the: (A) 450 and (B) 230 nm SiO_2 particles.

The distribution of the electric field gradients generated by the curved microelectrodes used in Platform 1, as well as the DEP forces, were modeled using Fluent 6.2 software package (Fluent, USA, Lebanon, NH), as described in [13]. Dr. Khashayar Khosmanesh from School of Electrical and Computer Engineering, RMIT University, helped the author in conducting the simulations.

Gambit 2.3.16 software (Fluent Inc., Lebanon, USA) was used for mesh generation. A total number of 29,500 elements were applied across the glass substrate, which formed the bottom surface of the DEP system. This included a combination of unstructured triangular elements inside the microelectrodes, structured quadrilateral boundary elements around the microelectrodes, and unstructured quadrilateral elements covering the rest of the microchannel, as shown in Figure 4.3A. The density of boundary elements was high enough to not only predict the sharp gradients of electric field along the microelectrode edges but also to predict the smooth variation of electric field across the elements located inside and outside of microelectrodes, as shown in Figure 4.3B and 4.3C.

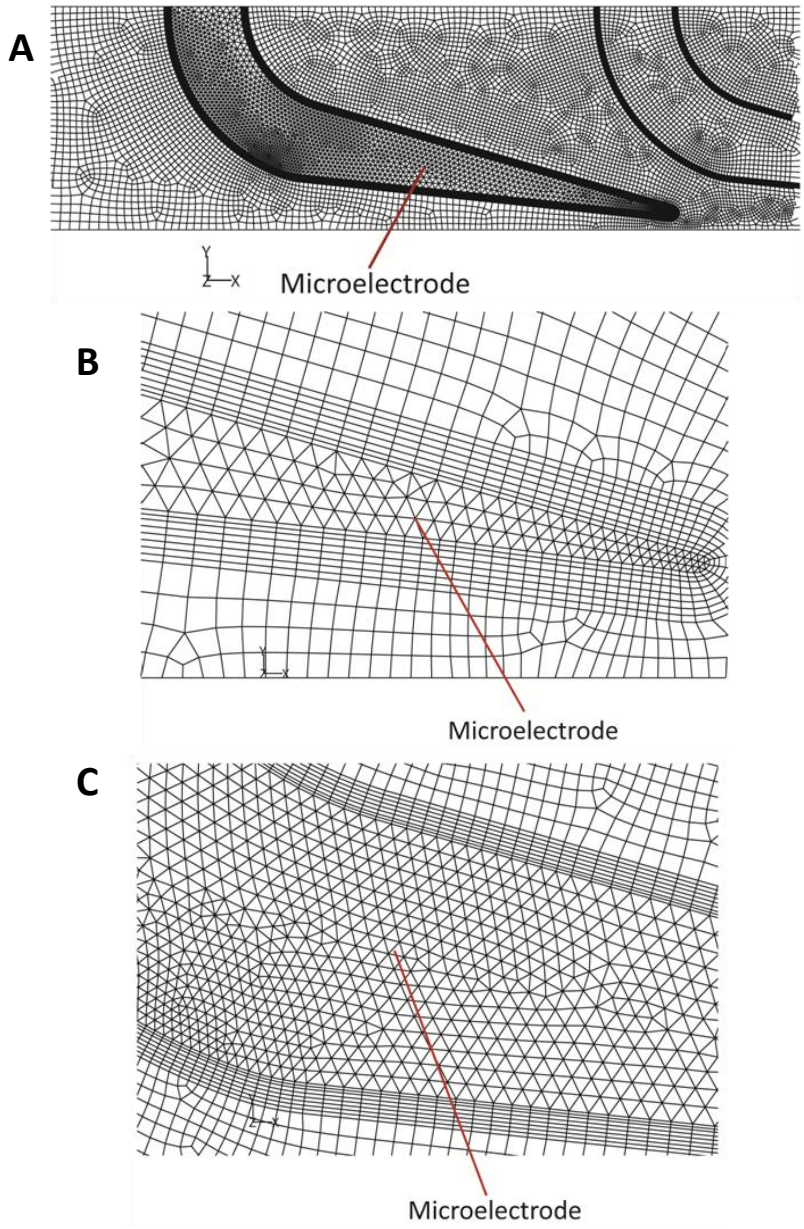

Figure 4.3: The layout of generated elements across the glass substrate: (A) Overall electrode view of mesh elements (B) Close up mesh at electrode tip (C) Mesh elements at electrode base.

The created elements were projected along the height of the microchannel. However, to reduce the number of elements and consequently the computational time, the height of the microchannel was divided into two segments. The first segment covered the first 20 µm close to microelectrodes and was divided into 20 elements while the second segment covered the rest of the microchannel depending on its height and was divided into 30

elements, as shown in Figures 4.4A and 4.4B. The density of elements across the first segment was the same as Figure 4.3 while it was decreased across the second segment. For comparison, the first segment hosted 29,500 elements across the z-axis while the second segment hosted only 14,270 elements. This did not affect the accuracy of calculations, as the gradient of electric field was much lower across the second segment.

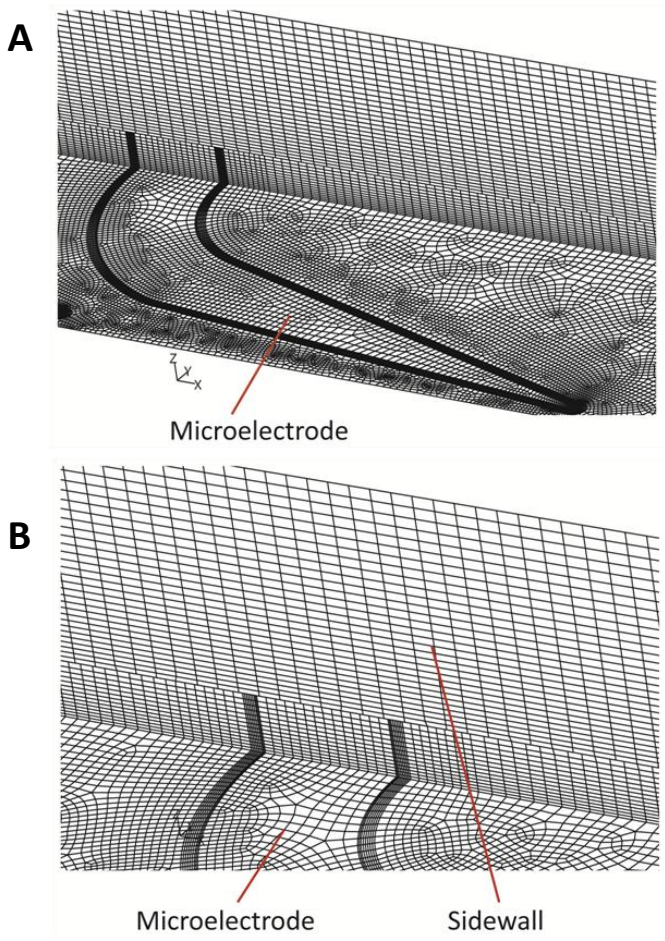

Figure 4.4: The projection of elements along the microfluidic channel height: (A) Side view and (B) Close up details of the channel mesh.

In order to obtain the E_{rms}, the author assumed that the permittivity of the medium is homogenous, and hence solved the Laplace equation, as below to acquire the electric potential field ($\nabla^2 \varphi_{rms} = 0$).The boundary conditions included constant electric potentials at the surface of microelectrodes, while zero electrical flux at the other surfaces of the system, including the bottom, top, and side walls of the microchannel as well as inlet and outlet.

Next, the electric potential was differentiated, as below to obtain the electric field ($E_{rms} = -\nabla \varphi_{rms}$).

The finite volume-based Fluent 6.2 software package (Fluent Inc, Lebanon, USA) was used as the solver. Although the Fluent software is commonly used for computational fluid dynamic (CFD) simulations by solving the Navier-Stokes differential equations governing the continuity of mass, momentum and energy within fluidic systems, its solver capabilities can be utilized to solve other differential equations such as Laplace equation to obtain the variations of electric field in DEP systems. The results were improved in consequent iterations and the iterations continued until the difference between the electric fields obtained from consequent iterations was less that 10^{-4} V m^{-1}.

Next, the electric field was obtained by calculating the gradient of the electric field potential. Consequently, the values of E^2_{rms} and ∇E^2_{rms} were calculated and substituted in the DEP force equation to obtain the F_{DEP} throughout the entire field. The Fluent software package applies a finite volume method to discretize the governing equations across each element of the field. Taking advantage of the user defined scalar module of the software ∇E^2_{rms} was substituted into the DEP force equation to obtain the DEP force magnitudes at different locations of the microelectrode array.

As presented in Figure 3.2 of chapter 3, the DEP microelectrode array was composed of many microelectrode pairs. The microelectrode pairs generate similar DEP field conditions hence, for the simulation the microchannel was shortened to contain only two microelectrode pairs, as shown in Figure 4.5A. Additionally, the DEP field is symmetric with respect to the centerline of the microchannel, therefore only half of the microchannel was simulated by applying proper boundary conditions. These simplifications reduced the number of elements and decreased the computation time significantly.

The simulations revealed that the E_{rms} reached a maximum of 2.6×10^6 V m^{-1} at the electrode tips. Figure 4.5 shows the distribution of DEP forces at the two planes along the *x*-axis, considering Re[$f_{CM}(\omega)$] for the spherical particles as 0.45. The values of the DEP forces along the *x*, *y*, and *z*-axes are given at different heights of $z = 10$ and 40 μm (Figure 4.5A). The particles were levitated at the average heights of $z = 15 - 40$ μm after passing the first microelectrode pair depending on the magnitude of the AC signal.

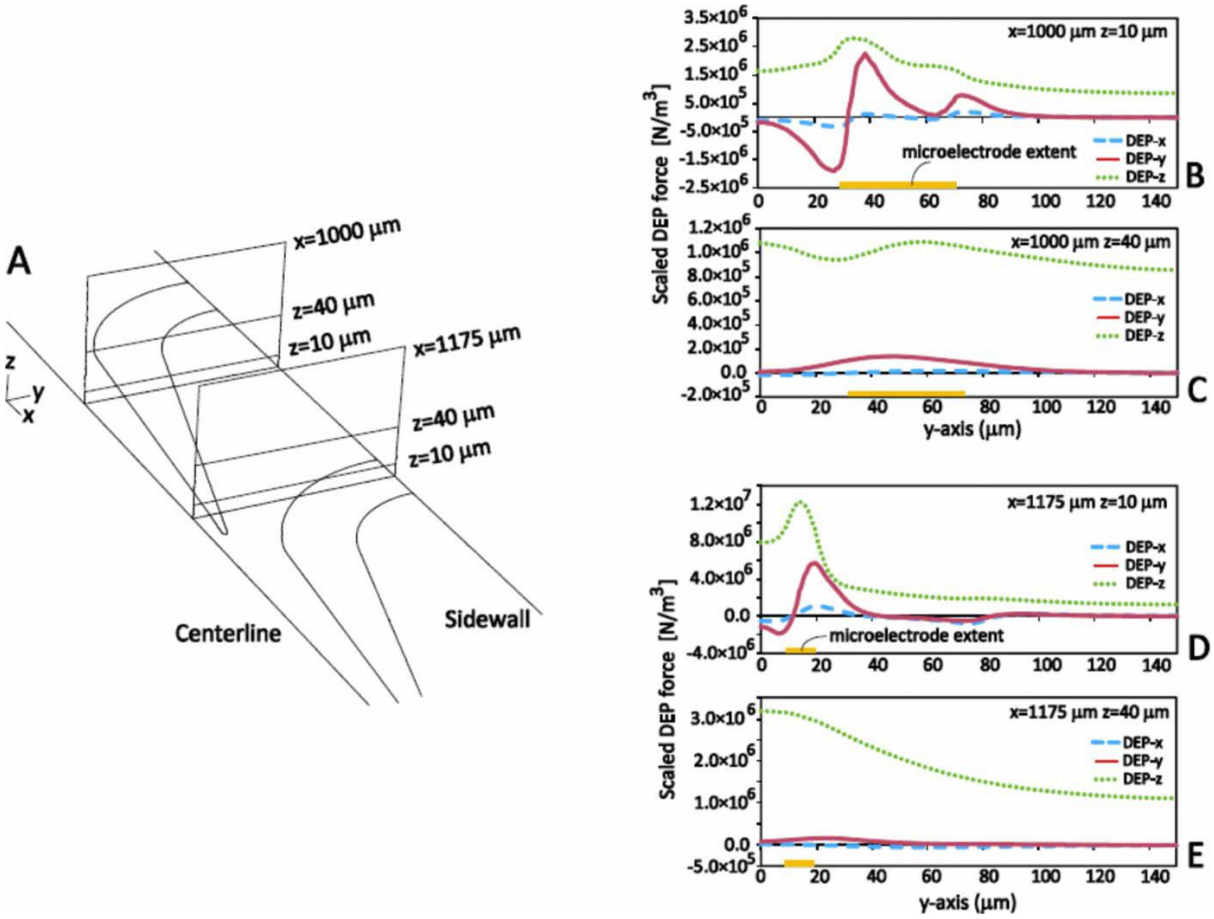

Figure 4.5: Variations in the DEP forces at different locations of the microchannel: (A) Schematic of curved microelectrodes; (B) Scaled DEP force for x = 1000 µm, z = 10 µm (C) Scaled DEP force for x = 1000 µm, z = 40 µm (D) Scaled DEP force for x = 1175 µm, z = 10 µm (E) Scaled DEP force for x = 1175 µm, z = 40 µm.

The DEP forces were divided by r^3 to make them independent from the size of the particles. The DEP-y force was the dominant force in pushing the particles toward/off the sidewalls. At z = 10 µm, the polarity of the DEP-y varied along the y-axis. The particles, moving at the left side of the microelectrode, were pushed toward the centerline, while the particles moving at the right side of the microelectrode, were pushed toward the sidewalls (Figure 4.7B and 4.7D). At z = 40 µm, the DEP-y force became much smoother and pushed all the particles toward the sidewalls (Figure 4.7C and 4.7E). Finally, the DEP-z force was upward all across the microchannel and could levitate the particles against the sedimentation force, due to the interaction of weight and buoyancy (Figure 4.7B to 4.7E). Applying a proper AC

signal was crucial to focus the particles along the centerline. At low-magnitude signals, particles were not affected efficiently, while at very high-magnitude signals, they were levitated and repelled toward the sidewalls rather than being focused. The Brownian motion and Van der Waals forces are several orders of magnitude smaller than DEP, sedimentation and hydrodynamic forces [14]. Hence, such passive forces have been neglected in the theoretical modeling of the thesis.

A schematic and actual photograph of the experimental setup is presented in Figures 4.6A and 4.6B. Platform 1 was sandwiched by a pair of polymethylmethacrylate (PMMA) transparent thermoplastic plates to homogenously apply pressure (using 6 nuts and bolts) and prevent any leakage. The multimode fiber used to couple light into the channel had a 62.5 µm core / 125 µm cladding diameter with a numerical aperture of 0.22. The light detected at the optically transparent output window was imaged through a 5 × objective lens, using a charge coupled device (CCD) camera (Philips SPC900NC). The optical source was a Class 2, 1 mW - 635 nm wavelength multi mode laser (OZ Optics).

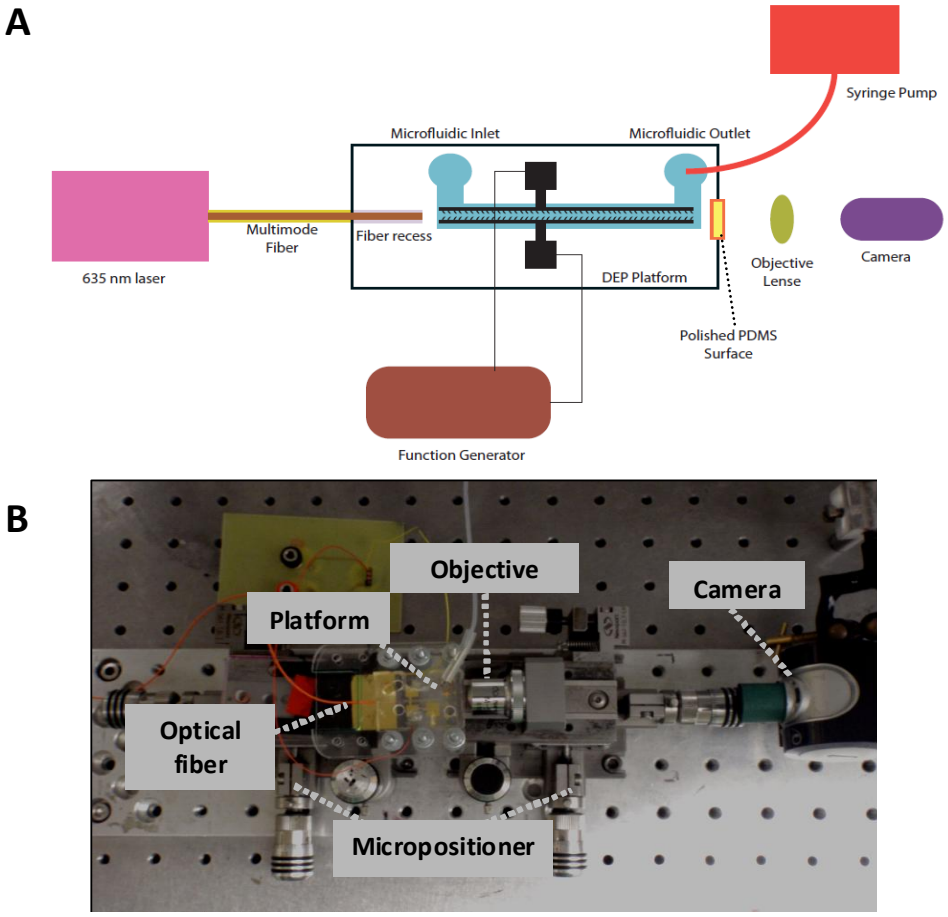

Figure 4.6: Experimental set-up: (A) Schematic (B) Photograph.

The SiO_2 particles had a volumetric dilution ratio of 3:100 (SiO_2: DI water). A 3 cc syringe (Luer lock Becton D Plastic) was mounted on a syringe pump (Harvard Apparatus PHD2000) in refill mode to provide suction. The DEP occurrence was observed using an inverted microscope (Nikon Te2000-U) and the images were captured using the CCD camera connected to the microscope (Basler High-Res). The flow rate was set to 2 µl min^{-1}, 5 µl min^{-1}, 7.5 µl min^{-1} and 10 µl min^{-1} to identify the optimal conditions for waveguiding, providing the best smoothness and alignment at the core/cladding interface as well as having the lowest possible diffusion mixing between the parallel streams.

4.4 Results and Discussion

The author conducted a series of experiments using the SiO_2 particles by changing the DEP applied voltage amplitude, frequency and flow rate. These experiments were conducted to study the effects of such parameters in establishing and tuning the optical waveguide. In each experiment, while two of these three parameters were kept constant, the third parameter was changed to see its effect independently. A series of photographs were taken, while illuminating with an incandescent light source (using the microscope broadband light) which was vertically impinged on the surface of the system.

4.4.1 230 nm SiO_2 particles

4.4.1.1 Effect of frequency variation

For the 230 nm diameter SiO_2 particles, the author applied a sinusoidal alternating current (AC) signal with an amplitude voltage of 15 V_p, flow rate of 10 µl min^{-1} and varied the frequency from 0 to 20 MHz using a function generator (Etabor Electronics 8200). As shown in Figure 4.7, the particles experienced a change from positive DEP to negative DEP behavior as the frequency was increased. Below 1.5 MHz, the curved DEP microelectrodes trapped the particles in the center (Figure 4.7A and 4.7B). As the frequency was increased from 1.5 to 20 MHz, the DEP force began to repel particles as they were no longer focused in the center of the channel (Figure 4.7C). The results show a mismatch between the experimental results and the theoretically expected crossover frequency. This mismatch can be attributed to surface conductance differences between assumed and actual values. According to the measurements, particles have a lower actual particle surface conductance. When particles are packed in the dense stream, they can be regarded as a single phase homogenous media such that their surface conductances can vary to a large degree depending on the particles' separation, concentration and alignment. At frequencies less than 300 kHz, the DEP forces trapped particles between the micro-tips, forming a particle barricade. A small amount of particles escaped the barricade due to hydrodynamic drag forces (Figure 4.7A). Interestingly, at frequencies above 2 - 3 MHz the center becomes

increasingly brighter (Figure 4.7C and 4.7D). The narrow center does not scatter the light anymore. It appeared that either particles were completely pushed to the sides, or they were in the center but did not scatter light. Apparently, the second assumption is correct, as when a horizontal light was applied (Figure 4.7E) the center was brighter than the liquid around it, suggesting a stronger scattering due to the presence of particles.

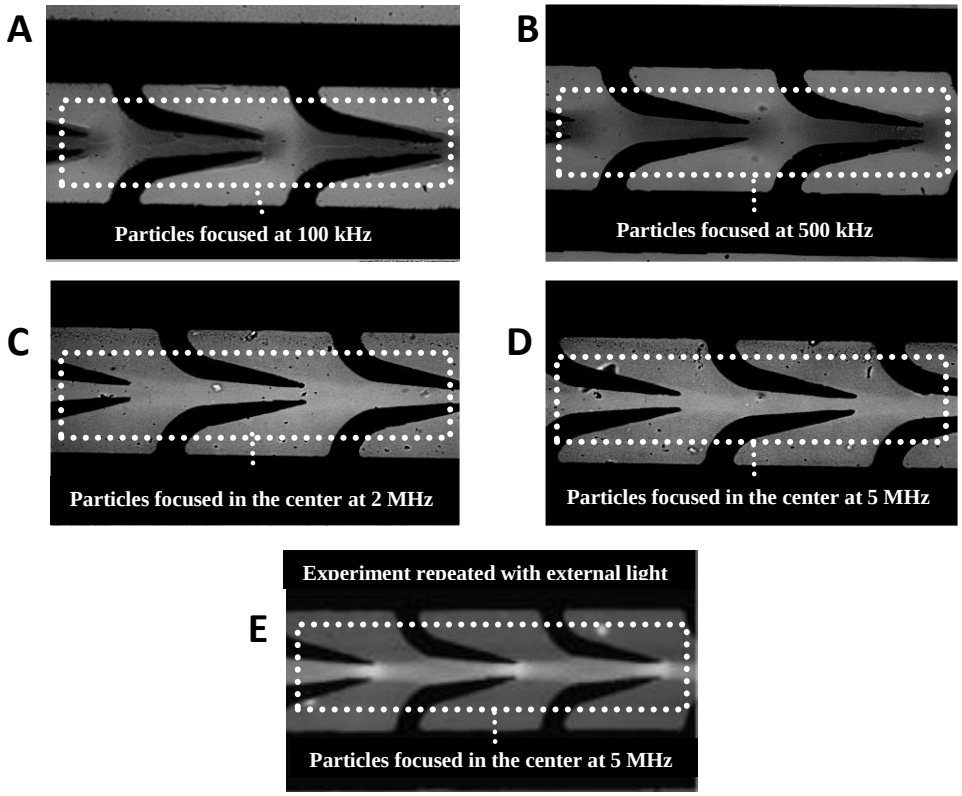

Figure 4.7: DEP manipulation of 230 nm particles at constant flow rate of 10 µl min^{-1}, AC voltage of 15 V_p and frequencies of: (A) 100 kHz (B) 500 kHz (C) 2 MHz (D) 5 MHz (E) 5 MHz experiment repeated with an external light. The intensity of light changes within the narrowband which is the proof of existence of the 230 nm particles within this area.

4.4.1.2 Effect of flow rate variation

The author observed the effects of the flow rate variation by applying a constant frequency and voltage, while the flow rate was changed. Figure 4.8 shows a set of experiments while the applied frequency was 1 MHz and voltage 15 V_p. The photos are for a set of flow rates of 2 µl min^{-1}, 5 µl min^{-1}, 7.5 µl min^{-1} and 10 µl min^{-1}. As can be seen, flow rate has a

significant effect on the smoothness of the particle core/liquid cladding boundaries. At low flow rates, the core/liquid cladding boundaries are not clearly visible in the microscopic images. However, as the flow rate is increased to 10 µl min^{-1}, the particle core exhibits a distinct shape resembling that of a waveguide in between the curved microelectrodes, whereby the center region represents the waveguide 'core' while the area surrounding it, represents the 'cladding'. The author realized that the optimal flow rate for these experiments was 10 µl min^{-1}.

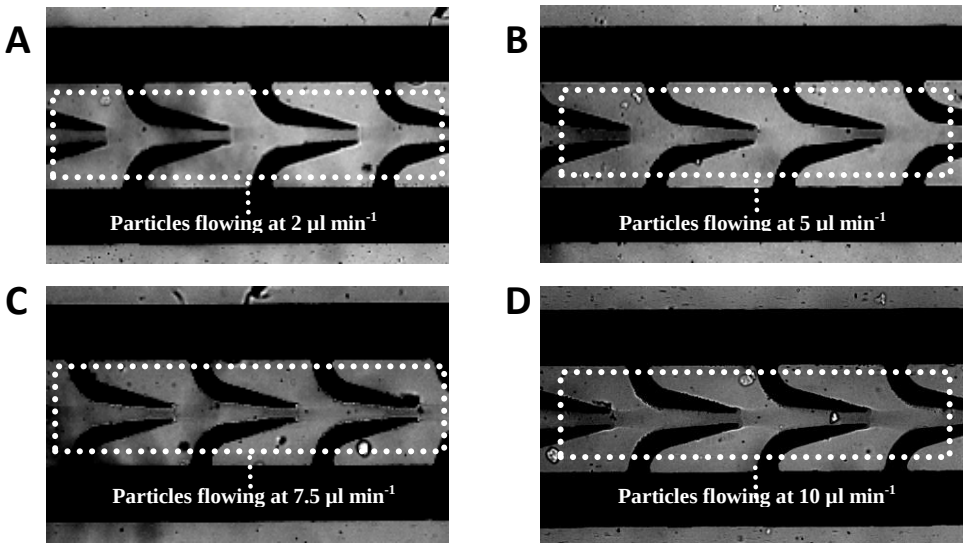

Figure 4.8: DEP manipulation of 230 nm particles at constant AC voltage of 15 V_p, frequency of 1 MHz and different flow rates of: (A) 2 µl min^{-1} (B) 5 µl min^{-1} (C) 7.5 µl min^{-1} (D) 10 µl min^{-1}.

4.4.1.3 Effect of voltage variation

Next, the author simulated the effects of varying AC voltage applied on the DEP patterns, while frequency and flow rate were kept constant. The amplitude of the AC voltage was increased from 5 to 15 V_p at a constant 1 MHz frequency and flow rate of 10 µl min^{-1} (Figure 4.9). It was observed that the core thickness increased from 15 µm to ~ 20 µm (± 4 µm) when the voltage was increased from 5 to 10 V_p. The change occurred due to the increased DEP force acting on particles dispersed throughout the channel, pushing them to the center and forming a thicker particle stream. However, after 10 V_p, the narrow band deviated from having smooth surfaces and a periodic variation in its pattern was observed.

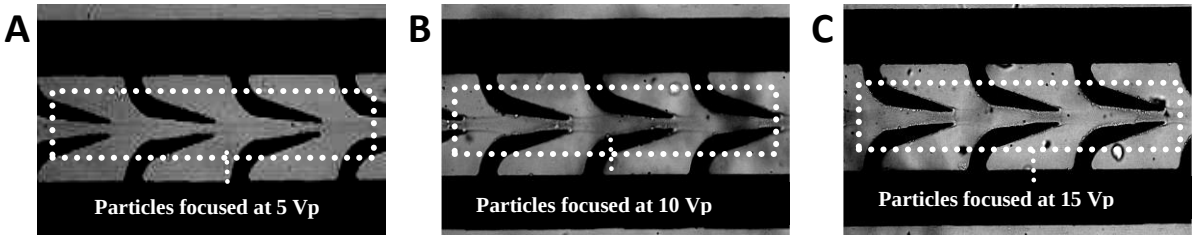

Figure 4.9: DEP of 230 nm particles at constant 10 µl min^{-1} flow rate and frequency of 1 MHz. The magnitude of AC voltage changed to: (A) 5 V_p (B) 10 V_p (C) 15 V_p.

4.4.2 450 nm SiO_2 particles

4.4.2.1 Effect of frequency variation

The effect of frequency change at a constant flow rate of 10 µl min^{-1} and the AC voltage of 15 V_p is shown in Figure 4.10. The 450 nm particles have larger masses and require stronger applied potential to disperse and repel themselves from the region between the microelectrodes as gravitational and inertial forces dominate their movements more than the 230 nm particle case. At frequencies of 100 and 500 kHz, the particles were densely trapped between the microelectrodes. As the frequency was increased above 1 MHz, a smooth narrowband was observed at the center of the microfluidic channel.

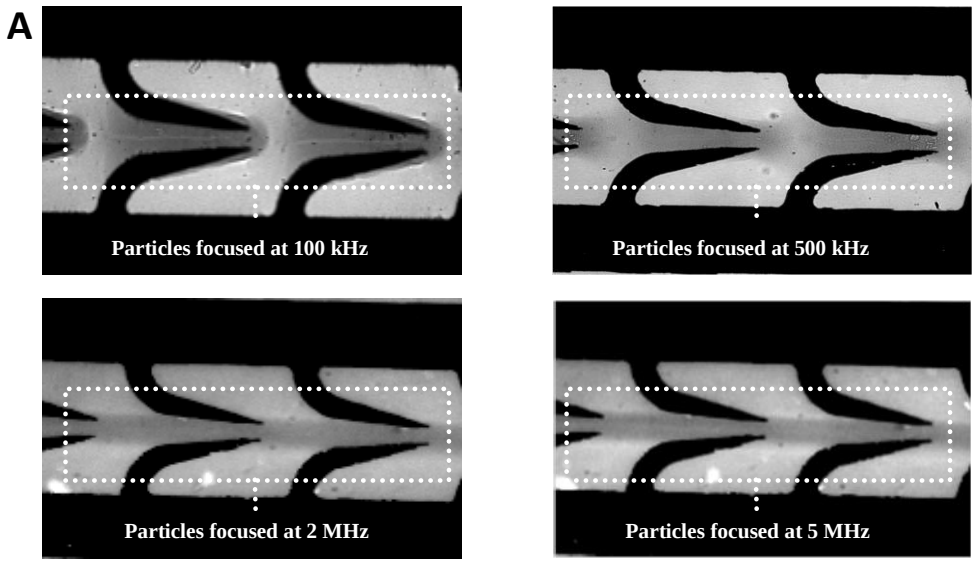

Figure 4.10: Effect of DEP force on 450 nm particles at constant 10 µl min^{-1} flow rate, AC voltage of 15 V_p and frequencies: (A) 100 kHz (B) 500 kHz (C) 2 MHz (D) 5 MHz.

4.4.2.2 Effect of flow rate variation

Changing the flow rate of the system with 450 nm particles resulted in a change of the core thickness of the liquid waveguide, similar to the 230 nm case. The example of the formation of the narrowband is shown in Figure 4.11 for the case of the applied frequency of 1 MHz and voltage of 15 V_p. Dissimilar to the 230 nm case, the higher flow rate did not increase the thickness of the center band. However, it appears that at higher flow rates, the center band gradually split into more than one band.

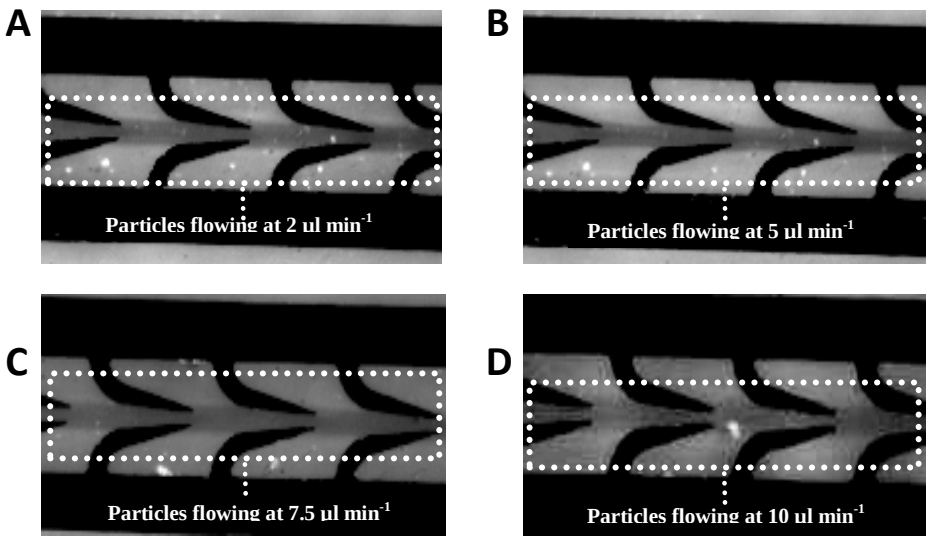

Figure 4.11: Effect of flow rate change on 450 nm particles at constant frequency of 1 MHz, AC voltage of 15 V_p and flow rates: (A) 2 µl min^{-1} (B) 5 µl min^{-1} (C) 7.5 µl min^{-1} (D) 10 µl min^{-1}.

4.4.2.3 Effect of voltage variation

For the 450 nm particles, increasing the AC voltage from 5 to 15 V_p increased the thickness of the center band. An example, which is presented in Figure 4.12, shows the effect of the change of the voltage at the constant applied frequency of 500 kHz and flow rate of 10 µl min^{-1}. At the low voltage of 5 V_p, two extra small bands were also observed near the central band of less than 10 µm thickness. It seems that increasing the voltage increases the band thickness. The thickness of the band increased from 10 µm (± 2 µm) at 5 V_p to 25 µm (± 5 µm) at 10 V_p and finally reached 30 µm (± 6 µm) at 15 V_p.

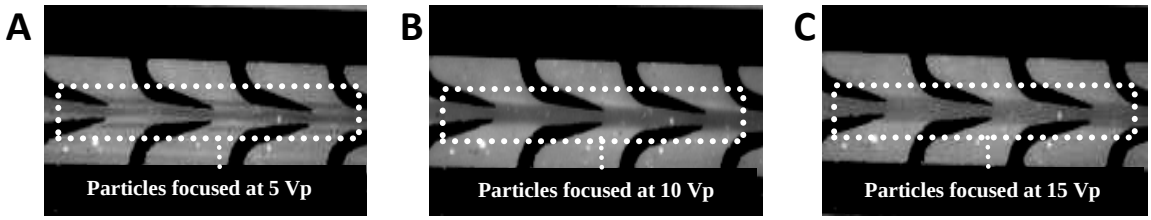

Figure 4.12: Effect of voltage variation on 450 nm SiO_2 particles at constant flow rate of 10µl min^{-1}, frequency of 500 kHz and AC voltage of: (A) 5 V_p (B) 10 V_p (C) 15 V_p.

4.4.3 Optical waveguiding response

For the next set of experiments, the author coupled a laser source to the microfluidic channel via the fiber recess (described in section 3.3) in the PDMS using a multimode optical fiber. The optical profiles at the output were investigated using the two particle sizes at DEP voltages and frequencies that were found to densely focus the particles in the center of the microchannel (Figure 4.13). The light was subject to coupling and interfacial losses as well as coherent surface interferences. However, the observed images provided strong evidence that DEP forces can and do change optical waveguiding properties. Figure 4.13A and 4.13C show the output of the waveguide without DEP forces for 230 and 450 nm particles, respectively, when no AC voltage applied. The flow rate was set in a range from 5 to 10 µl min^{-1}. The scattered light appears to be well dispersed in the channel indicating that the particles were homogenously dispersed. The output optical profile without the applied DEP force was fairly rectangular shaped, resembling the geometry of the output of the microfluidic channel.

By applying the AC signal and increasing the voltage to 15 V_p, waveguiding (for 230 nm particles) and scattering (for 450 nm particles) phenomena were observed. At these flow rates and the AC voltage of 15 V_p, the 230 nm SiO_2 particles appeared to show waveguiding properties for frequencies in the range of 500 kHz to 2 MHz. The optical beam was concentrated to the center of the output window (Figure 4.13B). However, at the same flow rates, the behavior of the system with 450 nm particles was quite different. It appeared that no light could pass through the center of the microfluidic channel (Figure 4.13D). The profile appeared separated in the center by a shadow, which formed a region of low intensity

light. The phenomenon was well observed for frequencies above 1 MHz. Although the particles were focused at the center, this narrowband seems to block the passage of the applied light completely. At low flow rates, the assembly of particles did not resemble a smooth waveguide but instead produced an array of particle barricades near the microelectrode tips that scattered the applied light.

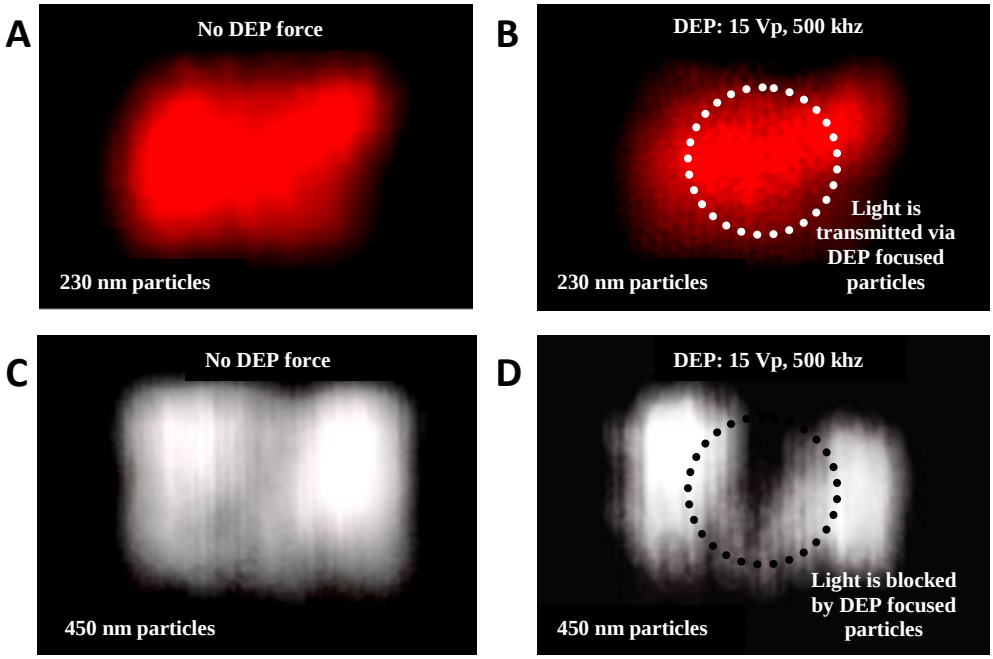

Figure 4.13: 635 nm laser output observed for the SiO_2 particles at 10 µl min^{-1} for the: (A) 230 nm particles with zero DEP force and (B) DEP voltage of 15 V_p and frequency of 500 kHz; (D) 450 nm with zero DEP force and (B) DEP voltage of 15 V_p and frequency of 500 kHz.

At the applied conditions for both 230 and 450 nm cases, when the AC voltage was increased, the DEP force focused the particles, forming a dense particle stream in the centerline. Figure 4.14 shows an illustration of how the laser light was scattered or guided as a function of the particles' separations and dimensions.

The Lorenz-Mie scattering theory [15, 16] indicates how light scatters as a function of particle diameter and at different wavelengths of incident light. Scattering is stronger at lower wavelengths and is proportional to the diameters of particles. Considering the laser source, λ = 635 nm (red light) used in these experiments, the scattering efficiencies of light

(http://omlc.ogi.edu/calc/mie_calc.html) are 0.043 and 0.185 for 230 and 450 nm particles, respectively, indicating that the 450 nm particles scatters light 4.3 times more than the 230 nm ones. Figures 4.14A and 4.14B show schematics of wave scattering and guiding for 450 and 230 nm particles, respectively. The center of the channel acts as the core of the optical waveguide while the adjacent streams are the cladding bearing a lower concentration of particles, therefore a lower refractive index. It is obvious from the results observed that the optical profile of the waveguide formed using the 230 nm SiO_2 particles were multi mode. This is because the dimensions of the dense particle streams were found to be in the range of 15 - 30 μm (± 6 μm), which in the case of a dielectric waveguide propagates multi mode based on the refractive indices of water and SiO_2 [17].

When the particles were tightly packed, the effective volumes in between the particles consisting of DI water were the cause of scattering rather than the particles themselves. For the 230 nm, this volume was approximately comparable and as effective as spherical particles with approximate diameters of 120 nm (Figure 4.14C). However for the 450 nm particles, this virtual sphere had an approximate diameter of 235 nm (Figure 4.14D). Therefore, when the 450 nm particles were focused by the DEP force, the particles were in close contact such that their center to center separation was larger than a quarter of a wavelength, causing the light to be strongly diffracted around these particles and thus strong scattering was observed. However, when the 230 nm particles were focused by the DEP force and they were in direct contact, their center to center separations were slightly less than a quarter of the wavelength (in the media). Thus, the particle aggregate appeared as a coarse homogenous material and hence transmission through the particles was possible. This approximation explains why 635 nm laser light was guided by the 230 nm particle but was conversely scattered by the 450 nm particles.

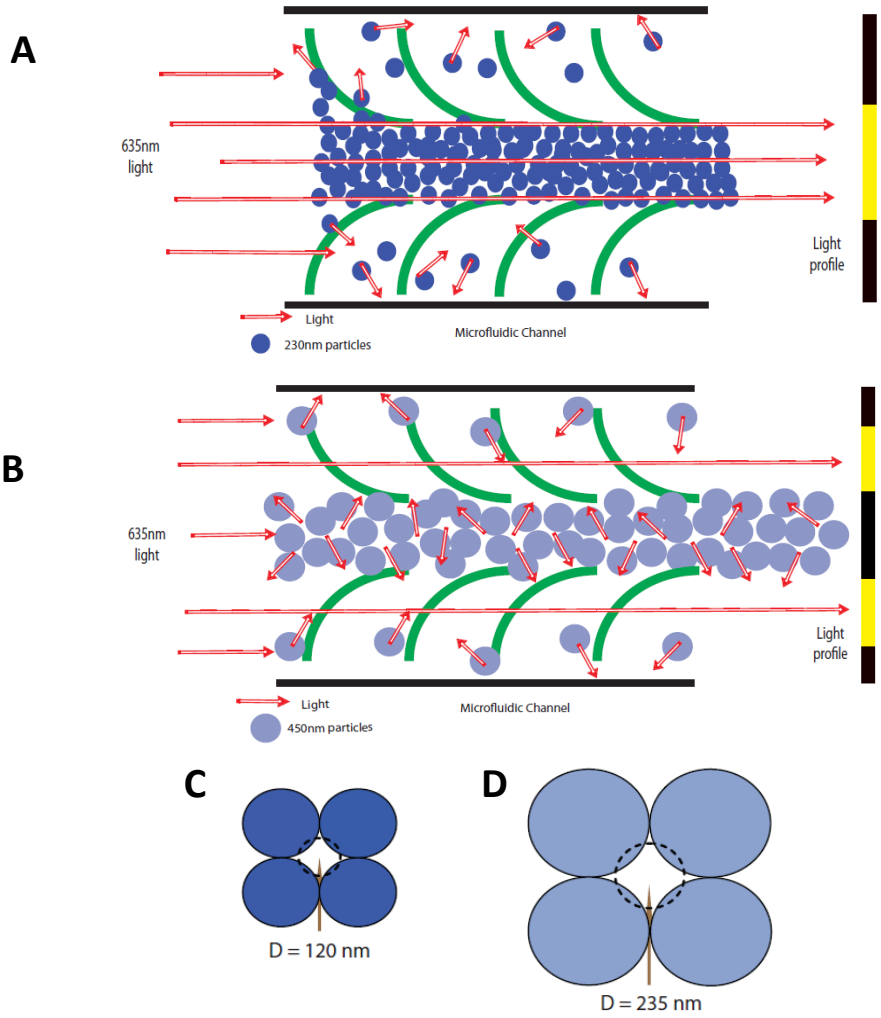

Figure 4.14: Scattering and waveguiding as a result of the DEP concentration of: (A) 230 nm and (B) 450 nm SiO_2 particles (C) Center to center separation for the closely packed 230 nm and (D) 450 nm SiO_2 particles.

4.5 Summary

Using Platform 1, the author demonstrated the feasibility of integrating particles into a microfluidic system and using DEP forces to manipulate these particles in order to create a tuneable waveguide in the microfluidics. The author showed that particles can be readily manipulated to form either optical waveguiding or scattering channels depending on their dimensions.

The author noted that when the 450 nm SiO_2 particles were closely packed and in intimate contacts with each other, their center to center separations were larger compared to the wavelength such that light diffracted strongly around the particles resulting in strong scattering. Conversely, when the 230 nm SiO_2 particles were closely packed, their center to center separations were smaller compared to the wavelength thus the densely packed particles appeared as an almost homogenous material, which promoted the transmission of light. The outcomes of this chapter were presented in an article that was published in the Journal of Electrophoresis [18].

One of the problems faced by the author associated with these experiments was the scattering caused by the particles that were focused aggregating in the vicinity of the microfluidic inlet and outlet reservoirs. Additionally, the flow of packed particles in and out of the microfluidic channel, due do the structure of the microfluidic system and the surface in the regions between the PDMS, air and liquid media caused deflections of the optical beam.

In order to address these issues and to enhance the performance of the system, the author devised Platform 2 (as presented in chapter 3). Platform 2 consists of a multimode polymeric waveguide integrated within the microfluidics and incorporates the DEP microelectrodes for particle motion control. Using Platform 2, light can be coupled into the densely concentrated particles via the polymeric waveguide, hence addressing the problems associated with scattering due to the non-focused particles and the interferences from the undesired elements caused by the direct coupling of light. In the next chapter, the author will introduce the concept of using dielectrophoretically focused particles to couple light from the multimode polymeric waveguide.

References

[1] Whitesides, G.M., The origins and the future of microfluidics. *Nature*, vol. 442, pp. 368-373, 2006.

[2] Schmidt, H. and A.R. Hawkins, Optofluidic waveguides: I. Concepts and implementations. *Microfluid Nanofluid*, vol. 4, pp. 3-16, 2008.

[3] Okamoto, K., *Fundamentals of optical waveguides* 2nd ed. 2006, Boston: Elsevier.

[4] Hong, J., J.S. Choi, G. Han, J.K. Kang, C.M. Kim, T.S. Kim, and D.S. Yoon, A Mach-Zehnder interferometer based on silicon oxides for biosensor applications. *Analytica Chimica Acta*, vol. 573, pp. 97-103, 2006.

[5] Guha, A., *Transport and deposition of particles in turbulent and laminar flow*, in *Annual Review of Fluid Mechanics*. 2008. p. 311-341.

[6] Ateya, D.A., J.S. Erickson, P.B. Howell, L.R. Hilliard, J.P. Golden, and F. Ligler, The good, the bad and the tiny: a review of microflow cytometry. *Anal Bioanal Chem*, vol. 391, pp. 1485-1498, 2008.

[7] Zhang, C., K. Khoshmanesh, F.J. Tovar-Lopez, A. Mitchell, W. Wlodarski, and K. Klantar-zadeh, Dielectrophoretic separation of carbon nanotubes and polystyrene microparticles. *Microfluid and Nanofluid*, vol. 7, pp. 633-645, 2009.

[8] Gaiduk, V.I. and D.S.F. Crothers, Basic molecular mechanisms underlying complex permittivity of water and ice. *Journal of Physical Chemistry A*, vol. 110, pp. 9361-9369, 2006.

[9] Cui, L., D. Holmes, and H. Morgan, The dielectrophoretic levitation and separation of latex beads in microchips. *Electrophoresis*, vol. 22, pp. 3893-3901, 2001.

[10] Durr, M., J. Kentsch, T. Muller, T. Schnelle, and M. Stelzle, Microdevices for manipulation and accumulation of micro- and nanoparticles by dielectrophoresis. *Electrophoresis*, vol. 24, pp. 722-731, 2003.

[11] Shimura, N. and M. Ogawa, Preparation of surfactant templated nanoporous silica spherical particles by the Stober Method. Effect of solvent composition on the particle size. *Journal of Material Science*, vol. 42, pp. 5299-5306, 2007.

[12] Stober, W., A. Fink, and E. Bohn, Controlled growth of monodisperse silica spheres in micron size range. *Journal of Colloid and Interface Science*, vol. 26, pp. 62-69, 1968.

[13] Khoshmanesh, K., C. Zhang, F.J. Tovar-Lopez, S. Nahavandi, S. Baratchi, K. Kalantar-zadeh, and A. Mitchell, Dielectrophoretic manipulation and separation of microparticles using curved microelectrodes. *Electrophoresis*, vol. 30, pp. 3707-3717, 2009.

[14] Wilson, H.J., L.A. Pietraszewski, and R.H. Davis, Aggregation of charged particles under electrophoresis or gravity at arbitrary Peclet numbers. Journal of Colloid and Interface Science, vol. 221 pp. 87-103, 2000.

[15] Bohren, C., F., Huffman, D., R., *Absorption and Scattering of Light by Small Particles* 1983: John Wiley and Sons.

[16] Conroy, R., S. , B. Mayers, T., D. Vezenov, V., D. Wolfe, B., M. Prentisst, and M. Whitesides G., Optical Waveguiding in Suspensions of Dielectric Particles. *Applied Optics*, vol. 44, pp. 7853-7857, 2005.

[17] Kapany, N.S. and J.J. Burke, *Optical Waveguides*. 1972, New York: Academic Press.

[18] Kayani, A., C. Zhang, K. Khoshmanesh, J.L. Campbell, A. Mitchell, and K. Kalantar-zadeh, Novel tuneable optical elements based on nanoparticle suspensions in microfluidics. *Electrophoresis*, vol. 31, pp. 1071-1079, 2010.

Chapter 5

Coupling of Light from a Multi Mode Waveguide into Dielectrophoretically Focused Particles

5.1 Introduction

In chapter 4, the author demonstrated the focusing of mesoparticles within microfluidic systems using a combination of dielectrophoretic (DEP) and hydrodynamic forces, which produced areas of concentrated particles with intimate contacts between them [1, 2]. The DEP force was used to concentrate the particles at the center of the microfluidic channel where a light source (635 nm) was directed through the focused particles. The author established that DEP concentrated particles induced the formation of a media of significantly different refractive index compared to the surrounding liquid within the microchannel [1, 2].

However, the author found it difficult to interface light from an optical source accurately. The coupled light was passed through interfaces and materials of varying refractive indices in the vicinity of the microfluidic reservoirs, causing significant deflection of the optical signal [1]. This deflection made it difficult to observe precisely the behavior of the optical beam.

In response to the issues, the author devised a solution, which forms the second stage of his PhD research project. The author addressed these issues by utilizing a waveguide platform that could guide light and used the interaction of light with the DEP focused particles as a means to couple light into the focused particles more efficiently. The platform was known as "Platform 2" in chapter 3 and consists of a multi mode polymeric waveguide fabricated using SU-8 and KMPR epoxies as the core and lower cladding layers, respectively. Above the core was a microfluidic channel which was filled with suspended particles. The author utilized the curved DEP microelectrodes in order to manipulate the motion and location of the particles while under liquid flow. The electrodes were patterned at the base of the microfluidic channel, which enabled the concentration of suspended particles in close vicinity to the multi mode polymeric waveguide.

In this chapter, silicon dioxide (SiO_2) and tungsten trioxide (WO_3) particle suspensions will be investigated. These particles were selected as they are easily dispersed in a microfluidic channel, their positions and motion can be easily manipulated using the DEP force and they possess refractive indices that are intrinsically lower (SiO_2) or higher (WO_3) than the polymeric waveguide. The author will demonstrate that the transmission of light (635 nm) through the polymeric waveguide can be altered significantly as a result of the DEP concentration of particles. The system is comprehensively investigated at different DEP applied signal frequencies to observe the transmission properties of the optical waveguide under different particle assembly conditions.

5.2 Principles

In this chapter, the author uses crude theoretical calculations to assess the type of materials and concentrations required to allow the coupling of light from the polymeric waveguide into the packed regions of particles.

The side and cross sectional view of the system and the depiction of its operation are presented in Figure 5.1. The minimum possible refractive index is achieved when the particles are entirely repelled from the region of interest (Figures 5.1A and 5.1B). In this case, the refractive index will be that of the suspending liquid. Given that both types of particles used in this experiment have a refractive index higher than that of the suspending liquid, the maximum refractive index is achieved when the particles are concentrated to the densest packing possible (Figures 5.1C and 5.1D). If it is assumed that identically sized spherical particles occupy a hexagonal closely packed lattice, then according to the Keppler conjecture, the material will be 74 % suspended particles and 26 % suspending fluid [3].

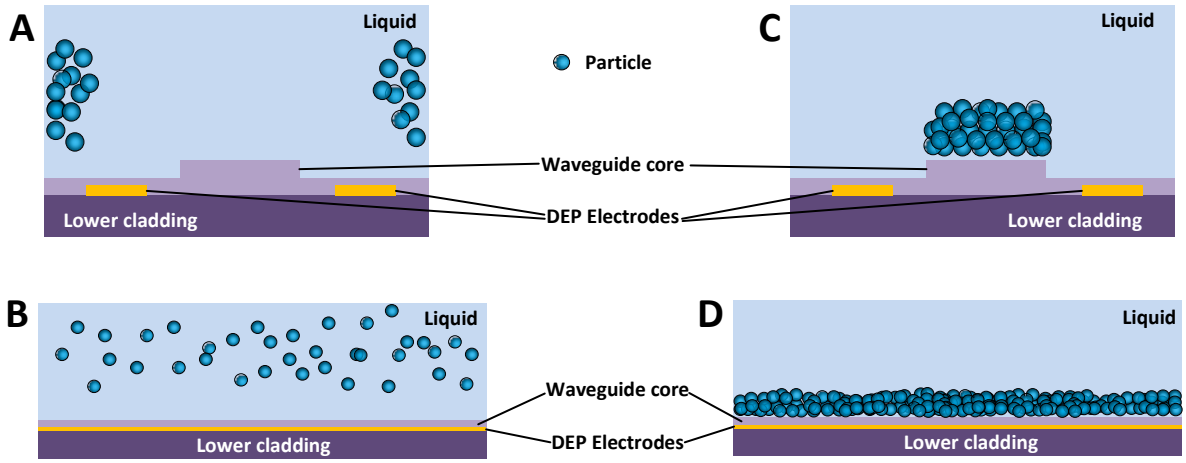

Figure 5.1: Schematic view of the system: (A) Cross sectional view and (B) side view of particles being repelled from the region close to the multi mode waveguide forming a media of minimum refractive index at the region of interest; (C) Cross sectional and (D) side view of particles being densely packed close to the multi mode waveguide forming a media of maximum refractive index at the region of interest.

If the suspending liquid in these experiments is DI water and the suspended particles are either SiO_2 or WO_3, and the operating wavelength of $\lambda = 635$ nm is assumed, then the refractive indices of these materials are $n_{DI\text{-}water} = 1.33$, $n_{SiO2} = 1.47$ and $n_{WO3} = 2.3$, and the range of refractive indices that can be achieved by tuning the concentrations of particles using the DEP forces are:

$$SiO_2: \; n_{min} = 1.33; \; n_{max} = 0.74n_{SiO2} + 0.26n_{DI} = 1.43 \tag{5.1}$$

$$WO_3: \; n_{min} = 1.33; \; n_{max} = 0.74n_{WO3} + 0.26n_{DI} = 2.04 \tag{5.2}$$

When using the SiO_2 particles, while it is possible to significantly alter the refractive index of the liquid through DEP particle manipulation, it is not possible even with ideal packing density to increase the refractive index of the media to the range of effective refractive indices (n_{eff}) of the polymer waveguide ($1.566 < n_{eff} < 1.592$). Thus attempting to manipulate the optical properties of the multi mode polymer waveguide using DEP concentrated SiO_2 particles should have little effect. Conversely, WO_3 particles can, in theory, achieve a staggeringly broad range of effective indices, with a theoretical maximum index of 2.04, well in excess of the effective refractive index of the polymer waveguide. Thus, even if a fraction of the theoretical maximum packing density is achieved, it is possible to adjust the cladding index through DEP concentration of the WO_3 particles such that the cladding significantly impacts the optical properties of the adjacent polymer waveguide with dramatic impact on the measured optical transmission.

5.3 Methods and Simulations

In this chapter, the author used visible light (λ = 635 nm) as the excitation source since it propagates with low loss through the material of the polymeric waveguide [4]. The waveguide core and cladding of Platform 2 was composed of curable photoresists known as SU-8 (Microchem) and KMPR (Microchem), respectively. Details of the platform structure were discussed in section 3.5.2 of chapter 3.

To obtain the greatest effect, the author aligned the DEP microelectrodes such that the optical waveguide was positioned between the gaps of the curved microelectrodes where the DEP force was the strongest. SiO_2 and WO_3 particles with diameters of 450 nm

(5 % weight-in-weight (*w/w*), SiO_2, Microspheres – Nanospheres) and 80 nm (6 % *w/w*, WO_3, Sigma Aldrich) were studied, respectively. The author chose the larger 450 nm SiO_2 particles because it was thought that viewing the larger SiO_2 particles would be easier compared to the case of the 230 nm SiO_2 particles. In particular, the present platform has a silicon substrate which is dark and thus viewing SiO_2 particles (which had a white color consistency in its suspension form) against a dark substrate was thought to be difficult. On the other hand, the WO_3 particles (in suspension form) although being much smaller (Ø80 nm) were darker in color and the author found viewing them using a microscope was not an issue. Additionally, the range of frequencies in the spectrum of the Claussius-Mossoti factor (Re[$f_{CM}(\omega)$]) for the WO_3 particles is much larger and hence the author expected that using this particle would provide the flexibility of tuning the DEP frequency over a wide range to achieve the desired particle concentration in the fluidics..

Samples of the particle suspensions were placed on glass slides and dehydrated. The samples were then viewed using an FEI Nova scanning electron microscope (SEM). The SEM image of the WO_3 particles is presented in Figure 5.2. The SEM image of the 450 nm SiO_2 particles was already presented in Figure 4.3 of chapter 4.

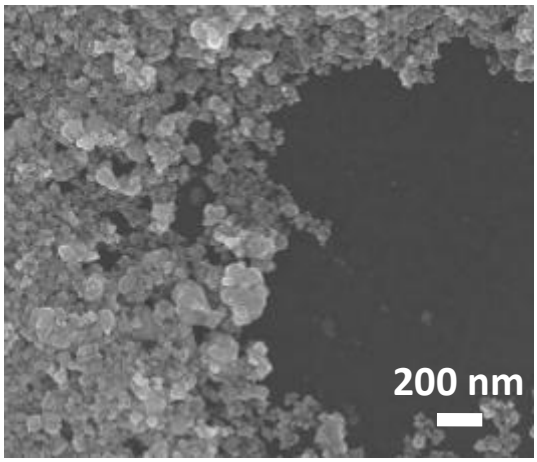

Figure 5.2: SEM image of the 80 nm diameter WO_3 particles.

Subsequently, the real value of the Re[$f_{CM}(\omega)$] was calculated for the WO_3 particles. The calculations of the Re[$f_{CM}(\omega)$] for the 450 nm diameter SiO_2 has been presented in section 4.2 of chapter 4, but is included in Figure 5.3 as a reference. The calculations were based on the relative permittivity and conductivity values of the suspending medium (DI water) taken

as ε_m = 77.6 and σ_m = 0.2 mS m^{-1} [5, 6]. The WO_3 particles have relative permittivities and conductivities of $\varepsilon_{p(WO_3)}$ = 80 and $\sigma_{p(WO_3)}$ = 100 mS m^{-1}, respectively [1, 7-10]. From Figure 5.2, it is evident that the WO_3 both particles should transition from positive to negative DEP behavior for the spectral range of 100 kHz < f < 1 GHz, while the cross-over frequencies for SiO_2 and WO_3 based on simulation occurred at 1 MHz and 24 MHz, respectively. This calculation suggests that it should be possible to use the curved microelectrode structure to densely concentrate both SiO_2 (at frequencies less than 1 MHz) and WO_3 (at frequencies less than 24 MHz) particles in the area between microelectrodes.

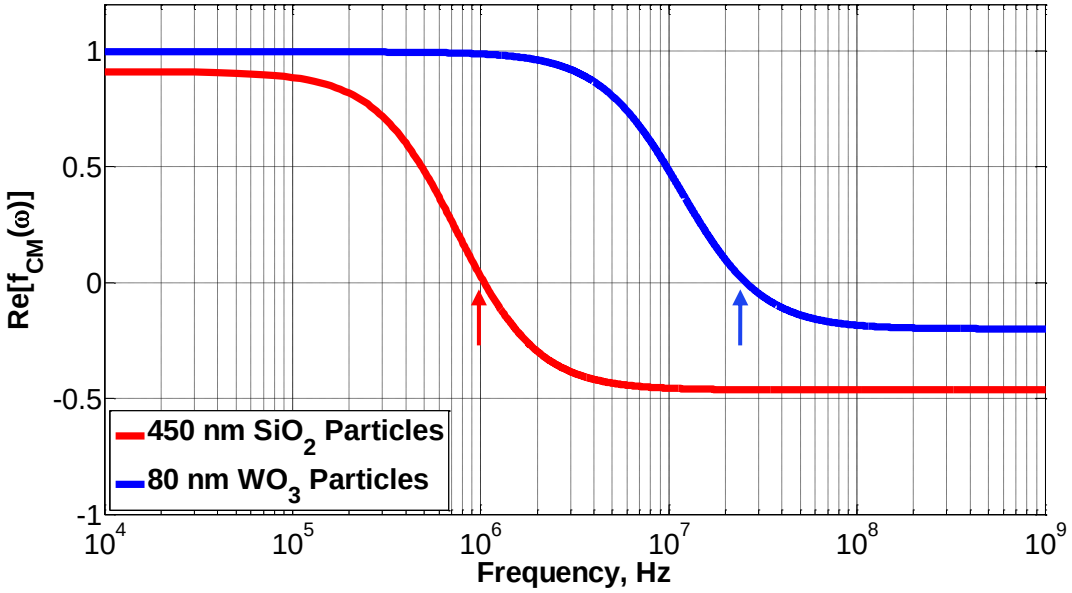

Figure 5.3: DEP spectrum for WO_3 and SiO_2 particles, the crossover frequencies are shown by the vectors.

The curved DEP microelectrode was used as it was established capable of producing evenly distributed electric field gradients which resulted in the formation of dense particle narrowbands along the center of the microfluidic channel [1, 2]. The DEP microelectrode array in Platform 2 was actually embedded between the SU-8 and KMPR layers as described in section 3.5.2 of chapter 3. This was because it was thought that placing the electrodes beneath the waveguide core layer would generate an electric field gradient capable of trapping and bring the particles as close as possible to the surface of the waveguide. Also, since initially the design of the multi mode polymeric waveguide was raised rib, it was expected that concentrating the particles close to the surface would actually engulf the raised

rib with the particles hence maximizing the interaction of light in the waveguide with the particles.

The simulations of the electric field gradients that follow are based on this DEP microelectrode configuration. The simulations were conducted with the help Dr Khashayar Khoshmanesh, from the School of Electrical and Computer Engineering, RMIT University using the method that was described in section 4.3 of chapter 4. In order to comprehend the performance of the device, the DEP field generated by the curved microelectrodes in Platform 2 was simulated using the Fluent 6.2 software package (Fluent Inc, Lebanon, USA). Applying an AC signal of 15 V_p, the electric field reached a peak value of 1.6×10^6 V m^{-1} at the tip of microelectrodes, Figure 5.4A. The *x*, *y* and *z* axes reference lines shown in the bottom left of Figures 5.4A, 5.4B and 5.4C denote the three dimensional reference lines used while simulating the DEP fields. The *z*-axis for all three figures starts from the polymer surface.

The spatial variation of the electric field induced a strong DEP force on the particles which could attract or repel them from the microelectrodes according to their polarization, as obtained from the DEP force equation (equation (2.10) of chapter 2) and depicted in Figure 5.4. The SiO_2 and WO_3 particles were attracted towards the microelectrodes at lower frequencies (Figure 5.4B), but were repelled from them at higher frequencies (Figure 5.4C). For example, at 500 kHz the SiO_2 particles were attracted towards the microelectrode tips by a maximum force of 8.54×10^{-14} N at z = 10 µm.

With the introduction of flow in the microfluidic channel moving in the positive *x*-direction, the particles should experience a hydrodynamic drag force that propels them along the center of the microchannel. Under a specific combination of DEP and drag forces achieved using an AC signal of 15 V_p, a frequency of 500 kHz and a flow rate of 4 µl min^{-1} (corresponding to an average velocity of 1.33 mm s^{-1}), the particles were focused along the microchannel centerline and marched above the waveguide rib (Figure 5.4B). This flow rate was selected based on the requirement to achieve a dense stream of particles in the center of the microfluidic channel. It should be noted that the magnitude of force was normalized as $F_{DEP}.(r^3\times\mathrm{Re}[f_{CM}(\omega)])^{-1}$ to make it independent from the radius of particles and the frequency of the applied field, and therefore can be used for both SiO_2 and WO_3 particles.

At 5 MHz the SiO_2 particles were repelled from the microelectrode tips by a maximum force of 8.14×10^{-14} N at z = 10 µm. The deflection of particles towards the sidewalls decreased under the effect of hydrodynamic drag force, but was enough to form a particle-free region around the waveguide rib (Figure 5.4C). The simulations of WO_3 particles were conducted under similar conditions, however, the frequency of the applied field was set to 800 kHz and 25 MHz to provide the appropriate combination of DEP and drag forces to position the particles at the desired locations along the microchannel. The magnitude of the normalized DEP force decreased substantially at higher heights along the microchannel, due to the weakening of the electric field (Figure 5.4D).

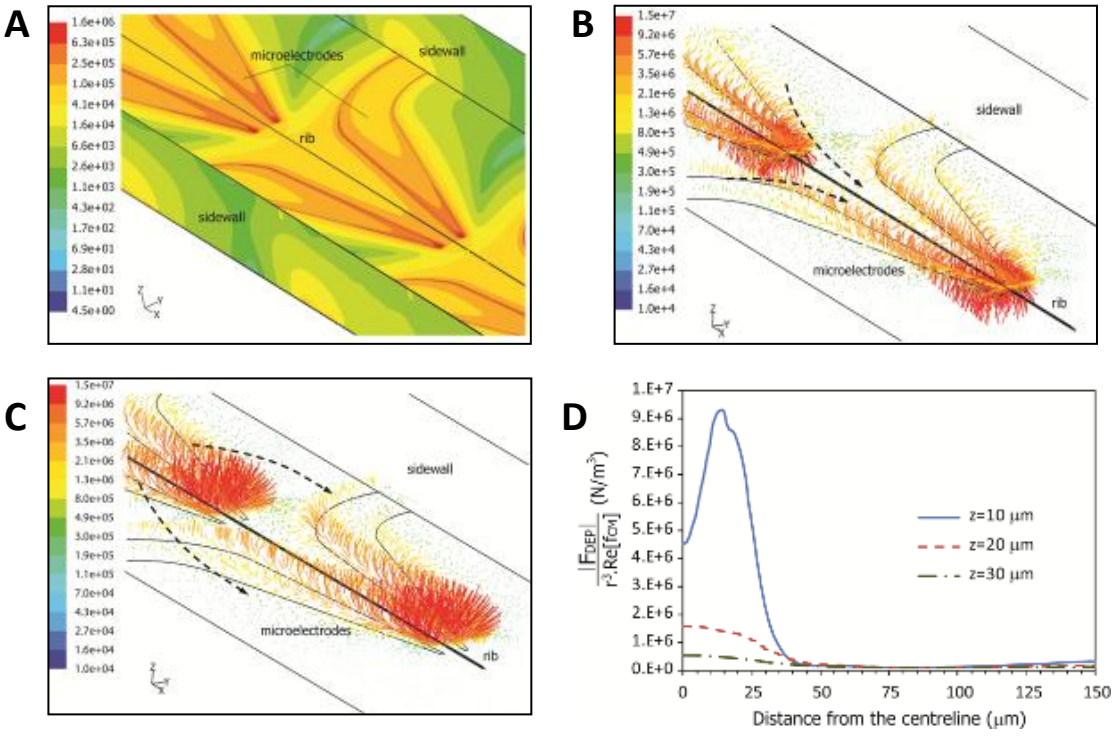

Figure 5.4: Simulation results at the cross-section of the microchannel: (A) Contours of electric field at the surface of SU-8 layer (V m^{-1}) (B) Vectors of the normalized positive DEP force F_{DEP} ($r^3\times\mathrm{Re}[f_{CM}(\omega)]$)$^{-1}$ (N m^{-3}) at z = 10 µm for both SiO_2 and WO_3 particles (C) Vectors of the normalized negative DEP force (N m^{-3}) at z = 10 µm (D) Variation of the magnitude of normalized DEP force (N m^{-3}) at different heights of the microchannel.

The details for the fabrication procedures for Platform 2 were presented in chapter 3. After the fabrication, the microfluidic channel was connected to a syringe pump (Harvard

Apparatus PHD 2000). The device was tested on an optical bench (Figures 5.5A and 5.5B) using a 635 nm Helium Neon laser (Model 105-1, Spectra Physics) which was lens-coupled to the polymer waveguide located between the DEP microelectrodes. The light exiting the optical waveguide was imaged onto an intensity mode profiler (Beamage CCD-12, Gentec EO). Each measurement was captured after 2 minutes of idle time to provide sufficient time to allow the samples to perfuse throughout the microchannel. Using the DEP force, particles were manipulated into forming a narrow band above the waveguide. The concentration of particles in this region can be adjusted by changing the frequency and the AC voltage amplitude applied to the microelectrodes (Rohde & Schwarz SMS signal generator with a frequency range of 0.1 to 250 MHz coupled to a home-made RF amplifier with a gain ~25 dB) and the flow rate of the suspending fluid drawn by the syringe pump.

In these experiments, the author kept the flow rate and the applied AC voltage magnitude constant at 4 μl min^{-1} and 15 V_p, respectively. This is because at such a low flow rate and high voltage amplitude, the suspended particles were able to respond to the applied DEP forces quite efficiently. On average, the author found that using these parameters, it took the suspended particles about 30 - 90 seconds to form dense concentrations of particles or to be completely repelled from the region between the microelectrodes. Higher flow rates and lower voltage amplitudes resulted in slower particle motions in response to the DEP field.

By adjusting the frequency to either attract or repel the particles, the refractive index of the media above the rib waveguide was tuned to: (i) a refractive index close to that of DI water (n = 1.33) using frequencies, above the particles' crossover frequency, to induce negative DEP force which repelled all particles to the sidewalls far from the optical waveguides, and (ii) theoretically a refractive index close to that of closely packed particles (~1.43 for SiO_2 and ~2.05 for WO_3) in DI water using frequencies, below the particles' crossover frequency, to induce positive DEP force, focusing the particles close to the optical waveguide. Before the experiments, isopropanol was flushed through the channel to remove surface contaminants from the microfluidic channel and the rib waveguide surface. This was followed by a mixture of 5 ml of DI water and 100 μl of Triton X-305 surfactant (Sigma Aldrich) which reduces the surface hydrophobicity of the waveguide/PDMS surface and to improve the homogenous distribution of the particles within the mixture.

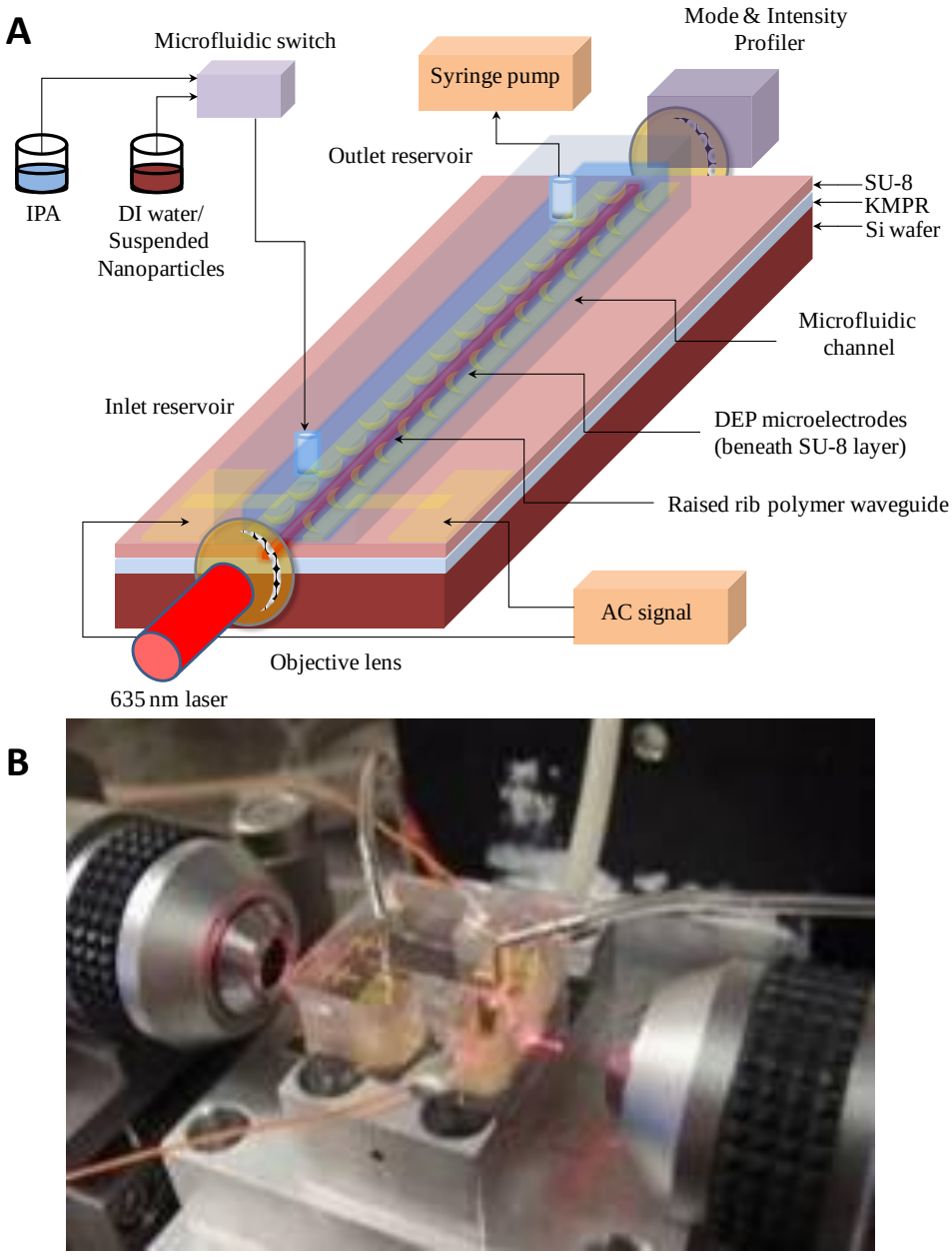

Figure 5.5: Experimental setup: (A) Schematic (B) Photograph.

5.4 Results and Discussions

To establish a baseline, the author conducted the experiments initially without activating the DEP electrodes. Platform 2 was tested with four samples as the top cladding including (i) air (treated as the reference), and an infiltration of (ii) DI water, (iii) suspended SiO_2 particles and (iv) suspended WO_3 particles.

The author then activated the DEP electrodes to analyze the optical response of the system in the presence of DEP focused particles. The particles were trapped and repelled from the vicinity of the rib waveguide by the application of different DEP frequencies as they were expected to induce opposing DEP conditions as obtained from the Re[$f_{CM}(\omega)$] spectral simulation in Figure 5.3.

5.4.1 Optical Response without DEP Force

First, the author observed the output optical intensity profile with an air-filled microfluidic channel (Figure 5.6A). This was treated as the reference measurement for subsequent analysis. Subsequently, output intensity profiles were captured while the microfluidic channel was infiltrated with DI water (Figure 5.6B), and then particle suspensions of SiO_2 (Figure 5.6C) and WO_3 (Figure 5.6D). Horizontal and vertical cross-hair markers were aligned to the peak intensity location of the reference for each output profile measurement. These intensity profile outlines, are presented in the bottom and left quadrants to indicate the intensity pattern as detected along the cross hairs (horizontal and vertical axis). In order to make a comparative analysis of the output intensity profiles obtained with different cladding materials, the author plotted two normalized intensity patterns along the horizontal (Figure 5.6E) and vertical (Figure 5.6F) axes.

With the DI water cladding, the peak intensity was attenuated to 92 % (± 1%) of the reference level. When the SiO_2 particle suspension was dispersed in the microchannel (without DEP force), the peak intensity remained at 92 % of the reference level. The refractive index increase of the liquid (n_{liq}) with the introduction of 5% *w/w* of SiO_2 can be calculated as $n_{liq} = 0.05 \times 1.47 + 0.95 \times 1.33 = 1.337$, which is much smaller than that of SU-8 waveguide ($n_{SU\text{-}8} = 1.592$). This evidence supports the author's prediction that the SiO_2 particles will have little effect on the optical waveguide properties.

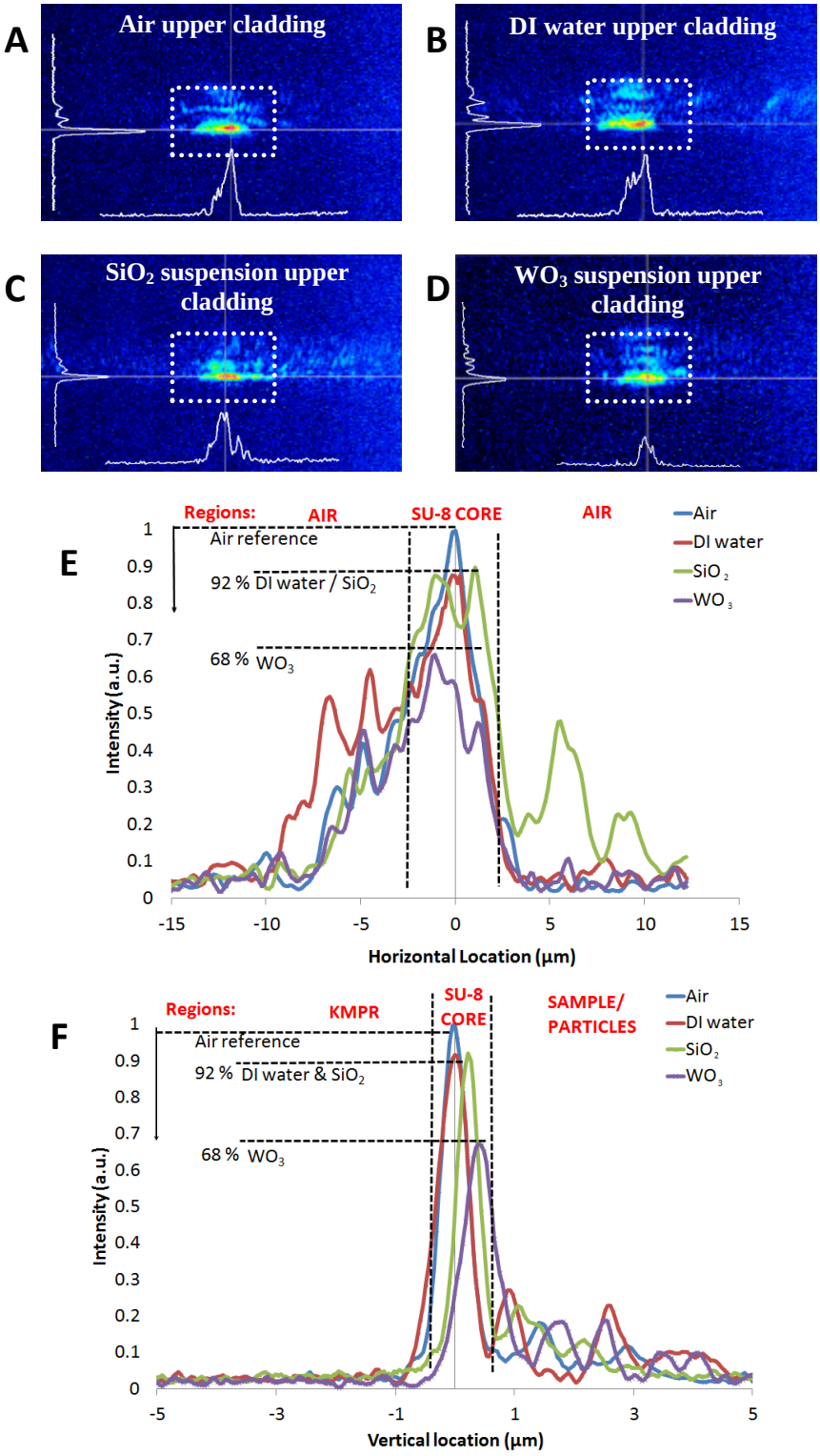

Figure 5.6: Mode profiles for: (A) Air (B) DI water (C) SiO_2 and (D) WO_3, cladding materials under 'no DEP force' and normalized intensity plots along (E) Horizontal and (F) Vertical cross-hair markers.

Alternatively, when the WO_3 particle suspension was dispersed in the microchannel (with no DEP force applied), the light intensity was reduced to 68 % (± 1%) of the reference level. In this case, the refractive index increase of the fluid with the introduction of 6% *w/w* of WO_3 was $n_{liq} \cong 1.39$, which was still far below the effective index range of the polymer waveguide. Therefore, it was unlikely that the refractive index increase, caused by the introduction of WO_3 alone, would significantly increase the evanescent interaction of the light with the fluid.

The refractive index contrast between the WO_3 and the surrounding DI water would be $\Delta n_1 = 2.3 - 1.33 = 0.97$, which is far greater than the index contrast of SiO_2 and DI water ($\Delta n_2 = 1.47 - 1.33 = 0.14$). The scattering caused by these particles would be proportional to this index contrast [11] and the inter particle spacing. It could thus be reasoned that the reduced transmission observed with WO_3 could be due to increased scattering loss from these high index particles.

Based on a particle density of 7.16 g ml^{-1} for WO_3 (Sigma Aldrich datasheet) and 2.4g ml^{-1} for SiO_2 (Microspheres-Nanospheres datasheet), the volume-in-volume (*v/v*) concentration of WO_3 and SiO_2 particles are approximately 0.8 % *v/v* and 2.1% *v/v*, respectively. These volume quantities are very low and hence do not have any significant effect on the DEP performance and conductivity of the media.

5.4.2 Optical Response with DEP Force

Next, an AC voltage was applied to the DEP microelectrodes to analyze the optical response of the system in the presence of DEP force. With SiO_2 particles, the microelectrodes were energized at different frequencies of 500 kHz and 5 MHz. These frequencies were selected as they were expected to induce opposing DEP conditions on the suspended SiO_2 particles. When the DEP electrodes were energized with an AC voltage of 15 V_p at 500 kHz, the SiO_2 particles were focused along the microchannel center and formed a dense narrow band adjacent to the waveguide rib (Figure 5.7A) in concurrence with the simulations.

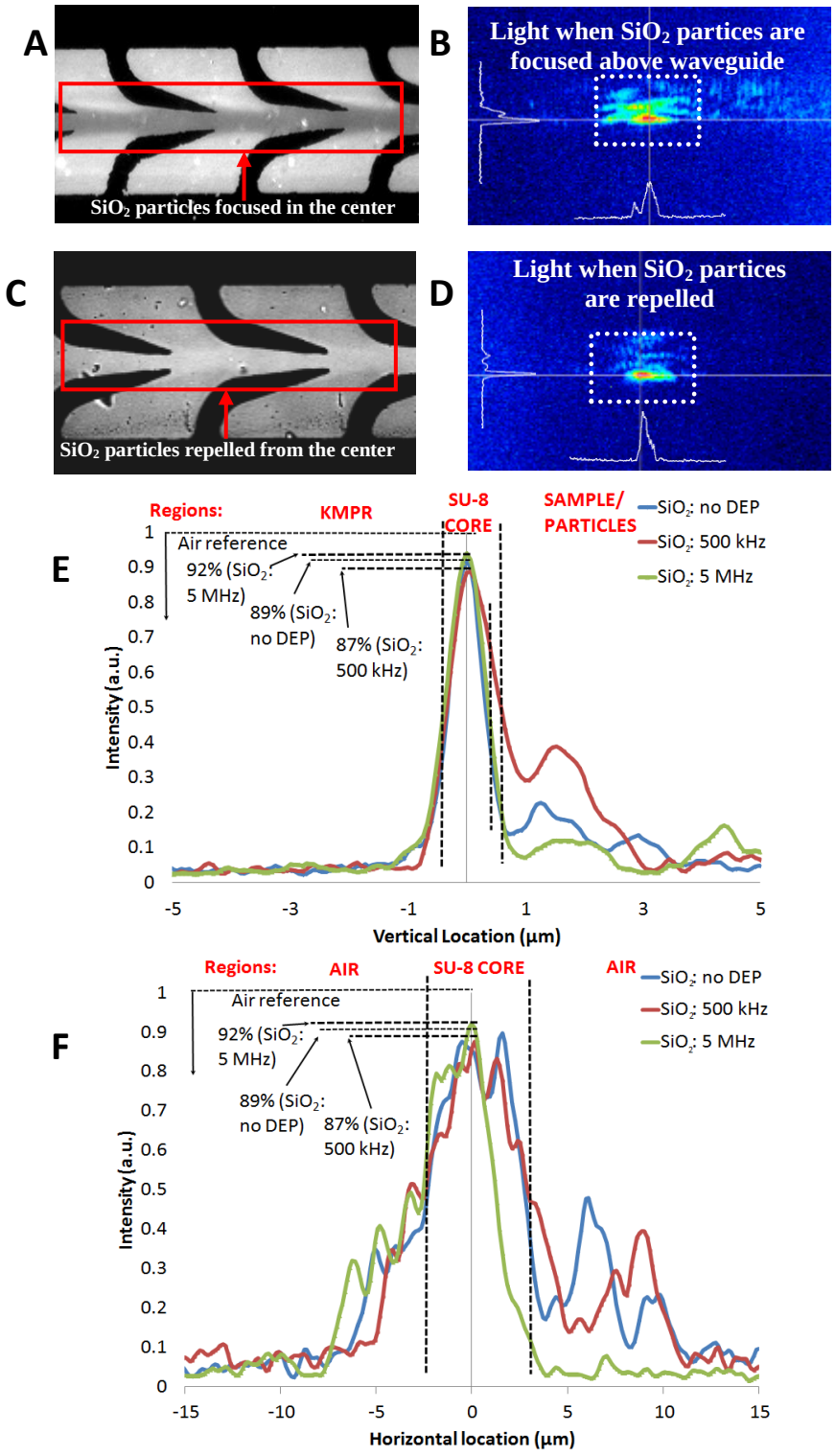

Figure 5.7: Optical response using the SiO_2 particles: (A) SiO_2 microscopic observation under positive DEP (B) Intensity profile for SiO_2 for DEP: 15 V_p and f = 500 kHz (C) SiO_2 microscopic observation under negative DEP (D) Intensity profile for SiO_2 DEP: 15 V_p and f = 5 MHz (E) Horizontal and (F) Vertical normalized intensity plots.

Microscopic observations indicated that the focused SiO_2 particles were moving at a height of 0 - 7.5 μm from the microchannel bottom surface adjacent to the rib. The focusing of particles was not disturbed by stochastic Brownian force, since the particles were not permanently trapped between the microelectrodes and instead were concentrated within a very short time (< 2 seconds) before being drifted by the hydrodynamic drag force. The associated optical intensity profile was captured (Figure 5.7B). Under the DEP focusing conditions for SiO_2, the optical intensity was attenuated to 87 % (± 2 %) of the reference level (Figures 5.7E and 5.7F).

This small attenuation was ascribed to the presence of a larger concentration of SiO_2 particles on the top of the rib-waveguide that marginally increases the scattering of the evanescent field above the waveguide. Apart from this marginal increase in attenuation, it is clear that the concentrated SiO_2 particles cannot significantly influence the properties of the polymer waveguide.

As the frequency was increased to 5 MHz with the same AC voltage amplitude, the SiO_2 particles were repelled from the center of the microchannel towards the sidewalls (Figure 5.7C). Conversely, when the particles were repelled from the waveguide surface (Figure 5.7D), the output intensity increased to 92 % (± 2 %) of the reference level, (Figures 5.7E and 5.7F) equivalent to the case with DI water as expected.

In the case of WO_3 particle suspension, the microelectrodes were energized at 15 V_p with selected frequencies of 800 kHz and 25 MHz which were expected to induce a DEP force that would concentrate and disperse these particles respectively. As expected, at 800 kHz, the WO_3 particles formed a narrow stream along the waveguide surface (Figure 5.8A). Similarly, the microscopic observations indicated that the focused WO_3 particles were moving at a height of 0 - 5 μm from the microchannel bottom surface. The corresponding intensity profile was captured (Figure 5.8B). From this image it can be seen that the output intensity was reduced dramatically to 19 % (± 2 %) of the reference intensity level (Figures 5.8E and 5.8F).

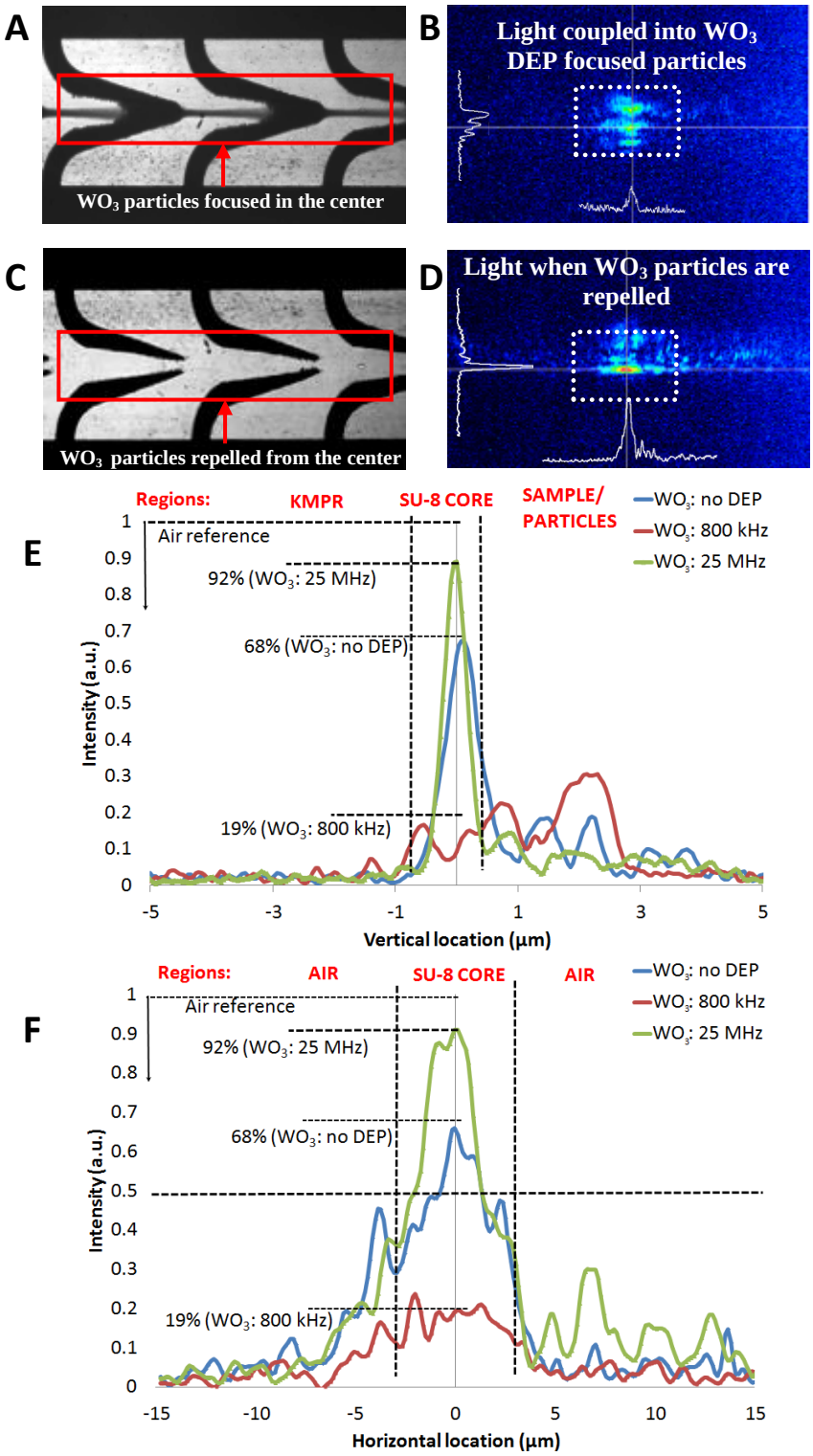

Figure 5.8: Optical response using the WO_3 particles: (A) WO_3 microscopic observation under positive DEP force (B) Intensity profile for WO_3 for DEP: 15 V_p and f = 800 kHz (C) WO_3 microscopic observation under negative DEP force (D) Intensity profile for WO_3 DEP: 15 V_p and f = 25 MHz (E) Horizontal and (F) Vertical normalized intensity plots.

This marked increase in attenuation cannot be attributed to a simple increase in the number of WO_3 particles present at the surface, rather it is anticipated that the average refractive index of the medium above the optical waveguide has increased to a value close to that of the SU-8 core and thus the guided wave has become significantly more evanescent and thus interacts more strongly with the suspended particles. Hence there is a significant increase in scattering loss. The fact that there is still some power measured at the output indicates that the refractive index of the concentrated WO_3 particles has not exceeded the core refractive index.

Conversely, as the same AC voltage amplitude with a DEP frequency of 25 MHz was applied, the WO_3 particles were repelled from the center of the microchannel (Figure 5.8C) leaving the evanescent region almost free from WO_3 particles. The corresponding optical intensity profile was captured (Figure 5.8D) and it was observed that the intensity increased to 92 % of the reference level, equivalent to that measured for DI water indicating that the WO_3 particles have been entirely removed from the surface of the waveguide.

Figure 5.9 presents a schematic that describes the system's operation. In order for light to be coupled into the DEP focused particles, the refractive index of the surrounding media must be higher than that of the SU-8 core, which is 1.592. Under the DEP focusing circumstances, this condition was met using highly packed WO_3 particles (Figure 5.9A), as discussed in section 5.2. The presence of such an effect, which is confirmed by the measurements, suggests that the DEP system can efficiently bring these particles into close affinity with each other as well as close proximity to the evanescent region of the polymeric waveguide. However, in the case of the SiO_2 particles (Figure 5.9B), light remains largely propagating in the polymeric waveguide with minimal intensity attenuation, as the average refractive index of the surrounding media composed of DEP focused SiO_2 particles cannot exceed that of the waveguide core.

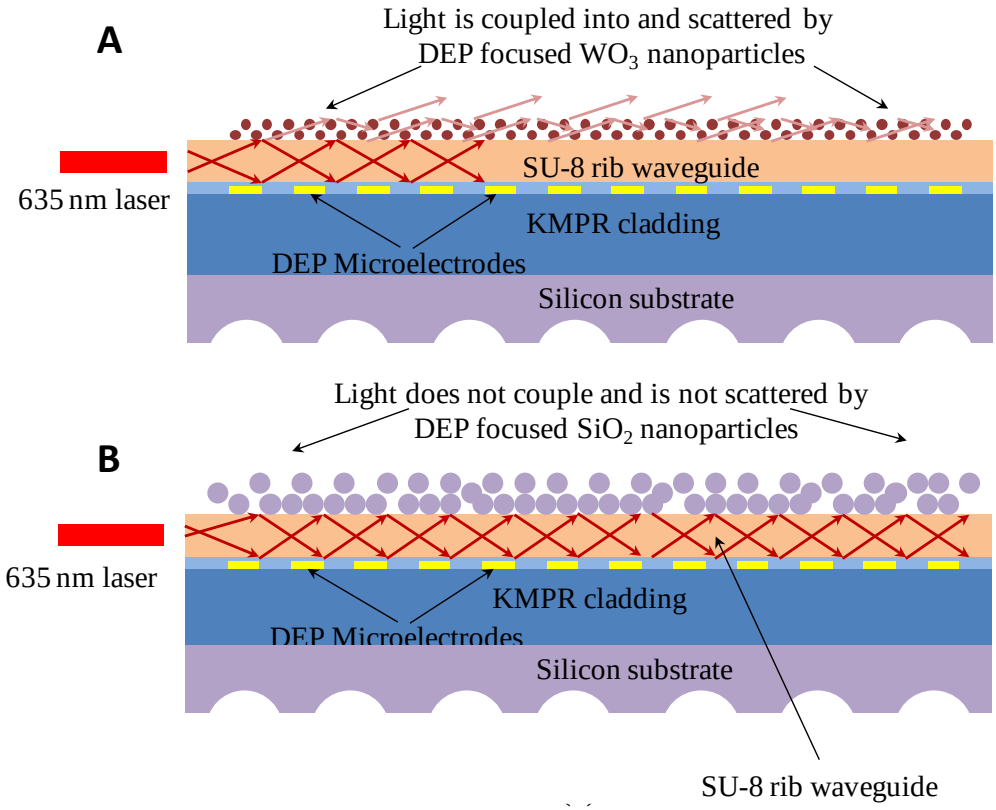

Figure 5.9: Schematic of the interaction of light with the DEP focused: (A) WO_3 and (B) SiO_2 particles.

5.5 Summary

Using Platform 2, which is made of an optical polymeric waveguide for coupling light in an out of the waveguide into microfluidics, the author managed to alleviate the problems faced by the direct coupling of light into the DEP focused particles, which was described in chapter 4. In particular, the scattering of light as a result of the accumulation of particles near the microfluidic reservoirs and the deflection of the optical beam as a result of the flow of particles into and out of the microfluidics, was no longer an issue as that light was coupled to the particles via the multi mode waveguide.

In addition to addressing those issues, the author successfully used Platform 2 to demonstrate the coupling of light from the multi mode polymeric optical waveguide into the DEP focused particles. The author established that the change in particle concentrations in the media controls the transmission properties of the incident light. In particular, he showed

that by controlling the frequency of the applied DEP signal, and applying a negative DEP force, it was possible to repel the particles from the vicinity of the optical rib waveguide, resulting in unperturbed transmission. Conversely, by adjusting the frequency to produce a positive DEP force, it was possible to dynamically concentrate the particles near the waveguide surface and in the case of high refractive index WO_3 particles, resulted in a significant reduction in optical transmission. The author believes that this was the first implementation of a tuneable optical waveguide using dielectrophoresis of particles in microfluidics. The outcomes of this chapter were presented in an article that was published in the Journal of Microfluidics and Nanofluidics [12].

Despite the accomplishments, the author realized the limitations of the current platform. In particular, the platform only allowed the propagation of multi mode, making it difficult to trace the behavior of the individual guided modes or extract information regarding the interaction of these modes with the suspended particles and the surrounding media. Additionally, modal dispersions and propagation losses in multi mode systems are generally high, which would impede the development of this platform into optofluidic sensors.

In order to enhance the performance of the system, it was necessary to develop a single mode or near single mode platform. Such a platform would be capable of providing vital information such as the impact of the packed particles on the individual guided modes. Additionally, such a platform may be used as a template for accurate optofluidic waveguiding and sensing incorporating well controlled suspended nanoparticles. In response to these issues, the author devised Platform 3 which consists of a quasi single mode polymeric waveguide integrated in the microfluidic system, which is presented in chapter 6.

References

[1] Kayani, A., C. Zhang, K. Khoshmanesh, J.L. Campbell, A. Mitchell, and K. Kalantar-zadeh, Novel tuneable optical elements based on nanoparticle suspensions in microfluidics. *Electrophoresis*, vol. 31, pp. 1071-1079, 2010.

[2] Kalantar-zadeh, K., K. Khoshmanesh, A.A. Kayani, S. Nahavandi, and A. Mitchell, Dielectrophoretically tuneable optical waveguides using nanoparticles in microfluidics. *Applied Physics Letters*, vol. 96, pp. 101108, 2010.

[3] Callister, W.D. and D.G. Rethwisch, *Materials science and engineering: an introduction*. 8th ed. 2010, Hoboken, NJ: John Wiley.

[4] Jiang, L., K.P. Gerhardt, B. Myer, Y. Zohar, and S. Pau, Evanescent-wave spectroscopy using an SU-8 waveguide for rapid quantitative detection of biomolecules. *Journal of Microelectromechanical Systems*, vol. 17, pp. 1495-1500, 2008.

[5] Zhang, C., K. Khoshmanesh, F.J. Tovar-Lopez, A. Mitchell, W. Wlodarski, and K. Klantar-zadeh, Dielectrophoretic separation of carbon nanotubes and polystyrene microparticles. *Microfluid and Nanofluid*, vol. 7, pp. 633-645, 2009.

[6] Gaiduk, V.I. and D.S.F. Crothers, Basic molecular mechanisms underlying complex permittivity of water and ice. *Journal of Physical Chemistry A*, vol. 110, pp. 9361-9369, 2006.

[7] Cui, L., D. Holmes, and H. Morgan, The dielectrophoretic levitation and separation of latex beads in microchips. *Electrophoresis*, vol. 22, pp. 3893-3901, 2001.

[8] Durr, M., J. Kentsch, T. Muller, T. Schnelle, and M. Stelzle, Microdevices for manipulation and accumulation of micro- and nanoparticles by dielectrophoresis. *Electrophoresis*, vol. 24, pp. 722-731, 2003.

[9] Gillet, M., K. Aguir, C. Lemire, E. Gillet, and K. Schierbaum, The structure and electrical conductivity of vacuum-annealed WO3 thin films. *Thin Solid Films*, vol. 467, pp. 239-246, 2004.

[10] White, C.M., L.A. Holland, and P. Famouri, Application of capillary electrophoresis to predict crossover frequency of polystyrene particles in dielectrophoresis. *Electrophoresis*, vol. 31, pp. 2664-2671, 2010.

[11] Schmid, J.H., A. Delage, B. Lamontagne, J. Lapointe, S. Janz, P. Cheben, A. Densmore, P. Waldron, D.X. Xu, and K.P. Yap, Interference effect in scattering loss of high-index-contrast planar waveguides caused by boundary reflections. *Optics Letters*, vol. 33, pp. 1479-1481, 2008.

[12] Kayani, A.A., A.F. Chrimes, K. Khoshmanesh, V. Sivan, E. Zeller, K. Kalantar-zadeh, and A. Mitchell, Interaction of guided light in rib polymer waveguides with dielectrophoretically controlled nanoparticles. *Microfluid Nanofluid*, vol. 11, pp. 93-104, 2011.

Chapter 6

Coupling of Light from a Quasi Single Mode Waveguide into the Dielectrophoretically Focused Particles

6.1 Introduction

In chapter 5, the author introduced a multi mode polymeric waveguide into the microfluidic system and demonstrated the coupling of light into the DEP focused particles via the multi mode waveguide. However, as the previously developed platform is multi mode, it allows the propagation of numerous modes simultaneously in the waveguide. As a result, it is almost impossible to trace the behavior of individual modes, extract information or obtain definitive evidence regarding the interaction of the optical waves with the suspended particles or the media that surrounds the waveguide. Additionally, modal dispersions and

propagation losses are relatively higher in multi mode platforms [1], hence inhibiting the potential development of the system as an optofluidic sensor with low detection limits.

In this chapter which forms the final experimental chapter of this PhD thesis, the author introduces a quasi single mode waveguide into the system. This platform offers relatively lower propagation loss and modal dispersions, in comparison to the multi mode platform, and since only a few modes are propagated, the behavior of the individual guided modes can be extracted and interpreted without any fuzziness [2, 3]. The author uses Platform 3 (described in section 3.5.3 of chapter 3), which consists of a quasi single mode polymeric waveguide integrated with DEP microelectrodes in the microfluidic system. He will demonstrate the coupling of the guided modes from the quasi single mode waveguide into the packed concentrations of DEP focused particles that can practically form a resonant and anti-resonant particle packed layer. By varying the parameters of the applied DEP force, the author will demonstrate the manipulation of the particles into forming a dynamic closely packed homogeneous dielectric layer with a tuneable refractive index above the polymeric waveguide.

6.2 Principles

Tungsten trioxide (WO_3), zinc oxide (ZnO) and silicon dioxide (SiO_2) particles were used in the experiments and their motion was controlled using the DEP force. These particles were chosen for the experiments as they had higher (WO_3 and ZnO) and lower (SiO_2) refractive indices compared to the material used for the polymeric waveguide (which will be detailed in section 6.3). Additionally, these particles are easily suspendable in liquid and as established in chapter 5, WO_3 and SiO_2 particles could be forced into forming dense particle streams and then be repelled using the DEP forces quite efficiently. The author introduced ZnO as it has a refractive index between that of SiO_2 and WO_3 and therefore could potentially generate interesting optical responses for comparison.

The depiction of the system's operation showing the side and cross sectional views of the quasi single mode platform is presented in Figure 6.1. Quote notably, the difference between the quasi single mode waveguide used in this chapter and the multi mode platform previously used in chapter 5 is in their structure and dimensions. In particular, the multi

mode waveguide used in chapter 5 was a raised rib waveguide, while the quasi single mode waveguide used in this chapter is an inverted rib waveguide (Figures 6.1A and 6.1C). Additionally, the dimensions for the quasi single mode waveguide rib features were 4.5×0.3 μm ($w \times h$), while the dimensions for that of the multi mode waveguide was 7×0.35 μm ($w \times h$). The waveguide configuration and dimensions guaranteed the propagation of single mode in contrast to larger waveguides that allow the propagation of many modes simultaneously [4].

Optical waves travel in a waveguide in distinct optical guided modes. A guided mode is a spatial distribution of optical energy that maintains the same transverse distribution and polarization at all locations along the waveguide axis [5, 6]. The distribution pattern depends on the variation in refractive indices that forms the waveguide core and its surroundings, the size and shape of the waveguide and the wavelength of the optical wave [7].

In this chapter, the author uses transverse electric (TE) polarized light as it has the electric field aligned parallel to the waveguide surface and therefore experiences stronger optical confinement within the waveguide, has a lower propagation loss and it is easily observed. Transverse magnetic (TM) polarized light however, has the electric field aligned normal to the waveguide surface and therefore experiences stronger scattering by the indiscriminate presence of particles or changes in the waveguide's upper media and has a larger propagation loss and thus was difficult to observe.

The number of TE modes supported by a planar dielectric waveguide can be approximated using the following relation [6]:

$$M = \frac{2d}{\lambda} NA \tag{6.1}$$

where NA is the numerical aperture of the waveguide defined as:

$$NA = \sqrt{n_1^2 - n_2^2} \tag{6.2}$$

These equations can be used to crudely estimate the number of modes propagating in the rib waveguide of Platform 3. For instance, given that $d = 2.5$ μm, $\lambda = 635$ nm, $n_1 = n_{SU\text{-}8} = 1.592$, $n_2 = n_{KMPR} = 1.566$, then $NA = 0.287$ and $M \sim 3$ indicating the waveguide is quasi single mode such that it propagates three TE polarized modes.

It is known that light propagating through the polymeric waveguide has evanescent fields radiating from the waveguides' surface that decay exponentially into the surrounding media [8]. As a result, these fields allow the optical waves, which consist of the guided modes to interact with the media surrounding it. Figures 6.1B and 6.1D present schematics of the fundamental guided mode in a single mode waveguide that has a liquid upper cladding containing suspended particles. According to the theory of total internal reflection [4], the fundamental mode remains confined in the waveguide core provided that $n_{waveguide} > n_{media}$, in which $n_{waveguide}$ and n_{media} are refractive indices of the waveguide and its surroundings, respectively (Figure 6.1B).

However, when particles are packed together such that the refractive index of the particle packed stream, $n_{packed\text{-}particles}$, is larger than that of the waveguide ($n_{packed\text{-}particles} > n_{waveguide}$), the fundamental mode is coupled out of the waveguide into the packed stream of particles (Figure 6.1D). The guided modes of the optical waves strongly interact with the particles packed near the waveguide surface, almost becoming confined within them. As a result, any small change in the physical or chemical properties of the area near or around the particles strongly affects the modal behaviour. Higher order modes propagating in the waveguide can also interact with the particles in a similar fashion.

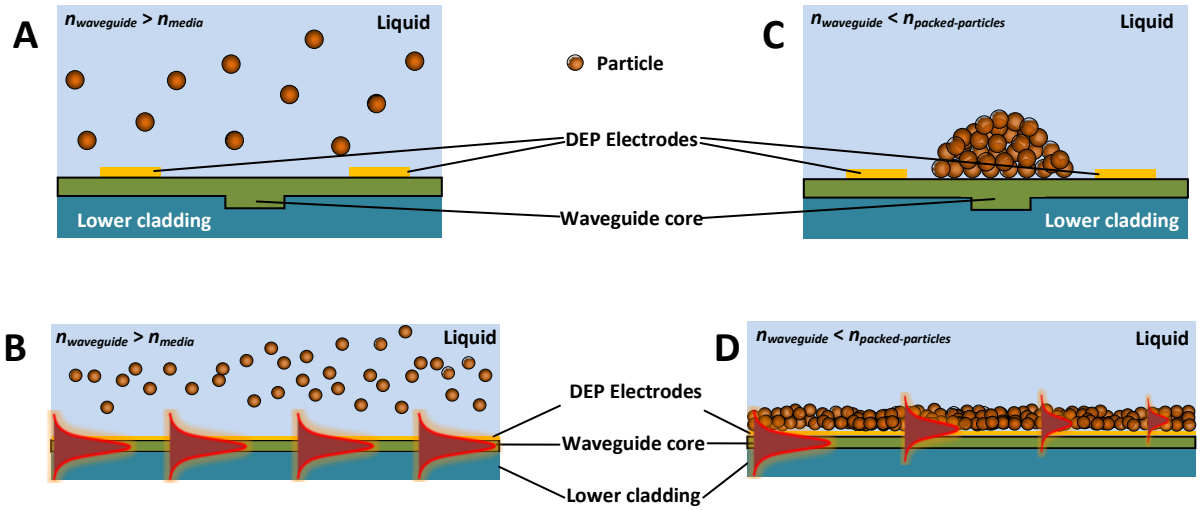

Figure 6.1: Cross sectional and side view of the system's operational schematic: (A) Cross sectional and (B) Side view showing particles randomly dispersed in a microfluidic channel. The fundamental mode remains confined in an optical waveguide when $n_{waveguide} > n_{media}$ (C) Cross sectional and (D) Side view showing particles tightly packed close to the quasi

single mode waveguide. The fundamental mode is coupled into the stream of packed particles $n_{waveguide} < n_{packed\text{-}particles}$.

Samples of the particle suspensions were placed on glass slides and dehydrated. The samples were then viewed using an FEI Nova SEM. The scanning electron microscope (SEM) image of the ZnO and SiO_2 particles are presented in Figure 6.2A and 6.2B, respectively. The SEM image of the 80 nm WO_3 particles was already presented in Figure 5.2 of chapter 5.

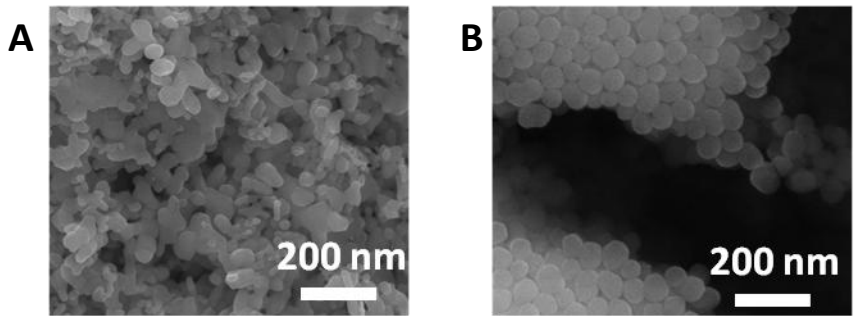

Figure 6.2: SEM image of the particles: (A) ZnO particles (Ø50 nm) (B) SiO_2 particles (Ø72 nm).

The real part of the Claussius-Mossoti factor (Re[$f_{CM}(\omega)$]) was calculated for these particles to explore the DEP behaviors of the particles, which allowed the determination of appropriate DEP applied frequencies for manipulating the particles' motion during the experiments. The Re[$f_{CM}(\omega)$] for WO_3 has been presented in chapter 5 but is included here for reference. In these experiments, the particles were suspended in deionized (DI) water and so the conductivity of the suspending media after the addition of the Triton X-305 surfactant (Sigma Aldrich) was taken as 0.2 mS m^{-1} and the relative permittivity was taken as 77.6 [9-11]. The diameters for the WO_3, ZnO and SiO_2 particles used in the experiments are 80, 50 and 72 nm, respectively. The conductivities of the particles were taken to be 100.25, 49 and 5.6 mS m^{-1} for WO_3, ZnO and SiO_2 particles, respectively [12-14]. The relative permittivities of the particles were taken as 80, 8.6 and 4.5 for the WO_3, ZnO and SiO_2 particles, respectively [10, 11, 14, 15]. Using these values, the Re[$f_{CM}(\omega)$] for the particles was calculated and plotted in Figure 6.3. It was observed that all the particles analyzed experience a transition from positive to negative DEP behavior about the cross over

frequency. The numerically calculated crossover frequencies for the WO_3, ZnO and SiO_2 particles are 24, 8.5, and 1.6 MHz, respectively.

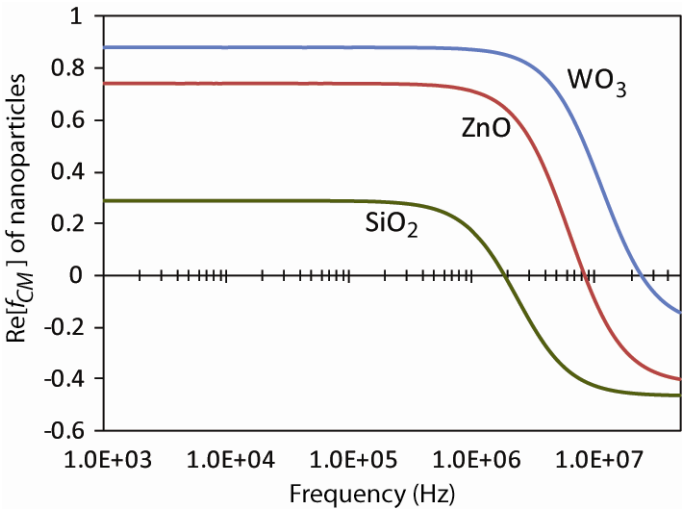

Figure 6.3: Re[$f_{CM}(\omega)$] for the particles used in the experiments. Variations of Re[$f_{CM}(\omega)$] for the WO_3 (Ø80 nm), ZnO (Ø50 nm) and SiO_2 (Ø72 nm) particles dispersed in DI water.

In chapter 5, the author described a method for approximating the refractive index of the reconfigurable particle packed media using the atomic packing factor (APF) [16]. In this chapter, the author extends this method by introducing a *posterior* approach which allows for estimating the range of refractive indices required to achieve the coupling of the guided modes into the particle media.

The minimum refractive index of the media in the region above the waveguide core occurs when suspended particles are completely repelled, leaving only DI water (n = 1.33) in this region. Conversely, the maximum possible refractive index is obtained when particles are closely packed. Therefore, the maximum refractive index of the media above the waveguide core, n_{max} can be approximated using:

$$n_{max} = pf_{particle} \times n_{particle} + pf_{suspending\text{-}media} \times n_{suspending\text{-}media} \qquad (6.3)$$

where $pf_{particle}$ and $pf_{suspending\text{-}media}$ are the packing fractions of the particle and the suspending media, respectively, and $n_{particle}$ and $n_{suspending\text{-}media}$ are the refractive indices of the particle material and suspending media, respectively. Given that $n_{particle}$ = 2.3 for WO_3 and that

$pf_{particle}$ = 0.74, $pf_{suspending\text{-}media}$ = 0.26 and $n_{suspending\text{-}media}$ = 1.33, the maximum refractive index of closely packed WO_3 particles is, according to equation (6.1) ~2.04.

The range of refractive indices required to achieve the coupling of the guided modes (the *posterior* approach) can be estimated as follows. If the refractive index of the waveguide, $n_{waveguide}$, is known, given that the coupling of light occurs when the refractive index of the upper cladding media is equal to or greater than the waveguide core, the packing fraction of the focused particles and the suspending media, $pf_{particle}$, and the $pf_{suspending\text{-}media}$, can be estimated using the following relation:

$$pf_{particle} \times n_{particle} + pf_{suspending\text{-}media} \times n_{suspending\text{-}media} \geq n_{waveguide} \qquad (6.4)$$

When focused particles are packed, the space between them is occupied by the suspending media, such that $pf_{suspending\text{-}media} = 1 - pf_{particle}$. Assuming that $n_{waveguide}$ = 1.592 (which is the refractive index of the SU-8 waveguide core), the minimum packing fraction of particles for the coupling of light according to equation (6.4) is 27 %. This means that the theoretical range of packing fractions of WO_3 particles above the waveguide that allows the coupling of light to occur is: $0.27 < pf_{particle} < 0.74$. Applying the minimum packing fraction into equation (6.2), the minimum refractive index of the media, n_{min} that induces the coupling of light from the waveguide is n_{min} = 1.59. Therefore, when light couples out of the waveguide into the packed particles, the refractive index of the upper cladding media actually ranges according to: 1.59 (n_{min}) < n_{media} < 2.04 (n_{max}).

The refractive indices for the ZnO and SiO_2 particles ($n_{particle}$) are 2.0 and 1.47, respectively. According to equation (6.3), the maximum refractive indices (n_{max}) of the media above the waveguide core when these particles are closely packed are 1.83 (ZnO) and 1.43 (SiO_2). Therefore, under maximum packing conditions, the densely packed ZnO mesoparticles are capable of coupling light from the rib waveguide, while SiO_2 particles may not be. Using equation (6.4), the refractive index of the media formed by the packed ZnO particles in order for light to couple out of the rib waveguide ranges according to: 1.59 (n_{min}) < n_{media} < 1.83 (n_{max}).

6.3 Methods and Simulations

Platform 3 was used for the experiments and it was placed on an optical micro-positioner stage while a focusing lens was used to direct visible light (λ = 635 nm) from a polarized Helium Neon laser source (Model 105-1, Spectra Physics) into the rib waveguide core. The waveguide core and cladding of Platform 3 was composed of curable photoresist polymers known as SU-8 (Microchem, n = 1.592) and KMPR (Microchem, n = 1.566), respectively. Details of the platform structure are provided in section 3.5.3 of chapter 3.

The outlet reservoir was connected to a syringe operated by a syringe pump (Harvard Apparatus PHD 2000), while the microfluidic inlet was connected to the suspended particle beaker. The suspended particles were sucked out from the microfluidic outlet reservoirs while applying a range of AC voltages and frequencies (Rohde & Schwarz SMS signal generator with a frequency range of 0.1 to 250 MHz coupled to a home-made RF amplifier with a gain ~25 dB), which were capable of manipulating the particles under DEP forces. The intensity profile of the waveguide output is captured by a charged couple device (CCD) camera via a focusing lens (Figure 6.4).

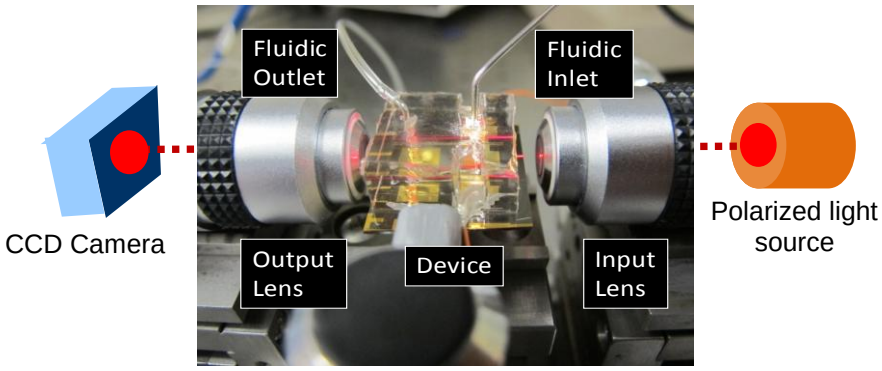

Figure 6.4: Device experimental setup.

The WO_3, ZnO and SiO_2 particles used in these experiments were suspended in DI water with a weight-in-weight (*w/w*) concentration of 0.5 %. This low concentration was chosen as the author intended to demonstrate that it is possible to reach high levels of particle packing using DEP manipulation forces alone. Triton X-305 (Sigma Aldrich) surfactant was added to the particle suspensions to prevent particle agglomeration. The quasi single mode waveguide

core was photolithographically aligned at the center of the curve shaped microelectrodes which were separated by the 20 µm gap at the tips (see Figure 6.5 and inset).

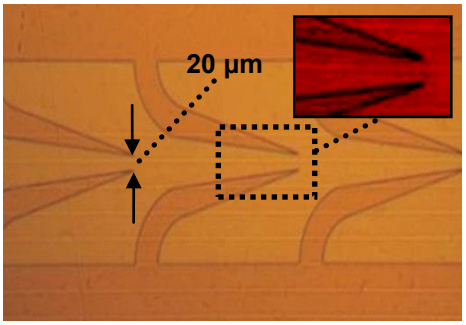

Figure 6.5: Microscopic image of DEP microelectrodes and the rib waveguide shown in the center (inset).

The curved DEP microelectrodes generated the DEP force required to focus or repel the suspended particles from the region close to the waveguide surface. The DEP field for the current platform was simulated to comprehend the performance of the system using Fluent 6.2 software package (Fluent Inc, Lebanon, USA) based on the model described in section 4.3 of chapter 4. The simulations were conducted with the help of the author's collaborator Dr Khashayar Khoshmanesh from the School of Electrical and Computer Engineering, RMIT University.

Simulations showed that applying an alternating current (AC) voltage of 15 V_p, the electric field reaches a peak value of 1.6×10^6 V m^{-1} at the tip of microelectrodes and smoothly decreases along the microelectrode structure (Figure 6.6). Applying frequencies less than the crossover frequency, induces positive DEP response and pushes the particles toward the center of the microelectrode pairs.

According to the observations, at low to medium flow rates (0.5 to 2.5 µl min^{-1}), the particles have enough time to immobilize between the opposite microelectrodes. However at medium to high flow rates (3 to 4.5 µl min^{-1}), although the particles are descended to lower heights they will be dragged by flow before immobilization. In this condition, the microelectrode pairs act as discrete funnels due to their symmetric shape and focus the passing particles along the centerline of the microchannel. The aforementioned conditions

were obtained by applying a flow rate of 4 µl min^{-1} (corresponding to an average velocity of 1.66 mm s^{-1}) and DEP voltage amplitude of 15 V_p.

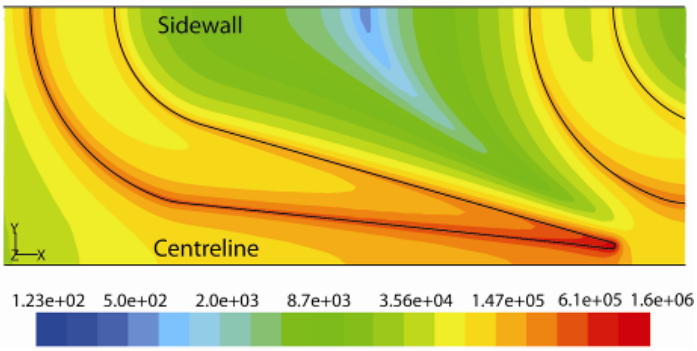

Figure 6.6: Electric field simulation of the DEP microelectrodes showing the contours of electric field (V m^{-1}) at the bottom surface of DEP system obtained by numerical simulations.

Subsequently, the author conducted the waveguide modal simulations of guided modes in the quasi single mode waveguide for TE polarizations of the coupled laser source. These simulations were conducted with the help of the author's collaborator, Dr. Thach Nguyen from the School of Electrical and Computer Engineering, RMIT University. The simulations were conducted assuming that the upper cladding of the waveguide was DI water and that the region above the waveguide was devoid of particles. The guided modes were simulated for TE polarizations using the rib waveguide dimensions as detailed in section 3.5.3 of chapter 3 and wavelength of incident light taken as λ = 635 nm.

A fully vectorial mode matching technique [17] was employed to calculate the transverse electric (TE) modal characteristics of the guided modes of the polymeric waveguide assuming a DI water upper cladding media. In the mode matching simulations, the computational window was fully open in the lateral direction. Therefore, the mode matching simulation accurately modelled waveguide modes with lateral leakage [18, 19]. Figure 6.7 shows the electric field distributions of the major components of the TE guided modes, which are composed of the fundamental, TE_{00} (Figure 6.7A), first order, TE_{10} (Figure 6.7B) and second order, TE_{20} (Figure 6.7C) modes. The calculated propagation losses given are shown. The simulations indicated that the rib waveguide is quasi single mode such that the fundamental, TE_{00} mode propagates with negligible loss, while the first order, $TE_{10,}$ and

second order, TE_{20} modes, have a loss of 0.65 and 29.3 dB cm^{-1}, respectively. Due to the high propagation loss of the TE_{20} mode, the author anticipated that the TE_{20} and higher order modes would not be observed in the experimental measurements.

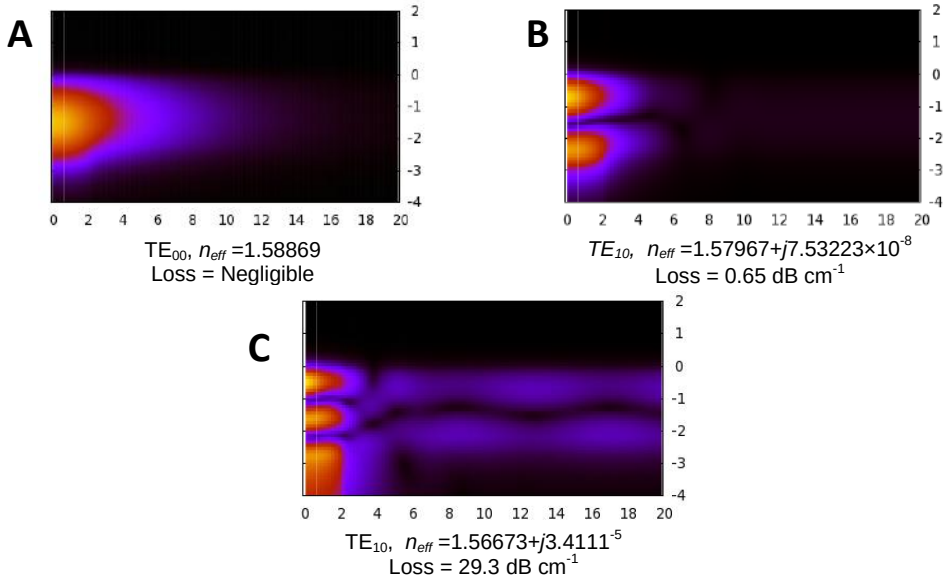

Figure 6.7: Waveguide modes for the quasi single mode waveguide: (A) TE_{00} mode (B) TE_{10} mode (C) TE_{20} mode.

Using an appropriate combination of DEP and hydrodynamic forces, the author was able to vary the concentration of particles above the waveguide core, which effectively tuned the refractive index of the upper cladding media. The intensity of concentration or repulsion was controlled by changing the amplitude of the applied DEP signal. The action is schematically demonstrated in Figures 6.8A - 6.8B. Figure 6.8A shows the device with suspended particles in the absence of DEP forces and Figure 6.8B shows the device when particles are closely packed by the positive DEP force, flowing near the rib waveguides.

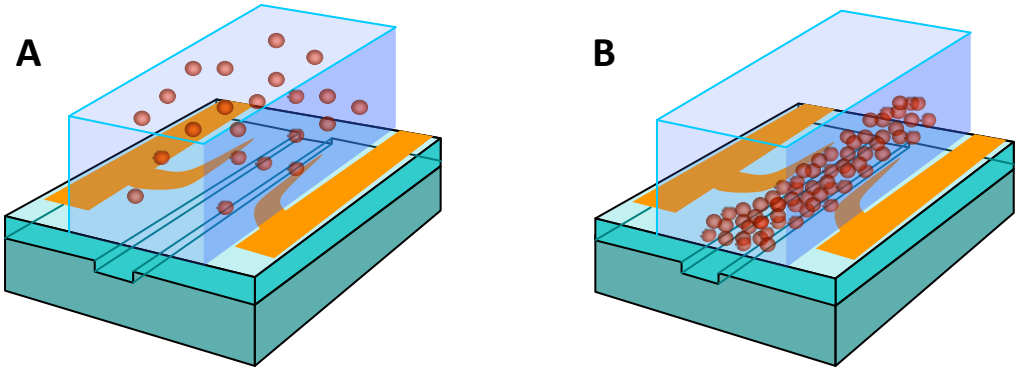

Figure 6.8: Platform operational schematic: (A) Schematic of the optofluidic device with suspended particles in the absence of DEP forces; and (B) particles closely packed near the waveguide surface due to positive DEP forces.

The author then carried out simulations to comprehend the variations of particle concentrations between the DEP microelectrodes in the microfluidic channel. Dr. Khashayar Khoshmanesh from the School of Electrical and Computer Engineering, RMIT University, helped in conducting these simulations as follows. The density of focused particles between the microelectrodes was correlated to the $\left|DEP\text{-}y\right|$, where *DEP-y* is the DEP force along the *y*-axis. Figure 6.9 shows the dimensionless contours of $\left|DEP\text{-}y\right|$ at different planes along the microfluidic channel *x*-axis. It indicates the formation of packed particle regions along the inner edge of microelectrodes. At the vicinity of the tips, the dense particle regions merge to form a packed particle stream along the microchannel centerline. The configuration of the packed particle stream after the tips depends on the balance of the DEP force, which holds the particles and the hydrodynamic drag force which drags them. The results indicate that the microelectrodes act as a funnel and closely pack the particles in the region between the microelectrode pairs and the resulting particle packing concentrations in close vicinity of the waveguide surface are as indicated in Figure 6.9.

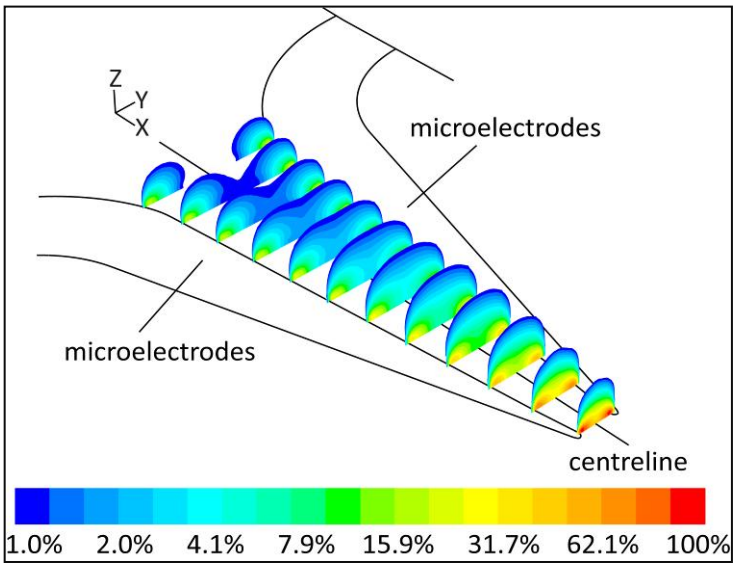

Figure 6.9: The variations of $\nabla_y E^2$ correlated with the variations of particle concentration distribution between the microelectrodes.

6.4 Results and Discussions

The author tested the platform by applying a range of DEP signals, while observing the intensity profile distribution at the waveguide output. In the experiments involving the WO_3 particles, the DEP frequencies of 5, 10, 20 and 30 MHz were applied. For the ZnO particles, the DEP frequencies of 1.5, 3, 8 and 13 MHz were applied and in the case of SiO_2 particles, the DEP frequencies of 800 kHz, 1.6 and 2.4 MHz were applied. For these three particle types, the DEP voltage was varied from 5 to 15 V_p. The author selected these combinations of DEP voltage magnitudes and frequencies as they were found to create a stream of packed particles with well-defined interfaces along the centerline of the microchannel (under positive DEP force) and pushing the particles toward the sidewalls (under negative DEP force).

The liquid flow rate was set to 4 µl min^{-1} as it was suggested appropriate by the simulations in section 6.3 (Figure 6.6). Additionally, this flow rate was selected because applying higher flow rates (~8 µl min^{-1}), some particles remained along the centerline and at the same time were levitated to higher heights under the negative DEP force. This is because while at

lower flow rates, the DEP force is the major force affecting the particles' motion, at such higher flow rates, hydrodynamic drag forces become increasingly dominant.

6.4.1 WO_3 particles

The author began the experiments by applying a constant DEP voltage amplitude of 15 V_p, while varying the frequency from 30 MHz to 10 MHz (Figures 6.10A-6.10C). At 30 MHz, particles were repelled from the center of the microchannel (Figure 6.10A) under negative DEP forces. As the frequency was decreased to 20 MHz, a weak positive DEP trapping force caused the particles to concentrate, forming a stream of packed particles above the quasi single mode waveguide core (Figure 6.10B).

The author observed and recorded the widths of the packed particle stream at various locations between the DEP microelectrodes and marked it in the images. These widths have an approximate error in measurement of ± 20 % and they provide an indication of the particle assembly conditions such as the geometry of the packed particle streams. The widths of the particle streams have an error. As the DEP frequency was decreased, the trapping DEP force became stronger, resulting in a densely packed concentration of particles at 10 MHz (Figure 6.10C). We observed the mode intensity profile change from a single lobe (Figure 6.10D) to two lobes separated vertically by a distinct null (Figure 6.10E) at 20 MHz. The intensity of the transmitted light reduced as we decreased frequency to 10 MHz (Figure 6.10F). The author believes that this can be attributed to the increase in the refractive index due to the formation of the particle packed layer above the polymeric waveguide.

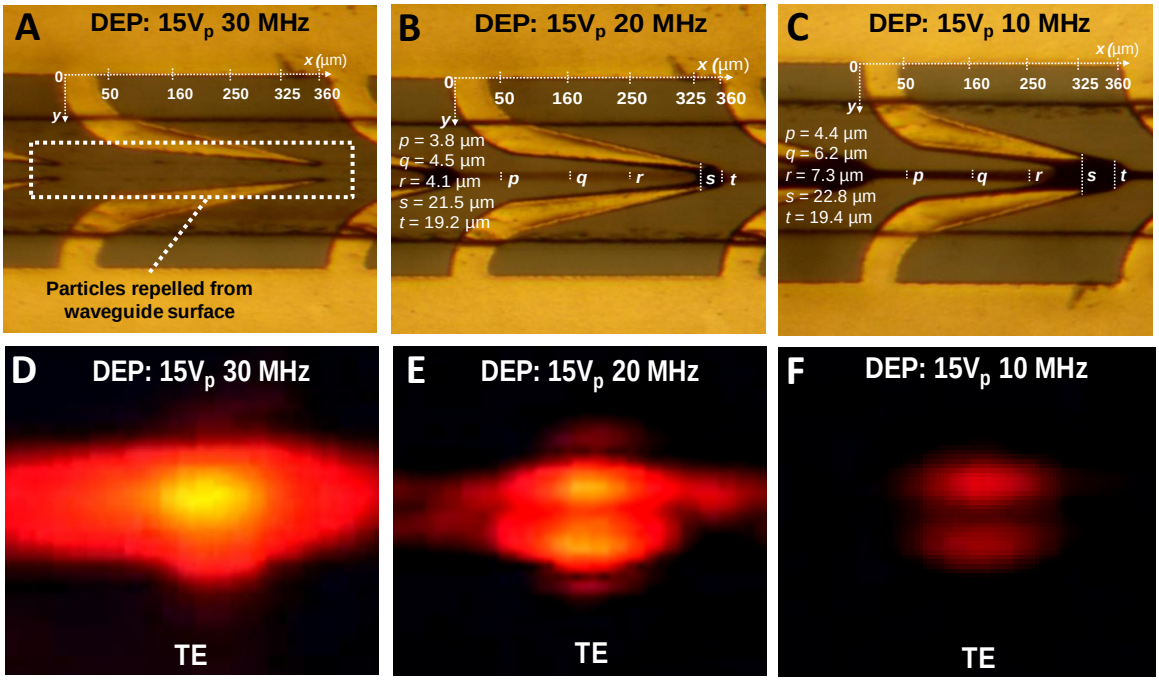

Figure 6.10: Particle formation conditions and intensity profiles with variation of DEP frequency: (A) WO_3 particles repelled from the center at 15 V_p and f = 30 MHz; (B) WO_3 particles form a particle packed stream at 15 V_p and f = 20 MHz; (C) WO_3 particles are densely packed at 15 V_p and f = 10 MHz; (D) TE mode intensity profile at DEP: 15 V_p and f = 30 MHz; (E) at DEP: 15 V_p and f = 20 MHz; and (F) at DEP: 15 V_p and f = 10 MHz.

The author then decided to increase the packing density to assure stronger coupling of the guided modes into the particle dense media by conducting a second series of experiments. At the constant frequency of 5 MHz (optimal trapping frequency for WO_3), the DEP voltage amplitude was increased from 0 to 15 V_p in increments of 5 V_p (Figures 6.11A-6.11F), while observing the changes in the mode intensity profile at the waveguide output. The mode intensity profile observed exhibited two lobes (Figure 6.11D). At 10 and 15 V_p, the mode intensity profile remained unvarying, but the transmitted intensity was reduced (Figures 6.11E and 6.11F).

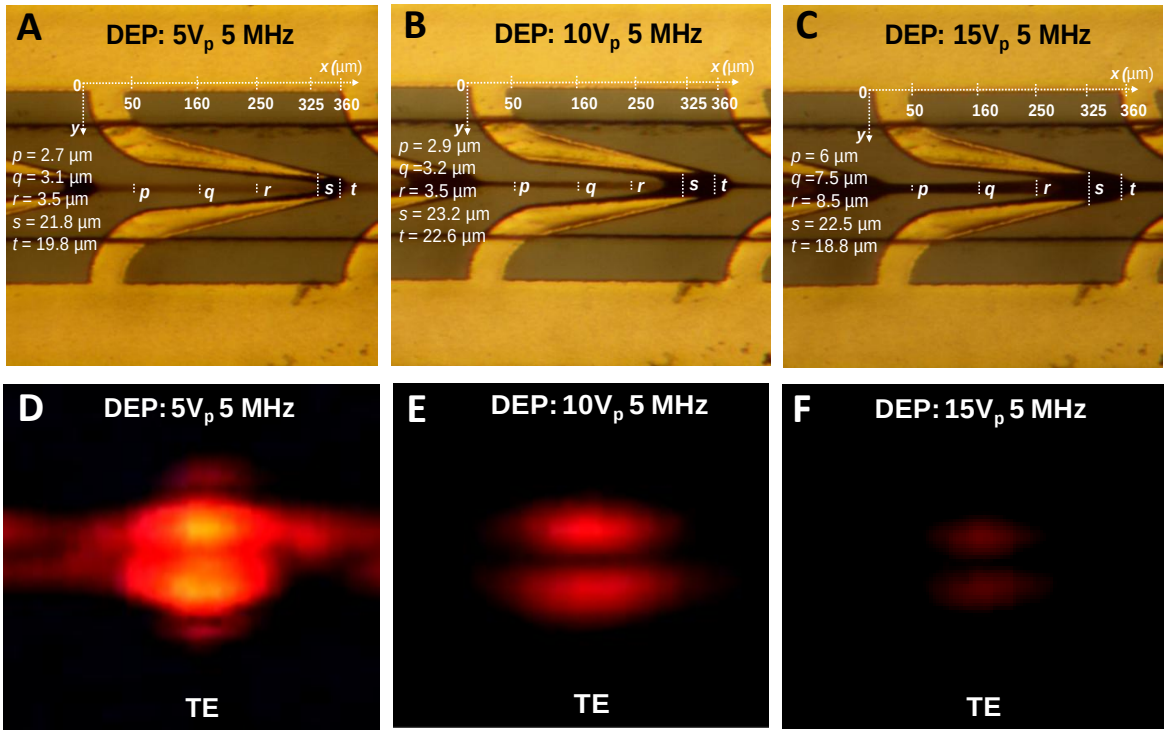

Figure 6.11: Particle formation conditions and intensity profiles with variation of DEP amplitude: (A) WO_3 particles packed in the center at 5 V_p and f = 5 MHz; (B) At 10 V_p and f = 5 MHz; (C) At 15 V_p and f = 5 MHz; (D) Waveguide TE mode profile at DEP: 5 V_p and f = 5 MHz (E) At DEP: 10 V_p and f = 5 MHz; and (F) At DEP: 15 V_p and f = 5 MHz.

By reducing the frequency from 30 MHz to 10 MHz at 15 V_p, the author effectively varied the suspended particle packing density near the polymeric waveguide and observed a transition of guided modes. The transitioning of modes is explained by obtaining the modal simulations for various particle packing conditions, which represent different media refractive index values as the upper cladding. To model the TE field distribution accurately, it was necessary for the author to know the density distribution of particles as a function of height above the polymeric waveguide surface.

Dr Khashayar Khoshmanesh, from the School of Electrical and Computer Engineering, RMIT University assisted the author in simulating the particle density distributions. The density of particles in any y direction was assumed to be proportional to the intensity of the DEP-y force (Figure 6.9) at that point and accordingly, the particle density distribution function presented in Figure 6.12 was obtained. At x = 350 μm (Figure 6.12A), maximum

trapping occurs causing the formation of a particle packed stream, when combined with hydrodynamic forces. From models of the DEP field (Figure 6.9) and particle density distribution of Figure 6.12B, the refractive index profile vertically across the waveguide core was calculated as depicted in Figure 6.13.

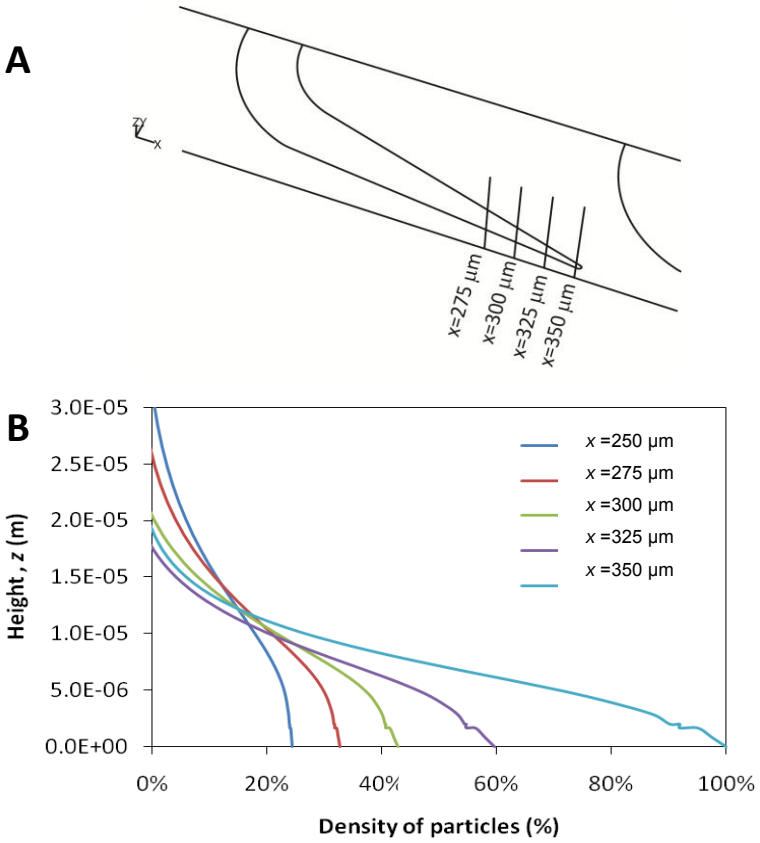

Figure 6.12: Calculation of the particle density distribution correlating the density of particles to the distribution of the DEP-*y* field: (A) DEP electrode single sided symmetry diagram; (B) DEP field intensity distribution at various *x* locations.

The refractive index profiles were calculated for $n_{max1} = 1.595$ and $n_{max2} = 1.65$ to obtain the variation of particle packing density with height in the microfluidic channel. The media refractive index profiles indicate that the density of the WO_3 particle packed stream was highest at the waveguide surface and reduces almost linearly with increasing height in the microfluidic channel.

Using the calculated refractive index profiles (Figure 6.13A), the corresponding guided modes of the quasi single mode polymeric waveguide structure was calculated. The author's

collaborator, Dr Thach Nguyen, from the School of Electrical and Computer Engineering, RMIT University helped the author in producing these calculations. Dr. Nguyen developed a transfer matrix method software package based on [20] which was used to simulate the guided mode distributions.

From the waveguide mode field profiles, the field intensity ratio of light guided in the region of packed particles relative to the total mode power was evaluated. Figure 6.13B shows the field intensity ratio of light guided in the region of packed particles relative to the total mode power as a function of the maximum refractive index, n_{max}. It is interesting to note that as the density and thus refractive index of the suspended particles increase, the fraction of the TE_{00} mode in the suspended particles increases progressively as the mode becomes evanescent, eventually propagating entirely within a particle waveguiding layer, which is formed by the particle suspension. Conversely, the fraction of the first order TE_{10} mode interacting with the particles experiences an anti-resonance, becoming isolated from the suspended particles at a particular concentration.

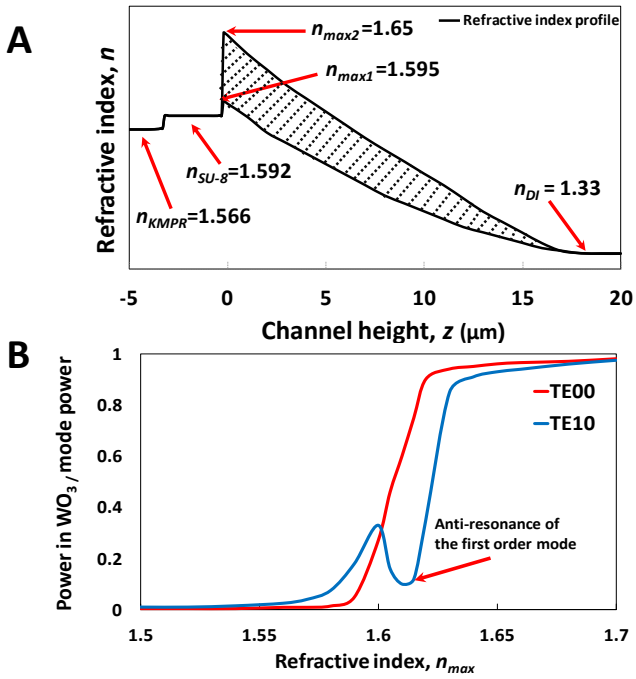

Figure 6.13: Refractive index profile and mode power ratio: (A) Refractive index profile as a function of microfluidic channel height. The shaded area represents the range of possible media refractive index profiles within the nominal n_{max} values; (B) Ratio of optical mode power in WO_3 particle dense media to the total power.

The waveguide modal simulations for various particle packed stream refractive indices were simulated with the help of Dr Nguyen and is presented in Figures 6.14A - 6.14C. The shaded region denotes the lateral boundaries of the polymeric waveguide core and the red and blue plots show the electric field distribution of the TE_{00} and TE_{10} order modes, respectively. These simulations are used to explain the observations in Figures 6.10 and 6.11. At low particle packing densities, where the maximum refractive index of the particle packed stream, n_{max} = 1.595 near the polymeric waveguide, the transmission of both TE_{00} and TE_{10} modes were observed however, TE_{00} was dominant (Figure 6.14A). It was observed that the modes were highly evanescent and a fraction of the TE_{00} and TE_{10} modal power was coupled into the resonant particle packed layer above the waveguide.

As the particle packing was increased, the TE_{00} mode becomes more strongly coupled into the resonant particle packed layer and was either scattered or guided away from the polymer waveguide by the particles (the latter occurs when the flow of particles departs from the axis of the waveguide as particles flow out of the microfluidic channel – Figure 6.14D). At a particular particle packing density, the TE_{10} mode, which may also be launched at the input, was mostly isolated from the particle packed layer due the anti-resonance observed in Figure 6.13B. The anti-resonance of the TE_{10} mode is explained by simulating n_{max} = 1.617. When such conditions prevail, a major fraction of the TE_{00} mode propagates in the particle packed layer while the TE_{10} mode propagates largely in the polymeric waveguide (Figure 6.14B). When the particle stream was separated from the waveguide near the waveguide output, the TE_{10} mode proceeded to the output where it was observed (Figure 6.14E).

The modal distribution was simulated for n_{max} = 1.65 to ascertain the modal behaviour when the density of particles was increased further (Figure 6.14C). It was observed that the interaction of both the TE_{00} and the TE_{10} modes with the suspended particles increased and thus the intensity of light remaining in the polymer waveguide decreased (Figure 6.14C) and was eventually coupled into the particle packed stream (Figure 6.14F).

These predictions and explanations matched the experimental observations as follows. In Figure 6.10D, the TE_{00} mode was dominant as the particles are repelled from the waveguide surface such that $n_{waveguide} < n_{packed\text{-}particles}$. Figures 6.10E and 6.11D show that the TE_{00} mode was coupled into the particle packed layer while the TE_{10} mode transitioned from higher to

lower loss (as shown in Figure 6.13B). The observations show that at certain particle packing concentrations, the DEP focused particles act as a homogenous high refractive index layer that supports the anti-resonance. The gradual intensity decline of the TE_{10} mode, without further modal transitions when the particle packing density was increased (Figures 6.10F and 6.11E - 6.11F) agrees with the simulations, as the TE_{00} mode was coupled out of the waveguide prior to the TE_{10} mode due to the anti-resonance (Figure 6.13B).

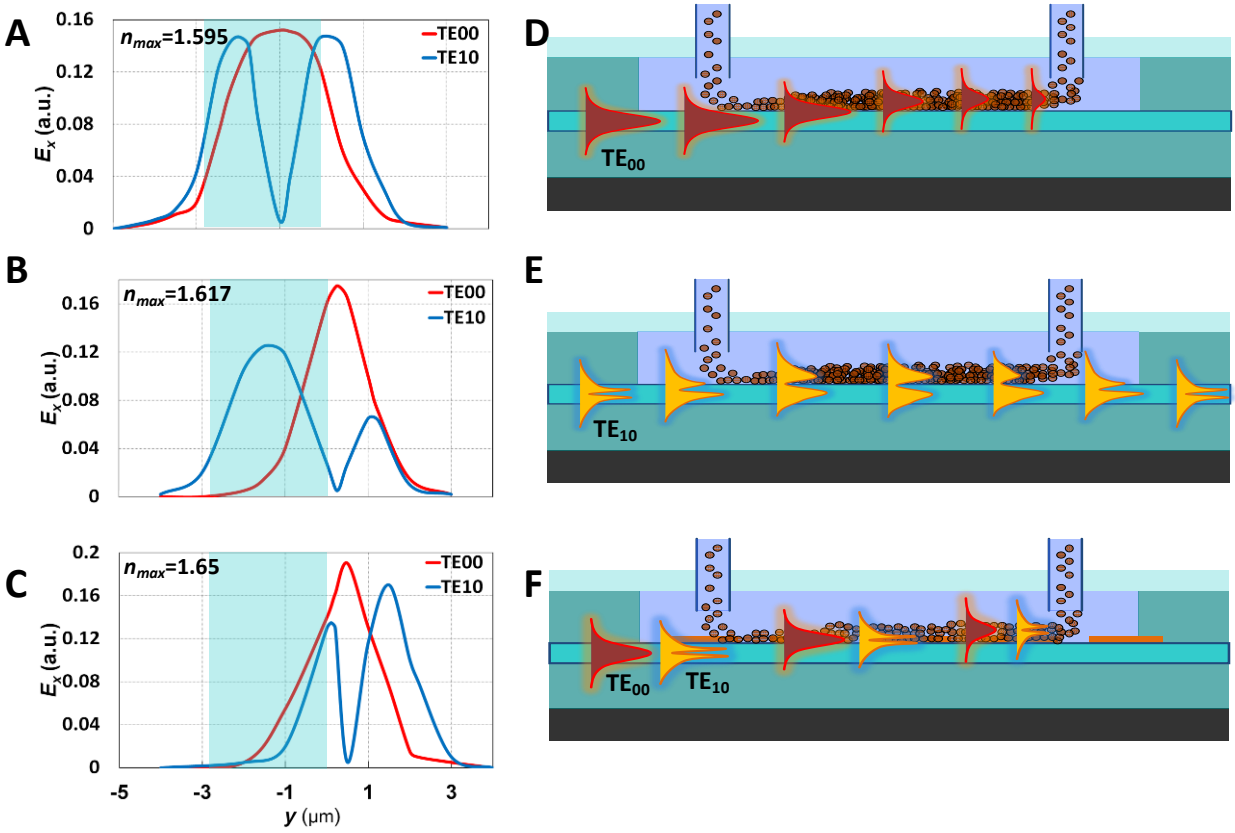

Figure 6.14: Modal simulations with varying packed particle stream refractive indices: (A) Waveguide modal profile when n_{max} = 1.595; (B) n_{max} = 1.617; and (C) n_{max} = 1.65. (D) TE_{00} mode is coupled into the particle packed layer as the particle stream begins to form a high index resonant layer. (E) At a particular particle packing density, the TE_{10} mode is anti-resonant with the particle packed layer; (F) As particle packing density increases, both the TE_{00} and TE_{10} modes are completely coupled into resonant particle packed layers.

6.4.2 ZnO particles

The ZnO particles (Sigma Aldrich, $n_{ZnO} = 2.0$) experienced a transition from negative to positive DEP behavior as the frequency was decreased from 13 to 3 MHz (in agreement with the simulations presented in Figure 6.3). The author first conducted the experiments by keeping the applied DEP voltage magnitude constant at 15 V_p while varying the frequency. The ZnO particles were repelled from the center by applying a 13 MHz frequency at 15 V_p (Figure 6.15A) and the corresponding mode intensity profile showing a single lobe was observed (Figure 6.15D). The frequency of the AC signal was then reduced to 8 MHz. The DEP repelling forces became weak as particles began to move towards the center of the microchannel leaving a narrow void strip between the microelectrode pairs (Figure 6.15B). The corresponding mode intensity profile observed was a single lobe with reduced intensity compared to the previous case (Figure 6.15E). This change was attributed to the increase in the media refractive index above the waveguide core which caused the waveguide to become increasingly evanescent. As the DEP frequency was further reduced to 3 MHz, a stream of packed ZnO particles was formed at the microchannel center (Figure 6.15C). The corresponding mode intensity profile was the single lobe with the intensity significantly reduced (Figure 6.15F).

Interestingly, the author observed lateral leakage of the guided mode which could be attributed to the agglomeration of ZnO particles close to the waveguide surface and in the regions near the DEP microelectrode surface. This agglomeration of ZnO particles may have caused the formation of a media of higher refractive index than the polymeric waveguide at indiscriminate locations in the microfluidic channel. These media may have induced the coupling the guided modes into these media.

The author then decided to increase the packing density of the particles and to induce stronger coupling of light into the particle concentration by conducting the second series of experiments using the ZnO particles. By keeping the frequency constant at 1.5 MHz, the DEP voltage magnitude was varied from 0 to 15 V_p at 5 V increments (Figure 6.15G - 6.15L). At 5 V_p, a weak positive DEP force trapped the ZnO particles in the center of the microfluidic channel (Figure 6.15G) causing the intensity of the mode to be reduced (Figure 6.15J). As the DEP voltage was increased, the particle packing density in

the center was increased (Figure 6.15H) which caused further reductions in the intensity of the guided mode (Figure 6.15K). When the DEP voltage magnitude applied was 15 V_p, the ZnO particles formed a distinct narrowband of packed particles (Figure 6.15K) while the intensity of the mode was significantly reduced (Figure 6.15L).

The observations from the ZnO experiments indicated that the guided mode was gradually coupled into the particle dense media as evidenced by Figures 6.15E - 6.15F. However, the transitioning of the guided modes was not observed in the ZnO experiments. The author attributes this to: (i) Problems forming dense particle streams with smooth and distinct boundaries (as evidenced from the DEP images) (ii) Refractive index of ZnO is lower (n_{ZnO} = 2.0) compared to WO_3 (n_{WO3} = 2.3), hence a really dense concentration of ZnO would be required to induce the formation of resonant or anti-resonant layers of ZnO particles which can selectively couple or isolate the guided modes (iii) ZnO particles tended to agglomerate close to the DEP microelectrode/waveguide core surface even after the DEP force was switched off, which makes the refractive index profile of the media formed in the fluidics uneven.

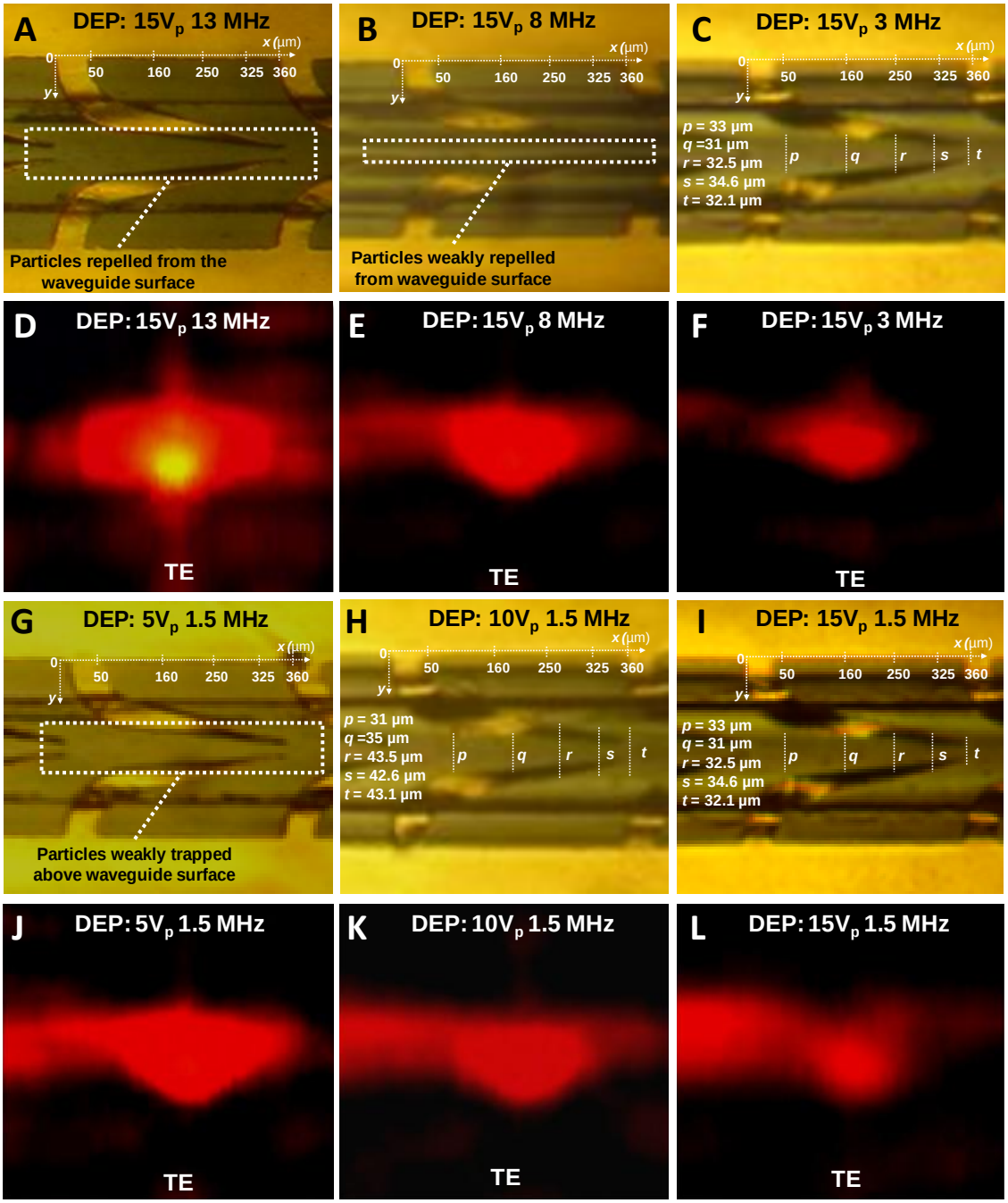

Figure 6.15: ZnO particles and intensity profiles with variation of DEP frequency and AC voltages: (A) ZnO particles flowing at 4 μl min^{-1} were repelled from the center at 15 V_p and f = 13 MHz; (B) ZnO particles flowing at 4 μl min^{-1} were weakly repelled at 15 V_p and f = 8 MHz; (C) ZnO particles were packed at 15 V_p and f = 3 MHz; (D) TE mode intensity profile at DEP: 15 V_p and f = 13 MHz; (E) at DEP: 15 V_p and f = 8 MHz; and (F) at DEP: 15 V_p and f = 3 MHz. (G) ZnO particles trapped in the center at 5 V_p and f = 1.5 MHz; (H) at 10 V_p and f = 1.5 MHz; (I) and at 15 V_p and f = 1.5 MHz; (J) Waveguide TE mode

profile at DEP: 5 V_p and f = 1.5 MHz (K) at DEP: 10 V_p and f = 1.5 MHz; and (L) at DEP: 15 V_p and f = 1.5 MHz.

6.4.3 SiO_2 particles

The suspended SiO_2 particles (Microspheres Nanospheres, n_{SiO2} = 1.47) were tested using the various DEP parameters that either focused or repelled the particles from the regions near the waveguide surface in the microfluidics. The SiO_2 particles experienced a transition from negative to positive DEP behavior as the applied DEP frequency was decreased from 2.4 MHz to 800 kHz (in agreement with the simulations presented in Figure 6.3).

First, the experiments were conducted by keeping the DEP voltage magnitude constant at 15 V_p while varying the DEP frequencies. At the DEP voltage magnitude of 15 V_p and frequency of 2.4 MHz, the SiO_2 particles flowed through the microfluidic channel with a weak repelling force which kept the particles from flowing to the microchannel center (Figure 6.16A). When the frequency was reduced to 1.6 MHz, the SiO_2 particles began to form a particle stream above the waveguide core (Figure 6.16B) and when the frequency was further reduced to 800 kHz, a dense particle stream was formed (Figure 6.16C). The mode intensity profiles corresponding to the particle concentrations formed by the applied DEP forces are presented in Figures 6.16D, 6.16E and 6.16F.

The SiO_2 particles did not induce the coupling or transitioning of the guided modes in the quasi single mode waveguide. Hence, the application of stronger positive DEP forces (at a constant frequency) was not conducted. However, it is interesting to note that in the case of the strong particle focusing at 15 V_p and frequency of 800 kHz (Figure 6.16C), the intensity of the guided mode was slightly reduced (Figure 6.16F). The author attributes this to the waveguide becoming increasingly evanescent due to the presence of highly concentrated SiO_2 particles which may have increased the media refractive index above the index of the polymeric waveguide, but not sufficiently high to induce significant coupling of the guided modes. The phenomena observed in the experiments therefore match the expected outcome that SiO_2 particles are not capable of coupling the guided modes from the quasi single mode waveguide as presented in section 6.2.

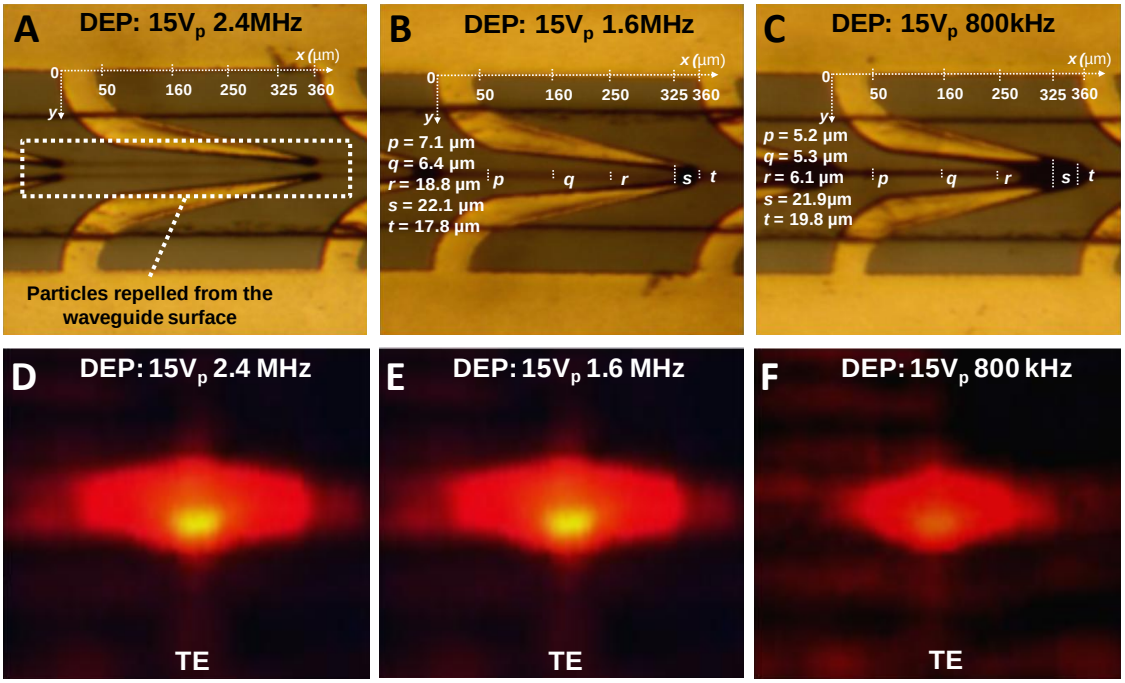

Figure 6.16: SiO_2 particles and intensity profiles with variation of DEP frequency and AC voltages: (A) SiO_2 particles flowing at 4 μl min^{-1} were repelled from the center at 15 V_p and f = 2.4 MHz; (B) SiO_2 particles were packed at 15 V_p and f = 1.6 MHz; (C) SiO_2 particles were densely packed at 15 V_p and f = 800 kHz; (D) TE mode intensity profile at DEP: 15 V_p and f = 2.4 MHz; (E) at DEP: 15 V_p and f = 1.6 MHz; and (F) at DEP: 15 V_p and f = 800 kHz.

6.5 Summary

The author addressed the issues concerning the previously developed multi mode platform, described in chapter 5, by employing the quasi single mode system in Platform 3. Platform 3 exhibits significant advantages in comparison. It is now possible to observe distinct modes and modal behaviours, which was previously unnoticeable using the multi mode platform. In particular, the author distinctly demonstrated the control of optical waves that is dynamic as it was induced by the presence of resonant layers of tuneable particles, which were controlled using a combination of DEP and hydrodynamic forces.

Additionally, the analysis of the waveguide output revealed valuable information regarding the behaviour of guided modes. It was shown that the DEP controlled suspended particles were capable of dynamically manipulating the modal guiding properties of the optical waveguide by forming resonant and anti-resonant layers of the particles in the microfluidics. Specific waveguide modes can be strongly coupled or alternatively isolated from the particle suspension, as the density and thickness of the particle packed layer is adjusted. Such behaviour potentially provides the ability to discriminate between different concentrations and densities of packed particle layers, which were previously not possible using multi mode platforms. Moreover, the observation of modal transitions enhances the system's selectivity and sensitivity as the transition of guided modes due to the anti-resonance which was triggered by the presence of particles with very specific particle densities close to the waveguide surface.

The outcomes of this chapter were published in the Journal of Electrophoresis [21]. In the next chapter, the author presents the summary of his PhD thesis and the future works related to his PhD research project.

References

[1] Chen, C.L., *Foundations for guided-wave optics*. 2007, Hoboken, New Jersey: Wiley.

[2] Kapany, N.S. and J.J. Burke, *Optical Waveguides*. 1972, New York: Academic Press.

[3] Black, R.J. and L. Gagnon, *Optical Waveguide Modes*. 2010, New York: McGraw-Hill.

[4] Okamoto, K., *Fundamentals of optical waveguides* 2nd ed. 2006, Boston: Elsevier.

[5] Hunsperger, R.G., *Integrated optics*. 6th ed. 2009, New York: Springer. 513.

[6] Saleh, B. and M.C. Teich, *Fundamentals of Photonics*. 2007, Hoboken, NJ: Wiley.

[7] Hecht, J., *Understanding fiber optics*. 2002, London: Prentice-Hall.

[8] Bluestein, B.I., I.M. Walczak, and S.Y. Chen, Fiber optic evanescent wave immunosensors for medical diagnostics. *Trends in Biotechnology*, vol. 8, pp. 161-168, 1990.

[9] Khoshmanesh, K., C. Zhang, F.J. Tovar-Lopez, S. Nahavandi, S. Baratchi, K. Kalantar-zadeh, and A. Mitchell, Dielectrophoretic manipulation and separation of microparticles using curved microelectrodes. *Electrophoresis*, vol. 30, pp. 3707-3717, 2009.

[10] Zhang, C., K. Khoshmanesh, F.J. Tovar-Lopez, A. Mitchell, W. Wlodarski, and K. Klantar-zadeh, Dielectrophoretic separation of carbon nanotubes and polystyrene microparticles. *Microfluid and Nanofluid*, vol. 7, pp. 633-645, 2009.

[11] Gaiduk, V.I. and D.S.F. Crothers, Basic molecular mechanisms underlying complex permittivity of water and ice. *Journal of Physical Chemistry A*, vol. 110, pp. 9361-9369, 2006.

[12] Chrimes, A.F., A.A. Kayani, K. Khoshmanesh, P.R. Stoddart, P. Mulvaney, A. Mitchell, and K. Kalantar-zadeh, Dielectrophoresis-Raman spectroscopy system for analysing suspended nanoparticles. *Lab on a Chip*, vol. 11, pp. 921-928, 2011.

[13] Kumar, S., Y.-K. Seo, and G.-H. Kim, Manipulation and trapping of semiconducting ZnO nanoparticles into nanogap electrodes by dielectrophoresis technique. *Applied Physics Letters*, vol. 94, 2009.

[14] Fan, Z.Y. and J.G. Lu, Zinc oxide nanostructures: Synthesis and properties. *Journal of Nanoscience and Nanotechnology*, vol. 5, pp. 1561-1573, 2005.

[15] Biaggio, S.R., R.C. RochaFilho, J.R. Vilche, F.E. Varela, and L.M. Gassa, A study of thin anodic WO3 films by electrochemical impedance spectroscopy. *Electrochimica Acta*, vol. 42, pp. 1751-1758, 1997.

[16] Callister, W.D. and D.G. Rethwisch, *Materials Science and Engineering: an Introduction*. 8th ed. 2010, Hoboken, NJ: John Wiley.

[17] Wu, X.H., A. Yamilov, H. Noh, H. Cao, E.W. Seelig, and R.P.H. Chang, Random lasing in closely packed resonant scatterers. *Journal of the Optical Society of America B-Optical Physics*, vol. 21, pp. 159-167, 2004.

[18] Chung, A.J. and D. Erickson, Optofluidic waveguides for reconfigurable photonic systems. *Optics Express*, vol. 19, pp. 8602-8609, 2011.

[19] Fei, P., Z. He, C. Zheng, T. Chen, Y. Men, and Y. Huang, Discretely tunable optofluidic compound microlenses. *Lab on a Chip*, vol. 11, pp. 2835-41, 2011.

[20] Chilwell, J. and I. Hodgkinson, Thin films field transfer matrix theory of planar multilayer waveguides and reflection from prism loaded waveguides. *Journal of the Optical Society of America A - Optics Image Science and Vision*, vol. 1, pp. 742-753, 1984.

[21] Kayani, A.A., K. Khoshmanesh, T.G. Nguyen, G. Kostovski, A.F. Chrimes, M. Nasabi, D.A. Heller, A. Mitchell, and K. Kalantar-zadeh, Dynamic Manipulation of Modes in an Optical Waveguide Using Dielectrophoresis. *Electrophoresis*, vol. 33, pp. 2075-2085, 2012.

Chapter 7

Conclusion and future works

7.1 Concluding remarks

The author began his PhD journey with the vision of establishing three dimensional (3D) optical objects in liquid and to investigate their functionality. The vision was realized using well controlled suspended particles. The author demonstrated that these suspended particles could be brought close to each other, while still remained unbounded. Hence the particles could be dynamically morphed into forming 3D objects using a range of applied forces. In this thesis, the location and motion of the particles were controlled using the dielectrophoretic (DEP) force. Using this force, particles were focused and repelled from regions of interest within the microfluidics, forming media having distinct physical, especially optical properties. The author sought to develop an optofluidic system

incorporating suspended particles which could exhibit waveguiding properties and have the ability to couple light into densely focused particles.

In order to achieve this objective, the author conducted the research in three stages. In the first stage, he demonstrated the direct coupling of light into a packed concentration of DEP focused particles. Subsequently, in the second stage, the author demonstrated the coupling of light from a multi mode polymeric waveguide into the dielectrophoretically focused particles. Finally, in the third stage of the PhD research project, the author implemented a quasi single mode and demonstrated the coupling and isolation of individual guided modes into the DEP focused particles.

The major findings in each stage of this PhD research project are summarized as follows:

7.1.1 Stage 1

- In the first stage of the research, the author demonstrated the manipulation of 230 and 450 nm diameter silicon dioxide (SiO_2) particles using the DEP forces. He successfully demonstrated the control of these particles into forming 3D suspended objects in liquid by tuning the DEP force and flow rate parameters. The local concentrations and positions of the particles were varied using a range of suitable applied DEP parameters.

- The author had the insight that the dense particle streams consisting of the DEP focused SiO_2 particles possessed a refractive index profile resembling that of an optical waveguide. Hence, he coupled visible light (λ = 635 nm) into the dense particle stream to observe whether the particles exhibited scattering or waveguiding properties. Interestingly, the transmission of light was guided by the dense concentration of 230 nm particles but was scattered by the 450 nm particles. The author established that scattering of light was dominant for the larger sized particles due to the scattering induced by the particle size and effective volumes occupied by the inter particle spacing, when the particles were closely packed under the DEP force. Conversely, the DEP focused concentration of 230 nm particles promoted the transmission of light as it was established that their size and inter particle spacing (when they were closely packed) were much smaller compared to the wavelength of incident light.

- To the best of the author's knowledge, this was the first demonstration of a dynamically formed "optical waveguide" formed using dielectrophoretically packed particles in microfluidics.

7.1.2 Stage 2

- In this stage of the PhD research project, the author demonstrated the coupling of light into the DEP focused particles *via* a multi mode polymeric waveguide. The platform used addressed the limitations of Platform 1 used in the preceding stage of research such as the scattering of light due to the accumulation and flow of non-focused particles. These limitations presented opportunities to further enhance the performance of the system by developing this second platform.

- Tungsten trioxide (WO_3) and SiO_2 particles of 80 and 450 nm diameters, respectively, were used. By applying DEP signals of varying intensities and frequencies, the author established packed concentrations of particles in close vicinity of the waveguide surface, significantly altering the optical properties in this region. In particular, light was coupled from the multi mode polymeric waveguide into the media formed by the DEP focused WO_3 particles. Conversely, light remained largely confined within the polymeric waveguide when the media was shaped by the DEP focused SiO_2 particles.

- This was the first implementation of a tuneable optical waveguide based on dynamically controlled particles in microfluidics.

7.1.3 Stage 3

- In the final stage of this PhD research project, the author implemented a quasi single mode polymeric waveguide and demonstrated the coupling of light into the DEP focused particles. The platforms' performance was a significant enhancement compared to that of the preceding multi mode platform that was developed in stage 2, which allow the propagation of numerous modes simultaneously.

- The author conducted investigations using the WO_3, zinc oxide (ZnO) and SiO_2 particles of 80, 50 and 72 nm diameters, respectively. It was established that under certain DEP

focusing conditions of the WO_3 particles, which resulted in the formation of a media having specific concentrations of particles above the polymeric waveguide, the fundamental mode was strongly coupled to the particle dense media while the first order mode remained largely isolated. This was attributed to the formation of a resonant and anti-resonant layer of packed particles in the microfluidics induced by the DEP forces.

- The author demonstrated the dynamic manipulation of the guided modes of the polymeric waveguide using the DEP focused particles. Additionally, the conditions for establishing the resonant and anti-resonant layers of packed particles using the DEP forces were presented.

- This was the first demonstration of manipulating the guided modes of a quasi single mode polymeric waveguide using suspended particles. Additionally, this was the first demonstration of developing a re-configurable layer of packed particles using the DEP force with resonant and anti-resonant properties.

In conclusion, the author's research project has resulted in accomplishments which bring a new body of knowledge to the field of optofluidics incorporating suspended particles. The outcomes of his PhD research project were published in prestigious peer reviewed scientific journals and proceedings of international conferences. A complete list of publications by the author is as follows:

Journal publications:

- **A.A. Kayani**, K. Khoshmanesh, S.A. Ward, A. Mitchell and K. Kalantar-zadeh, "Optofluidics Incorporating Actively Controlled Micro- and Nanoparticles," Biomicrofluidics, vol. 6, 2012.

- **A.A. Kayani**, K. Khoshmanesh, T.G. Nguyen, G. Kostovski, A.F. Chrimes, M. Nasabi, D.A. Heller, A. Mitchell and K. Kalantar-zadeh, "Dynamic manipulation of modes in an optical waveguide using dielectrophoresis", Electrophoresis, vol. 33, pp. 2075-2085, 2012.

- A.F. Chrimes, K. Khoshmanesh, P.R. Stoddart, **A.A. Kayani**, A. Mitchell, H. Daima, V. Bansal, K. Kalantar-zadeh, "Active Control of Silver Nanoparticles Spacing Using Dielectrophoresis for SERS" Analytical Chemistry, vol. 84, pp. 4029-4035, 2012.

- P. Yi, K. Khoshmanesh, **A.A. Kayani**, A.F. Chrimes, K. Ghorbani and K. Kalantar-zadeh, "Heat transfer investigations of suspended Al_2O_3 nanoparticles in microfluidics", Lab on a Chip, vol. 12, pp. 2520-2525, 2012.

- **A.A. Kayani**, A.F. Chrimes, K. Khoshmanesh, V. Sivan, E. Zeller, K. Kalantar-zadeh and A. Mitchell, "Interaction of Guided Light in Rib Polymer Waveguides with Dielectrophoretically Manipulated Nanoparticles", Microfluidics and Nanofluidics, vol. 11, pp. 93-104, 2011.

- A.F. Chrimes, **A.A. Kayani**, K. Khoshmanesh, P. Mulvaney, P. Stoddart, A. Mitchell and K. Kalantar-zadeh, "Dielectrophoresis-Raman Spectroscopy System for Analyzing Suspended Nanoparticles", Lab on a Chip, vol. 11, pp. 921-928, 2011.

- K. Kalantar-zadeh, K. Khoshmanesh, **A.A. Kayani**, S. Nahavandi, and A. Mitchell, "Dielectrophoretically tuneable optical waveguides using nanoparticles in microfluidics," Applied Physics Letters, vol. 96, 2010.

- **A.A. Kayani**, C. Zhang, K. Khoshmanesh, J. L. Campbell, A. Mitchell, and K. Kalantar-zadeh, "Novel tuneable optical elements based on nanoparticle suspensions in microfluidics," Electrophoresis, vol. 31, pp. 1071-1079, 2010.

- K. Khoshmanesh, C. Zhang, J.L. Campbell, **A.A. Kayani**, S. Nahavandi, A. Mitchell and K. Kalantar-zadeh, "Dielectrophoretically assembled particles: feasibility for optofluidic systems," Microfluidics and Nanofluidics, vol. 9, pp. 755-763, 2010.

Conference publications:

- **A.A. Kayani**, A. Mitchell and K. Kalantar-zadeh, "Nanoparticle dielectrophoresis in evanescent sensitive optofluidic devices", 2nd Nano Today Conference, Waikoloa, Hawaii, USA, 11-15 December, 2011.

- **A.A. Kayani**, A. Mitchell and K. Kalantar-zadeh, "Dielectrophoresis for the manipulation of polymer waveguide properties: feasibility for optofluidic sensing", accepted for publication in the 1st European Optical Society (EOS) Conference on Optofluidics 2011, Munich, Germany, 23-25 May, 2011.

- **A.A. Kayani**, A. Mitchell and K. Kalantar-zadeh, "Dielectrophoresis of nanoparticles for polymer waveguide manipulation", accepted for publication in the Conference on Lasers and Electro Optics (CLEO) 2011, Baltimore, Maryland, USA, 1-5 May, 2011.

- A.F. Chrimes , **A.A. Kayani**, K. Khoshmanesh, A. Mitchell and K. Kalantar-zadeh"Dielectrophoresis-Raman Spectroscopy System for Analysing Suspended WO_3 Nanoparticles", accepted for publication in the SPIE International Symposium on Defense, Security and Sensing, Orlando, Florida, USA, 25-29 April, 2011.

- **A.A. Kayani**, K. Khoshmanesh, A.F. Chrimes, A. Mitchell and K. Kalantar-zadeh, "Tuneable optical waveguide using dielectrophoretically controlled nanoparticles in microfluidics", accepted for publication in the SPIE International Symposium on Defense, Security and Sensing, Orlando, Florida, USA, 25-29 April, 2011.

- **A.A. Kayani**, K. Khoshmanesh, C. Zhang, A. Mitchell and K. Kalantar-zadeh, "Dielectrophoretic Manipulation of Silica Nanoparticles in Optofluidics", accepted for publication in the μFlu2010, 2nd European Conference on Microfluidics 2010, Toulouse, France, December 8-10, 2010.

- **A.A. Kayani**, K. Khoshmanesh, C.Zhang, A. Mitchell and K. Kalantar-zadeh, "Dielectrophoresis of Silica Nanoparticles as Tuneable Optical Devices", accepted for publication in the AiChE, American Institute of Chemical Engineers Annual Meeting 2010, Salt Lake City, UT, USA, November 7-12, 2010.

- C.Zhang, K. Khoshmanesh, **A.A. Kayani**, F.J. Tovar-Lopez, W. Wlodarski, A. Mitchell and K. Kalantar-zadeh, "Dielectrophoretic Manipulation of Polystyrene Micro Particles in Microfluidic Systems", accepted for publication in the ASME 2009 2nd Micro/Nanoscale Heat & Mass Transfer International Conference, Shanghai, China, December 18-21, 2009.

7.2 Recommendations for future work

Despite the accomplishments attained in this PhD research project, the author feels that there are numerous opportunities for continuing his research and recommends the following as the future work:

- The evolution of microfabrication methods could realize much more advanced and accurate particle manipulation platforms: in particular, more sophisticated electrodes (such as 3D or travelling wave DEP electrodes) for creating well controlled DEP generated electric field gradients. Such electric field gradients could be utilized to provide improved access and control of particles down to the individual level, yielding interesting optical responses. The likelihood of particles agglomerating close to the microfluidic channel surfaces would also decrease since 3D microelectrodes can levitate and focus the particles in the center of the microchannel [1] as opposed to the authors' platforms which focus the particles close to the microchannel floor.

- Other actively applied forces such as acoustic [2-4], optical [5-7] or magnetic [8-10] as well as elements for thermal fields as described in chapter 2 can be employed in combination with the DEP force to provide accurate particle positioning and control which is key to achieving the desired concentration and placement of particles relative to the optical waveguides. DEP forces manipulate particles by virtue of their permittivity and conductivity. Conversely, using acoustic, optical and magnetic manipulations, particles can be manipulated depending on other parameters such as particle elasticity, volume and magnetic susceptibility.

- Introducing biological particles for investigating and expanding the existing experimental platforms' biosensing capabilities could provide the future researcher with the ability of conducting rapid and complicated assays, and developing single particle sensors controlled by DEP and/or actively applied particle manipulation forces.

- In order to develop the experimental platforms into a robust optofluidic sensor, the sensitivity and selectivity needs to be enhanced so that it is capable of detecting and distinguishing particles of different concentrations, physical and chemical properties. This

could be achieved by exploring the precise impact of the DEP focused particles on the radiation, scattering and phase velocity of the guided modes [11].

- Analysis of SERS-active particles under microfluidic flow which are focused by DEP and other actively applied forces could yield interesting responses. For instance, the coupling of optical signals as demonstrated by the author, which indicates the presence of optical fields in the DEP focused particle dense media could result in the amplification of SERS signals, producing highly sensitive Raman sensing platforms [12].

- Examination of waveguiding and scattering properties of individual or clusters of closely packed particles over a wider wavelength range, using a supercontinuum laser source [13] and utilizing different particle candidates with distinct optical confinement, surface chemistry, and refractive index properties could yield promising results for developing the experimental platform into an advanced optofluidic sensor.

- Investigate the feasibility of using metallic particles that exhibit surface plasmon resonance activity [14] when excited with a resonant optical source. These particles could be brought close together using actively applied forces and owing to the fact that they have a greater capacity for confining optical waves *via* plasmon resonance, the optical response of the system due to the presence of such particles integrated with organic or inorganic particle entities could be explored. Such investigations could yield interesting results, realizing sensitive and dynamic plasmonic optofluidic platforms, which are both tuneable and reconfigurable.

References

[1] Khoshmanesh, K., S. Nahavandi, S. Baratchi, A. Mitchell, and K. Kalantar-zadeh, Dielectrophoretic platforms for bio-microfluidic systems. *Biosensors & Bioelectronics*, vol. 26, pp. 1800-1814, 2011.

[2] Friend, J. and L.Y. Yeo, Microscale acoustofluidics: Microfluidics driven via acoustics and ultrasonics. *Reviews of Modern Physics*, vol. 83, pp. 647-704, 2011.

[3] Shi, J., H. Huang, Z. Stratton, Y. Huang, and T.J. Huang, Continuous particle separation in a microfluidic channel via standing surface acoustic waves (SSAW). *Lab on a Chip*, vol. 9, pp. 3354-3359, 2009.

[4] Petersson, F., L. Aberg, A.-M. Sward-Nilsson, and T. Laurell, Free flow acoustophoresis: Microfluidic-based mode of particle and cell separation. *Analytical Chemistry*, vol. 79, pp. 5117-5123, 2007.

[5] Jonas, A. and P. Zemanek, Light at work: The use of optical forces for particle manipulation, sorting, and analysis. *Electrophoresis*, vol. 29, pp. 4813-4851, 2008.

[6] Erickson, D., X. Serey, Y.F. Chen, and S. Mandal, Nanomanipulation using near field photonics. *Lab on a Chip*, vol. 11, pp. 995-1009, 2011.

[7] Halas, N.J., S. Lal, W.-S. Chang, S. Link, and P. Nordlander, Plasmons in Strongly Coupled Metallic Nanostructures. *Chemical Reviews*, vol. 111, pp. 3913-3961, 2011.

[8] Suwa, M. and H. Watarai, Magnetoanalysis of micro/nanoparticles: A review. *Analytica Chimica Acta*, vol. 690, pp. 137-147, 2011.

[9] Ivon Rodriguez-Villarreal, A., M.D. Tarn, L.A. Madden, J.B. Lutz, J. Greenman, J. Samitier, and N. Pamme, Flow focussing of particles and cells based on their intrinsic properties using a simple diamagnetic repulsion setup. *Lab on a Chip*, vol. 11, pp. 1240-1248, 2011.

[10] Peyman, S.A., E.Y. Iwan, O. Margarson, A. Iles, and N. Pamme, Diamagnetic repulsion-A versatile tool for label-free particle handling in microfluidic devices. *Journal of Chromatography A*, vol. 1216, pp. 9055-9062, 2009.

[11] Kayani, A.A., A.F. Chrimes, K. Khoshmanesh, V. Sivan, E. Zeller, K. Kalantar-zadeh, and A. Mitchell, Interaction of guided light in rib polymer waveguides with dielectrophoretically controlled nanoparticles. *Microfluidics and Nanofluidics*, vol. 11, pp. 93-104, 2011.

[12] Kayani, A.A., K. Khoshmanesh, T.G. Nguyen, G. Kostovski, A.F. Chrimes, M. Nasabi, D.A. Heller, A. Mitchell, and K. Kalantar-zadeh, Dynamic Manipulation of Modes in an Optical Waveguide Using Dielectrophoresis. *Electrophoresis*, vol. 33, pp. 2075-2085, 2012.

[13] Alfano, R., *The Supercontinuum Laser Source: Fundamentals with Updated References*. 2006, New York: Springer.

[14] Maier, S., *Plasmonics: fundamentals and applications*. 2007, New York: Springer.

Appendix A

List of publications

A.1 Journal publications:

- **A.A. Kayani**, K. Khoshmanesh, S.A. Ward, A. Mitchell and K. Kalantar-zadeh, "Optofluidics Incorporating Actively Controlled Micro- and Nanoparticles," Biomicrofluidics, vol. 6, 2012.

- A.F. Chrimes, K. Khoshmanesh, P.R. Stoddart, **A.A. Kayani**, A. Mitchell, H. Daima, V. Bansal, K. Kalantar-zadeh, "Active Control of Silver Nanoparticles Spacing Using Dielectrophoresis for SERS", Analytical Chemistry, vol. 84, pp. 4029-4035, 2012.

- P. Yi, K. Khoshmanesh, **A.A. Kayani**, A.F. Chrimes, K. Ghorbani and K. Kalantar-zadeh, "Heat transfer investigations of suspended Al_2O_3 nanoparticles in microfluidics", Lab on a Chip, vol. 12, pp. 2520-2525, 2012.

- **A.A. Kayani**, K. Khoshmanesh, T.G. Nguyen, G. Kostovski, A.F. Chrimes, M. Nasabi, D.A. Heller, A. Mitchell and K. Kalantar-zadeh, "Dynamic manipulation of modes in an

optical waveguide using dielectrophoresis", Electrophoresis, vol. 33, pp. 2075-2085, 2012.

- **A.A. Kayani**, A.F. Chrimes, K. Khoshmanesh, V. Sivan, E. Zeller, K. Kalantar-zadeh and A. Mitchell, "Interaction of Guided Light in Rib Polymer Waveguides with Dielectrophoretically Manipulated Nanoparticles", Microfluidics and Nanofluidics, vol. 11, pp. 93-104, 2011.

- A.F. Chrimes, **A.A. Kayani**, K. Khoshmanesh, P. Mulvaney, P. Stoddart, A. Mitchell and K. Kalantar-zadeh, "Dielectrophoresis-Raman Spectroscopy System for Analyzing Suspended Nanoparticles", Lab on a Chip, vol. 11, pp. 921-928, 2011.

- K. Kalantar-zadeh, K. Khoshmanesh, **A.A. Kayani**, S. Nahavandi, and A. Mitchell, "Dielectrophoretically tuneable optical waveguides using nanoparticles in microfluidics," Applied Physics Letters, vol. 96, 2010.

- **A.A. Kayani**, C. Zhang, K. Khoshmanesh, J. L. Campbell, A. Mitchell, and K. Kalantar-zadeh, "Novel tuneable optical elements based on nanoparticle suspensions in microfluidics," Electrophoresis, vol. 31, pp. 1071-1079, 2010.

- K. Khoshmanesh, C. Zhang, J.L. Campbell, **A.A. Kayani**, S. Nahavandi, A. Mitchell and K. Kalantar-zadeh, "Dielectrophoretically assembled particles: feasibility for optofluidic systems." Microfluidics and Nanofluidics, vol. 9, pp. 755-763, 2010.

A.2 Conference publications:

- **A.A. Kayani**, A. Mitchell and K. Kalantar-zadeh, "Nanoparticle dielectrophoresis in evanescent sensitive optofluidic devices", 2nd Nano Today Conference, Waikoloa, Hawaii, USA, 11-15 December, 2011.

- **A.A. Kayani**, A. Mitchell and K. Kalantar-zadeh, "Dielectrophoresis for the manipulation of polymer waveguide properties: feasibility for optofluidic sensing", accepted for publication in the 1st European Optical Society (EOS) Conference on Optofluidics 2011, Munich, Germany, 23-25 May, 2011.

- **A.A. Kayani**, A. Mitchell and K. Kalantar-zadeh, "Dielectrophoresis of nanoparticles for polymer waveguide manipulation", accepted for publication in the Conference on Lasers and Electro Optics (CLEO) 2011, Baltimore, Maryland, USA, 1-5 May, 2011.

- A.F. Chrimes , **A.A. Kayani**, K. Khoshmanesh, A. Mitchell and K. Kalantar-zadeh"Dielectrophoresis-Raman Spectroscopy System for Analysing Suspended WO_3 Nanoparticles", accepted for publication in the SPIE International Symposium on Defense, Security and Sensing, Orlando, Florida, USA, 25-29 April, 2011.

- **A.A. Kayani**, K. Khoshmanesh, A.F. Chrimes, A. Mitchell and K. Kalantar-zadeh, "Tuneable optical waveguide using dielectrophoretically controlled nanoparticles in microfluidics", accepted for publication in the SPIE International Symposium on Defense, Security and Sensing, Orlando, Florida, USA, 25-29 April, 2011.

- **A.A. Kayani**, K. Khoshmanesh, C. Zhang, A. Mitchell and K. Kalantar-zadeh, "Dielectrophoretic Manipulation of Silica Nanoparticles in Optofluidics", accepted for publication in the μFlu2010, 2nd European Conference on Microfluidics 2010, Toulouse, France, December 8-10, 2010.

- **A.A. Kayani**, K. Khoshmanesh, C.Zhang, A. Mitchell and K. Kalantar-zadeh, "Dielectrophoresis of Silica Nanoparticles as Tuneable Optical Devices", accepted for publication in the AiChE, American Institute of Chemical Engineers Annual Meeting 2010, Salt Lake City, UT, USA, November 7-12, 2010.

- C.Zhang, K. Khoshmanesh, **A.A. Kayani**, F.J. Tovar-Lopez, W. Wlodarski, A. Mitchell and K. Kalantar-zadeh, "Dielectrophoretic Manipulation of Polystyrene Micro Particles in Microfluidic Systems", accepted for publication in the ASME 2009 2nd Micro/Nanoscale Heat & Mass Transfer International Conference, Shanghai, China, December 18-21, 2009.